Properties of Sulfide Solid Electrolytes Studied by Electronic Structure Calculations

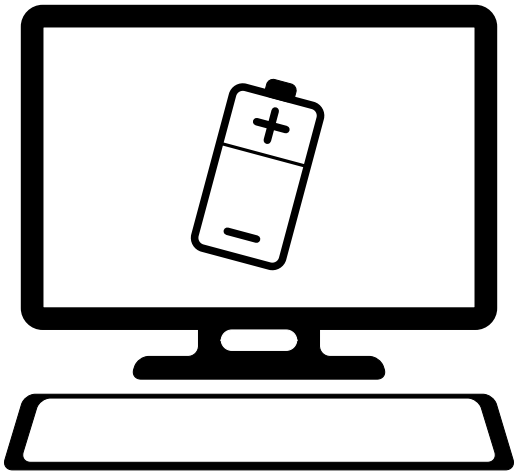

Marcel Sadowski
Technische Universität Darmstadt
2023

On the cover: Sketch of a desktop computer visualizing a battery.

Properties of Sulfide Solid Electrolytes Studied by Electronic Structure Calculations

Zur Erlangung des akademischen Grades Doktor der Naturwissenschaften (Dr. rer. nat.)
genehmigte Dissertation vorgelegt
von Marcel Sadowski
geboren in Rüsselsheim

Fachgebiet: Materialmodellierung
Fachbereich: Material- und Geowissenschaften
Technische Universität Darmstadt

Berichter:	Prof. Dr. rer. nat. Karsten Albe, Technische Universität Darmstadt
Mitberichter:	Prof. Dr. rer. nat. Jan Philipp Hofmann, Technische Universität Darmstadt
1. Prüfer:	Prof. Dr. rer. nat. Wolfgang Zeier, Westfälische Wilhelms-Universität Münster
2. Prüfer:	Prof. Dr. rer. nat. Oliver Clemens, Universität Stuttgart

Tag der Einreichung: 27.07.2022
Tag der Prüfung: 11.11.2022
Jahr der Veröffentlichung: 2023

Darmstadt 2022
D17

Please cite this document as:
URN: urn:nbn:de:tuda-prints-237527
URL: https://tuprints.ulb.tu-darmstadt.de/id/eprint/23752

Sadowski, Marcel: Properties of Sulfide Solid Electrolytes Studied by Electronic Structure Calculations
Darmstadt, Technische Universität Darmstadt
Jahr der Veröffentlichung auf TUprints: 2023
URN: urn:nbn:de:tuda-prints-237527
URL: https://tuprints.ulb.tu-darmstadt.de/id/eprint/23752
Tag der mündlichen Prüfung: 11.11.2022

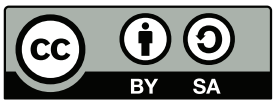

Erklärung laut Promotionsordnung

§8 Abs. 1 lit. c PromO

Ich versichere hiermit, dass die elektronische Version meiner Dissertation mit der schriftlichen Version übereinstimmt.

§8 Abs. 1 lit. d PromO

Ich versichere hiermit, dass zu einem vorherigen Zeitpunkt noch keine Promotion versucht wurde. In diesem Fall sind nähere Angaben über Zeitpunkt, Hochschule, Dissertationsthema und Ergebnis dieses Versuchs mitzuteilen.

§9 Abs. 1 PromO

Ich versichere hiermit, dass die vorliegende Dissertation selbstständig und nur unter Verwendung der angegebenen Quellen verfasst wurde.

§9 Abs. 2 PromO

Die Arbeit hat bisher noch nicht zu Prüfungszwecken gedient.

Darmstadt, 24. April 2023

Marcel Sadowski

Abstract

Rechargeable all-solid-state batteries (ASSBs) are traded as next-generation power sources for mobile applications, because they are believed to provide increased energy densities, higher power densities and improved cyclability compared to conventional Li-ion batteries (LIBs).[1] Moreover, the replacement of flammable liquid organic electrolytes, used in LIBs, with non-flammable solid electrolytes (SEs) might eliminate safety issues and enables new battery designs.[2] In this regard, sulfide SEs are promising candidates because they show ionic conductivities of up to ≈10 mS/cm at room temperature and convince with favorably soft mechanical properties that enable an easy integration into the battery.[3–5] Their disadvantage, however, is a lack of electrochemical stability against most electrode materials.[3,6,7] Despite the huge effort to study sulfide SEs, however, many of the related processes, such as exact diffusion mechanisms or interface degradation reactions, have not been understood in detail. Such an understanding could offer new optimization strategies, and we have therefore used atomistically resolved density functional theory (DFT) calculations and *ab-initio* molecular dynamics (AIMD) simulation over the past years to investigate selected sulfide SEs.

A detailed introduction into the topic is given in Chapter 1 and a literature review for the materials of interest in Chapter 2 will lay out the specific research questions tackled in this work. The applied methods and theoretical background are explained in Chapter 3 and lay the foundation for the following chapters.

In Chapter 4 we will discuss the litium thiophosphate (LiPS) system that comprises multiple crystalline phases such as Li_3PS_4, $Li_7P_3S_{11}$ and $Li_4P_2S_6$. Structurally, the situation is further complicated by the coexistence of glass phases exhibiting an amorphous structure.[8] Hence, most sulfide SEs are actually glass-ceramics whose properties are determined by the types and amounts of the underlying phases. We strongly focus on glass phases as their structure is difficult to analyze by experiments. To this end, we generated structure models for LiPS glasses at various compositions by applying a computational melt-quenching approach and compare the stability, structure and Li^+ transport properties of crystalline and glassy phases. We find that all glasses are metastable and exhibit similar Li^+ diffusion coefficients despite the fact that they are comprised of different basic structural units (PS_4^{3-}, $P_2S_7^{4-}$, $P_2S_6^{4-}$). Furthermore, the occurrence of unusual structural units is observed and the association of structural units via cross-linking S−S bonds is derived as compensation mechanism in case of local Li deficiency. Finally, the interfacial stability against Li metal and internal interfaces are investigated. In this regard, the usage of defect formation energies as descriptors to judge the stability of interfaces is discussed.

Next, the quaternary, argyrodite-type system Li_6PS_5Br is analyzed in Chapter 5. The key question concerns the experimentally observed Br^-/S^{2-} site-exchange among its 4*a* and 4*d* sites, that can be controlled via the synthesis procedure without altering the composition.[9,10] How does the Br^-/S^{2-} site-

exchange influence the structure and properties of the material? We will show that the ordered structure is the most stable configuration and that the lattice constants show a minimum at 50% site-exchange. The main part discusses the Li^+ transport properties and how the introduction of Br^-/S^{2-} site-exchange enables the transition from local to long-range Li^+ diffusion. Moreover, we were able to identify the underlying diffusion mechanism and show that especially the Br^- ions on S^{2-} sites facilitate the generation of Li^+ Frenkel pairs with mobile Li^+ interstitials. Finally, we have a closer look on the Li^+ substructure and analyze how the Br^-/S^{2-} site-exchange interacts with the Li^+ transport properties of symmetrical tilt and twist grain boundaries.

In Chapter 6 we will deal with the recently developed Li_7SiPS_8, which was found to crystallize in an orthorhombic phase (ortho-Li_7SiPS_8) with rather poor Li^+ transport properties and a more promising tetragonal phase (tetra-Li_7SiPS_8).[11] As not much is known about the material we examined several of its properties, also in light of the Si/P disorder that is observed experimentally. We show that ortho-Li_7SiPS_8 is the more stable phase and experimental trend of poor transport properties is confirmed. Tetra-Li_7SiPS_8 is the much better conductor owing to its fast diffusion along the c axis. The Si/P distribution was found to have a negligible influence on the transport properties, and a compression of the material leads to decreased diffusion coefficients. Finally, the interfacial instability of tetra-Li_7SiPS_8 against Li metal was probed by means of explicit interface calculations.

At long last, we will conclude this work in Chapter 7 and present open questions and promising directions for future studies.

Zusammenfassung

Wiederaufladbare Feststoffbatterien [engl.: all-solid-state battery (ASSB)] werden als zukunftsträchtige Energiequellen für mobile Anwendungen gehandelt, da von ihnen im Vergleich zu konventionellen Li-Ionen-Batterien [engl.: Li-ion battery (LIB)] erhöhte Energie- und Leistungsdichten sowie eine verbesserte Zyklierbarkeit erwartet werden.[1] Zusätzlich beseitigt die Substitution der leicht entzündlichen, organischen Flüssigelektrolyten, wie sie in LIBs zum Einsatz kommen, mit nicht brennbaren Feststoffelektrolyten [engl.: solid electrolyte (SE)] Sicherheitsprobleme und ermöglicht neue Batteriebauweisen.[2] Die Klasse der sulfidische SEs stellt dabei vielversprechende Materialien welche die mitunter höchsten ionischen Leitfähigkeiten von bis zu 10 mS/cm bei Raumtemperatur aufweisen und mit vorteilhaften mechanischen Eigenschaften überzeugen, die eine leichte Integration in die Batterie ermöglichen.[3–5] Zu den größten Nachteilen zählen allerdings eine limitierende elektrochemische Stabilität gegenüber den meisten Elektrodenmaterialien.[3,6,7] Trotz des großen Forschungsaufwandes sind viele Prozesse, wie beispielsweise Diffusionsmechanismen oder Grenzflächenreaktionen, nicht genau verstanden. Dieses Verständnis ist allerdings notwendig, um neue Optimierungsstrategien zu entwickeln und wir haben deshalb innerhalb der letzten Jahre atomistisch aufgelöste Simulationen im Rahmen der Dichtefunktionaltheorie [engl.: density functional theory (DFT)] und *ab-initio* Molekulardynamik [engl.: *ab-initio* molecular dynamics (AIMD)] angewandt, um relevante Eigenschaften sulfidischer SEs zu untersuchen.

In Kapitel 1 wird zunächst eine detaillierte Einführung in das Thema gegeben. Im folgenden Literaturüberblick in Kapitel 2 zu den behandelten Materialien werden die grundlegenden Fragestellungen dieser Arbeit eingeführt. Das theoretische Hintergrundwissen wird in Kapitel 3 vorgestellt und stellt die Grundlagen für die folgenden Kapitel.

In Kapitel 4 wird zunächst das System der Lithiumthiophosphate behandelt, das einige kristalline Phasen wie Li_3PS_4, $Li_7P_3S_{11}$ oder $Li_4P_2S_6$ beinhaltet. Strukturell wird die Situation durch die Koexistenz von amorphen Glasphasen verkompliziert.[8] Dementsprechend handelt es sich bei dem Material meist um Glaskeramiken, deren Eigenschaften von der Art und Menge der zugrundeliegenden Phasen abhängt. Wir haben uns auf Glasphasen fokussiert, weil deren Struktur im Experiment schwer zu erfassen ist. Dazu wurden Strukturmodelle verschiedener Zusammensetzungen durch simuliertes Abschrecken aus Schmelzen generiert und deren Stabilität, Struktur und Li^+ Transporteigenschaften mit denen der Kristallphasen verglichen. Es konnte gezeigt werden, dass alle Gläser metastabil sind und vergleichbare Li^+ Diffusionskoeffizienten aufweisen, obwohl sie aus verschiedenen Struktureinheiten (PS_4^{3-}, $P_2S_7^{4-}$, $P_2S_6^{4-}$) aufgebaut sind. Außerdem wurde das Auftreten von unüblichen Struktureinheiten beobachtet und ein Kompensationsmechanismus im Falle lokaler Lithiumarmut abgeleitet bei dem sich Struktureinheiten über S–S Bindungen vernetzen. Zuletzt wird die Grenzflächenstabilität gegenüber Li-Metall sowie die interne

Grenzflächen der Glaskeramiken betrachtet. In diesem Zusammenhang wird die Anwendung von Defektbildungsenergien als Deskriptoren zur Einschätzung der Grenzflächenstabilität diskutiert.

Im darauf folgenden Kapitel 5 wird das quaternäre System Li_6PS_5Br behandelt. Die Hauptfragen betreffen die experimentell beobachtete Br^-/S^{2-} Unordnung unter den 4*a* und 4*d* Plätzen, die über die Synthesebedingungen ohne Kompositionsänderungen kontrolliert werden kann:[9,10] Wie beeinflusst die Br^-/S^{2-} Unordnung die weitere Struktur und Eigenschaften des Materials? Wir werden zeigen, dass die stabilste Konfiguration ohne jegliche Unordnung erreicht wird und die Gitterparameter bis zu einem Austausch von 50% der Br^-/S^{2-} Ionen abnehmen. Im Hauptteil werden die Li^+ Transporteigenschaften diskutiert und gezeigt, wie die lokale Diffusion durch die Einführung von Br^-/S^{2-} Unordnung in eine langreichweitige überführt wird. Darüber hinaus konnte der genaue Diffusionsmechanismus identifiziert werden. So ermöglichen vor allem Br^- Ionen auf S^{2-} Plätzen die Generierung von Li^+ Frenkel-Paaren mit mobilen Li^+ Zwischengitterionen. Daraufhin wird ein genauer Blick auf die Li^+ Substruktur geworfen und analysiert welche Einwirkungen die Br^-/S^{2-} Unordnung auf Li^+ Transporteigenschaften von symmetrischen Kipp- und Drehkorngrenzen hat.

Das kürzlich entwickelte Material Li_7SiPS_8 steht im Fokus von Kapitel 6.[11] Es kristallisiert in einer orthorhombischen Phase (ortho-Li_7SiPS_8) mit geringen Li^+ Transporteigenschaften und einer vielversprechenden tetragonalen Phase (tetra-Li_7SiPS_8). Da nicht viel über das Material bekannt ist wurden verschiedene Aspekte, wie der Einfluss der gefunden Si/P Unordnung auf die Eigenschaften, untersucht. So ist ortho-Li_7SiPS_8 die stabilere Phase, weist aber tatsächlich eine langsame Li^+ Diffusion auf. Hingegen ist tetra-Li_7SiPS_8 aufgrund der schnellen Diffusion entlang der *c*-Achse der bessere Ionenleiter. Die Si/P Unordnung scheint dabei keinen nennenswerten Einfluss auf die Diffusion zu haben, wohingegen die Kompression des Materials zu einer verminderten Diffusion führt. Die Instabilität von tetra-Li_7SiPS_8 gegenüber Li-Metall wird schließlich in expliziten Grenzflächensimulationen analysiert.

Zu guter Letzt schließen wir die Arbeit in Kapitel 7 ab, geben eine kurze Zusammenfassung der wichtigsten Punkte und erörtern aussichtsreiche Forschungsperspektiven für zukünftige Arbeiten.

Danksagung

Zunächst gilt mein Dank Prof. Dr. Karsten Albe, ohne den meine Promotion nicht in dieser Art und Weise abgelaufen wäre. Danke für Dein Vertrauen, mich weitestgehend selbständig am FestBatt-Projekt arbeiten zu lassen. Deine ehrliche und humorvolle Art und die motivierenden Diskussionen gaben mir wieder Auftrieb, wenn die Frustrationstoleranz stark beansprucht wurde. In diesem Sinne, und natürlich auch unvergessen als Bergführer in den französischen Alpen, hast Du es immer geschafft das Gefühl *ain't no mountain high enough*[a] zu übermitteln.

Danken für Ihre investierte Zeit und den Aufwand, sich meiner Thesis anzunehmen, möchte ich den Mitgliedern meiner Prüfungskommission: Prof. Dr. Jan Philipp Hofmann, Prof. Dr. Oliver Clemens und Prof. Dr. Wolfgang Zeier. Ich hoffe, dass es für keinen *it's been a hard day's night*[b] bei der Lektüre dieser Arbeit wurde. Insbesondere Prof. Dr. Wolfgang Zeier und seinem Team danke ich für die erfolgreiche und angenehme Zusammenarbeit innerhalb der letzten Jahre, welche diese Arbeit stark geprägt hat.

Innerhalb des Fachgebiets Materialmodellierung gebührt ein großer Dank Gabriele Rühl, auf die man sich getreu dem Motto *I'll be there for you*[c] in allen organisatorischen Angelegenheiten immer voll verlassen kann.

Hervorheben möchte ich außerdem Dr. Sabrina Sicolo, ohne die ich mich vielleicht nie getraut hätte, in die theoretische Untersuchung von Materialien einzusteigen. Vielen Dank für die investierte Zeit, Dein kontinuierliches Mentoring, sorgfältiges Korrekturlesen und die hoffentlich weiterhin anhaltende, gute Zusammenarbeit – *This is our time now \ To create and invent*.[d]

Ich danke allen MMs, die ich nicht nur als Kollegen, sondern zum Großteil auch als Freunde schätze. Hervorzuheben ist vor allem Dr. Constanze Kalcher, deren Engagement und gute Laune die Arbeitsgruppe zusammengehalten hat, und ohne deren technischen Supports so manches Ovito-Skript nie das Tageslicht erblickt hätte. Wie hatte es ein Eintrag im Ovito Support Forum so schön zusammengefasst: "You are a kind man." Ich danke Lisette Haarmann, der liebsten Kollegin die man sich wünschen kann, für ein hervorragendes Zusammenspiel im FestBatt-Projekt und an diversen Spieleabenden. Ich danke Dr. Daniel Utt für viele Diskussionen, das Palaver zwischendurch und alle Stunden die er geopfert hat, um Server-Probleme zu lösen damit die Gruppe arbeitsfähig bleibt – wahrscheinlich würde er sagen: *Yeah, das ist einfach nur normal*.[e] Dank geht an Dr. Jochen Rohrer für hilfreiche Diskussionen und Ausführungen zu den Grundlagen von DFT und Bandanpassungen, Deine bodenständige Art sowie schrammelige Gitarren-Sessions. Danke an Arne Klomp für diverse Feierabend-Bierchen und Dr. Leonie Koch für Erörterungen zu wichtigen Themen, wie zum Beispiel der Definition von "Spaß-Nudeln". Besten Dank auch meinen Büro-Kollegen David Kasdorf für Debatten zu allen mögliche Themen und Linus Erhard für Hilfe bei der Berechnung von elastischen Konstanten, quasi *under*

pressure.[f] Ein Dankeschön geht an Lorenzo Villa für Spaghetti Aglio, Olio e Peperoncino in Kombination mit der richtigen Musik, *so all must be well*.[g] Ebenfalls danke ich den ehemaligen MMs Dr. Kai Mayer für das Aufzeigen beruflicher Alternativen und Dr. Tobias Brink in seiner Rolle als Fremdenführer in Lausanne, dessen "Avez-vous aussi du chasselas?" uns vor Nüchternheit bewahrte. Danke an alle restlichen und ehemaligen MMs, die mit Ihren hilfreichen Kommentaren und Diskussionen zu fachlichen und außerfachlichen Themen den Arbeitsalltag stets bereichert haben.

I thank Prof. Dr. Nicola Marzari, Irène Laroche and Dr. Iurii Timrov for welcoming and supporting me in the THEOS group at EPFL Lausanne. I enjoyed the collaboration as well as the beautiful region – *Les beautés de la patrie* \ *Parlent à l'âme attendrie*.[h]

Ein liebevolles Dankeschön geht an Fabienne Franz, die mir in anstrengenden Phasen immer den Rücken freigehalten hat, so viele Interessen wie Freizeit, Musik, Kultur bis hin zum Lebensstil, aber zuweilen auch Weltschmerz, mit mir teilt, und die ich immer an meiner Seite weiß – *Wenn irgendwas gut ist dann das hier*.[i]

Meinen Eltern und meiner Schwester danke ich dafür, dass sie mich immer untersützt haben und weiterhin werden – *And I know when I need it, I can count on you like four, three, two and you'll be there*.[j]

Ich danke den Jungs von der Band und allen meinen restlichen Freunden, die mich über die Jahre unterstützt, von der Arbeit abgelenkt, mit mir musiziert und schöne Stunden mit mir verbracht haben – *thank you for being a friend*.[k]

Für finanzielle Unterstützung möchte ich mich noch bei dem Bundesministerium für Bildung und Forschung (03XP0174A) und dem Deutschen Akademischen Auslandsdienst, sowie bei der Technischen Universität Darmstadt und dem Forschungszentrum Jülich für Rechenzeit auf den Lichtenberg- und JUWELS-Hochleistungsrechnern bedanken.

Abschließend bleibt mir nur zu sagen: *Und ich bereue nix, ich bereue nix* \ *Ich würde alles wieder ganz genau so machen, oh yeah*.[l]

Dank geht ebenso an all die Künstler, deren Musik mir Kraft und Inspiration geliefert hat. Alle können hier nicht genannt werden, aber einige passend ausgewählte Titel und Interpreten seien hier berücksichtigt:

[a] Marvin Gaye, Tammi Terrell – Ain't no mountain high enough
[b] The Beatles – A hard day's Night
[c] The Rembrandts – I'll be there for you
[d] Donots, Frank Turner – So long
[e] Kafvka – Alle hassen Nazis
[f] Queen – Under pressure
[g] Mumford and Sons – Below my feet
[h] Schweizer Nationalhymne
[i] Muff Potter – Wenn dann das hier
[j] Bruno Mars – Count on me
[k] Andrew Gold – Thank you for being a friend
[l] Bosse – Ich bereue nichts

Contents

Abstract **III**

Zusammenfassung **V**

Danksagung **VII**

1 From Li-Ion Batteries to All-Solid-State Batteries **1**
1.1 Li^+ Batteries, their Applications and the Scope of this Work in a Nutshell . . . 1
1.2 Setup and Working Principle of Batteries . . . 3
1.3 Challenges of High Energy Density Electrodes . . . 5
1.4 All-Solid-State Batteries: Requirements on Solid Electrolytes . . . 6

2 Sulfide Solid Electrolytes – State of the Art **11**
2.1 Pure LiPS Phases . . . 11
2.1.1 Synthesis and Structure . . . 11
2.1.2 Crystalline LiPS Phases . . . 13
2.1.3 LiPS Glasses . . . 22
2.2 Quarternary Sulfide Solid Electrolytes . . . 23
2.2.1 Li_6PS_5X Argyrodites . . . 24
2.2.2 Recently Discovered Li_7SiPS_8 . . . 27
2.3 Guiding Thoughts and Research Questions Tackled in this Work . 28

3 Theoretical Background **31**
3.1 Atomistic Modeling . . . 31
3.1.1 Classical Approach . . . 31
3.1.2 Quantum Mechanics: The Schrödinger Equation . . . 32
3.1.3 Density Functional Theory . . . 33
3.2 Electronic Structure . . . 37
3.2.1 Charge Density, eDOS and Band Gap . . . 37
3.2.2 Excursus 1: The Exchange-Correlation Functional . . . 39
3.3 Atomic Structure . . . 39
3.3.1 Crystalline Materials . . . 40
3.3.2 Excursus 2: Periodicity and the Basis Set . . . 40

3.3.3 Supercell Approach . . . 42
3.3.4 Excursus 3: Pseudopotentials . . . 43
3.3.5 Amorphous Materials . . . 44
3.3.6 Excursus 4: Ab-initio Molecular Dynamics . . . 46
3.3.7 Glass Formation . . . 47
3.3.8 Preparation of Glass Structures via Melt-Quenching . . . 48
3.4 Stability . . . 51
3.4.1 Thermodynamical Stability . . . 51
3.4.2 Relative Stabilities . . . 52
3.4.3 Phase Diagrams . . . 53
3.4.4 Stability at finite Temperatures – Assessing Entropy Contributions . . . 55
3.4.5 Excursus 5: Phonon Calculations . . . 55
3.4.6 Kinetic Stabilization . . . 57
3.4.7 Chemical Stability: Explicit Interface Simulations . . . 58
3.4.8 Electrochemical Stability . . . 61
3.5 Defects . . . 65
3.5.1 Point Defects . . . 65
3.5.2 Defect Formation Energies as Descriptors for the Interface Stability . . . 69
3.5.3 Grain Boundaries . . . 71
3.6 Ionic Transport Properties . . . 72
3.6.1 Static approach . . . 73
3.6.2 Excursus 6: Nudged Elastic Band Calculations . . . 74
3.6.3 Dynamic approach . . . 76
3.6.4 Limitations of the Dynamic Approach . . . 77
3.6.5 Pressure Dependence and the Activation Volume . . . 78
3.7 Elastic Properties . . . 79
3.7.1 Bulk Modulus . . . 79
3.7.2 Elastic Constants . . . 80
3.7.3 Macroscopically Averaged Elastic Moduli . . . 82

4 Pure Lithium Thiophosphates (LiPS) 85
4.1 Initial Steps . . . 87
4.1.1 Structure Generation . . . 87
4.1.2 Structure Validation of LiPS Glasses . . . 88
4.2 Stability . . . 90
4.2.1 Formation Energy of Crystalline LiPS Phases . . . 90
4.2.2 Relative Stabilities of LiPS Glasses . . . 91
4.2.3 Inclusion of Vibrational Entropy . . . 94
4.3 Structural Analysis . . . 98
4.3.1 Short-Range Order . . . 98
4.3.2 Structural Aspects of Crystalline Phases . . . 99
4.3.3 Distinct Features of LiPS Glasses . . . 102

4.3.4 Influence of Structural Units on Li^+ Ions in Glasses 103
4.3.5 Resolving Intra- and Intermolecular S−S Correlations . . 104
4.3.6 Occurrence of "Unusual" Structural Units 106
4.3.7 Formation of S–S Bonds 108
4.3.8 Electronic Structure 109
4.4 Transport Properties 112
4.4.1 Analysis of MSD Plots − Common Pitfalls 112
4.4.2 Li^+ Transport From AIMD Simulations 114
4.4.3 Li^+ Diffusion Mechanisms in LiPS Glasses 118
4.4.4 NEB-based Migration Barriers in c-$Li_4P_2S_7$ 122
4.4.5 Li^+ Transport in c-$Li_4P_2S_6$: Revisited Defect Thermodynamics 124
4.5 Defect Formation Energies: Descriptors for the Interface Stability 127
4.5.1 SE | Li Interfaces 127
4.5.2 SE | SE Interfaces in LiPS Glass-Ceramics 131
4.6 Summary 135

5 Influence of Br/S Site-Exchange on the Properties of Li_6PS_5Br 139
5.1 General Approach 140
5.2 Stability and Structure 141
5.2.1 Relative Stability and Lattice Constant at 0 K 141
5.2.2 Assessment of Entropy Contributions at Finite Temperatures 143
5.3 Bulk Transport Properties 149
5.3.1 Local Li^+ Motion at 0% Site-Exchange 149
5.3.2 Intercage Jumps at 0% Site-Exchange 151
5.3.3 Enhanced Li^+ Motion due to Site-Exchange 154
5.3.4 Diffusion Under Mechanical Loading 157
5.3.5 Haven Ratio 162
5.4 Diffusion Mechanism at Low Degrees of Site-Exchange 163
5.4.1 S'_{Br} – A Sink for Interstitials 164
5.4.2 $Br^{\bullet}_{S}$ – The Initiator of Li^+ Frenkel Pairs 166
5.4.3 Combining S'_{Br} and $Br^{\bullet}_{S}$ 168
5.5 Changes in the Li^+ Substructure 171
5.5.1 Influence of S'_{Br} and $Br^{\bullet}_{S}$ on Tetrahedral Occupancies . . . 171
5.5.2 Tetrahedral Occupancies at Increased Site-Exchange . . . 173
5.5.3 Connection between Li^+ Distribution and Lattice Constants 175
5.6 Influence of Grain Boundaries on Li^+ Diffusion 178
5.6.1 $\Sigma 5$ Twist Grain Boundaries 178
5.6.2 $\Sigma 5$ Tilt Grain Boundaries 181
5.6.3 Anisotropic Diffusion due to Grain Boundaries 185
5.7 Summary 187

6 Properties of Li_7SiPS_8 **191**
6.1 Structure and Stability . . . 191
6.1.1 Structure generation . . . 192
6.1.2 Stability . . . 194
6.2 Transport Properties: Ortho- vs. Tetra-Li_7SiPS_8 . . . 197
6.2.1 Bulk Diffusion of Ortho-Li_7SiPS_8 . . . 197
6.2.2 Bulk Diffusion of Tetra-Li_7SiPS_8 . . . 200
6.2.3 Diffusion and Conductivity Comparison . . . 201
6.2.4 Transport Properties of Tetra-Li_7SiPS_8 Under Mechanical Loading . . . 203
6.3 Elastic Properties . . . 205
6.3.1 Bulk Modulus via Equation of State . . . 206
6.3.2 Full Elastic Tensor . . . 207
6.3.3 Macroscopically Averaged Mechanical Properties . . . 208
6.4 Interfacial Instability of Tetra-Li_7SiPS_8 Against Li Metal . . . 209
6.4.1 Setup of Explicit Interface Simulations and Reactivity during Static Calculations . . . 209
6.4.2 Interface Evolution During AIMD Simulations . . . 212
6.4.3 Formation of an Ordered Interphase . . . 216
6.4.4 Influence of the Interphase Formation on the Electronic Structure . . . 218
6.4.5 Identification of the Ordered Phase via Visual Inspection 220
6.5 Summary . . . 223

7 Conclusion and Outlook **227**
7.1 Pure Lithium Thiophospates . . . 227
7.2 Influence of Br/S Site-Exchange on the Properties of Li_6PS_5Br . . . 228
7.3 Properties of Li_7SiPS_8 . . . 229
7.4 Similarities, Differences and General Issues . . . 230
7.5 Open Questions and Next Steps . . . 231

Curriculum Vitae **233**

Bibliography **237**

1 From Li-Ion Batteries to All-Solid-State Batteries

1.1 Li^+ Batteries, their Applications and the Scope of this Work in a Nutshell

Batteries are electrochemical systems that are able to store and release electric energy. One distinguishes between primary batteries that can only be used once and secondary batteries that can be recharged many times. This work only covers materials designed for secondary batteries. If not stated otherwise, in the following we will omit the qualifying adjective and use the mere term battery to refer to secondary batteries.

Since the commercialization of the first Li-ion battery (LIB) in 1991 by Sony,[12,13] batteries have more and more become indispensable power sources for various kinds of applications. The palette of devices is highly diverse and ranges from portable electronics like smartphones, cameras or laptops,[14] medical devices as heart or brain pacemakers[15] to electric vehicles.[16] Also the variation in size is broad and ranges from miniature batteries on the micro and nanoscale, used as power source for niche applications such as lab-on-a-chip devices or microelectromechanical systems,[17] to large battery storage power stations that are key to the transition toward renewable energies and enable fast supply of energy to the power grid.[18]

With such a diversity of applications the requirements that are posed to the battery vary strongly from case to case. This is the reason why over the last few decades much effort has been put into the improvement of established materials, the discovery of new materials and the development of all-new battery concepts. Although Na^+, Mg^{2+}, Zn^{2+} and other technologies progress fast, they are not mature enough to compete with LIBs, yet.[19–21] Therefore, LIBs still represent the state-of-the-art technology at the commercial level.

Major advantages of LIBs are their high gravimetric and volumetric energy densities (i.e., the amount of energy that can be stored per mass or volume) that exceed those of other established battery technologies as shown in Figure 1.1. The high energy density originates from the low specific weight of Li and the high cell potentials attainable.[25] In particular, a high energy density is desired

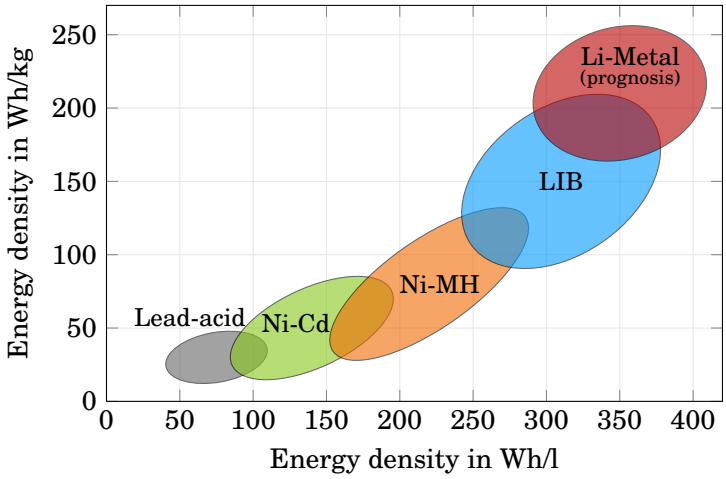

FIGURE 1.1: Approximate placement of established battery technologies (Ni-MH = nickel-metal hydride) with respect to volumetric and gravimetric energy density. A further jump in energy density can be achieved by employing Li metal as anode, which will be discussed further below. This figure was compiled based on similar diagrams from various other works.[20–24]

for electric vehicles or other mobile applications because the battery itself adds to the weight and volume of the device it is designed to drive.

Furthermore, LIBs exhibit comparably high power densities.[26] This does not only imply that they can be charged quickly: they are also able to release a large amount of electric energy within a short time. Such a property is essential if the powered device is subjected to high loads, which would be the case if an electric vehicle is driving up a steep road. Other advantages comprise high energy efficiency, high cycle stability and a low self-discharge.[27]

Despite these respectable properties, advanced applications place ever-increasing demands on the battery and an electric vehicle is again a good example for that.[28] Ideally, it should exhibit a high durability, comparable to the lifetime of the car, and demonstrate a constant performance independent of the ambient temperature in summer as well as in winter.[29] Additionally, the battery needs to be reliable in order to overcome the phenomenon of range anxiety, the fear that the battery will run out of energy before the destination or a recharging station is reached.[30] Furthermore, recharging the battery up to a reasonable degree should not take much longer than refueling a classical car, or alternatively, the stored energy of the battery should be sufficient to avoid recharging during an average ride. In these contexts, an increased energy density of the battery might be able to tackle the mentioned issues, which is the reason why much research is devoted to develop high energy LIBs.

With more and more energy stored, however, safety issues become increasingly important.[2] In this regard, one approach aims at replacing the conventional

electrolyte, which typically employs non-aqueous flammable liquids, with non-flammable solid materials. The usage of these solid electrolytes (SEs) leads to the transformation of conventional LIBs to all-solid-state batteries (ASSBs). Several unsolved issues concerning SEs and ASSBs, however, have prevented their broad commercial application so far and further development is needed in order to achieve an effective breakthrough of ASSBs.[31,32]

Within the scope of this thesis, we have investigated a promising class of materials, namely sulfide SEs. By employing electronic structure calculations, we focused on unraveling structure-property relationships to derive how the underlying atomistic mechanisms govern the materials performance. A strong emphasis was put on the Li^+ transport properties and the generated knowledge is useful for the understanding of experimental observations as well as deriving further optimization strategies for related materials.

Before we dive right into the results, let us use the following sections to briefly review the basic principles of batteries, the advantages and challenges of ASSBs, and the resulting requirements for the SE. Next, Chapter 2 will introduce the issues and the state of the art of the materials of interest. Based on this, various research questions will be formulated. The relevant theory, computational methods and how they can be used to access the properties of interest are outlined in Chapter 3. The obtained results for the different material systems are discussed throughout Chapter 4 to Chapter 6 and the whole work is finally concluded in Chapter 7.

1.2 Setup and Working Principle of Batteries

LIBs come with various material combinations, vary in size and geometry, and may therefore exhibit considerably different properties. Regardless of these specifics, the basic setup and functioning are always the same.[33–35] Every LIB can be partitioned into different compartments. The electrochemically active parts are the two electrodes. Each of them is connected to a current collector and they are spatially and electrically separated by an electrolyte and a separator. During charge and discharge Li^+ is shuffled between the two electrodes. By definition, the electrodes are named based on their role during discharge. Therefore, the electrode that releases electrons, and in the case of LIBs simultaneously also Li^+ ions, during discharge is called anode or negative electrode. Consequently, the electrode that absorbs electrons and Li^+ during discharge is called cathode or positive electrode.

A simplified setup of a conventional, (partly) charged LIB during discharge is shown in Figure 1.2. In this state, the anode and cathode have already been lithiated and delithiated beforehand, respectively. As a result, a chemical potential difference is established that generates a driving force for Li^+ to migrate from the anode to the cathode. In order to do so, Li^+ needs to travel through the electrolyte and the separator. The electrolyte only allows for ionic

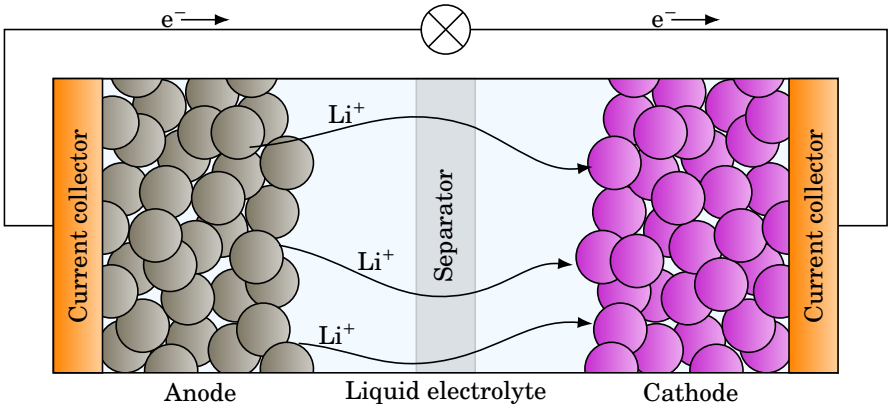

FIGURE 1.2: Schematic illustration of a conventional LIB during discharge. Charging, the reverse process, is realized by connecting the LIB to a power source that transfers Li^+ ions and electrons back from cathode to anode. Note that other materials such as binders, carbon black, protective coatings and further additives are commonly employed in a battery but have been omitted in the figure for clarity.

conduction and is insulating for electrons. Typically, non-aqueous liquids with dissolved lithium salts are employed. The separator is a porous membrane that prevents direct contact between anode and cathode. Both the separator[36–39] and the materials used as liquid electrolytes[40–42] are research fields on their own.

Because the electrolyte is insulating for electrons, an effective flux of Li^+ can only be achieved if the external circuit is closed. The electrons are then able to reach the cathode and the resulting current is used to power a device. If the external circuit is opened, electrons cannot follow the Li^+ anymore. Still, a small amount of Li^+ ions is transfered due to the chemical potential difference between anode and cathode. Therefore, a charge imbalance between anode and cathode is established and the resulting electrostatic potential opposes the chemical potential difference. If the two opposing potentials compensate each other, the electrochemical potential difference vanishes and any further Li^+ flux is prevented. However, any parasitic reactions or small electron leakage currents through the electrolyte can cause discharge of the LIB over time even under open circuit condition, which is referred to as self-discharge.[43]

Even though this working principle can be transfered to any kind of LIB, the final properties of the device depend on many aspects. In this regard, the nominal electrochemical properties are determined to a large degree by the choice of the electrode materials. For example, the combination of anode and cathode sets the theoretical cell voltage and they are jointly responsible for the maximal capacity.[44] With that, they determine the total amount of energy that can be stored by the device. It is therefore clear that the research commu-

nity continuously strives for improved electrode materials to achieve increased energy densities.[45]

1.3 Challenges of High Energy Density Electrodes

Various anode and cathode materials are employed in present LIBs systems. Commercial LIBs have mostly relied on graphite and $Li_4Ti_5O_{12}$ for the anode.[46–48] Both are intercalation materials that allow for the incorporation of Li^+ into their host lattices. Among the more advanced materials, also including conversion- and alloy-type materials,[45] especially Si-related anodes[49,50] and Li metal anodes[51–54] have attracted much interest because of their high theoretical capacity. However, several issues need to be solved before they can be used without concerns.[55,56]

For example, one of the most critical aspects for Li metal anodes concerns the formation of Li dendrites.[57] In particular, when operated under high currents, localized overpotentials accelerate the growth of Li dendrites toward the cathode. Because the liquid electrolyte hardly poses any resistance against its growth and also the separator is penetrated eventually, the dendrite can reach the cathode after a certain amount of cycles.[58] Once the direct contact between anode and cathode is established via the dendrite, the battery becomes short-circuited. This can lead to local chemical reactions and high currents at the contact causing temperature spikes inducing a so-called thermal runaway. In the worst case, the battery fails because gas evolution leads to explosion and/or the flammable liquid electrolyte is ignited. Because batteries are usually arranged in packs, the failure of one cell can initiate a catastrophic chain-reaction. Even systems that do not apply Li metal anodes suffer from issues related to Li dendrites and electrolyte decomposition.[59]

Safety issues are also faced for the cathode. State-of-the-art LIBs mostly employ intercalation materials and the most prominent choices are $LiFePO_4$ or layered lithium transition metal oxides such as $LiCoO_2$.[60] Among the more advanced materials, much effort has been devoted to $LiCoO_2$-related materials toward $Li(Co,Ni,Mn)O_2$ and even more complex compositions.[61,62] These materials, however, typically exhibit high working potentials and react with the liquid electrolyte. The resulting layer of reaction phase is commonly termed solid electrolyte interphase/interface (SEI) and crucially affects the performance of the battery.[63] Besides the formation of solid phases, however, the decomposition of the liquid electrolyte, potentially also involving structural changes in the cathode, can cause the formation of gaseous compounds.[64] Therefore, similar safety issues as described above for the anode arise.

Numerous accidents throughout recent years have proven that advanced safety concepts are necessary,[57,65] and concerning this matter modifications have been applied to electrodes, separator, additives, and/or the liquid electrolyte.[40,66] A conceptually different approach aims at completely replacing the flammable

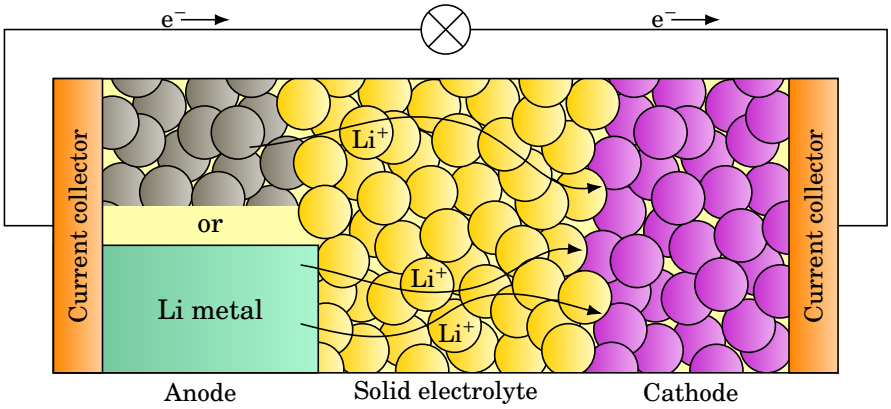

FIGURE 1.3: Schematic illustration of a ASSB during discharge. In comparison to conventional LIBs (see Figure 1.2), the liquid electrolyte and separator have been replaced by a SE. Possibly, this setup enables the usage of Li metal as anode. Note that other materials such as binders, carbon black, protective coatings and further additives are commonly employed in a battery but have been omitted in the figure for clarity.

liquid electrolyte with a non-flammable SE.[67] This steps transforms the conventional LIB to an ASSB. ASSBs hold promise in solving the safety issues and exhibit other advantages. Several challenges, however, need to be overcome to make ASSBs competitive with conventional LIBs.

1.4 All-Solid-State Batteries: Requirements on Solid Electrolytes

The basic setup and working principle of ASSBs are similar to the ones of conventional LIBs as illustrated in Figure 1.3. The only difference is that Li^+ needs to diffuse through the SE instead of the liquid electrolyte. With that, the SE also takes the role of the separator and the usage of SEs holds promise to enable Li metal anodes as indicated in the figure.[68] The spider diagram shown in Figure 1.4 compares selected properties of the three main material classes of SEs that are currently under consideration: sulfides, oxides and polymers.[7] Naturally, every material class comprises plenty of specific materials with their individual advantages, disadvantages, and open issues.

An obviously important property of SEs is the Li^+ conductivity, which needs to be comparable to liquid electrolytes to deliver an acceptable performance in terms of battery power and charging time. As benchmark, ionic conductivities in the range of 0.1-1 mS/cm with negligible electronic conductivity to prevent excessive self-discharge are mentioned in the literature.[32,69] Most notably, the highest ionic conductivities of up to 10 mS/cm and more have been reported for sulfide SEs.[3,4] With regard to their ionic conductivity, inorganic SEs are

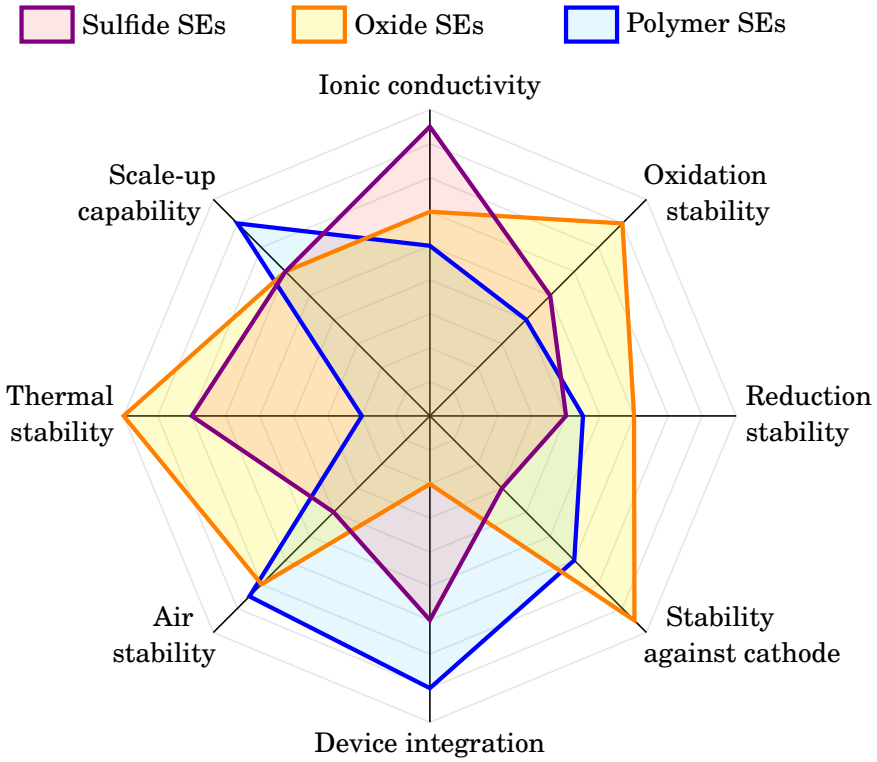

FIGURE 1.4: Spider diagram of the properties of sulfide, oxide and polymer SEs as estimated by Li *et al.*[7]

advantageous over polymer SEs because their crystal structure provides a fixed "backbone" and Li^+ is the only moving species. Therefore, the transference number, defined as the ratio between the current of a specific species and the total current for these single-ion conductors is close to unity.[70] In polymer SEs, on the contrary, further species such as dissolved counter ions need to move in accordance with the Li^+ ions. This does not only decrease the Li^+ transference number, but can also lead to undesirable polarization effects that negatively influence the Li^+ conductivity.[71–73]

However, also the ionic conductivity of oxide SEs is comparably low, which is often caused by increased grain boundary (GB) resistance.[74–76] For sulfides, the effect of GBs resistances is less pronounced and therefore barely discussed in the literature.[77] In contrast to liquid electrolytes and soft polymer SEs, sulfide and oxide SEs may suffer from issues related to porosity and tortuosity.[76,78] Moreover, realizing a good contact between SEs and the electrodes becomes challenging for inorganic SEs. In particular, the stiffer oxides suffer from this issue and demand high pressures during cycling or high temperature treatments to enable good contact, potentially leading to undesirable reactions.[5,79,80] The

contact issue needs less attention in the case of the softer sulfides[5] and is barely of concern for polymers. Unfortunately, the electrochemical stability of sulfide and polymer SEs against the electrodes becomes a limiting factor. In this regard, one needs to distinguish between (i) thermodynamically stable, (ii) mixed electronic-ionic conducting (i.e., unstable), and (iii) kinetically stable interfaces.[1,81]

When considering the interface with the Li metal anode, the first category seems to be a rare case and only $Li_7La_3Zr_2O_{12}$ (LLZO)-related compounds show high stability against Li metal.[82–85] Other oxides such as $Li_{3x}La_{2/3-x}TiO_3$ (LLTO), $Li_{1-x}Al_xGe_{2-x}(PO_4)_3$ (LAGP) or $Li_{1-x}Al_xTi_{2-x}(PO_4)_3$ (LATP) clearly fall into the second category, which makes it necessary to rely on protective coatings or prevent the ongoing interface reaction by other means.[86–88] Sulfide/thiophosphate SEs are generally very reactive with Li metal and the reaction products seem to always involve Li_2S and Li_3P.[89,90] Because these materials exhibit negligible electronic conductivity, the resulting interfaces likely fall into the third category and the ongoing interface reaction becomes diffusion-controlled. Depending on further constituents of the SE and their reaction products, the situation can certainly change. In any case, it needs to be guaranteed that the additional resistance originating from the interphases stays on an appropriate level throughout the lifetime of the battery. Therefore, also for sulfide SEs the usage of protective coatings seems to be inevitable.[91] Various methods to address the topic of electrochemical and interface stability have been developed and will be discussed in more detail throughout Section 3.4.

However, further contact issues may even arise for electrochemically stable interfaces with good initial contact. This is due to the repetitive lithiation/delithiation of the electrodes that results in volume changes. The emerging strains can then lead to cracking and contact loss.[92–94] With the introduction and growth of cracks, the formation of Li dendrites also becomes a challenge again.[95] Furthermore, also negative influences of space charge layers need to be avoided.[96,97]

From an industrial point of view, also the scale-up capability, the associated costs and handling issues of all involved materials during the whole process chain determine the feasibility of ASSBs. At this point, we can conclude that one material alone will most certainly not be able to meet the necessary requirements of an ideal SE. Instead, composite SEs will eventually provide a solution.[98–101] Before composite materials can be effectively developed, however, the individual components need to be understood on a reasonable level. To this end, a detailed knowledge about atomistic mechanisms is necessary to derive optimized design strategies. Most notably, various computational approaches have been especially helpful for accelerating the material development.[102–111]

In the same spirit, we have relied on electronic structure calculations in the framework of density functional theory (DFT) to analyze relationships between structure and properties of SEs. Because the many open issues are complex and the research field itself is vast, we cannot consider all material systems at once

within the scope of this work. Owing to their beneficial Li^+ conductivity, we have decided to focus on sulfide SEs. We will introduce the considered material systems in the following chapter and review their current state of the art.

2 Sulfide Solid Electrolytes – State of the Art

All relevant sulfide SEs are closely related to the $Li_2S-P_2S_5$ system and for the majority of synthesis procedures one of the them or even both compounds appear as starting materials.[112] We will see that already the ternary system, consisting of the elements Li, P, and S inheres a high degree of complexity. These pure litium thiophosphate (LiPS) phases will be shortly screened in the following. Afterward, we will extend this ternary system to quaternary phases, but mostly limit the focus to the two materials that have been investigated here: Li_6PS_5Br and Li_7SiPS_8.

2.1 Pure LiPS Phases

A ternary diagram of the LiPS system is shown in Figure 2.1. This diagram does not indicate stable phases (for a true phase diagram see Figure 3.8), but marks all compositions at which crystalline LiPS phases have been experimentally verified (blue spheres).[113] These phases are $Li_2P_2S_6$, $Li_7P_3S_{11}$, Li_3PS_4, Li_7PS_6 and $Li_4P_2S_6$. The inset highlights a region of high technological relevance that has been thoroughly investigated in this work. The red spheres mark additional glassy phases and the hypothetical crystalline phase $Li_4P_2S_7$ that have been considered as well. Let us first review the general synthesis procedure of LiPS materials and its complicated relation to the resulting structure before addressing the individual phases in more detail.

2.1.1 Synthesis and Structure

What makes the LiPS system especially intricate are not only the various crystalline phases, but rather the occurrence and coexistence of glassy phases as experimentally verified by Tsukasaki *et al.*[8] via high resolution transmission electron microscopy, see Figure 2.2. Particularly, depending on composition and synthesis procedure, LiPS samples can show purely glassy character,[114,115] but can also be prepared as glass-ceramics,[116–119] where crystallites are embedded in a glassy matrix. The final properties of the material therefore depend on the

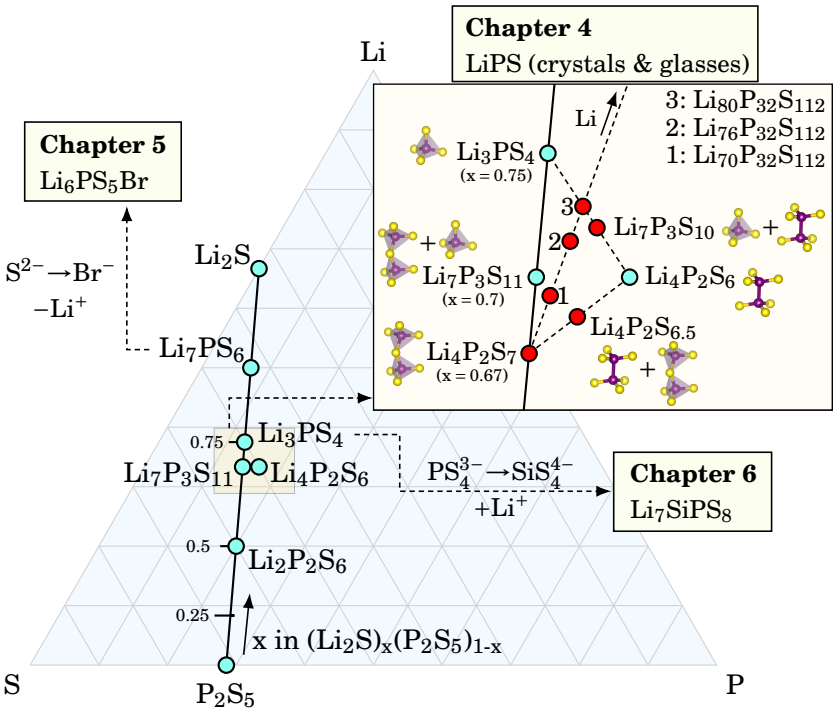

FIGURE 2.1: Illustration of the ternary LiPS diagram, marking all compositions with known crystalline phases (blue spheres). Note that the majority of binary phases along the edges of the diagram have been omitted for clarity. The inset shows a magnified region and includes additional compositions that have been investigated in this work (red spheres). Furthermore, the close relations to the covered quaternary phases are indicated.

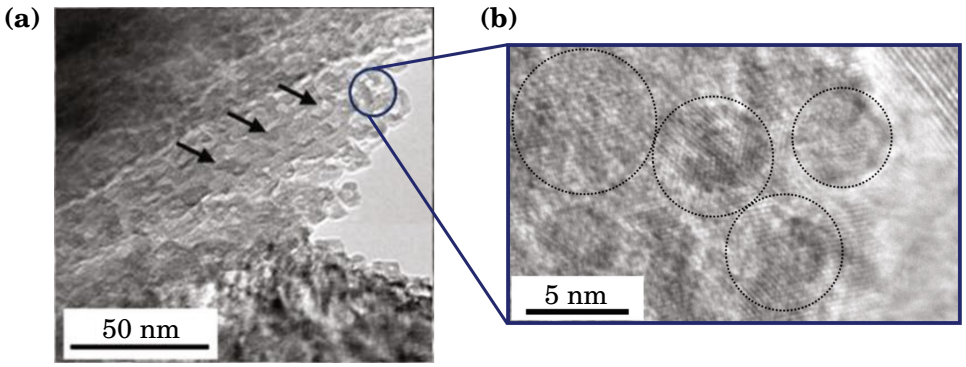

FIGURE 2.2: (a) Transmission electron microscopy bright field image showing the microstructure of a $(Li_2S)_{80}(P_2S_5)_{20}$ glass-ceramic. (b) High resolution transmission electron microscopy image of the marked region indicating that small crystallites of approximately 5 nm size are embedded in an amorphous matrix.
[Original figure and caption have been prepared by Tsukasaki *et al.*[8] and were published by Springer Nature under a Creative Commons Attribution 4.0 International License. Figure and caption were slightly modified.]

types, ratios and distribution of the underlying phases. It seems that only classical solid state syntheses lead to a purely crystalline material with negligible content of residual glassy phase.[120] Because the resulting materials typically show poor ionic conductivity,[120,121] however, other techniques are commonly employed for the successful synthesis of LiPS SEs with desirable properties.

The preparation of glasses is usually achieved by relying on mechanochemical methods.[114,119,122,123] Thus, the crystalline starting materials Li_2S and P_2S_5 are ball-milled until no crystalline phases can be identified anymore. Melt-quenching procedures are an alternative method to prepare glasses.[124] Crystalline phases are then obtained by initiating crystallization from the glass via temperature treatments.[116,125] Alternatively, recently developed wet-chemical procedures deliver promising results.[126–129]

The atomic structure of the crystalline compounds has been solved by conventional diffraction experiments. Because the sensitivity to Li^+ is low for standard X-ray measurements, synchrotron X-ray or neutron experiments are commonly used to capture the Li^+ substructure.[123,130] For glasses and glass-ceramics, however, a structural analysis is hampered, because the absence of long-range order in the amorphous parts limits the effectiveness of diffraction experiments. Hence, a multitude of methods such as transmission electron microscopy,[8] Raman and nuclear magnetic resonance (NMR) spectroscopy,[131] or advanced scattering and diffraction methods are applied.[132] Only few computational approaches investigated the structure and mechanisms of glassy phases,[133–136] and we will refer to these works later in more detail.

It has been found that all crystalline and amorphous LiPS compounds comprise anionic structural units ions with Li^+ distributed between them. The most relevant stuctural units are PS_4^{3-} tetrahedra, corner-sharing $P_2S_7^{4-}$ ditetrahedra and ethane-like $P_2S_6^{4-}$. These structural units can be viewed in the inset of Figure 2.1. In the glassy phases, the structural units are randomly arranged and typically several different types of the structural units are found.[115] In contrast, the crystalline phases only contain one or two types of structural units with an ordered arrangement. Moreover, the crystalline phases typically comprise several symmetrically distinct Li^+ sites. As reviewed in the following, we will see that the crystalline phases, especially those with promising properties, have already been examined thoroughly. For the glassy phases, however, there is a lack of atomistic understanding.

2.1.2 Crystalline LiPS Phases

Because the ion transport is an important feature of SEs, a short overview of reported ionic conductivities of the crystalline phases, mostly present as glass-ceramics, is shown in Figure 2.3. Additionally, the ionic conductivities of LiPS glasses have been added. The figure shows that the reported values may vary by orders of magnitude within the same composition. Most notably, at compositions of $Li_7P_3S_{11}$ and Li_3PS_4, the spread of ionic conductivities is larger than two

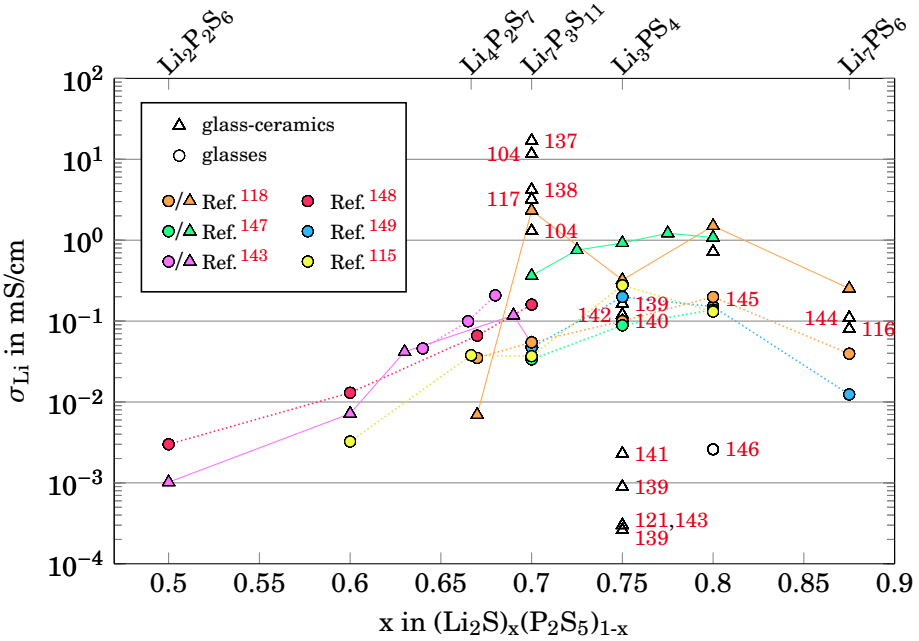

FIGURE 2.3: Compilation of Li^+ conductivity data of LiPS glass-ceramics and glasses as function of composition. Several data sets of the same reports are shown with the same color and lines are added as a guide to the eye.

orders of magnitude due to the presence of certain phases with especially good or poor transport properties. Let us first inspect the individual crystalline phases and afterward summarize what is known about the glasses.

$Li_2P_2S_6$ – A Rather Ionic Insulator

Starting from low fractions x in $(Li_2S)_x(P_2S_5)_{1-x}$, the first crystalline compound is $Li_2P_2S_6$ at x = 0.5. Structurally, the $Li_2P_2S_6$ phase crystallizes in a monoclinic $C2/m$ symmetry and comprises $P_2S_6^{2-}$ units, a structural unit that can be described as two edge-sharing P_2S_4 tetrahedra.[123] These units, however, have not been observed in crystalline or glassy samples at higher x, likely because a higher Li content leads to a reduction of $P_2S_6^{2-}$ units.[115] The structure is shown in Figure 2.4.

Owing to its low bulk ionic conductivity of $7.8{\cdot}10^{-8}$ mS/cm, $Li_2P_2S_6$ has no relevance as SE.[123] The ionic conductivity of is low for several reasons: (i) the $C2/m$ symmetry does not allow for isotropic diffusion, (ii) unfavorable distances between Li^+ sites are encountered, (iii) Li^+ sites are fully occupied, and (iv) possible one-dimensional diffusion channels can be easily blocked by point defects.[123]

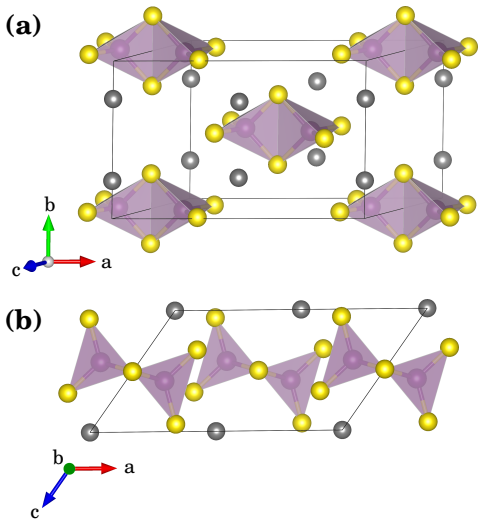

FIGURE 2.4: Crystal structure of $Li_2P_2S_6$. (a) Side view and (b) view along the b axis. The structure contains $P_2S_6^{2-}$ units and an ordered arrangement of fully occupied Li^+ sites.

An earlier report claimed an ionic conductivity of approximately 10^{-3} mS/cm for a glass-ceramic obtained at x = 0.5.[143] The authors, however, do not mention the $Li_2P_2S_6$ phase in this regard. Presumably, the increased conductivity can rather be attributed to residual glass phases.[115] In conclusion, $Li_2P_2S_6$ glass-ceramics are likely to be unsuitable for the usage as SE.

$Li_4P_2S_7$ – A Hypothetical Phase

At x = 0.67, the hypothetical crystalline phase $Li_4P_2S_7$ has only been covered by computational means.[150,151] Therefore, not much is known about the material. It was derived from the corresponding phosphate analogue[152] with triclinic $P\bar{1}$ symmetry by substitution of O with S and the structure is shown in Figure 2.5. The underlying structural unit of $Li_4P_2S_7$ is $P_2S_7^{4-}$, which is observed in LiPS glasses at various compositions.[115,126,131,132,153,154] These units are also constituents of the crystalline phase $Li_7P_3S_{11}$ as discussed below.

A successful synthesis of $Li_4P_2S_7$ has never been proven thoroughly and needs further confirmation.[115] The difficulty in preparing $Li_4P_2S_7$ fits to computational results that attest only thermodynamic metastability to the material.[151] In terms of Li^+ transport properties, however, $Li_4P_2S_7$ seems to be a promising compound because relatively low migration barriers up to only 0.3 eV have been predicted for Li^+ vacancy jumps along an exemplary path throughout the crystal.[150]

$Li_7P_3S_{11}$ – The Currently Fastest LiPS Conductor

$Li_7P_3S_{11}$ is located at x = 0.7, shows a triclinic $P\bar{1}$ symmetry and is composed of PS_4^{3-} and $P_2S_7^{4-}$ units in equal amounts (see Figure 2.6).[130,155] This superionic

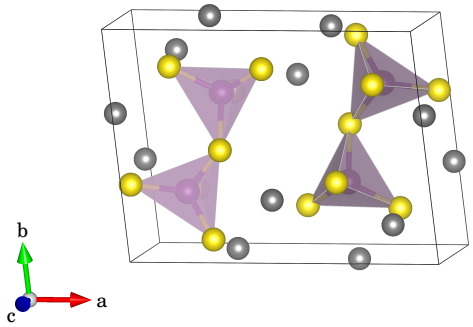

FIGURE 2.5: Crystal structure of the hypothetical phase $Li_4P_2S_7$ derived from $Li_4P_2O_7$. The structure contains $P_2S_7^{4-}$ units.

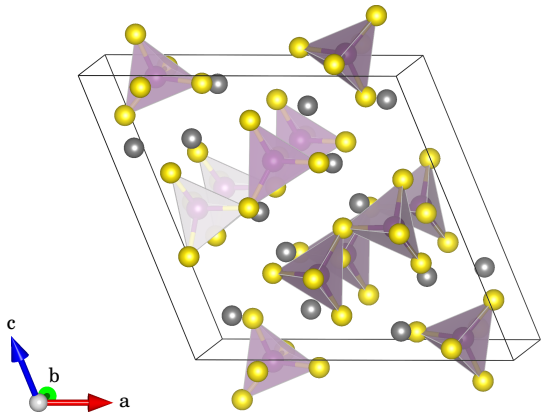

FIGURE 2.6: Crystal structure of the superionic phase $Li_7P_3S_{11}$. The structure contains $P_2S_7^{4-}$ and PS_4^{3-} units.

compound seems to deliver the highest ionic conductivity among all LiPS phases as shown in experimental,[156,157] theoretical[107,158] and combined[104,159] studies. The highest measured room temperature conductivities reach 17 mS/cm, and low activation energies in the range of 120 to 190 meV have been reported.[104,117,137] Note, however, that there are also other reports by Onodera *et al.*[133] and Busche *et al.*,[160] who report similar conductivities of 2 and 5-8 mS/cm but with significantly higher barriers of approximately 230 and 300 meV, respectively. In this regard one should keep in mind that reported conductivities and activation barriers can vary considerably depending on the synthesis route, sample preparation, measurement setup and other parameters. This was recently shown in a round-robin study among different laboratories focusing on the reliability of conductivity measurements.[161] For example, Wenzel *et al.*[89] reported similar ionic conductivities as mentioned above. Their activation barriers, however, were found to be considerably higher (approximately 290-400 meV) and strongly depended on the preparation procedure.

Despite these inconsistencies, theoretical studies substantiate that $Li_7P_3S_{11}$ exhibits good transport properties.[104,107,151] It is noteworthy, however, that the ionic conductivities determined by *ab-initio* molecular dynamics (AIMD)

simulations are often overestimated: Reported values for $Li_7P_3S_{11}$ are 57 and 72 mS/cm.[104,107]. The reasons for this mismatch with experiment have not been clarified unambiguously and similar trends are also observed for other crystalline SEs.[162,163] Differences could, on the one hand, originate from limited accuracy and statistics of the simulations.[164] On the other hand, only tracer diffusion coefficients D^* are often calculated in theoretical studies, whereas so-called jump or conductivity diffusion coefficients D_σ are actually needed.[165] A more detailed discussion on transport properties obtained from AIMD simulations is presented in Section 3.6.3 with a focus on its limitations in Section 3.6.4. Another point needs to be kept in mind when transport properties from simulations are compared to experiments: Most simulations only treat the bulk material, virtually representing a single crystal, and disregard any kind of defects, whereas the real compound is much more complicated. For measured samples of $Li_7P_3S_{11}$, for example, it is likely that residual glass phases or GBs reduce the ionic conductivity.[89,115,149]

$Li_7P_3S_{11}$ cannot be synthesized by means of classical solid-state reactions and needs to be crystallized from glasses[153,154,166] or prepared via wet-chemical procedures.[126–129] DFT calculations have analyzed the stability and showed that $Li_7P_3S_{11}$ is metastable at 0 K but becomes thermodynamically stable at elevated temperature, if vibrational contributions to the free energy are taken into account.[104] However, the authors of the study acknowledge that the phase equilibrium is very sensitive to the choice of the sulfur chemical potential. Measurements prove that a decomposition to $Li_4P_2S_6$, β-Li_3PS_4 and elemental sulfur takes place at higher temperatures.[160] Furthermore, $Li_7P_3S_{11}$ is unstable against Li metal and decomposes to Li_2S and Li_3P.[89]

Li_3PS_4 – A Promising Solid Electrolyte

Li_3PS_4 (x = 0.75) shows a high stability against other LiPS phases,[104] and is therefore a suitable candidate for the usage in ASSBs. The structure of Li_3PS_4 has been analyzed by Homma *et al.*[121,167] and various phase transitions have been reported. According to them, different phases can be distinguished based on the arrangement of the PS_4^{3-} structural units. Upon heating, the room temperature γ-phase (orthorhombic, $Pmn2_1$ symmetry) transforms to β-Li_3PS_4 (orthorhombic, $Pmna$ symmetry) at 573 K followed by a transition to the α-phase (orthorhombic, $Pbcn$ symmetry) at 746 K. Upon cooling, the α-phase directly converts back to γ-Li_3PS_4 without going through the β-phase. For completeness, a high pressure δ-phase has been predicted theoretically and was experimentally verified at pressures above 5 GPa.[168] Low ionic conductivities disqualify the γ-Li_3PS_4 as suitable SE and the usage of the α-phase is prevented by the high temperatures needed for its stabilization.[121]

The β-phase of Li_3PS_4, however, has been subject of many studies and might be a potential SE. Its structure is shown in Figure 2.7 and comprises 3 different Li^+ sites. Whereas the occupancies of Li1 sites were reported to be unity, the Li2

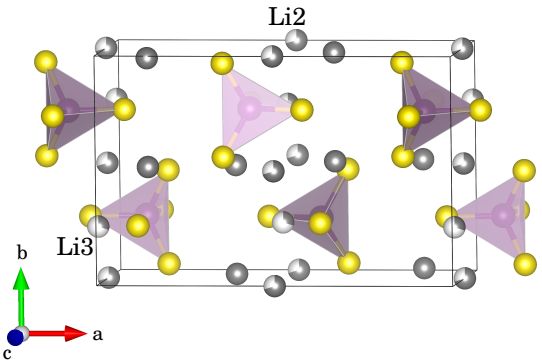

FIGURE 2.7: Crystal structure of β-Li_3PS_4. It contains PS_4^{3-} units and three different Li^+ sites. The Li2 and Li3 sites are reported to be partially occupied.[121,169,170]

and Li3 sites exhibit partial occupancies of 0.7 and 0.3, respectively, according to two reports.[121,169] A third report mentions occupancies of 0.4 and 0.6.[170]

The level of information concerning the Li^+ transport properties of Li_3PS_4 is rather diffuse.[140] Initial reports first attributed poor ionic conductivities of the order of 10^{-3} to 10^{-2} mS/cm, if the high temperature data is extrapolated to low temperatures.[121,143] An increasing interest for the material developed upon the observation of 0.16 mS/cm in nano-porous β-Li_3PS_4.[139] It was speculated that the conductivity increase is related to a surface conduction mechanism,[139] fitting to results obtained for nano-flakes of β-Li_3PS_4.[142] Similar conductivities of approximately 0.1 mS/cm have later also been reported for samples without significant porosity obtained via conventional[140] and liquid-phase syntheses.[171] These materials, however, comprised significant amounts of glassy phase. Indeed, a NMR study proved that glassy Li_3PS_4 exhibits slightly better transport properties than the crystalline phase.[172] These results indicate that the structure and transport properties are very sensitive to the synthesis and measurement conditions. The synthesis-dependent structure might be a reason for the scattered activation barriers that have been reported: they range from 0.24[140] up to 0.49 meV.[143,173]

Theoretical approaches with well defined structures were helpful in understanding the material and measured trends. An early theoretical study predicted vacancy migration barriers below 300 meV and showed that the γ-phase is slightly more stable than β-Li_3PS_4.[174] In the same work the authors demonstrate that Li_3PS_4 is unstable against Li metal and it is speculated that a thin layer of Li_2S could help in the stabilization of the interface. Similar conclusions are drawn based on a purely thermodynamic approach and it is suggested that reaction products might act as passivating layers to inhibit further reactions.[175] From an analysis of point defects and migration barriers obtained from nudged elastic band (NEB) calculations the experimental trend, that β-Li_3PS_4 is a better conductor compared to γ-Li_3PS_4, is confirmed.[175] The absolute conductivity for β-Li_3PS_4, however, was found to be much larger than the experimental one.[175]

Also the transport properties obtained with AIMD simulations were reported to surpass the experimental ones.[103] However, a small cluster model of β-Li_3PS_4, emulating nano-porous β-Li_3PS_4, indeed exhibits improved transport properties compared to the bulk.[103] Moreover, interfaces toward the cathode were investigated on an atomistic level. The results indicate that a protective layer of $LiNbO_3$ improves the interface properties,[110,176,177] which is confirmed by experiments.[178]

Li_7PS_6 – The Parent Phase of Li_6PS_5X Argyrodites

There are only few studies covering pure Li_7PS_6, which is found at a composition of x = 0.875 in $(Li_2S)_x(P_2S_5)_{1-x}$. It comprises PS_4^{3-} structural units and single S^{2-} ions, as shown in Figure 2.8. Although it has been known for quite some time,[179] more interest only started to set in lately when Deiseroth and coworkers elaborated on the connection between argyrodites and the $Li_2S{-}P_2S_5$ system.[180] A low temperature (LT) phase was found to be closely related to orthorhombic LT-α-Cu_7PSe_6 with $Pna2_1$ symmetry and showed well defined Li^+ sites.[181] Furthermore, a cubic high temperature (HT) phase with $F\bar{4}3m$ symmetry and a smeared Li^+ distribution was found.[182]

Early studies of Tatsumisago *et al.*[116,145] reported that the room temperature conductivity of glasses at x = 0.8 improves from approximately 0.1 to 1 mS/cm after being transformed to glass-ceramics via temperature treatment. Besides Li_3PS_4 and an unknown phase, the partial crystallization leads to the formation of Li_7PS_6 and the authors speculated that they have beneficial influence on the transport properties. In a later study, they reported 0.25 mS/cm for glass-ceramics at x = 0.875.[118] Deiseroth *et al.*[183] reported lower values of 10^{-5} to 10^{-3} mS/cm for the LT-phase at 313 K and 0.056 mS/cm for the HT-phase at 500 K. Li_7PS_6 synthesized using a wet-chemical approach exhibited a higher room temperature conductivity of 0.11 mS/cm.[144]

Theoretical investigations determined a much higher ionic conductivity for the material,[184] an issue that is also observed for other sulfide SEs. Similar to other LiPS compounds, Li_7PS_6 seems to be unstable against Li metal.[144]

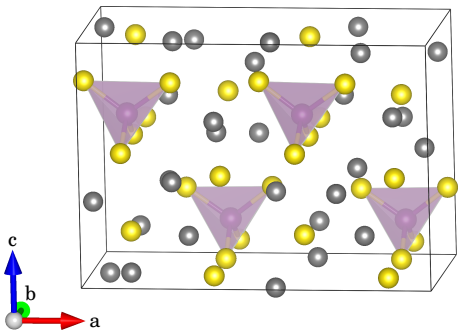

FIGURE 2.8: Crystal structure of the LT-phase of Li_7PS_6. It contains PS_4^{3-} units and single S^{2-} ions.

By adding further elements, mostly halides, the HT-phase can be stabilized at room temperature.[183] The resulting phases, such as Li_6PS_5X argyrodites (X = Cl, Br, I), have attracted much interest due to promising transport properties and will be discussed in more detail in Section 2.2.1 and Li_7PS_6 has been observed in the early stages during heat treatments of Li_6PS_5Cl glass-ceramic particles.[185] We included the orthorhombic LT-phase of Li_7PS_6 in our investigations.

$Li_4P_2S_6$ – An Ionic Insulator Outside the Li_2S–P_2S_5 System

Up to now, $Li_4P_2S_6$ seems to be the only known crystalline LiPS phase outside the Li_2S–P_2S_5 system. Compared to the Li_2S–P_2S_5 system it can be viewed as a S-deficient phase , e.g., $Li_4P_2S_7 \rightarrow Li_4P_2S_6$+S. $Li_4P_2S_6$ typically forms when LiPS compounds are subjected to high temperatures or when temperature treatments are performed over long periods of time.[120,154] The material contains only ethane-like $P_2S_6^{4-}$ structural units that possess a P–P bond. Various phases that differ in the arrangements of the $P_2S_6^{4-}$ units have been discussed in literature.[186,187]

In a preceding work,[120] we have analyzed the $P\bar{3}1m$ phase that exhibits a layered arrangement of the $P_2S_6^{4-}$ units, as shown in Figure 2.9 (a). The material comprises two Li^+ sites, of which Li1 is located within the $P_2S_6^{4-}$ layers and Li2 between the layers. Three interstitial sites, see Figure 2.9 (b), were identified and the defect thermodynamics and migration paths of Li^+ vacancies and interstitials were investigated. All long-range diffusion paths that involve Li^+ interstitials were found to comprise barriers of approximately 0.5 eV. For a two-dimensional diffusion path that involves chains of Li2–$Li_{i,1}$–Li2 sites, however, Li^+ vacancies jumps only need to overcome a relatively low migration barrier of approximately 0.2 eV and were assumed to be the most mobile charge carrier.

Nevertheless, the ionic conductivity of approximately 10^{-7} mS/cm is low, because the material does not possess structural vacancies that enable diffusion.[120] Instead, costly Frenkel pairs with a formation energy $\Delta E_{FP} \approx 1$ eV need to form and lead to a low concentration of mobile point defects. According to our findings, the measured activation energy for diffusion should consist of the migration barrier but also comprise half the Frenkel pair formation energy, $E_m^{measured} = E_m^{calc.} + 0.5E_{FP} \approx 0.7$ eV. Experimentally, however, the activation energy was found to be 0.48 eV and we believe that the difference stems from small amounts of residual glassy phases that are able to bypass the $Li_4P_2S_6$ crystallites.[120] These assumptions fit to a study by Hood *et al.*,[186] who report a considerably higher ionic conductivity of $2.4 \cdot 10^{-4}$ mS/cm and a reduced activation energy of 0.29 eV, presumably because a higher amount of glass phase is present.

For the mentioned calculations in our preceding study, only intrinsic Li-related defects were considered and the virtual Li reservoir was always assumed to be Li metal. Because the specific synthesis route of our experimental partners relied on temperature-driven sulfur loss from $Li_4P_2S_7$, however, it is reasonable

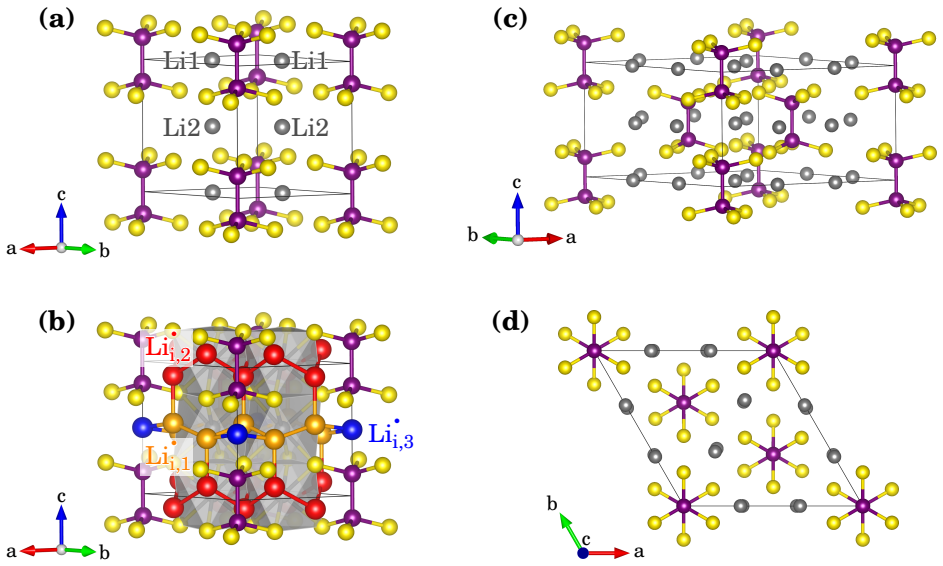

FIGURE 2.9: (a) Crystal structure of $Li_4P_2S_6$ with $P\bar{3}1m$ symmetry with a layered arrangement of the underlying $P_2S_6^{4-}$ units. The Li1 sites are within the $P_2S_6^{4-}$ layers, whereas Li2 sites are located in between the layers. (b) The same structure as in (a), but including the three types of interstitial sites. Parts (c) and (d) show a side view and top view of $Li_4P_2S_6$ with $P321$ symmetry, respectively. The $P_2S_6^{4-}$ units are located on different planes.

to assume that the material is in contact to a sulfur reservoir during the synthesis. This could facilitate the formation of external, S-related defects that enable different charge compensation mechanisms and could influence the concentration of mobile defects. The influences of such external defect equilibria were not investigated so far and we will therefore revisit the defect thermodynamics of $Li_4P_2S_6$ in Section 4.4.5.

For completeness, we note that other $P_2S_6^{4-}$ arrangements seem to favor an interstitial-mediated diffusion mechanism.[186,188] A later work indeed anticipates that the structure of $Li_4P_2S_6$ is not composed of planar arrangements of $P_2S_6^{4-}$ units and rather crystallizes in a trigonal phase with $P321$ symmetry.[187] This crystal structures is shown in Figure 2.9 (c) and (d) and we have partly included this structure in our analysis.

In summary, crystalline $Li_4P_2S_6$ exhibits ionic conductivities that are orders of magnitudes lower than observed in the remaining LiPS materials.[120,160,189] Therefore, $Li_4P_2S_6$ can rather be seen as an ionic insulator, unsuitable for the usage as SE. Still, if the formation of $Li_4P_2S_6$ during synthesis cannot be avoided, an increase of the concentration of Li^+ point defects, for example via doping,[188] might be an attractive approach to improve its conductivity.

Other Crystalline LiPS Materials

For the sake of completeness, we want to mention few other reports that speculated on further crystalline LiPS compounds. Examples are $Li_{3.25}P_{0.95}S_4$[145] or $Li_{3.2}P_{0.96}S_4$[119] whose XRD-patterns are described to resemble thio-LISICON (lithium superionic conductor) phases. These phases are originally derived from $Li_{14}Zn(GeO_4)_4$.[190] Furthermore, crystalline solid solutions in the $Li_{3+5x}P_{1-x}S_4$ were mentioned.[173] However, because no thorough structural investigations of these phases have been published, their existence is questionable and we will not treat any of them in this work.

2.1.3 LiPS Glasses

Glasses with compositions of $0.5 \leq x \leq 0.875$ in the $(Li_2S)_x(P_2S_5)_{1-x}$ system have been investigated in various studies.[191] Differential thermal analysis and differential scanning calorimetry have been used to identify glass transition temperatures T_g around 200°C depending on the compositions.[115,116,124,138] Due to favorable ionic conductivities in the range of 0.03 to 0.3 mS/cm (see Figure 2.3), most studies focus on the composition ranges $0.67 \leq x \leq 0.8$.[115,147,149,192] Migration barriers range from 400 to 520 meV, but seem to depend both on the composition and synthesis procedure.[115,119,160]

Dietrich *et al.*[115] have summarized the measured trends for the glasses and showed that the lowest ionic conductivity is obtained at $x = 0.5$. With increasing x the ionic conductivity generally increases up to $x = 0.75$, as shown in Figure 2.3. For $x \geq 0.75$, two different trends are observed. On the one hand, some studies report a decreasing ionic conductivity.[115,149] On the other hand, there are reports about a further increase up to $x = 0.8$.[118,147]

Structurally, the same structural units that appear in crystalline phases are found in LiPS glasses. Additionally, also chains of PS_4 groups are found in glasses at low x.[115] Interestingly, in apparently all $(Li_2S)_x(P_2S_5)_{1-x}$ glasses the appearance of $P_2S_6^{4-}$ units is reported.[115] Strictly speaking, $P_2S_6^{4-}$ units do not fulfill the ideal composition of $(Li_2S)_x(P_2S_5)_{1-x}$ and imply that glasses have become S-deficient, if no compensating unit is formed. Whether this is a local or global property has not been clearly determined, yet.

The experimental structural analysis of glasses is difficult. Therefore, computational approaches can be used to shed light on this issue. There are, however, only few theoretical studies that analyze the structure of LiPS glasses on an atomistic level. This is because no reliable structural models, essential input parameters for most simulations, exist. Instead, they need to be generated in the first place, which is an intricate task itself and outlined in Section 3.3.8. Nevertheless, glasses at $x = 0.5, 0.6, 0.7$ and a glass-ceramic at $x = 0.7$ containing a $Li_7P_3S_{11}$ crystallite were generated based on synchrotron X-ray and neutron diffraction data using a reverse Monte Carlo method.[158] The authors then applied a bond valence sum approach to analyze conduction pathways. In a

follow-up work they could show that bottlenecks in the glass are tighter and that the conduction pathway is less favorable compared to $Li_7P_3S_{11}$.[156] Baba *et al.*[135] generated atomistic glass structures at $x = 0.67, 0.7, 0.75, 0.8$ using a melt-quenching procedure with AIMD simulations. Their initial models relied on known crystalline or pseudo-random starting structures, but did not include any $P_2S_6^{4-}$ units. They showed that the transport properties are similar among all their glasses. Ohara *et al.*[134] generated models based on experimental data of glasses with nominal compositions at $x = 0.67, 0.7, 0.75$ that accounted for a slight S-deficiency and the occurrence of $P_2S_6^{4-}$ units. Transport properties, however, were not calculated. Using classical molecular dynamics (MD) simulations, the interface between γ-Li_3PS_4 and a Li_3PS_4 glass was investigated and it was found that the ionic conductivity of the glass is approximately 100 times larger than the one of the crystal.[136] Furthermore, PS_4^{3-} units were found to accelerate the Li^+ dynamics in the glass via a "paddle wheel" mechanism at room temperature that is not observed in the crystal.[193] Just recently, the $(Li_2S)_x(P_2S_5)_{1-x}$ system was studied using a combination of electronic structure calculations and artificial intelligence methods.[194] The authors found two miscibility gaps and argue that compositions with $0.5 < x < 0.67$ and $0.75 < x < 0.875$ are prone to phase transitions. Moreover, they propose a promising candidate structure with $x = 0.724$.

The mentioned reports show that there are only scattered atomistic studies for glassy LiPS systems. They are based on different assumptions and focus on different aspects, which prevents a thorough comparison. More systematic investigations are therefore needed to increase the understanding of amorphous LiPS SEs on the atomistic level.

We note that for other amorphous materials in the context of batteries and SEs atomistic modeling studies are similarly rare. There is one report that analyzes the effect of an amorphous phase on the transport properties of Li_4PS_4I.[163] Furthermore, a few theoretical studies investigated amorphous lithium phosphorus oxynitrides (LiPON) phases.[195–197] Additionally, the crystallization behavior of $LiCO_3$ from an amorphous phase was simulated, but this issue is more relevant for understanding interfaces with liquid electrolytes.[198]

2.2 Quarternary Sulfide Solid Electrolytes

Quarternary sulfide SEs are usually obtained by adding a further element to the $Li_2S{-}P_2S_5$ system. For small contents, the fourth element is typically used as substitutional to adjust the Li content or polarizability.[199] Examples are $Li_{3.25}[Si_{0.25}P_{0.75}]S_4$[200] or $Li_{4.4}[M_{0.4}M'_{0.6}]S_4$ ($M{=}Al^{3+}$, Ga^{3+}; $M'{=}Ge^{4+}$, Sn^{4+}).[201]

By analyzing solid solutions of $Li_{4-x}Ge_{1-x}P_xS_4$ and $Li_{4-x}Si_{1-x}P_xS_4$, compounds such as $Li_{10}MP_2S_{12}$ (M = Si, Ge, Sn) were identified and especially the superionic phase $Li_{10}GeP_2S_{12}$ (LGPS) showed a high ionic conductivity of 12 mS/cm.[4,202] Since then, LGPS was used as basis to derive and ana-

lyze further variants of the materials. For instance, one of the highest reported room temperature ionic conductivities of 25 mS/cm was observed for $Li_{9.54}Si_{1.74}P_{1.44}S_{11.7}Cl_{0.3}$.[203] Another compound which is related to the LGPS family is the recently observed Li_7SiPS_8.[11] Li_7SiPS_8 has been analyzed thoroughly in this work and will be introduced in more detail in Section 2.2.2.

A different family of compounds are argyrodite-type phases. The basic structure originates from Ag_8GeS_6, but via substitution a vast amount of compositions can be realized: $Li^+_{12-m-x}(M^{m+}Ch^{2-}_4)Ch^{2-}_{2-x}X^-_x$ (M=P, As, Ge, Si, Sn, Sb; Ch=O, S, Se; X=Cl, Br, I, BH_4).[4,199] Some basic questions, however, are still unsolved and will be addressed for Li_6PS_5X (X=Cl, Br, I) argyrodites in the next section.

2.2.1 Li_6PS_5X Argyrodites

Since the initiating work by Deiseroth *et al.*[180] much effort has been devoted to the development of Li_6PS_5X (X=Cl,Br,I) argyrodites. The material is usually prepared using a combination of mechanochemical and solid state reactions or by applying wet-chemical approaches.[204] Its cubic crystal structure is shown in Figure 2.10 and exhibits a $F\bar{4}3m$ symmetry. The halide ions (Wyckoff 4*a*) are arranged on a face-centered cubic lattice. All its octahedral sites are occupied by PS^{3-}_4 units (P ion on Wyckoff 4*b*) which can likewise be seen as a shifted face-centered cubic lattice of PS^{3-}_4 units. Half of the tetrahedral sites are occupied by S^{2-} (Wyckoff 4*d*). Note that depending on the choice of the coordinate system, the 4*d* sites are labeled as 4*c* sites in some reports.[205–207]

The Li^+ substructure of Li_6PS_5X is rather complicated because various partly occupied Li^+ sites have been identified. These sites are always tetrahedrally coordinated by anions and Deiseroth *et al.*[182] labeled them as type 1-5. We will abbreviate them as T1, T2, T3, T4 and T5 sites in the course of this work. Their configurations are shown in Figure 2.10 (b). To a first approximation, six Li^+ sites (Wyckoff 24*g*, also called T5a sites) form an octahedron around the S^{2-} on 4*d*. The T5a sites are located on the shared face of two T5 tetrahedral sites (Wyckoff 48*h*). Due to the short distances between the T5 and T5a sites, they form T5-T5a-T5 triplets, similar to a mega-basin of sites. Every T5-T5a-T5 triplet is believed to be only occupied by one Li^+ at a time and the six triplets around every 4*d* site can be viewed as a "Li^+ cage".

Three different Li^+ jump types have been identified.[184] The first type describes localized jumps within a T5-T5a-T5 triplet, also called doublet jumps. The second jump is characterized by intracage jumps from one T5-T5a-T5 triplet to a neighboring triplet of the same cage. These jumps are highly concerted and involve the rearrangement of multiple Li^+ at the same time, e.g., via rigid octahedral rotations or trigonal-prismatic internal reorganization mechanisms.[207] Because they only involve intracage motion, these two jumps do not contribute to long-range transport. The third type involves intercage jumps between neighboring Li^+ cages. Intercage jumps have been identified as the bottleneck of

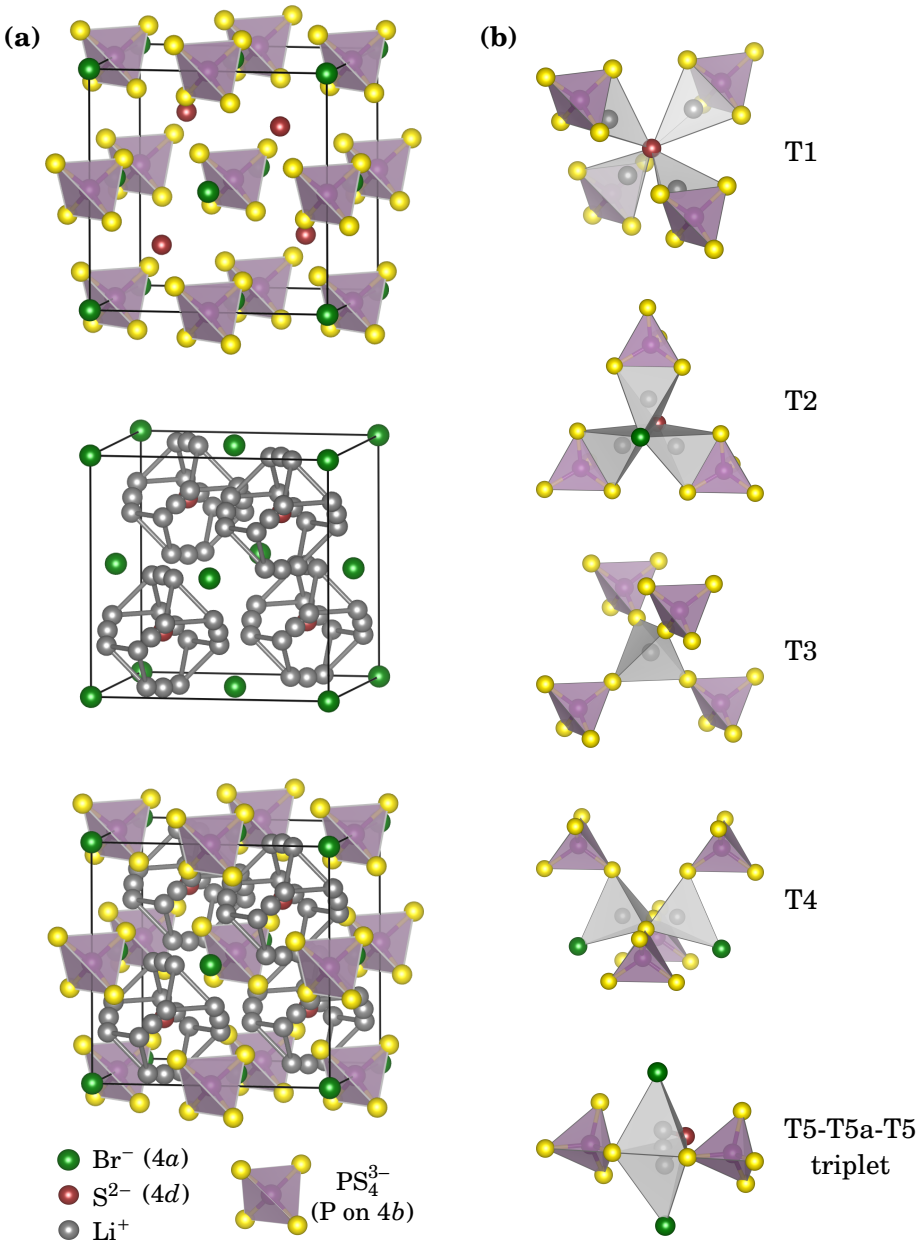

FIGURE 2.10: (a) Structure of Li_6PS_5Br. Top: Structure without Li^+. Center: Structure without PS_4^{3-} units, but with Li^+ sites (T5-T5a-T5 triplets) that form a Li^+ cage around the 4*d* sites. Bottom: Complete structure. (b) Configurations of the tetrahedral Li^+ sites.[182]

long-range diffusion[184] and in this regard the diffusion path seems to involve T2 and potentially T4 sites.[207,208]

To enhance the properties of the material, various substitution schemes have been applied aiming at optimizing the Li^+ content, the lattice polarizability or replacing Li^+ with Na^+.[209–215] A number of theoretical studies has helped corroborating the experimental findings by analyzing structure-property relationships in argyrodite materials.[150,184,207,210,213,216–221] Most notably, one interesting feature of the material is X^-/S^{2-} anion site-exchange between halide ions on 4*a* and S^{2-} ions on 4*d* sites. Theoretical studies indicate that the site-exchange is key for good transport properties[184,207,221] and measured ionic conductivities up to several mS/cm for Li_6PS_5Cl and Li_6PS_5Br have been reported.[4,180,222,223] Compared to Cl^- and Br^-, the larger size of I^- ions, however, was claimed to be the reason why insufficient site-exchange and poor transport properties are observed in Li_6PS_5I. Nevertheless, structural disorder was also realized for Li_6PS_5I by mechanical treatment and an ionic conductivity of 0.5 mS/cm was reached.[224]

In most studies, the anion X^-/S^{2-} site-exchange was controlled by varying the composition of the material,[212,216,225,226] e.g., toward halide-rich stoichiometries. Such schemes, however, also affect the Li^+ content. Therefore, it has not fully been understood which effect is responsible for the conductivity increase as the influence of the site-exchange and the varied Li^+ content could not be disentangled. Fortunately, our experimental partners found a way to also control the site-exchange in stoichiometric Li_6PS_5Br via temperature treatments: At high temperatures, a high degree of disorder between the Br^- and S^{2-} ions seems to equilibrate and quenching the material can be used to kinetically freeze this site-exchange.[9,10] The approach is illustrated in Figure 2.11. The possibility to exclusively control the Br^-/S^{2-} site-exchange enables a more systematic investigation on other properties. For example, shrinking lattice constants and changes in the Li^+ substructure have been linked to increased Br^-/S^{2-} site-exchange.[9,10] We have therefore supported this effort with DFT calculations.

A further point that has barely been analyzed so far is the effect of GBs on the ionic transport. In this regard, Yu *et al.*[227] showed that annealing of Li_6PS_5Br lowers the GB resistance and that the bulk and GB conductivity do not differ much for the annealed samples. Furthermore, they speculate that the Br^-/S^{2-} site-exchange is responsible for the good Li^+ mobility at the interface. Using a mixture of Li_6PS_5Br and Li_6PS_5Cl, Ganapathy *et al.*[228] used a NMR method and found that GBs are not rate-limiting for the Li^+ diffusion and exhibit comparable activation energies as the bulk. There is, however, no comment about if and how the GB relates to the site-exchange. Therefore, many questions concerning the interplay between synthesis, structure and transport properties are still unclear and an improved understanding will certainly contribute to the derivation of further optimization strategies for argyrodite SEs.

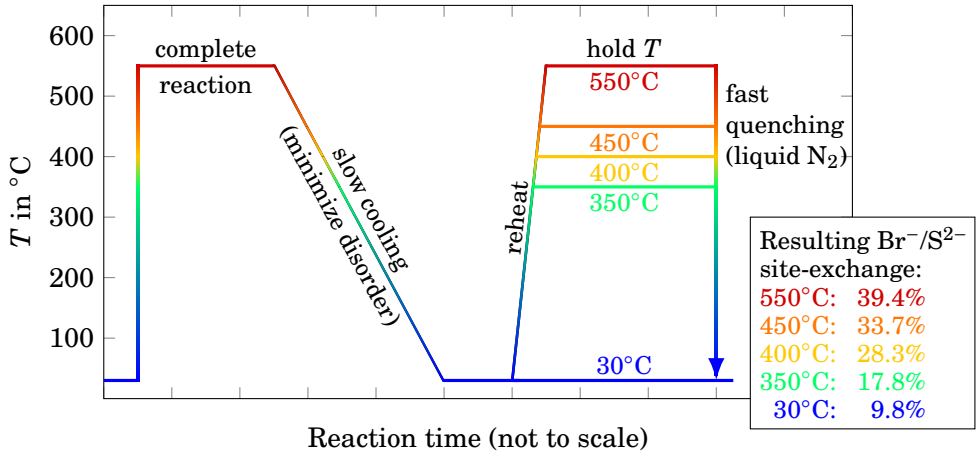

FIGURE 2.11: Schematic protocol of the temperature treatment of Li_6PS_5Br to kinetically freeze Br^-/S^{2-} site-exchange. Prior to the temperature treatment, the initial compounds (Li_2S, P_2S_5, LiBr) have been treated mechanochemically by ball milling. The resulting powder was then subjected to 550°C for 30 minutes to ensure a complete reaction and afterward slowly cooled down to 30°C within five days. Next, the samples were reheated at various temperatures for 30 minutes and finally quenched in liquid nitrogen. The resulting degrees of Br^-/S^{2-} site-exchange are listed in the inset.[10]

2.2.2 Recently Discovered Li_7SiPS_8

The discovery of Li_7SiPS_8 has only been achieved recently by Harm *et al.*[11] and no follow-up studies have been published, yet. The most important conclusions of this study are summarized in the following. The structure is composed of an equal number of PS_4^{3-} and SiS_4^{4-} structural units and two different phases have been identified. These are shown in Figure 2.12.

When quenching from higher temperatures, an orthorhombic structure with $Pnma$ symmetry (ortho-Li_7SiPS_8) is obtained. Its unit cell is shown in Figure 2.12 (a) and resembles β-Li_3PS_4 in the way the structural units are arranged. No ordering among the PS_4^{3-} and SiS_4^{4-} structural units is observed and a rather low ionic conductivity of 0.13 mS/cm is reported. At lower temperatures, a tetragonal phase (tetra-Li_7SiPS_8) with $P4_2/nmc$ symmetry emerges. In contrast to ortho-Li_7SiPS_8, the structural units of the tetra-phase are partly ordered. As shown in Figure 2.12 (b), there are two sites exclusively occupied by PS_4^{3-} units per unit cell. The remaining four sites are shared. Moreover, with 2 mS/cm tetra-Li_7SiPS_8 is a much better conductor than ortho-Li_7SiPS_8.

Similarly to other sulfide SEs, a residual glass phase is observed, which indicates the glass-ceramic character of Li_7SiPS_8. Interestingly, the composition of the glassy phase is believed to be different from the crystalline phases and seems to lower the overall ionic conductivity. Moreover, for compressed powder samples with tetra-Li_7SiPS_8 as majority phase, our experimental partners found

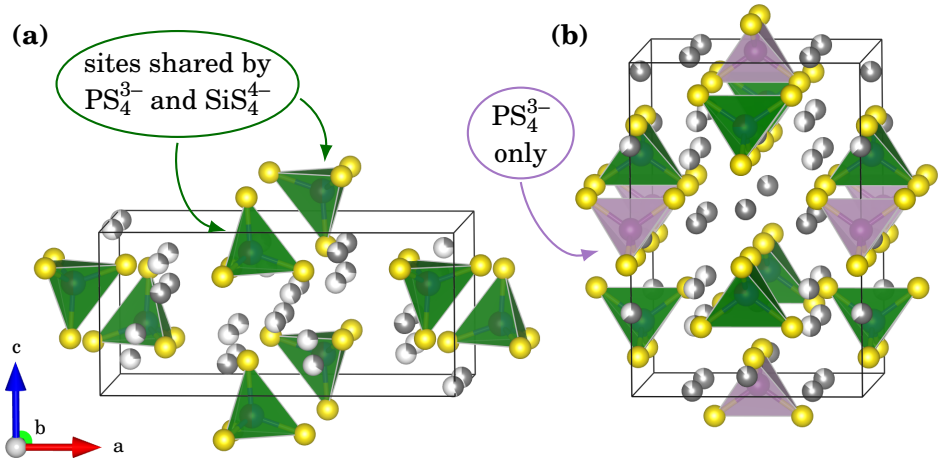

FIGURE 2.12: Crystal structure of (a) ortho-Li_7SiPS_8 and (b) tetra-Li_7SiPS_8. The occupancy ratio of the PS_4^{3-} : SiS_4^{4-} structural units on the shared sites, shown in green, is 1:1 for the ortho-phase and 1:3 for the tetra-phase. Both phases contain several Li^+ sites that are partly occupied.

that the conductivity increases if pressure is applied. This process proved to be reversible: upon release of the pressure, the conductivity decreased again. The reasons for this phenomenon were not entirely clear and three possible explanations have been suggested: First, a strong dependence of the bulk transport properties of tetra-Li_7SiPS_8 on the applied pressure. Second, a pressure-induced and reversible phase transition leading to a phase with improved transport properties. Third, improved particle-particle contact, i.e., closure of remaining voids between the particles, leading to larger contact areas and more diffusion pathways. Our partners assumed that the improved particle contact was the most likely reason for the conductivity increase. The reversible phase transition was evaluated as least likely because there were no indications of a phase transition had been observed. The role of the bulk transport properties under pressure, however, remains unclear.

In conclusion, Li_7SiPS_8 shows high promise as SE. Because not much is known about the material, however, more basic research is necessary to prove its suitability for ASSBs.

2.3 Guiding Thoughts and Research Questions Tackled in this Work

Based on the previous reviews, we can identify several knowledge gaps for the considered materials. These will be addressed in the following in terms of specific research questions that we focus on within the scope of this work.

LiPS Compounds

1. Can we generate reasonable LiPS glass structures by applying simulated melt-quenching schemes? How do the structures compare to experiments?

2. What can we learn about the thermodynamics of the LiPS system? How stable are the glasses in comparison to the crystalline phases?

3. How does the structure of LiPS glasses compare to the crystalline phases? What is the role of the underlying structural units PS_4^{3-}, $P_2S_7^{4-}$ and $P_2S_6^{4-}$? Are only these units observed or do other (defective) units occur, too?

4. In terms of Li^+ transport properties, can we derive structure-property relationships between the structural units and the diffusion coefficients? What is the diffusion mechanism in LiPS glasses?

5. For structures such as c-$Li_4P_2S_6$ that exhibit a poor ionic conductivity due to a low concentration of intrinsic point defects, is it possible to tweak the concentration by allowing for external defect equilibria?

6. Can we deepen the understanding of the interfaces, both against Li metal anodes as well as internal interfaces in LiPS glass-ceramics? How insightful is the defect thermodynamics in this regard?

Li_6PS_5Br

1. Are the experimental trends (decreasing lattice constant and changing Li^+ substructure with increasing Br^-/S^{2-} site-exchange) captured in the DFT calculations and can they be explained?

2. How does the thermodynamic stability of the material depend on the Br^-/S^{2-} site-exchange? As high degrees of Br^-/S^{2-} site-exchange are reached at high temperatures, entropic contributions seem to play a role in this regard. Can they be assessed and used to predict the equilibrium site-exchange at arbitrary temperatures?

3. What is the reason for enhanced bulk ionic conductivities upon the introduction of Br^-/S^{2-} site-exchange? Can we understand the atomistic mechanism behind it, and how does it relate to the observed changes in the Li^+ substructure? With respect to cycling under pressure or the occurrence of local strains upon volume changes of the electrodes during (de)lithiation, how does mechanical loading influence the Li^+ diffusion?

4. What is the role of GBs? How do they locally interact with the Li^+ diffusion and different degrees of Br^-/S^{2-} site-exchange?

Li_7SiPS_8

1. How does the ortho- and tetra-phases of Li_7SiPS_8 relate to each other in terms of relative stability? Is the stability influenced by the (dis)order of the PS_4^{3-}/SiS_4^{4-} units? Are both phases thermodynamically stable, or is a decomposition into other materials more favorable?

2. How high is the ionic diffusion in both phases? Do the orthorhombic and tetragonal symmetries of both phases lead to distinct anisotropy in the Li^+ mobility?

3. What is the reason for the conductivity improvement upon the application of pressure on tetra-Li_7SiPS_8 powder samples? Can we confirm/exclude that it is due to a distinct dependence of the bulk transport properties on the applied pressure?

4. What are the mechanical properties of the material? These are essential input parameters for our theoretical partners to perform mesoscopic particle simulations investigating the particle-particle contact under pressure.

5. How is the interface (in)stability against Li metal? Can reaction paths and intermediate interphases be deduced?

3 Theoretical Background

In the previous chapter we saw that sulfide SEs are rather complex systems exhibiting intricate relationships between composition, synthesis, structure and properties. Therefore, theoretical approaches and simulations can be especially helpful as complimentary methods to experiments. In the following we will explain why electronic structure calculation in the framework of DFT have been used as method of choice for this work. Furthermore, the properties of interest will be introduced and we will show how these can be assessed from the calculations. Where applicable, a short excursus into the theoretical background is given.

3.1 Atomistic Modeling

3.1.1 Classical Approach

In the context of materials research a typical question we like to ask is: For a given material, how do specific changes in the atomic structure or external variables (e.g., adding dopants, introducing defects, applying strain, ...) influence a certain property? The answer to such a question then ideally leads to optimization strategies and finally to improved materials. To answer such questions, it is obviously necessary to resolve the structure on an atomic scale in the simulations.

This can, for instance, be done using classical atomic modeling approaches. The term "classical" indicates that the smallest modeled entity is the atom or ion; electrons are not explicitly treated. The interactions between particles are described by interatomic potentials that are able to determine the potential energy of a system, from which interatomic forces can be derived.[229,230] Interatomic potentials should not be confused with force fields, which directly determine the interatomic forces.[231] Recently, interatomic potentials generated based on machine learning approaches have become more and more prominent.[232] Typically, such approaches enable the analysis of atomic models consisting of several thousands up to millions of atoms within simulation times of nanosecond up to microseconds. Unfortunately, issues with respect to reactivity, charge transfer, transferability or the treatment of several chemistries simultaneously.[233] In the context of battery materials this is clearly disadvantageous when it comes to

the modeling of (de)lithiation processes or the modeling of interfaces between sulfide SEs (at least containing Li, P, S) and cathodes (in the simplest case containing Li, Co, O). Furthermore, the generation of interatomic potentials for complex systems is a difficult task. Therefore, potentials are typically not available for systems that have only been discovered recently or are too complex, and a theoretical treatment must rely on other modeling techniques.

3.1.2 Quantum Mechanics: The Schrödinger Equation

To be able to still model the systems of interest on an atomic scale, electronic structure calculations need to be employed. In theory, these types of calculations do not need any other input except for the types of investigated atoms and their initial positions. This is best reflected in the time-independent Schrödinger equation,[233]

$$\hat{H}\Psi(\mathbf{r}_1,...,\mathbf{r}_N,\mathbf{R}_1,...,\mathbf{R}_N) = E\Psi(\mathbf{r}_1,...,\mathbf{r}_N,\mathbf{R}_1,...,\mathbf{R}_N)\,, \tag{3.1}$$

where the electronic many-body wave function Ψ depends on the coordinates of all electrons $\mathbf{r}$ and nuclei $\mathbf{R}$ (vectorial variables are indicated in bold). In this eigenvalue equation $\hat{H}$ is the Hamilton operator and the energy E represents the eigenvalue of the system. Formally, $\hat{H}$ comprises the kinetic energy of all electrons and nuclei, the Coulomb interaction among all them and the interaction with an external field. Owing to the Born-Oppenheimer approximation, the slow movements of the nuclei compared to the fast movements of the electrons allows for a separation of their wave functions.[234] Therefore, the positions of the nuclei can be considered fixed in space while treating only the electronic part of the wave function. In absence of an external field $\hat{H}$ can therefore be reduced to

$$\hat{H} = \sum_i -\frac{\hbar^2}{2m_\mathrm{e}}\nabla^2 + \sum_{i<j}\frac{q^2}{|\mathbf{r}_i-\mathbf{r}_j|} + \sum_{ik}\frac{Q_k q}{|\mathbf{r}_i-\mathbf{R}_k|}\,. \tag{3.2}$$

In this form, $\hat{H}$ now only features, from first to last term, the electron kinetic energies, electron-electron Coulomb interactions and electron-nuclei Coulomb interactions. Here, $\hbar$ is the reduced Planck constant, m_e the electron mass, ∇ the Nabla-Operator, q the elementary charge and Q_k the charge of nucleus k.

Once the Schrödinger equation is solved, i.e., E and Ψ are known, the system of interest is fully characterized and all its properties can be deduced. For example, a comparison of E could reveal which isomer of a molecule or crystal phase of a solid material is the most stable one (at 0 K). If a chemical reaction is considered, and E of all products and educts is known, a reaction energy can be calculated. Based on Ψ further properties such as the polarizability and spectroscopic properties are obtained.

Despite the introduced simplification, however, the exact or numeric solution of the Schrödinger equation is only possible for small systems.[235,236] For systems of the sizes that we are interested in (approximately 10-250 atoms with 100-2000

electrons) it is virtually impossible to solve the Schrödinger equation. This is due to its exponential increase in complexity with the number of particles. For example, using a rough grid of only $10 \times 10 \times 10$ points for the representation of a five-electrons wave function requires the storage of $(10^3)^5 = 10^{15}$ floating point numbers. Assuming 8 bytes per float with double precision accuracy, it would consume 8 Petabytes of disk space. We clearly see that further steps are required in order to make electronic structure calculations more practical. DFT is a clever workaround to the solution of the many-body problem that won Walter Kohn, one of the conceptual founders of DFT, the Nobel Prize in Chemistry in 1998.[237]

3.1.3 Density Functional Theory

The aim of DFT is the same as solving the Schrödinger equation: We want to assess certain properties of the investigated system only based on the coordinates of an atomic model. Not to lose track of the big picture, let us postpone the basic theory of DFT to the following subsections. Instead, let us first briefly outline to what extent DFT has been used in the present work and how it connects to our main properties of interest. This is also roughly illustrated in Figure 3.1. The individual methods and properties will be discussed in more detail throughout this chapter.

To be able to start a calculation, it is the scientist's task task to provide a reasonable structural model that proves descriptive for the problem setting at hand. Frequently, as in the case for amorphous structures, this is far from a straightforward task. As an approximate method, descending from Schrödingers approach, DFT is an electronic structure method that gives access to the electronic structure of a many-body system. For example, it allows for the calculation of the electronic density of states (eDOS) and band gap as outlined in Section 3.2.

Similarly to solving the Schrödinger equation, also DFT can be used to calculate E_{tot}, the total energy of the system. This quantity has been used to determine reaction energies or relative stabilities among systems with the same composition but different atomic arrangements (see Section 3.4). Furthermore, it allows for the calculation of many other properties that are related to the energy, such as defect formation energies (Section 3.5.1) or GB energies (Section 3.5.3).

Another important output of DFT calculations are the forces acting on each atom. The forces enable static structure optimizations, an important prerequisite for many analyses. Moreover, they allow for the calculation of phonons within static approaches, which can be used to assess the vibrational entropy (Section 3.4.5). Forces are also indispensable for the determination of transport properties (Section 3.6). Using the NEB approach, which applies particular force constraints to virtually connected images of the same system, also the migration barrier of ionic migration paths can be calculated (Section 3.6.2).

Furthermore, AIMD simulations are only possible if the forces are known (Section 3.3.6). These types of calculations enable the investigation of various dynamic properties, including ionic transport. In the case of unstable interfaces,

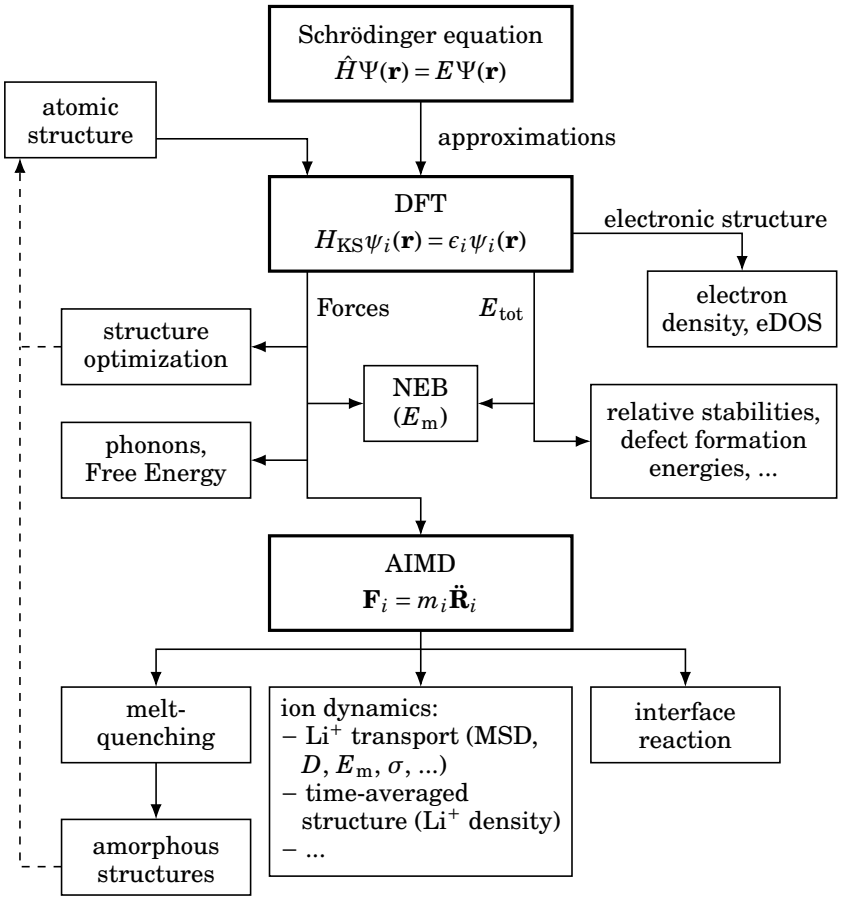

FIGURE 3.1: Schematic overview of properties that can be accessed using DFT calculations and their relations.

as it seems to be the general case when sulfide SEs are brought into contact with Li metal, it is possible to monitor interface reactions in an AIMD simulation and deduce reaction paths and products (Section 3.4.7). Additionally, AIMD lets us mimic certain experimental procedures such as melt-quenching schemes which have been used in order to generate amorphous LiPS structures (Section 3.3.8).

In conclusion, DFT calculations are quite versatile when it comes to analyzing materials properties. The electronic structure, E_{tot} and atomic forces represent basic output quantities that are indispensable for further analyses and approaches. We will therefore briefly show in the following how they can be obtained within DFT. To this end, and in order to have a complete picture, let us revisit the basic thoughts that led to the development of DFT first. Afterwards, we will review the mentioned properties in more detail and introduce the relevant theory where necessary in short excursuses.

Conceptual Background of Density Functional Theory

We saw that the many-body wave function is a quantity that heavily complicates the treatment of Schrödinger's equation. Hohenberg and Kohn realized this issue and formulated two theorems that put a much simpler quantity, namely the electron density $n(\mathbf{r})$, into focus:[238]

1. There is a unique functional dependence between the external potential (caused by the fixed nuclei) and the real ground state electron density $n_0(\mathbf{r})$ of a system. Consequently, also the energy is a functional of the density.

2. The ground state electron density $n_0(\mathbf{r})$ minimizes the energy functional, $E_0 = E[n_0(\mathbf{r})]$.

In other words, if we are able to derive $n_0(\mathbf{r})$ and know the relation to calculate E_0 we would be able compute relative stabilities, reaction energies and further properties of the system. This leaves us with the question of how to determine $n_0(\mathbf{r})$ and its relation to E_0.

Calculation of the Electronic Structure and E_{tot}

To calculate $n(\mathbf{r})$ Kohn and Sham developed a self-consistent scheme that avoids dealing with the many-body wave function.[239] Instead, the many-body wave function is split into a set of one-electron wave functions. The term "self-consistent" indicates that an initial guess for $n(\mathbf{r})$ is needed. Next, during the calculation this initial guess is processed and after one cycle an updated $n(\mathbf{r})$ is obtained. This procedure is repeated until $n(\mathbf{r})$ is converged within the desired accuracy. The workflow for such an optimization of $n(\mathbf{r})$ is:

1. Start with an atomic structure and a trial electron density.

2. Calculate the effective Kohn-Sham potential v_{KS} based on the supplied electron density, the external potential v_{ext} due to the fixed nuclei and the exchange-correlation potential v_{ext},

$$v_{\mathrm{KS}}(\mathbf{r}) = v_{\mathrm{ext}}(\mathbf{r}) + \int \frac{n(\mathbf{r}')}{|\mathbf{r}-\mathbf{r}'|}\,\mathrm{d}\mathbf{r}' + v_{\mathrm{xc}}(\mathbf{r})\,. \tag{3.3}$$

3. Using the Kohn-Sham Hamilton operator $H_{\mathrm{KS}} = -\frac{1}{2}\nabla^2_{\mathbf{r}} + v_{\mathrm{KS}}$ determine the one-electron Kohn-Sham wave functions ψ_i by solving the Kohn-Sham equations,

$$H_{\mathrm{KS}}\psi_i(\mathbf{r}) = \epsilon_i\psi_i(\mathbf{r})\,. \tag{3.4}$$

4. Update the electron density,

$$n(\mathbf{r}) = \sum_i^N |\psi_i(\mathbf{r})|^2\,. \tag{3.5}$$

5. Stop if the desired convergence criterion is reached. Otherwise, restart the cycle at step 2 with the updated electron density as new input keeping the atomic structure untouched.

Once the electronic structure is converged the electronic energy E_{el} of the system can be calculated,

$$E_{\mathrm{el}} = \sum \epsilon_i - \frac{1}{2}\int\int \frac{n(\mathbf{r})n(\mathbf{r}')}{|\mathbf{r}-\mathbf{r}'|}\,\mathrm{d}\mathbf{r}\,\mathrm{d}\mathbf{r}' - \int v_{\mathrm{xc}}(\mathbf{r})n(\mathbf{r})\,\mathrm{d}\mathbf{r} + E_{\mathrm{xc}}[n(\mathbf{r})]\,. \tag{3.6}$$

The exchange-correlation energy E_{xc} and v_{ext} mentioned above are correction terms that should compensate for all introduced approximations. For now, they should not distract us and we will revisit them in Section 3.2.2. As a last step, the total energy E_{tot} of the initially provided atomic structure is obtained if the energy due to the ionic system is added to E_{el}.

Force Calculation and Structure Optimization

The positions of the nuclei are initial input parameters of a DFT calculations and kept fixed during the self-consistent electronic cycle as described in the previous section. In many case, however, the provided nuclei positions might not correspond to a (local) minimum in phase space with the given choice of computational settings. Therefore, they need to be structurally optimized before accurate properties of the material can be obtained. The structure optimization requires knowledge of the atomic forces $\mathbf{F}$ acting on each nuclei. The calculation of $\mathbf{F}$ is formalized by the Hellmann-Feynman theorem,[240]

$$\frac{\mathrm{d}E}{\mathrm{d}\lambda} = \frac{\mathrm{d}}{\mathrm{d}\lambda}\langle\psi|H|\psi\rangle = \left\langle \psi \middle| \frac{\mathrm{d}H}{\mathrm{d}\lambda} \middle| \psi \right\rangle\,, \tag{3.7}$$

which allows to replace the dummy variable λ with atomic positions $\mathbf{R}$ of atom i,

$$\mathbf{F}_i = -\frac{\partial E(\mathbf{R}_1,...,\mathbf{R}_N,)}{\partial \mathbf{R}_i}\,. \tag{3.8}$$

After all forces are known the ions can be displaced accordingly in a direction that minimizes the forces. Most commonly this is done using conjugate-gradient or quasi-Newton methods.[241] The updated positions can be used as new initial atomic structure to restart the self-consistent electronic cycle, to calculate new forces and to optimize the atomic positions again. This loop is repeated until the desired convergence criterion for forces or total energy is reached. The convergence criterion needs to be defined by the user and can depend on the investigated property and the size of the system.

Computational Details

For all electronic structure calculations performed in this work we have used the Vienna ab Initio Simulation Package (`VASP`).[242–245] The convergence criterion for

the electronic cycle was set to 10^{-6} eV or lower. Standard structure optimizations were performed using different algorithms until all forces fell below 10^{-2} eV/Å. Mostly, the conjugated gradient and Newton-like algorithms as implemented by `VASP` were applied. Occasionally, we relied on algorithms as implemented by the Henkelmann group (see their website).[246] For more details concerning related mathematical algorithms, the interested reader is referred to textbooks on this subject.[241]

3.2 Electronic Structure

Above we illustrated the basics of DFT as a method to determine the electronic structure. Based on the electronic structure, selected electronic properties can be analyzed as follows.[247]

3.2.1 Charge Density, eDOS and Band Gap

The analysis of the electron density $n(\mathbf{r})$ can be the first step if the electronic structure of a system is of interest. Typically, this is done graphically. One way is to plot $n(\mathbf{r})$ for a specific plane, e.g., between two atoms to investigate their bonding character. Alternatively, isosurfaces of $n(\mathbf{r})$ are visualized using programs such as `VESTA`[248] or `OVITO`[249] as shown in Figure 3.2 (a) and (b). The latter approach was used to verify whether "unusual" structural units observed in LiPS glasses are indeed covalently bonded (see Section 4.3.6).

The eDOS can be computed based on the eigenvalues ϵ_i, i.e., the energy states, of the solved Kohn-Sham equations (Equation 3.4). These can be used to determine $N_{\text{el.}}(E)$, the number of states encountered up to a given energy E. The eDOS indicates how many electronic states are present within an energy interval,

$$\text{eDOS}(E) = \frac{\mathrm{d}N_{\text{el.}}}{\mathrm{d}E} \approx \frac{\Delta N_{\text{el.}}}{\Delta E} = \frac{N_{\text{el.}}(E+\Delta E) - N_{\text{el.}}(E)}{\Delta E} \,. \tag{3.9}$$

To avoid a step-like behavior in eDOS plots, some sort of smoothing is typically applied.[250] A common Gaussian smearing has mainly been utilized in this work.

An exemplary eDOS of tetra-Li_7SiPS_8 is shown in Figure 3.2 (c). The total eDOS can be broken down into the orbital contributions of individual ions. These projected eDOS can therefore also be used to deduce the bonding character by analyzing orbital hybridization: For the illustrated example, the contributions of S often overlap with those of P or Si, indicating a covalent S–P and S–Si bonds, as present in the SiS_4^{4-} and PS_4^{3-} units. We have used the projected eDOS also in the context of interface reactions between Li_7SiPS_8 and Li metal in Section 6.4.4. In this regard, the partial and total eDOS were used to confirm the formation of reaction products.

The energy of the highest occupied state and the lowest unoccupied state of the eDOS define the electronic band gap E_g of the material. Physicist typically call these states valence band maximum (VMB) and conduction band minimum

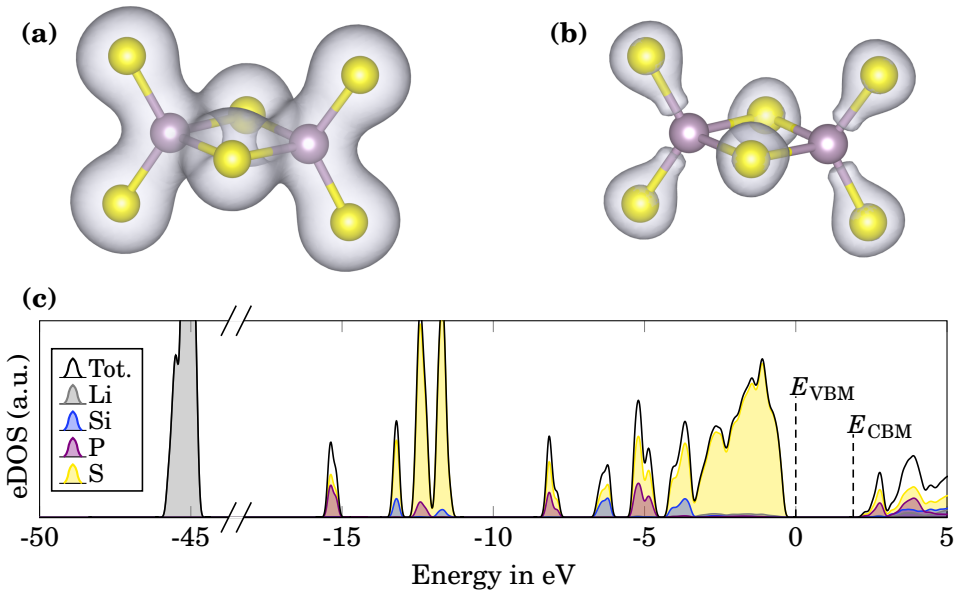

FIGURE 3.2: (a) Exemplary isosurface of the electron density within a $P_2S_6^{2-}$ unit. (b) The same electron density at an higher level of the isosurface. (c) The calculated eDOS of tetra-Li_7SiPS_8. Conventionally, $E_{VBM} = 0$.

(CBM), respectively, while chemist often prefer the terms highest occupied molecular orbital (HOMO) and lowest unoccupied molecular orbital (LUMO).[251] If VMB and CBM are directly adjacent, only small excitations are needed to promote electrons into the conduction band. As a result, the material should exhibit metallic character. If VMB and CBM are not adjacent to each other, the distance between them defines the band gap,

$$E_g = E_{CBM} - E_{VBM} \,. \tag{3.10}$$

In the context of our generated amorphous LiPS structures we calculated E_g in Section 4.3.8 to verify that they are true ionic conductors: If no band gap or only small values for E_g had been obtained, the amorphous structures would have been electronic or mixed electronic-ionic conductors. This would have disqualified them for the usage as SEs.

When analyzing band gaps, however, two issues need to be kept in mind. First, if one is interested in whether the material exhibits a direct or indirect band gap, the calculation of the full band structure is necessary. Because such a question is usually only important for understanding the electronic conductivity in semiconductors,[252] it is of no interest here. Second, standard DFT approaches commonly underestimate the band gap.[253] This can be problematic because materials that seem to be metallic based on the calculated electronic structure might actually exhibit a band gap in reality. The underestimation of E_g is a

result of a spurious electron self-interaction. The corrections to this term and to all approximations that have been applied are embedded in the exchange-correlation terms.

3.2.2 Excursus 1: The Exchange-Correlation Functional

Equation 3.6, presented above, is formally exact because the two exchange-correlation terms v_{xc} and E_{xc}, with

$$v_{xc} = \frac{\partial E_{xc}[n(\mathbf{r})]}{\partial n(\mathbf{r}))} \,, \tag{3.11}$$

compensate for all approximations that have been introduced. The complex task of solving the Schrödinger equation has therefore been passed down to finding a suitable expression for the unknown exchange-correlation functional E_{xc}. Hence, the accuracy of the DFT calculation depends on the quality of E_{xc} and different levels of theory have been applied in order to derive expressions for it.[254]

Within the local density approximation (LDA), as the name implies, E_{xc} is a local property and only depends on the local value $n(\mathbf{r})$.[238] The LDA approach was then advanced to the generalized gradient approximation (GGA). Within GGA, also local electron density gradients $[\nabla n(\mathbf{r})]$ are accounted for. Among the various existing GGA functionals, a famous example is the Perdew-Burke-Ernzerhof (PBE) functional that has been used for all DFT calculations in this work.[255–258]

For completeness we mention further types of exchange-correlation functionals that go beyond GGA theory. The most common ones are meta-GGA functionals (including second derivatives of the density), DFT+U approaches (addition of a Hubbard correction term U for a better description of strongly localized electrons), or computationally demanding hybrid functionals (relies on Hartree-Fock theory).[259]

3.3 Atomic Structure

The atomic structure is one of the few necessary inputs needed to execute DFT calculations. It is typically provided as a list of atomic coordinates within a chosen crystallographic cell of the material. For solid materials the atomic structure can be classified based on different aspects such as dimensionality (2D or 3D materials) or symmetry considerations.[260] One of the most fundamental classifications distinguishes between crystalline and non-crystalline (i.e., amorphous or glassy) materials.[261] As described in Chapter 2, both these forms are important in the context of sulfide SEs. Let us therefore review their features and what implications they pose on the simulations.

3.3.1 Crystalline Materials

Crystalline materials are characterized by a periodic arrangement of its constituents. The so-called unit cell is the smallest repetitive unit in a crystal. It is spanned by three lattice vectors and can contain an arbitrary amount of atomic species whose positions are commonly given in fractional coordinates of the lattice vectors. The unit cell and its arrangement of atomic species define the crystal symmetry or so-called space group of the material.[262] By applying translational symmetry operations to the unit cell a macroscopic crystal is formed.

Where does a crystalline starting structure for the calculations come from? Typically, they can be obtained from databases (e.g., the *Crystallography Open Database*[263] or the *Materials Project*[264]), from literature or experimental partners. The base crystalline structures analyzed in this work have all been resolved experimentally beforehand and were provided by our experimental partners or retrieved from literature. We note, however, that it is not compulsory to start with a known structure. In the field of theoretical structure prediction, an analytically unsolvable problem, the aim is to find reasonable crystal structures based on a defined composition by utilizing specific heuristic and meta-heuristic algorithms.[265] Also in high-throughput studies unknown materials are commonly treated.[266] Typically, such studies start with well defined crystal structures. Next, the atomic sites are systematically occupied with various atomic species and the property of interest is monitored. If a promising new material is identified in the calculations, such studies can serve as guide to the experiment.

Regardless of the origin of the initial structural model, its underlying periodicity depicts an ideal advantage for effectively performing DFT calculations. This is because DFT is still rather limited with respect to the system size: Even when relying on high-performance computing facilities, the handling of systems with approximately 2000 electrons or more becomes hardly practical. Obviously, such small systems could at most represent nanoparticles but not bulk materials. The periodicity observed in crystals, however, benefits the calculations and allows for simulating a bulk material by applying periodic boundary conditions (PBCs).

3.3.2 Excursus 2: Periodicity and the Basis Set

In the spirit of Bloch's theorem we acknowledge that we do not need to model a full crystal consisting of 10^{23} atoms.[267] Instead, it is sufficient to properly describe only the smallest repetitive unit, or few of them, to represent a bulk material. The infinite crystal and its electronic structure are then simulated by applying PBCs as depicted in Figure 3.3.

When solving the differential Kohn-Sham equations (Equation 3.4) it is therefore beneficial to express the Kohn-Sham wave functions ψ in terms of a basis set, or in other words, as a superposition of a set of specific functions.[268] A

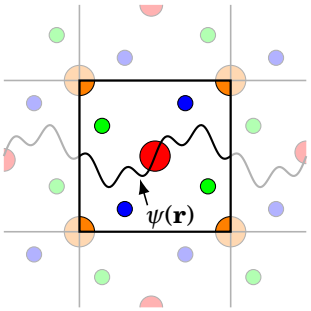

FIGURE 3.3: Illustration of a bulk material modeled with one unit cell under periodic boundary conditions (PBCs). The periodicity applies to both the atomic arrangement and electronic structure, i.e., the wave functions.

prominent choice, which has also been used in this work, is to apply a plane wave basis.[245] This is because plane waves are inherently compatible with periodicity,

$$\psi_{\mathbf{k}}(\mathbf{r}) = \sum_{\mathbf{G}} c_{\mathbf{G}+\mathbf{k}} \exp^{i(\mathbf{G}+\mathbf{k})\cdot\mathbf{r}} \ . \tag{3.12}$$

The k-points $\mathbf{k}$ are wave vectors confined to the first Brillouin zone (the primitive cell of the reciprocal crystal lattice), $\mathbf{G}$ is a reciprocal lattice vector and $c_{\mathbf{G}+\mathbf{k}}$ the respective plane wave coefficient.

For accurate simulations, two settings need to be converged, and in many case a compromise between accuracy and computational effort has to be made. The first one is the number of sampled k-points. The choice depends on the property of interest, the system at hand and its cell size. A small system in real space corresponds to a large system in reciprocal space and therefore requires a large number of k-points. For large cells in real space, often only one k-point, namely the gamma-point at (0,0,0) in reciprocal space, is considered.[250] The same holds true for AIMD simulation which will be presented in Section 3.3.6. The second setting is the cutoff energy E_{cut} of the plane wave basis set,

$$E_{\text{cut}} = \frac{\hbar^2}{2m_{\text{e}}} G_{\text{cut}}^2 \qquad \text{with} \qquad |\mathbf{G}+\mathbf{k}| < G_{\text{cut}} \ . \tag{3.13}$$

Larger values for E_{cut} will include more plane waves with higher energies resulting in a more accurate representation of the wave function.

Computational Details

All AIMD simulations were only performed at the gamma-point. For static calculations, we made use of the `KSPACING` tag used by `VASP` instead of manually defining the k-points. This ensures consistency when comparing the properties of differently sized or differently shaped supercells. Using this approach, the number of k-points $N_{\mathbf{k}}$ is automatically calculated according to size of the reciprocal simulation cell,

$$N_{\mathbf{k}} = \max\left(1, \ \frac{\mathbf{b}_i}{\texttt{KSPACING}}\right), \tag{3.14}$$

TABLE 3.1: Used values for E_{cut} and KSPACING for the respective calculations. Values of E_{cut} marked with † represent calculations that have been performed using a pseudopotential for Li that only treats one electron explicitly as described in Section 3.3.4.

Material system	Calculation type	E_{cut}	KSPACING
LiPS	Static	600 / 420†	0.25
	AIMD	420†	gamma-only
	Phonons	600	0.25
	eDOS	420†	0.25
Li_6PS_5Br	Static	600	0.25
	AIMD	499	gamma-only
	Phonons	800	0.25
Li_7SiPS_8	Static	600	0.25
	AIMD	499	gamma-only
	Elast. prop.	900	0.25
	eDOS	600	0.125

where $\mathbf{b}_i$ is a reciprocal lattice vector. Our final sets of parameters for the various investigations are listed in Table 3.1.

3.3.3 Supercell Approach

Several bulk properties such as E_{tot}, the eDOS or elastic constants can be obtained by simulating only one unit cell. For other cases, however, one unit cell might not be representative. This becomes clear when a simple example is treated: Let us assume we are interested in vacancies in Li metal. Li metal crystallizes in a body-centered cubic structure and contains two atoms per unit cell. If we treated only one unit cell and removed one Li atom from it, we would simulate an unreasonable system with a vacancy concentration of 50%. Viewed differently, this corresponds to simple cubic arrangement of Li atoms with an absurdly large lattice constants.

To circumvent such a scenario, the so-called supercell approach is commonly applied.[269] Instead of treating only a single unit cell, the system is replicated as often as necessary and/or computationally feasible. For the example above, a more reasonable approach could be to set up $5 \times 5 \times 5$ supercell and only introduce a single Li vacancy in one of the 125 unit cells. The full supercell is then subjected to the PBCs. In this context, care needs to be taken that the vacancy does not interact with itself via its periodic images. To this end, the size of the supercell needs to be chosen such that spurious self-interaction between periodic images is kept on a negligible level and/or correction schemes, especially for charged systems, need to be applied.[270]

3.3.4 Excursus 3: Pseudopotentials

If the calculations demand the usage of supercells, the number of treated atoms can increases quickly. Eventually, the number of electrons is likely to exceed what can be reasonably simulated. This is especially critical if the material consists of heavier elements that possess many electrons. In the majority of cases, however, the electrons close to the nucleus barely affect the physics of interest and only a correct description of the valence electrons might be necessary. This led to the development of pseudopotentials that replace the complicated potential originating from the interplay of nucleus and core electrons with an effective potential.[271] Outside a given cutoff the pseudopotential restores the real potential as shown in Figure 3.4.

This approach has two advantages. First, much fewer electrons need to be handled explicitly and the computational demand is reduced substantially. Second, the energy cutoff E_{cut} of the plane wave basis set can be reduced. This is because the pseudopotentials lead to much smoother wave functions compared to the real ones that are strongly oscillating close to the nuclei. For the latter case, much high-energy plane waves (i.e., a high E_{cut}) would be needed to adequately reproduce the wave functions adequately.

Pseudopotentials have been developed in different "flavors".[271] These include norm-conserving or ultra-soft pseudopotentials. More elaborate approaches make use of projector augmented-wave (PAW) pseudopotentials which allow to reconstruct the original core wave functions.[273,274]

Computational Details

All DFT calculations reported in this work have been executed using PAW pseudopotentials as included in the VASP code. They are summarized in Table 3.2. For the treatment of pure LiPS phases, we have initially relied on a pseudopotential for Li where only the outermost electron is explicitly modeled. Later,

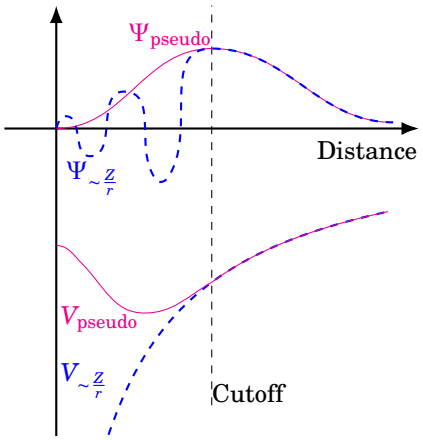

FIGURE 3.4: Schematic comparison of the resulting wave functions based on the real potential (blue) and based on a pseudopotential (magenta).[272]

TABLE 3.2: Used pseudopotentials (names as referenced in the files provided by VASP) for the elements simulated in this work together with the number of electrons that are treated as valence electrons.

Element	Pseudopotential Name	number of valence electrons
Li	PAW_PBE Li 17Jan2003	1
Li	PAW_PBE Li_sv 10Sep2004	3
Si	PAW_PBE Si 05Jan2001	4
P	PAW_PBE P 06Sep2000	5
S	PAW_PBE S 06Sep2000	6
Br	PAW_PBE Br 06Sep2000	7

the pseudopotential including all three electrons has been used to recalculate relative stabilities of glasses compared to crystalline phases and to calculate phonons. For all remaining calculations, the pseudopotential for Li with three electrons has been used from the very beginning.

3.3.5 Amorphous Materials

So far, we have only considered DFT for the simulation of crystalline materials. As addressed in Section 2.1.3, however, amorphous phases play an important role for sulfide SEs and also addressed in this work. In contrast to crystalline materials, all amorphous materials are characterized by the absence of a distinct long-range order.[261] As a result, two dilemmas are faced when simulating amorphous structures. First, there are typically no structural models available for amorphous phases that could be used as input for the DFT calculations. Instead, such models need to be created first, which is a complex task[134,135] and topic of Section 3.3.8. Second, PBCs will lead to an artificial long-range order due to the periodic images. Therefore, sufficiently large systems need to be modeled to limit self-interaction between periodic image when simulating bulk glasses.

Despite the lack of long-range order, most amorphous materials exhibit a unique short-range order.[275] For the glassy LiPS materials the obvious short-range order is reflected in the various well defined phosphorous sulfide structural units.[115] For such a case it is helpful to analyze whether a more extensive order in the vicinity of the structural units is observed. To this end, an analysis of radial distribution function (RDFs) can be applied.[276] RDFs illustrate how likely particles are in the vicinity of other particles and an example is sketched in Figure 3.5. The computation of an RDF can easily be performed based on the atomic positions of DFT simulations. RDFs are calculated by counting the number of ions N_r within shells of thickness Δr at an interatomic distance r,

$$\mathrm{RDF}(r) = \frac{1}{\rho_0} \frac{N_r}{4\pi r^2 \Delta r} , \tag{3.15}$$

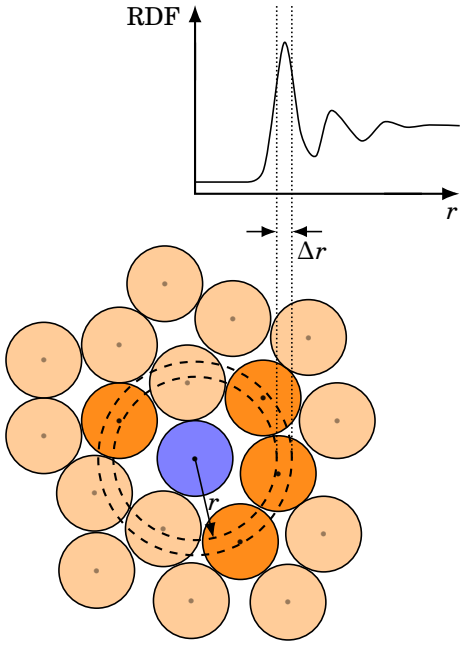

FIGURE 3.5: Illustration of the relation between an amorphous structure and its RDF. In the absence of any order the RDF of an amorphous structure converges to a value of unity at large interparticle distances.

where $\rho_0 = N/V$ is the average particle density that only depends on the simulation cell volume V and total number of particles N. For truly amorphous materials, the RDF should converge to a value of 1, which indicates no preferential correlation between the interparticle distances. Such a converging behavior can be a first estimate of whether a sufficiently large system has been simulated. Whereas the total radial distribution function (tRDF) involves all atoms, partial radial distribution function (pRDFs) only take into account specific atomic species and can enable a more detailed analysis of how the atomic structure is correlated.

Computed RDFs can be compared to experimental ones, commonly obtained by scattering methods, to estimate the quality of generated structures. Such a case is presented in Section 4.1.2, where experimentally taken reduced pair distribution functions $G(r)$ needed to be converted to RDFs first,

$$\mathrm{RDF} = \frac{G(r)}{4\pi r \rho_0} + 1 \,. \tag{3.16}$$

Different elements in the material, however, typically possess different scattering powers with respect to the experimental particle source (X-ray or neutrons). Therefore, the scattering intensity is influenced and weighting factors w_{ij}, for every pair of atomic types i and j, need to be applied to the simulated RDFs to make the data comparable. For simplicity, we used constant weighting factors,

$$w_{ij} = \frac{(2-\delta_{ij}) c_i c_j f_i f_j}{\sum_{i,j\leq i}(2-\delta_{ij}) c_i c_j f_i f_j} \,, \tag{3.17}$$

where c depicts the atomic concentrations. As we have only used experimental data obtained vie X-rays, the scattering factors f were chosen to emulate the number of electrons attributed to different atom types: $f_{\mathrm{Li}} = 2$, $f_{\mathrm{P}} = 12$ and $f_{\mathrm{S}} = 17.5$. Finally, the weighted RDF is obtained based on the determined pRDFs,

$$\text{weighted RDF} = 1 + \sum_{i,j \leq i} w_{ij} \left[\frac{\text{pRDF}_{ij}}{(2-\delta_{ij}) c_i c_j} - 1 \right] . \tag{3.18}$$

There are two remaining issues that need to be kept in mind. First, RDFs are non-univocal; different structures can lead to similar RDFs. Second, DFT can only handle relatively small structures and the resulting RDFs from static calculations will be rather coarse. Simple smearing methods certainly help smoothing the data but might be inappropriate. A more sophisticated approach relies on dynamic DFT calculations. These AIMD calculations allow for the simulation of materials at finite temperature and feature the full ion dynamics. A smooth RDF is then obtained by taking the time-average over entire trajectories. Because AIMD simulations are an essential method of this work, let us shortly examine their basic principles in the following.

3.3.6 Excursus 4: Ab-initio Molecular Dynamics

The aim of MD simulations is to progress the system in time in order to study its dynamics.[277] To this end one needs to solve the equations of motion tat are described in the framework of classical Newtonian dynamics,

$$\mathbf{F}_i = m_i \ddot{\mathbf{R}}_i \ , \tag{3.19}$$

where m_i and $\mathbf{R}_i$ are the mass and acceleration of atom i. Whereas classical MD simulation obtain $\mathbf{F}$ based on interatomic potentials, AIMD simulations perform a full electronic optimization of the system at every time step to calculate to calculate $\mathbf{F}$. This is the reason why the computational demands for AIMD simulations are orders of magnitude higher than classical MD.

The time integration of Equation 3.19 can be done in various ways. Typically, a Verlet algorithm is employed.[278,279] Depending on the desired calculation settings, a thermostat and/or a barostat can be coupled to the simulation box to control temperature and/or pressure.[280,281] Due to the small system sizes of typical DFT simulations, however, these thermodynamic variables are naturally subjected to spurious fluctuations.[282] For most AIMD studies, the simulations are therefore performed at constant volume.

The capabilities of AIMD simulations are manifold: In addition to th calculation of smooth RDFs, as described above, we have used AIMD simulations (i) to generate amorphous structures via melt-quenching schemes (Section 3.3.8), (ii) to determine the ionic transport properties (Section 3.6), (iii) to analyze the structure, i.e., the average Li^+ distribution, at finite temperature, and (iv) to study the interface stability of SEs against Li metal at finite temperature.

Computational Details

All AIMD simulations of this study have been performed in the canonical (NVT) ensemble (see Section 3.4.1), i.e. with a fixed number of particles and a fixed simulation box. A Nosé-Hoover thermostat is used for temperature control and the time step has been set to 1 fs.[283] To keep the computational demand on a reasonable level, the convergence criterion for the electronic optimization cycle has been reduced compared to static calculations and was set to 10^{-5} eV. Moreover, only the gamma-point was sampled and E_{cut} was reduced to the recommended value as specified in the pseudopotential files that are shipped with `VASP`.

3.3.7 Glass Formation

Before we explain how amorphous structures have been generated using a melt-quenching scheme, it is useful to address the glass formation process. For many materials this is a complex competition between crystalline and glassy phases that involves thermodynamics as well as kinetics.[284,285] As an example, Figure 3.6 shows the temperature dependence of phase volume and highlights the different melting behaviors of crystalline and glassy materials.[286] Whereas crystalline phases possess a well defined melting temperature T_{m}, glasses exhibit a glass transition. The glass transition is located around the glass transition temperature T_{g} and represents a temperature regime during which the properties of the glass change gradually until it cannot be distinguished from the melt anymore or starts to crystallize.

Let us assume we have fully melted the system and the melt is above T_{m}. Next, it is cooled until it reaches T_{m}. There are two possibilities for the further evolution of the system. First, the material is able to form crystallization seeds. Once these reach a critical size they start to grow. The released heat

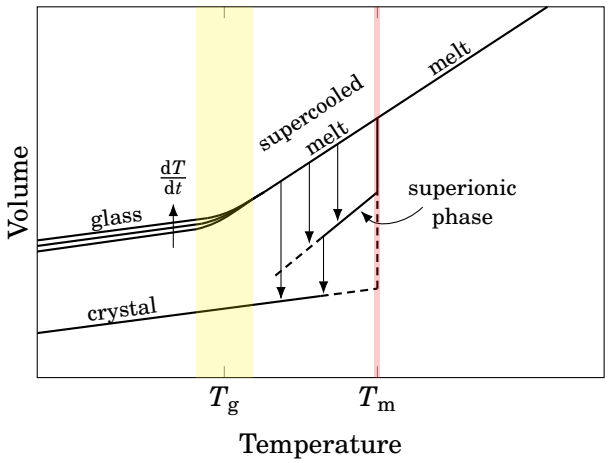

FIGURE 3.6: Illustration of the temperature-volume dependence of a system that comprises crystalline and glassy phases. The glass transition temperature T_{g} indicates the onset of the glass transition.

of crystallization maintains T_m as long as both phases are present. Assuming that the crystal is more dense than the melt, the system moves vertically down but remains at T_m. Once the crystallization is complete we reach the corner of the dashed line in the lower right part of Figure 3.6. Form this point on the temperature can be decreased further and the system moves to the left along the line labeled with "crystal".

Alternatively, when coming from the melt, the crystallization can be prevented due to multiple reasons such as fast cooling or the inherent properties of the material. As a result, the melt is able to remain in a supercooled state.[286] Once temperatures close to T_g are reached, the properties of the supercooled melt start to change gradually. This is strongly pronounced for the viscosity, which typically changes by several orders of magnitude and reveals the formation of a solid glass.[287] In this regard, kinetics can influence the final properties of the glass. This is indicated in Figure 3.6 as different cooling rates $\mathrm{d}T/\mathrm{d}t$ can result in different volumes: When being cooled quickly, the constituents of the supercooled melt do not have enough time to properly rearrange. Instead, kinetic freezing of unfavorable local configurations from the supercooled melt lead to larger volumes or less stable materials. If high cooling rates are chosen, such a scheme are referred to as melt-quenching procedures and will be topic of Section 3.3.8.[288]

Experimentally, mechanochemical approaches seem to be favored over melt-quenching for the synthesis of sulfide SEs.[116,118,124,138,149,289] Subsequently, these glasses are often subjected to heat treatments. Under such conditions the systems starts on one of the lines labeled with "glass" in Figure 3.6. Once it surpasses the glass transition regime during the heat treatment, it is again in the state of a supercooled melt. If enough time is provided at this stage, (partial) crystallization is commonly observed for sulfide SE glasses and the system follows one of the arrows pointing downwards.

It can then reach back to the line labeled "crystal". Alternatively, the system might as well be able to form a different, less stable phase (labeled as "superionic phase") with more desirable properties than the thermodynamically stable one. This is the case for the superionic $Li_7P_3S_{11}$ phase, which is not accessible by means of standard solid state reactions.[133] For extended heat treatments, the superionic phase might as well be converted to the low-energy crystal, which should be avoided for $Li_7P_3S_{11}$.

3.3.8 Preparation of Glass Structures via Melt-Quenching

We have already mentioned that reliable structural models for amorphous materials are typically not readily available. As a consequence, they must be generated first. This is not a straightforward task, especially if the material of interest exhibits a complex short-range order.

Experimentally, the three main synthesis approaches involve mechanochemical routes, wet-chemical methods or melt-quenching schemes. Whereas the first

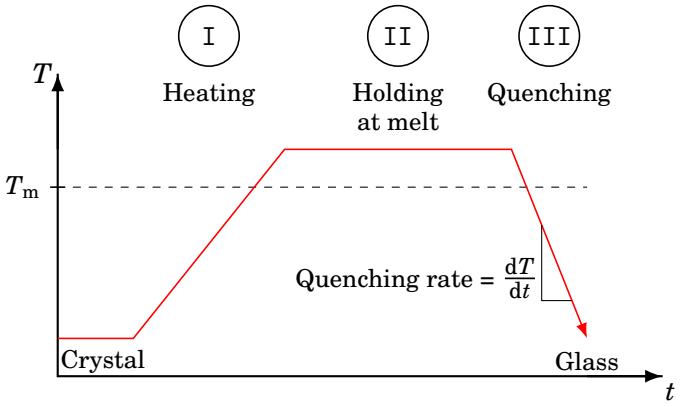

FIGURE 3.7: Illustration of a melt-quenching scheme.

two approaches are hardly transferable to electronic structure calculations, a melt-quenching scheme can be mimicked with atomistic simulations,[290] even at the AIMD level.[291] It was therefore chosen as the preferred method to prepare amorphous structures in this work.

The concept of melt-quenching approaches is simple and illustrated in Figure 3.7. First, the material is heated above its melting temperature T_m. Typically, it is then held at a constant temperature for a certain amount of time. Finally, the melt is quenched quickly enough to avoid crystallization and an amorphous structure is obtained.

This approach can be transfered to AIMD, keeping in mind the accessible time scales of the simulations: In practice, simulation times of the order of 100 ps with approximately 200 atoms are considered to be of medium to long lengths for a system of reasonable size. If temperature differences of several hundreds Kelvin need be covered within these time scales, only ultrafast quenching rates of the order of 10 K/ps (= 10^{13} K/s) are feasible. These are typically several orders of magnitude higher than what can be reached in conventional experiments.[292] Nevertheless, melt-quenching schemes using AIMD represent an unbiased way to prepare amorphous structures. Our performed melt-quenching simulations can be divided in two categories. We distinguish between a "soft" and "brute-force" approach.

"Soft" Melt-Quenching Approach

The concept behind the "soft" melt-quenching approach was to apply temperatures that are sufficiently high to initialize amorphization, but still low enough to avoid dissociation of the underlying structural units (PS_4^{3-}, $P_2S_7^{4-}$, $P_2S_6^{4-}$). This goes back to the fact that in the amorphous samples the same structural units

as in crystalline LiPS phases are found. We therefore wanted to preserve these structural features.

The known crystalline LiPS phases were used as starting structures. Based on these, we prepared supercells typically containing approximately 200 atoms to ensure sufficiently large systems. To save computing time, we omitted the heating step and directly applied moderate to elevated temperatures of up to 1000 K to initiate the amorphization process. During this process, the volume of the supercells was increased stepwise up to a total volume increase of 25%. The aim of the volume increase was not to account for thermal expansion as it might be intuitive to think, but to facilitate the atomic reordering by providing enough space.

Because none of the initial crystalline LiPS phases has a cubic structure, the resulting supercells also resulted in anisotropic supercells. To avoid a correlation between the initial cell geometry and the resulting atomic arrangement, we also stepwise transformed the supercell shape. Depending on the situation, this was either done by combining static calculations with AIMD simulations or by directly employing AIMD simulations. During this process a temperature of 700 K was applied. After a cubic cell was eventually obtained, the material was maintained at the elevated temperature for a sufficient amount of time. The dilated volume was then again compressed until a value close to the initial volume was reached. The total AIMD simulation time for the amorphization process amounted to approximately 50 ps.

Again, in order to save computing time, we omitted an explicit simulation of the quenching process. Instead, the structures obtained from the amorphization process were directly subjected to static optimizations of the atomic positions and simulation cell to finally obtain amorphous LiPS models. This corresponds to an immediate quenching with an infinite quenching rate. At this point, we found that in some cases individual structural units had dissociated during the amorphization. To retrieve the ideal structural units, we tried to manually rearrange the atoms locally. Afterward we performed static structural optimization and/or AIMD simulations at low temperature to verify if the processed structures are stable. This approach was successful in the majority of cases. For one case, however, we observed an atomic rearrangement corresponding to $2 \cdot \mathrm{P_2S_7^{4-}} \rightarrow \mathrm{PS_4^{3-}} + \mathrm{P_3S_{10}^{5-}}$ that could not be recovered after several attempts.

Because the glasses were immediately quenched or partly modified manually, their E_{tot} from a subsequent structural optimization might be unrepresentative. To obtain more reliable values the glass models were subjected to AIMD simulations. These simulations were not only used to analyze the $\mathrm{Li^+}$ diffusion, but can also be considered as an annealing step that allows for a better equilibration and restructuring of the material. The annealing was performed for approximately 40 ps at 300 K followed by a structural optimization. The corresponding E_{tot} are then used as representative energy for the glasses.

"Brute-Force" Melt-Quenching Approach

The "brute-force" melt-quenching approach was only applied for the generation of additional amorphous models with $Li_4P_2S_7$ composition in the course of a preceding work. These structures were recalculated and used as basis for further investigations here. Compared to the soft melt-quenching approach, the brute-force approach is characterized by much higher temperatures during the amorphization process. The heating step was omitted and a $2 \times 2 \times 2$ supercell of $Li_4P_2S_7$ was directly subjected to starting temperatures T of 2000 K or 2500 K for approximately 30 ps at a volume increased by 10%. During this step a complete dissociation of all structural units was observed.

Explicit quenching simulations with quenching rates k of 10, 50 and 100 K/ps were then performed until a temperature of 300 K was reached. The atomic positions and simulation cell were optimized in static simulations and six as-prepared amorphous structural models, labeled with the respective starting temperatures T and quenching rates k as g-quench$_k^T$ (e.g., g-quench$_{50\,\mathrm{K/ps}}^{2000\,\mathrm{K}}$), were obtained. The prefix "g-" is always used to indicate glass structures. The applied melting temperature and quenching rate are shown as subscript and superscript, respectively.

These as-prepared structural models contained various "unusual" structural units that will be discussed in more detail in Section 4.3.6. Furthermore, these structures were used as basis to prepare three idealized structures (labeled as g-$Li_4P_2S_7$-mod$_1$, g-$Li_4P_2S_7$-mod$_2$, g-$Li_4P_2S_7$-mod$_3$) by manually reconstructing the commonly observed structural units. These three idealized structures were later further lithiated to obtain another set of three structures with the compositions g-$Li_{70}P_{32}S_{112}$, g-$Li_{76}P_{32}S_{112}$ and g-$Li_{80}P_{32}S_{112}$.

3.4 Stability

In the context of material properties the term "stability" can relate to various concepts depending on the material, the considered time and length scales, or the conditions of interest. Examples are corrosive stability or mechanical stability (fatigue, wear, ...) and in many cases the exact meaning of stability needs to be deduced from the context. In this work, the term stability is exclusively used from a thermodynamic point of view and more detailed specifications are given in the following sections.

3.4.1 Thermodynamical Stability

To assess the thermodynamic stability we need to define thermodynamic potentials that depend on the outer constraints (the controlled state variables) and the materials phase space (positions and velocities of all atoms). The most prominent thermodynamic ensembles are summarized in Table 3.3 and a state that is truly thermodynamic stable (thermodynamic equilibrium) is reached if the relevant

thermodynamic potential of a system is at its extremum.[293] For example, in the microcanonical ensemble the energy of the system is a defined quantity and thermodynamic equilibrium is reached once the entropy S is maximized. For the remaining ensembles listed in Table 3.3 the thermodynamic potentials represent energy expressions that are globally minimized at thermodynamic equilibrium. Besides global minima, also local minima can occur and represent metastable states. This is especially relevant for amorphous phases as outlined in Section 3.4.6.

In the optimal case, the chosen ensemble reflects the real conditions of the material as close as possible. The microcanonical ensemble could therefore be used to model isolated systems, such as individual nanoparticles in vacuum.[294] It is rather unsuitable, however, to model SEs because they are able to exchange heat with the environment. The grand canonical ensemble can be used to analyze electrode materials whose Li content varies during cycling of the battery.[105,295]

For the simulation of bulk SEs, the presumably most appropriate ensemble is the isothermal-isobaric ensemble that is characterized by the Gibbs Free Energy G and conserves particles, temperature and pressure. Unfortunately, controlling the pressure via barostats within DFT calculations requires high computational efforts that cannot be afforded in the majority of cases. Therefore, the NVT ensemble is favored in the majority of AIMD simulations.[104,107,135,163,184,207,219,221,296] The thermodynamic stability in the NVT ensemble is determined by the Free Energy $F = E - TS$ and the total energy E_{tot} obtained from static DFT calculations can be considered as the Free Energy at 0 K.

3.4.2 Relative Stabilities

The absolute value of E_{tot}, F or G are usually of little interest. Instead, the evaluation of energy differences ΔE, ΔF or ΔG between different structures gives insights about the relative stability of compounds. If entropy and pressure contributions are small, the stability is mostly governed by E and the resulting E_{tot} from DFT calculations can be deployed to characterize the relative stability:[105]

$$\Delta E = E_{\text{tot}}^{\text{mod}} - E_{\text{tot}}^{\text{ref}} \approx \Delta F \approx \Delta G \ , \tag{3.20}$$

TABLE 3.3: Summary of selected statistical ensembles. The state variables involve the number of particles N, volume V, inner or total energy E, temperature T, pressure p and chemitcal potential μ.

Ensemble	State variables	Thermodynamic potential
microcanonical	N, V, E	S
canonical	N, V, T	$F = E - TS$
isothermal-isobaric	N, p, T	$G = F + pV$
grand canonical	μ, V, T	$\Omega = F + \mu N$

where $E_{\mathrm{tot}}^{\mathrm{ref}}$ and $E_{\mathrm{tot}}^{\mathrm{mod}}$ correspond to the total energy of a reference and a modified system, respectively. If the reference system is the most stable state, then ΔE will always be positive. The modified system, for example, could correspond to a different polymorph of the investigated material and we have used this concept to analyze the dependence between ΔE and the degree of Br^-/S^{2-} site-exchange of Li_6PS_5Br in Section 5.2 or to judge the relative stability of the orthorhombic and tetragonal phase of Li_7SiPS_8 in Section 6.1.

Relative stabilities can also be calculated to relate the stability of several phases. Considering the formation reaction of a generic SE from a set i of educts A,

$$\sum_i a_i A_i \longrightarrow \mathrm{SE}\,, \tag{3.21}$$

the corresponding formation energy $\Delta_f E$,

$$\Delta_f E = E_{\mathrm{tot}}(\mathrm{SE}) - \sum_i a_i E_{\mathrm{tot}}(A_i)\,, \tag{3.22}$$

is determined based on the individual E_{tot} of all involved compounds. Negative values of $\Delta_f E$ indicate that the reaction is favorable and proceeds spontaneously unless it is not kinetically hindered.

Equation 3.21 can also be considered in an inverted form and then rather represents a decomposition reaction. Hence, $\Delta_f E$ is also sometimes denoted as decomposition energy depending on the situation. Just as E_{tot}, relative energies are extensive quantities and is helpful to normalize them. To enable a proper comparison, all relative energies presented in this work are therefore normalized by the number of atoms.

3.4.3 Phase Diagrams

Instead of probing only a selected set of reactions, relative stabilities can be used in a more overarching way to analyze the stability of compounds. This involves the construction of phase diagrams, which was already achieved for several material systems in the context of battery materials.[104,162,297–299] As an example, the LiPS phase diagram according to Chu *et al.*[104] is shown in Figure 3.8. Compared to the ternary diagram previously shown in Figure 2.1 (comprising all *known* ternary and the two binary phases Li_2S and Li_3P), Figure 3.8 comprises all *stable* phases and therefore lacks $Li_2P_2S_6$, $Li_7P_3S_{11}$ and Li_7PS_6 because they were found to be unstable.

The construction of phase diagrams demands the calculations of the individual E_{tot} of all phases that can be realized with the set of involved atomic species. For the ternary LiPS system this implies all elemental polymorphs and all binary and ternary phases. Next, the elemental phases are used to calculate $\Delta_f E$ for every compound and a convex hull algorithm can be used to pinpoint only the thermodynamically stable phases, which are then plotted in the diagram.[300] In some cases, especially if the phase diagram involves dimensions larger than

three, binary or ternary phases are chosen as boundary phases to generated a comprehensible graphical representation.[297]

Computational Details

In Section 4.2 we investigated the stability of crystalline LiPS phases using a pseudo-binary phase diagram of Li_2S and P_2S_5. For Li_7SiPS_8 we looked into decomposition reactions involving Li_3PS_4 and Li_4SiS_4. When analyzing the stability of SEs against Li metal, the decomposition energy of selected reactions was investigated and the reaction products were chosen based on commonly observed reaction phases.[86,89,90] Therefore, Li_2S and Li_3P were used when treating LiPS compounds (see Section 4.5) and for Li_7SiPS_8 we additionally considered elemental Si (see Section 6.1.2). The calculated relative stability of ternary LiPS glasses is presented in Section 4.2.2 in diagrams that resemble phase diagrams, with the difference that it is used to characterize metastable phases.

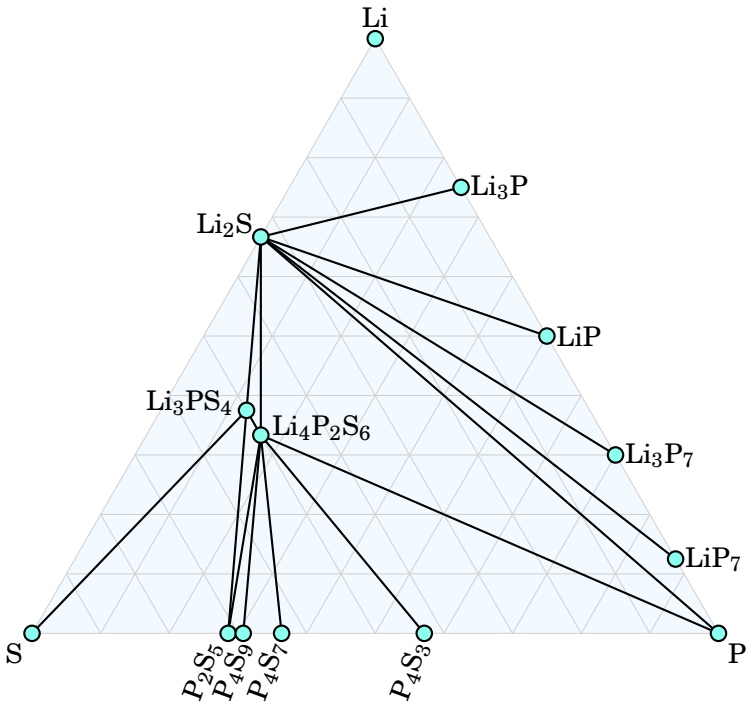

FIGURE 3.8: LiPS phase diagram according to the data of Chu *et al.*[104] when applying a correction for the S chemical potential.

3.4.4 Stability at finite Temperatures – Assessing Entropy Contributions

So far, we have only considered stabilities calculated based on E_{tot} obtained from static (0 K) DFT calculations because we neglected any other energy contributions. If relative stabilities are small, however, the approximation $\Delta E \approx \Delta F$ might not hold anymore for elevated temperatures and entropy contributions S need to be taken into account explicitly,

$$\Delta F = \Delta E - T\Delta S \ , \tag{3.23}$$

where, in analogy to ΔE, ΔS accounts for entropy differences between materials.

There are various sources for entropy, but in this work we have only analyzed two contributions. The first contribution is the configurational entropy S_{conf} and we included it in the stability analysis of Li_6PS_5Br in Section 5.2.2 to acknowledge the effect of the Br^-/S^{2-} site-exchange. S_{conf} can be determined with the well known Gibbs entropy formula,[301]

$$S_{\text{conf}} = -k_{\text{B}} \sum_i p_i \ln p_i \ , \tag{3.24}$$

which takes into account the probabilities p_i of finding a specific configurational microstate i. Here, p_i simply represent the probabilities of finding Br^- or S^{2-} ions on the $4a$ or $4d$ sites.

The second contribution to S is the vibrational entropy S_{vib}. It was also included in the analysis of Li_6PS_5Br, but also when investigating the temperature-dependent stability of LiPS glasses in Section 4.2.3. To determine S_{vib} phonon calculations within the harmonic approximation have been conducted as outlined in the following section.

3.4.5 Excursus 5: Phonon Calculations

Phonons are quasi-particles characterized by collective motions of particles without effective particle transport.[302] These modes of vibration affect the thermal transport and also interact with the electronic transport in metals. Computationally, they are commonly calculated within the harmonic approximation using density functional perturbation theory (DFPT), a frozen-phonon approach or finite displacements.[303] Here, we inly applied the latter method to determine the vibrational entropy S_{vib} for LiPS compounds and for Li_6PS_5Br at various degrees of Br^-/S^{2-} site-exchange.

The finite displacement approach needs very well converged structures with extremely low residual forces. Next, all atoms are individually displaced from their equilibrium position by a small displacement u in all spatial directions, which corresponds to a total number of $6N$ single-point DFT calculations. This

allows the computation of all forces as a function of the displacement and leads to the second-order force constant Φ,

$$\Phi_{ij}^{\alpha\beta} = \frac{\partial^2 E}{\partial u_i^\alpha \partial u_j^\beta} = -\frac{\partial F_j^\beta}{\partial u_i^\alpha} \,, \tag{3.25}$$

where the atoms i and j are displaced along directions α and β. F^β is the β component of the force vector $\mathbf{F}$. Calculating the mass-reduced Fourier transform of the Φ matrix results in the dynamical matrix. Based on its eigenvalues the phonon frequencies $\omega(q)$ can be determined. These depend on the wave vector q, but oftentimes only the gamma-point is considered. With the knowledge of all phonons and their frequencies the partition function Z of a system with total energy E_{tot} is defined as,

$$Z = \exp\left(-\frac{E_{\text{tot}}}{k_\text{B}T}\right) \prod_q \frac{\exp\left(-\frac{\hbar\omega(q)}{2k_\text{B}T}\right)}{1-\exp\left(-\frac{\hbar\omega(q)}{k_\text{B}T}\right)} \,. \tag{3.26}$$

Based on Z the Helmholtz Free energy $F = -k_\text{B}T\ln(Z)$ reads as

$$F = E_{\text{tot}} + \frac{1}{2}\hbar\omega(q) + k_\text{B}T \sum_q \ln\left[1-\exp\left(\frac{-\hbar\omega(q)}{k_\text{B}T}\right)\right] \,, \tag{3.27}$$

where the second term represents the temperature-independent zero-point energy E_{ZP}. Finally, S_{vib} can be calculated according to

$$S_{\text{vib}} = -\frac{\partial F}{\partial T} = -\frac{\partial(-k_\text{B}T\ln Z)}{\partial T} \,. \tag{3.28}$$

Computational Details

The structures of interest were optimized with increased convergence criteria. For the LiPS structures we initially aimed at minimizing forces below $1\cdot10^{-4}$ eV/Å. Unfortunately, such tight conditions could not always be achieved and especially the amorphous phases could not be further optimized in some cases. Still, all structures could be converged to forces below $1\cdot10^{-3}$ eV/Å. The only exception is the glass structure of $Li_4P_2S_6$ that exhibited residual force up to $1.33\cdot10^{-3}$ eV/Å. For all Li_6PS_5Br structures forces below $5\cdot10^{-4}$ eV/Å could be obtained.

The `Phonopy` code[304] was used to generate all needed structures with the individual atomic displacements for the LiPS compounds. Every particle was displaced by ±0.01 Å (default value used by `Phonopy`) in every cartesian direction. Therefore, six structures for every atom need to be calculated in the absence of symmetry reduction. We note that this is a computationally demanding task as it involves up to ≈ 1500 calculations for structures with ≈ 250 atoms. The structures were evaluated by performing single-point DFT calculations.

Because we used smaller system sizes for the Li_6PS_5Br (4 formula units per unit cell) we made use of the capabilities of VASP and used its finite difference approach via the input tag IBRION = 5. This approach computes all displacements subsequently in one single simulation, which reduces the computational demands but cannot be used for bigger systems due to the typical time constraints for simulations at high performance computing facilities. Here, we used displacements of 0.015 Å (default value used by VASP).

In both cases Phonopy was used for postprocessing, which returned E_{ZP}, the phonon density of states (pDOS) and S_{vib} as function of temperature. The pDOS, similar to the eDOS, illustrates the number of phonon states as function of phonon frequency, where imaginary, i.e., unstable, phonon modes are displayed as negative frequencies. Imaginary modes indicate a dynamical instability of the system and they either arise because the base structure could not be optimized accurately enough (i.e., a numerical issue) or because the system truly strives toward a more stable state (e.g., displacive phase transition). For the considered SEs the situation is even further complicated by the non-trivial distribution of Li^+ ions. It is therefore likely that subtle rearrangements of some Li^+ ions might lead to a slightly more favorable structures.

3.4.6 Kinetic Stabilization

Metastable states play an important role in the context of our LiPS glasses but also in the context of SEs with complicated Li^+ substructure or ion disorder.[104,156] Let us therefore address the topic of kinetic stabilization.

A well known example of a kinetically stabilized material is diamond,[305] which is found to be thermodynamically stable under high pressure and elevated temperature. The stable phase under standard conditions, however, is graphite. Nevertheless, diamond does not spontaneously transform into graphite once the extreme conditions are released. This is because the diamond phase is kinetically stabilized, meaning that its reaction path to rearrange into the graphite phase involves such high energy barriers that a reaction is unlikely to be observed within relevant time scales. In other words, the system is trapped in a metastable state for time scales that surpass typical observation times.

A similar behavior is observed for many amorphous systems.[306] Once an amorphous phase is solidified, a conversion to a more stable crystalline configuration would involve substantial atomic reordering on a local or even extended scale. This is schematically illustrated in Figure 3.9. The potential energy landscape shows the energy of system as function of phase space.[307] The deep and narrow global minimum represents the thermodynamically stable state. This could, for example, correspond to a certain crystalline phase. Deviations from this phase lead to different coordinates in phase space and less stable configurations. The system exhibits another low-lying minimum that could correspond to a metastable, e.g., glassy, phase. As indicated in the inset of Figure 3.9, a system far from the global minimum needs to overcome substantial changes in phase

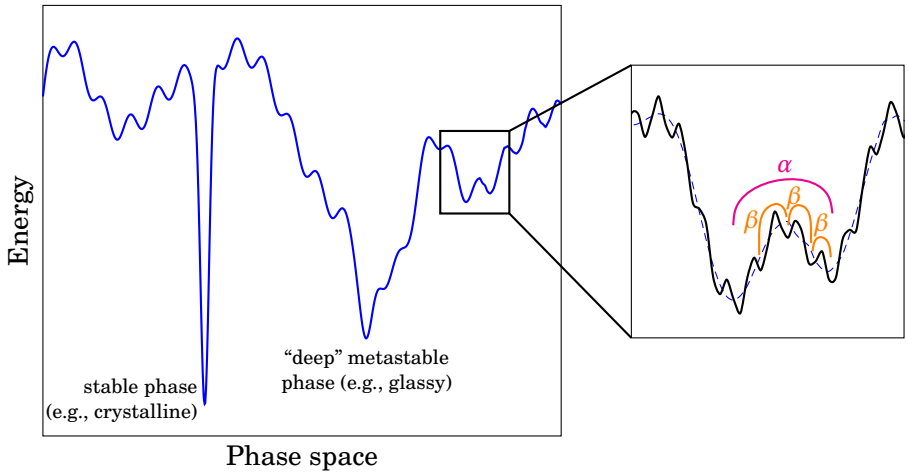

FIGURE 3.9: Illustration of the potential energy landscape (PEL) of a material that can be kinetically stabilized: A high barrier needs to be overcome during the transformation of a material from the "deep" metastable state to the stable phase in the global minimum of the PEL. Smaller local barriers, however, might be overcome (see inset).

space, accompanied with various small and large energy barriers, to reach the global minimum. Without driving forces or high temperature, it is unlikely that the system will ever reach the thermodynamic equilibrium within a reasonable amount of time.

The inset, however, shows that the system is able to evolve based on small local rearrangements (intrabasin jumps indicated with β). Eventually, also larger configurational adjustments are possible that drive the system from one mega-basin to a neighboring one (interbasin jumps indicated with α). The probability that such changes are observed depends on many aspects such as the relevant time scale, involved barrier heights, temperature or other internal and external conditions.

We will meet kinetically stabilized structures regularly throughout this work. This does not only involve the metastable LiPS glasses in Section 4.2.2. Additionally, Li_6PS_5Br structures with Br^-/S^{2-} site-exchange also turned out to be less stable than perfectly ordered structures (Section 5.2). Still, neither Br^-/S^{2-} reordering in Li_6PS_5Br nor crystallization of LiPS glasses could be observed during the time scales covered by our AIMD simulation.

3.4.7 Chemical Stability: Explicit Interface Simulations

It is clear that utilizing materials exhibiting the most favorable properties when considered individually does not suffice to realize a functional battery: More importantly, all components must be compatible with each other. Therefore, the

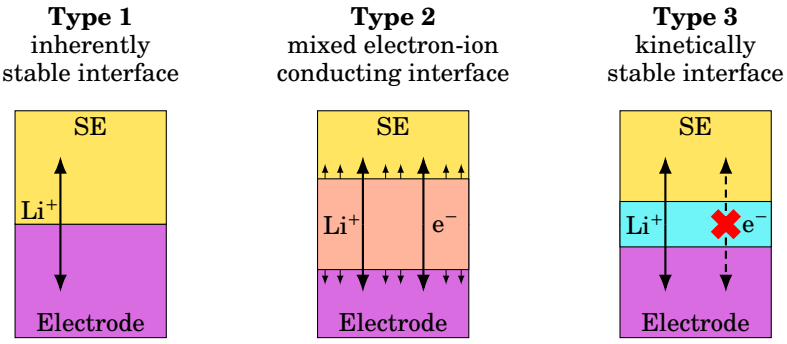

FIGURE 3.10: Illustration of the three different interface types.[1,81,311]

topic of chemical stability at interfaces of LIBs and ASSBs has become more and more important in current research projects.[6,102,108,109,308,309]

As explained in the previous sections, the thermodynamics of a system can give valuable insights into the expected stability of SEs. Still, an approach only relying on thermodynamics has two major disadvantages. First, it is difficult to assess kinetic effects: The formation of metastable phases at the interface could form passivating layers that prevent further reactions.[310] Second, all thermodynamic approaches depend on the prior knowledge of all relevant phases, which makes it difficult to screen unknown composition spaces. If some relevant phases are not considered in the analysis (e.g., because they are not known, yet), wrong results are obtained and incorrect conclusion might be drawn.

Because of these disadvantages it can be helpful to explicitly model an interface,[312] as has been demonstrated for various interfaces between SE and electrode materials.[174,196,313–318] To this end, the compounds of interest are mostly simulated in a sandwich-like fashion: A slab of one material is attached to a slab of a second material. The slabs are of finite thickness but infinite in the remaining directions due to the PBCs. Because PBCs usually also apply in the direction perpendicular to the interface, the simulation cell always contains two interfaces unless a vacuum layer is added.

As shortly mentioned in Section 1.4, interfaces between SEs and electrodes can be classified according to three different types.[1,81,311] These are illustrate in Figure 3.10. Type 1 interfaces are inherently stable and they enable the calculation of properly defined interface energies γ,

$$\gamma = \frac{E_{\text{tot}}^{\text{interface}} - E_{\text{tot}}^{\text{ideal}}}{A} \,, \tag{3.29}$$

where $E_{\text{tot}}^{\text{interface}}$ is the energy of the system containing the interface, $E_{\text{tot}}^{\text{ideal}}$ the reference energy of the ideal bulk system(s) without interfaces, and A the interface area. Type 2 interfaces are unstable because the formed interphases are able to grow due to their mixed electron-ion conduction character. Depending

on the compounds at hand this can lead to increased interface resistances (increasing cell impedance) or might ultimately induce a short-circuit if the SE is fully converted.[319] Type 3 interfaces are kinetically stable because the formed interphases can only be passed by Li^+ ions and effectively block electrons. Once the interphase has reached a sufficient thickness, any further growth is therefore prevented. Because interfaces of type 2 and 3 are reactive, γ is ill-defined and cannot be properly determined.

The main drawback of explicit calculations relates to the size limitations of DFT.[312,318,320] This has different consequences. First, high interfacial strains can arise if the lattice constants of the two slabs are distinctly different. For example, two different materials with a lattice constant of 9 and 10 Å would both needed to be elongated or compressed by approximately 5% to fit into a common simulation box with a width of 9.5 Å. Such values are typically used in explicit interface calculations.[176,313,321] Although the constraint simulations within DFT might allow for such conditions to be modeled, most SE materials would likely fail under these pathological conditions in reality. The second drawback is of similar nature: The slab geometries must comply with the PBCs. Therefore, only certain orientations can be realized within reasonably sized simulation cells.

Unfortunately, even if the materials are compatible and reasonable orientations can be realized, there are more issues to consider if the basic structure of one or both materials is complex. This is best expressed in terms of questions that need to be kept in mind when constructing initial interface models. Some of these questions are of general or technical concern, others are more specific to sulfide SEs: How thick should the individual slabs be to avoid spurious interaction between the interfaces while keeping the computational effort feasible? Should the composition of the individual materials be conserved or is it allowed to change at the interface? Which termination of the interface planes should be chosen? Is it possible to arbitrarily cut the material in order to obtain mostly planar configuration or are rough interfaces acceptable? Should cleaving of structural units be avoid or should units such as PS_4^{3-}, $P_2S_7^{4-}$ and $P_2S_6^{4-}$ remain intact? What distance between the planes should be chosen for the initial setup? Should other defects be introduced intentionally at the interface?

Note that similar questions also arise if grain boundaries are constructed (see Section 3.5.3). For both cases, support to answering these question can be obtained by consulting experimental methods such as transmission electron microscopy, if sample preparation and measurement conditions allow for it. If these are not available, either automated preparation schemes of interface models or scientific intuition are necessary for the generation of atomic interface models. By relying on the latter approach, and despite all the mentioned complications and issues, we were able to construct different interfaces and obtained interesting results for c-$Li_4P_2S_6$ | Li and c-$Li_4P_2S_6$ | g-$Li_4P_2S_7$ interfaces in Section 4.5 and tetra-Li_7SiPS_8 | Li interfaces in Section 6.4 that could not have been obtained via a purely thermodynamics-based approach.

Computational Details

For the different material combinations we manually produced a limited amount of carefully assembled interfaces without the cleaving of any structural units. We only considering low-index planes such as (100) and (001) and maintained the composition of the SE. For the interfaces with Li metal, the Li metal slab was subjected to the necessary strain to fit it to the SE in the initial interface model. For the c-$Li_4P_2S_6$ | g-$Li_4P_2S_7$ interface an additional glass was generated in a simulation cell exhibiting the same cell dimension as needed to comply with c-$Li_4P_2S_6$.

The slab distance was chosen such that the interatomic distances between the closest atoms of the opposing slabs was approximately 2 Å. Afterward, a static structural optimization of the initial models was performed. In selected cases, this was followed by AIMD simulations to study the evolution of the interface at finite temperature.

3.4.8 Electrochemical Stability

So far, we have only considered the thermodynamic stability in the sense of the chemical stability under normal conditions. Due to the potential differences occurring in a battery during operation, however, it is beneficial to extend this model to the electrochemical stability. In this regard, different approaches have been developed to analyze the electrochemical stability window of SEs and we will briefly review the basic concepts of commonly applied methods following the summary of Binninger *et al.*[109] According to that, the electrochemical stability window refers to the stability of an SE material against reactions that involve the transfer of neutral atoms (not ions) of the mobile species.[109] In our case this implies the transfer of Li, for example if the SE is in contact with Li metal or other electrode materials. Note that approaches to determine the electrochemical stability window can also be reduced to only inspect the chemical stability.

Phase Stability Window

The definition of the electrochemical stability window above can be used to formulate a generic chemical reaction that implies instability of the SE:

$$\mathrm{SE} + a\,\mathrm{Li} \quad \longrightarrow \quad \sum_i b_i B_i \ , \tag{3.30}$$

where a can take positive or negative values. The equilibrium potential ϕ_{eq} for such an electrochemical instability reaction can be expressed in terms of the reaction energies,

$$\phi_{\mathrm{eq}} = -\frac{\Delta G}{aq} \approx -\frac{1}{q}\left(\frac{\left[\sum_i b_i E_{\mathrm{tot}}(B_i)\right] - E_{\mathrm{tot}}(\mathrm{SE})}{a} - \mu_{\mathrm{Li}}\right) . \tag{3.31}$$

A reduction of the SE ($a > 0$) can only occur if the electrode potential $\phi < \phi_{\mathrm{eq}}$ and an oxidation ($a < 0$) only if $\phi > \phi_{\mathrm{eq}}$. To obtain the electrochemical

stability window, ϕ_{eq} of all possible reactions according to Equation 3.30 need to be calculated. It is therefore helpful to calculate the phase diagram of the system of interest beforehand. Finally, the electrochemical stability window is obtained by the limiting maximal ϕ_{eq} of the reduction reactions and the minimal ϕ_{eq} of the oxidation reactions. Because instabilities are probed against all competing phases, the determined electrochemical stability window is termed phase stability window.[109]

Equation 3.31 shows that ϕ_{eq} depends on the choice of the chemical potential of Li, μ_{Li}. This offers the possibility to investigate how the stability window in influenced by the conditions of the Li reservoir. In the simple case, $\mu_{Li} = E_{tot}(Li)$, the analysis is equivalent to the study of the chemical stability. Depending on the situation of interest, however, other terms can be included to mimic certain electrochemical situations, such as the application of potentials, specific charge states of the electrodes, or phase equilibria under Li-rich or Li-poor conditions.[81,322]

Because the phase stability methods relies exclusively on thermodynamics, it suffers from the same limitations as described above: Unknown phases cannot be considered and kinetic aspects are disregarded. Hence, the phase stability methods typically results in narrower electrochemical phase stability windows than predicted by the approaches described in the following or found experimentally.[109,323]

HOMO-LUMO Window

The stability window of a SE is, to a first approximation, determined by its HOMO-LUMU gap, or band gap, E_g.[308] If the electronic states of materials that are brought into contact are properly aligned, it enables an assessment of the interface stability, rationalized by the ability to transfer electrons between the materials. This is illustrated in Figure 3.11.

In Figure 3.11 (a) the ideal open circuit voltage V_{OC} is determined by the redox potentials μ_A and μ_C of anode and cathode, respectively. The redox potentials are identical to the Fermi levels of the compounds.[324] In this configuration no interface reaction is expected because the Fermi levels are within the stability window of the SE. More specifically, the Fermi level of the anode is below the LUMO of the SE and therefore the anode cannot transfer electrons to the SE. On the cathode side the Fermi level of the cathode is above the HOMO of the SE, and therefore the cathode cannot extract electrons from the SE.

The situation is different in Figure 3.11 (b). Compared to the previous case the anode has been shifted to higher and the cathode to lower energies, which could happen during charging of the battery or if a different set of materials is utilized. This leads to an increase of V_{OC} which, on the one hand, is favorable for the battery energy density. On the other hand, the stability window of the SE is exceeded and unstable interfaces are expected because the relative positions of the electronic levels will lead to electron transfer reactions. As a result, the SE

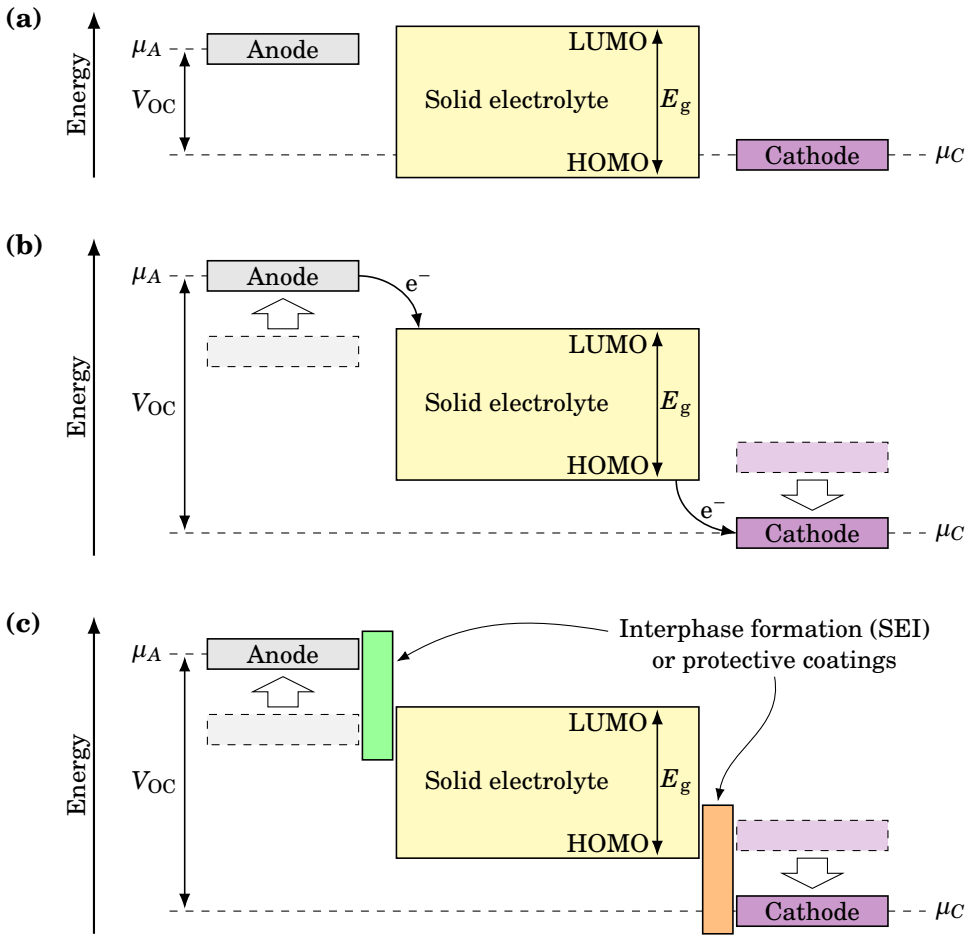

FIGURE 3.11: Schematic open-circuit diagrams of an SE in contact with an anode and a cathode.[108,308] V_{OC} is the open circuit voltage and μ_A and μ_C the redox potentials of anode and cathode, respectively. Part (a) shows a stable configuration because the Fermi level of the anode is below the LUMO of the SE and the Fermi level of the cathode is above the HOMO of the SE. In (b) the position of the anode and cathode have been shifted to allow for electron transfer reactions, i.e., an unstable interface. (c) If beneficial interphases form, which is not granted, or suitable coatings are utilized, a protection of the SE can be achieved.

is reduced at the anode and oxidized at the cathode. Note that an instability is not necessarily encountered at both interfaces simultaneously.

The reduction and oxidation will lead to the formation of interphases, often also denoted as SEI, at the interfaces between the electrodes and the SE as shown in Figure 3.11 (c). Whether and how the reactions between electrodes and SE proceed depends on the properties of the formed interphases.[1] Beneficial

properties are high Li^+ conductivity and low electronic conductivity to stop further reduction and oxidation of the SE. Applying a protective layer on either the electrodes or the SE can be an effective way to prevent reactions.

The HOMO-LUMO method is only an approximate approach. One reason is the limited capability of DFT to represent the exact electronic structure as outlined in Section 3.2.1 and Section 3.2.2. Another reason is the formation of dipoles at the interfaces that shift the relative positions of the electronic states near the interface. One source of dipoles are space charge layers (SCLs), but it is still under debate whether they have a negligible[325] or significant[326] influence in ASSBs.[327] Furthermore, the electrodes are assumed to be chemically inert, which is not always a realistic assumption.[109] The stability window obtained based on the HOMO-LUMO method can therefore be seen as an upper limit for the electrochemical stability window.[298,328]

Stoichiometry Stability Window

This method has been comprehensively summarized by Binninger *et al.*[109] and the interested reader is referred to their publication for further details. In essence, the stability window is determined by analyzing how the energy of a SE behaves if it is subjected to small changes in stoichiometry of the mobile species. Translated into a chemical reaction,

$$\mathrm{Li}_n\mathrm{R} \pm a\,\mathrm{Li} \longrightarrow \mathrm{Li}_{n\pm a}\mathrm{R}\,, \tag{3.32}$$

$\mathrm{Li}_n\mathrm{R}$ corresponds to the formula unit of a SE with an arbitrary matrix R and $a \ll n$. In practice, sufficiently large supercells (leading to large n) of the SE need to be prepared and one neutral Li atom ($a = 1$) is added or removed. The potential limits for reduction and oxidation, ϕ_{red} and ϕ_{ox}, are then obtained,

$$\phi_{\mathrm{red}} = -\frac{1}{q}[\,E_{\mathrm{tot}}(\mathrm{Li}_{n+1}\mathrm{R}) - E_{\mathrm{tot}}(\mathrm{Li}_n\mathrm{R}) - \mu_{\mathrm{Li}}\,]\quad, \tag{3.33}$$

$$\phi_{\mathrm{ox}} = -\frac{1}{q}[\,E_{\mathrm{tot}}(\mathrm{Li}_n\mathrm{R}) - E_{\mathrm{tot}}(\mathrm{Li}_{n-1}\mathrm{R}) - \mu_{\mathrm{Li}}\,]\quad, \tag{3.34}$$

where the corresponding E_{tot} of the various systems need to be calculated. E can be used as an approximation to the Gibbs Free Energy G if errors of about ± 0.1 V are acceptable.[109] Equation 3.33 and Equation 3.34 can again be used analyze the dependence between the stability window and the electrochemical potential of Li. Consequently, the approximation $\mu_{\mathrm{Li}} = E_{\mathrm{tot}}(\mathrm{Li})$ serves to probe the chemical stability in the same manner as used when analyzing the phase stability window.

The shortcoming of the stoichiometry stability method is the assumption that all relevant processes are determined by Li or Li^+ as the mobile species. Other species or reaction processes that might influence the interface stability are neglected. Overall, the method resembles our approach to assess the interface

stability of two contacted materials as described in Section 3.5.2. Because this method involves defect formation energies, let us briefly introduce review defects first.

3.5 Defects

Materials science is centered around defects in materials and it is the aim of a materials scientist to understand how defects influence a material's properties. Based on this knowledge materials with targeted properties can be developed by choosing specific synthesis conditions and/or by applying tailored treatments to omit, cure or intentionally introduce the desired types of defects. These defects can vary in size and range from atomic point defects to line (dislocations) and planar defects (stacking faults, grain boundaries) up to macroscopic defects (inclusions, pores). In this work, we have only addressed point and planar defects and will elaborate on these in the following. The interested reader is referred to textbooks for a more thorough introduction into the topic of defects.[329]

3.5.1 Point Defects

These kind of defects appear at the atomic level and can be identified easily as lattice defects in crystalline materials. They comprise vacancies, interstitials, Frenkel pairs (a combination of vacancy and interstitial), Schottky pairs (combination of anion and cation vacancies), substitutionals (e.g., achieved by doping), antisites (one atom/ion occupying the "wrong" site), and defect complexes thereof. For amorphous materials the classification of point defects is less straightforward from a crystallographic point of view due to the absence of defined lattice sites. Still, vacancies have been reported in glassy sulfide SEs samples.[330] Moreover, the identification of defective atomic arrangements is possible if the material possess a distinct short-range order. For example, we were able to identify defective structural units in our generated LiPS glasses as presented in Section 4.3.6.

Point defects interact with the host material on different levels.[331] First, they typically represent a size mismatch compared the defect-free material. As a result, strain fields evolve that mechanically interact with the surrounding. Examples are vacancies in metals or isovalent substitutionals in ionic or covalent compounds.[332,333] The interaction between the defect and any external or internal stress/strain can be described via the elastic dipole tensor of the defect. This quantity is accessible via DFT calculations but was not pursued here and the reader is referred to other sources for a more in-depth discussion.[334–336]

If the point defect is also charged, which is often the case for ionic materials, the interaction includes an electrostatic contribution. A charged defect, however, inevitably requires a charge compensation mechanism to keep the system neutral.[337] For example, Li^+ vacancies are generated in the cathode during charging of the battery. Every such Li^+ vacancy can be considered negatively charged

because the positive charge of the original Li^+ is missing. This is expressed in the Kröger-Vink notation as V'_{Li}. The negative charge is compensated by a change of the oxidation states of the transition metal ions, e.g., in $LiCoO_2$ upon delithiation: $Co^{3+} \rightarrow Co^{4+}$.

The considered sulfide materials in this work, or SEs in general, do not offer such electronic compensation mechanism in the majority of cases because they are pure ionic conductors that ideally should not take part in any electrochemical reactions. Hence, every ionic defect needs to be compensated via other ionic defects. For electronic conductors and especially semiconductors, however, the adopted charge states of defects critically depend on the Fermi level energy E_{Fermi}, which corresponds to the chemical potential of the electrons. The Fermi level itself depends on the types and amounts of defects that are present in the material.[338]

E_{Fermi} is an important property that needs to be included in the analysis of the defect thermodynamics in SEs. This becomes apparent if we consider intrinsic point defects that may form spontaneously due to entropic reasons. Their concentration c can be determined based on the defect formation energy E_{f},

$$c = \frac{N_{\mathrm{def}}}{N_{\mathrm{sites}}} = A \exp\left(-\frac{E_{\mathrm{f}}}{k_{\mathrm{B}}T}\right), \tag{3.35}$$

where N^{def} is the number of defects, N^{sites} the number of lattice sites and A is a pre-exponential factor that accounts for entropy effects. Oftentimes, A is considered to be equal to unity and can be neglected.[339] By employing DFT calculations, E_{f} of a generic defect X with charge state q can be calculated according to

$$E_{\mathrm{f}}(X^q) = E^{\mathrm{def}}_{\mathrm{tot}}(X^q) - E^{\mathrm{ideal}}_{\mathrm{tot}} - \sum_i n_i \mu_i + q(E_{\mathrm{VBM}} + E_{\mathrm{Fermi}}) + E^{\mathrm{Correction}}, \tag{3.36}$$

where $E^{\mathrm{def}}_{\mathrm{tot}}$ and $E^{\mathrm{ideal}}_{\mathrm{tot}}$ refer to the total energy of the defective and the defect-free system, respectively, n_i is the number of added ($n_i > 0$) or removed ($n_i < 0$) atomic species i, and μ_i their respective chemical potential.[340] The approach is illustrated in Figure 3.12 (a). If the system is charged ($q \neq 0$), E_{Fermi} enters the energy term and its position is typically considered with respect to the energy of the valence band maximum E_{VBM}. Correction terms $E^{\mathrm{Correction}}$ might be needed to account for charged systems or finite size effects.[270]

The concentration of intrinsic defects is usually low under normal conditions and can be considered to represent the dilute limit. This means that defects are well separated, if attractive interactions between them can be neglected. Hence, defects are typically considered in separate simulations, but their individual results can be combined for any further analysis. This is indicated by means of an energy level diagram in Figure 3.12 (b) showing how the formation energy of V'_{Li} and $Li^{\bullet}_i$ can be combined for the Frenkel pair formation energy E_{FP}.

Due to the dependence on E_{Fermi}, defect formation energies E_{f} are usually shown in so-called defect formation energy diagrams. A schematic version is

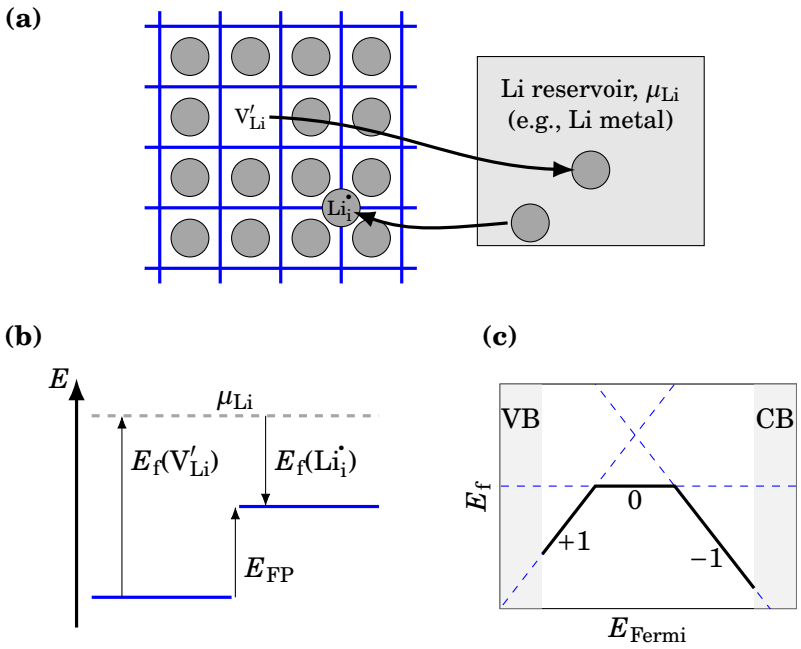

FIGURE 3.12: Illustration of how defect formation energies can be used as descriptors to assess the interface instability. In the case of interstitials, the defect formation energy is a measure of how costly/beneficial it is to transfer a species from its chemical reservoir into the material of interest.

shown in Figure 3.12 (c). For the given example, the defect needs to be simulated with different charge states q (here: -1, 0, and $+1$) and the corresponding E_f needs to be calculated according to Equation 3.36. To avoid diverging energies for non-neutral cells, periodic DFT calculations can make use of a compensating background charge.[341] Instead of plotting the full curves for every charge state, only the most stable charge states at a given Fermi energy are commonly shown, here with a solid line. The kinks in the solid curve mark the charge transition levels. By using a self-consistence scheme, the formation energies of all considered defects can be used to calculate the expected Fermi level position.[342]

The last point is only valid, if the system is exclusively governed by intrinsic defects and if the kinetics are fast enough to reach this equilibrium. This is not always the case and extrinsic defects offer another opportunity to influence the properties of a material. These defects do not form spontaneously and need to be introduced into the system by means of doping or particular treatments. They are especially important for semiconductors in the form of dopants and are used to tailor the electronic properties of the material.[333] However, they also play a crucial role for SEs, where the composition and the synthesis protocol can be used to adjust the Li content and to influence the ionic conductivity. For

example, the Li content in $Li_{6-x}PS_{5-x}[Cl,Br]_{1+x}$ argyrodites is coupled to the amount of halide ions.[212,214,343] Moreover, the halide content also influences the halide/S^{2-} occupation ratio on 4*d* and 4*a* sites.

Another interesting example of extrinsic defects is the one explained in Section 2.2.1 for Li_6PS_5Br: Our experimental partners could show that Br^-/S^{2-} site-exchange intrinsically evolves at high temperatures.[9,10] After quenching, however, the site-exchange does not correspond to the equilibrium anymore. In other words, a defect concentration which is intrinsic at high temperatures can become an extrinsic feature at low temperatures if quenching the material does not allow for an equilibration of the system due to limited kinetics. We will see in Chapter 5 that this has a profound influence on the properties of Li_6PS_5Br.

Computational Details

We have limited our analysis to Li- and S-related defects for LiPS materials. Li metal was chosen as Li reservoir, where μ_{Li} corresponds to the total energy per Li atom in the metal (E_{bulk}/N) and was determined to be −1.90 eV. To verify μ_{Li}, the closely related cohesive energy E_{coh},[344]

$$E_{coh} = -(E_{bulk}/N - E_{atom}) = -(\mu_{Li} - E_{atom}) \,, \tag{3.37}$$

where E_{atom} is the energy of an isolated atom in a sufficiently large simulation cell. Our calculated E_{coh}(Li) =1.602 eV is in good agreement with the experimental value of 1.63 eV.[345]

S defects have only been considered in c-$Li_4P_2S_6$ and the S reservoir is chosen to be elemental S because the synthesis approach of $Li_4P_2S_6$ involves temperature-driven sulfur loss from $Li_4P_2S_7$. Elemental S, however, is a molecular crystal comprised of S_8 rings and the same problems as described in Section 4.2.1 for the accurate description of P_2S_5 are encountered. To still calculate a reference energy for the chemical potential μ_S of elemental S, we relied on the following chemical reaction,

$$2\,Li + \frac{1}{8}\,S_8 \xrightarrow{\Delta H} Li_2S \,, \tag{3.38}$$

where the experimental reaction enthalpy of $\Delta H = -445.9$ kJ/mol[346] was used to solve for μ_S according to,

$$\mu_S = E(Li_2S) - 2\mu_{Li} - \Delta H \,, \tag{3.39}$$

and amounting to −3.55 eV. Again, the resulting cohesive energy of 2.64 eV compares well to the experimental value of 2.85 eV.[345]

Charged cells were compensated using a homogeneous background charge. No correction terms $E^{Correction}$ for the calculation of E_f were considered.

3.5.2 Defect Formation Energies as Descriptors for the Interface Stability

In Section 3.4 we introduced several methods to analyze the interface stability and the method presented in this section can be seen as a complementary approach. It relies on discussions by Hausbrand *et al.*[309] about the connection between defect formation energies and energy level diagrams of the electronic/ionic states in the context of $LiCoO_2$ | LiPON interfaces. The main idea is that calculated defect formation energies of point defects can be used as descriptors to assess the interface stability. As a first measure, comparable to the stoichiometric stability window method (Section 3.4.8), we can assume that the most mobile species will initiate and drive interface reactions. Therefore, only mobile defects are of interest and in this work we will restrict the analysis to Li defects.

The approach is comprehensively illustrated in Figure 3.13. The conceptual idea is to calculated the energy needed for transferring a species from one material to the other. Here, the chosen example shows the transfer of one Li *atom* from material A (creation of a Li vacancy, $V_{Li}^{\times}$) to material B (creation of a Li interstitial, $Li_i^{\times}$). In other words, a Li Frenkel pair "across material boundaries" is created. The associated formation energy, E_{FP}^{across}, is the sum of the individual defect formation energies $E_f(V_{Li}^{\times})$ and $E_f(Li_i^{\times})$ in the different materials, and can be understood as a direct measure of the driving force for the Li transfer.

If $E_{FP}^{across} < 0$, as indicated in Figure 3.13 (b), the transfer of a Li from one material to the other is favorable and suggests an unstable interface. If the Li transfer is not favorable ($E_{FP}^{across} > 0$), as indicated in Figure 3.13 (c), the interface can be considered to be stable. The choice of the reservoir only matters if the stability of a material is directly probed against the reservoir itself. Otherwise, the reservoir only acts as a mediator, i.e., the chemical potentials cancels in the sum,

$$E_{FP}^{across} = E_f^A(V_{Li}^{\times}) + E_f^B(Li_i^{\times}) \tag{3.40}$$

$$= [E_{tot}^A(V_{Li}^{\times}) - E_{tot}^A(\text{bulk}) + \mu_{Li}] + [E_{tot}^B(Li_i^{\times}) - E_{tot}^B(\text{bulk}) - \mu_{Li}] \tag{3.41}$$

$$= [E_{tot}^A(V_{Li}^{\times}) - E_{tot}^A(\text{bulk})] + [E_{tot}^B(Li_i^{\times}) - E_{tot}^B(\text{bulk})] \,. \tag{3.42}$$

Here, we assume neutral defects ($q = 0$) and that individual correction terms can be neglected. This approach allows to calculate every material and defect species in separate simulations.

A close inspection reveals the similarity of the stoichiometry stability method and the approach by Hausbrand *et al.*: If the factor of $-1/q$ in the computation of ϕ (Equation 3.33 and Equation 3.34) is omitted, in the stoichiometry stability method equals the calculation of defect formation energies of neutral Li vacancies or interstitials. The approach of using defect formation energies as descriptors, however, is not limited to neutral defects and can in principle be extended to charged defects. To this end, we recall that the two materials in contact install a constant Fermi level.[347] The positions of the VMB, on

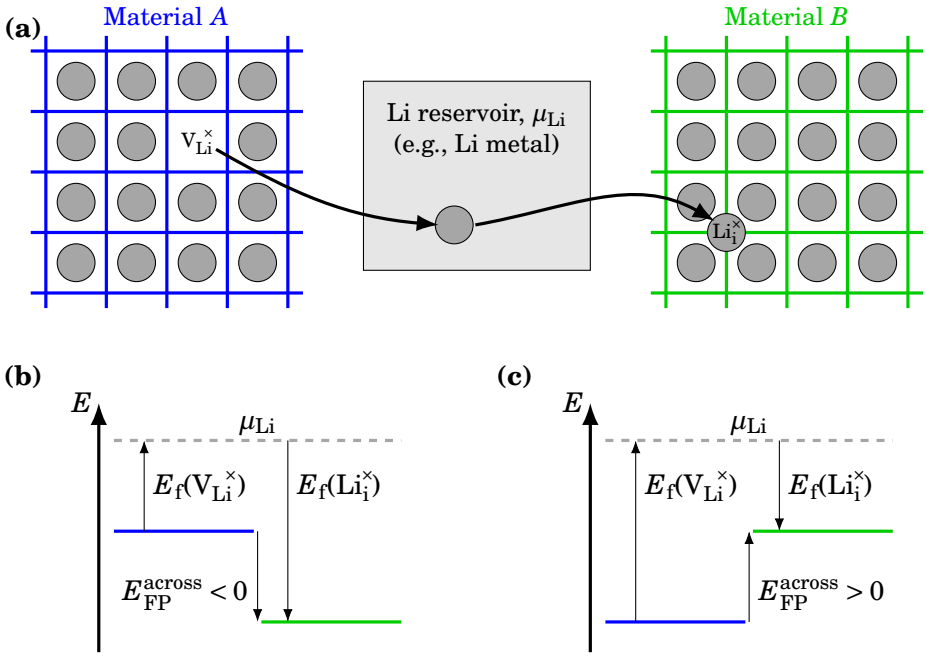

FIGURE 3.13: (a) Illustration of how defects and their formation energies can be used to assess the interface stability of two materials. The creation of a Li vacancy ($V_{Li}^{\times}$) in one material and a Li interstitial ($Li_i^{\times}$) in the other material can be understood as a Frenkel pair formation "across material boundaries". The summed defect formation energies yield the corresponding formation energy E_{FP}^{across}. The reservoir only acts as mediator for the defect formation energies and can be chosen arbitrarily. (b) Energy level diagrams of an unstable interface with $E_{FP}^{across} < 0$. (c) If $E_{FP}^{across} > 0$, there is no driving forces for Li transfer from one compound to the other and the system should exhibit a stable interface.

the other hand, are likely to differ, leading to a relative shift of the VMBs by E_{VBM}^{offset}. Setting the position of the VMB of material A as reference value, the term $q(E_{VBM} + E_{Fermi})$ in Equation 3.36 needs to be modified for material B to $q\left(E_{VBM} + E_{Fermi} + E_{VBM}^{offset}\right)$. Combining a charged Li vacancy and a charged Li interstitial, the calculation of the respective E_{FP}^{across} then simply reads as

$$E_{FP}^{across} = E(V_{Li}^{\times}) + E(Li_i^{\times}) \pm E_{VBM}^{offset} , \tag{3.43}$$

where the sign in front of E_{VBM}^{offset} depends on whether Li^+ is transfered from material A to B or vice versa. If E_{FP}^{across} for charged defects is negative, Li^+ is expected to be transfered from one material to the other. Obviously, this will lead to a redistribution of charges and a electrostatic potential will be generated that opposes further Li^+ transfer. Under these conditions, and if the transfered Li^+ does not initiate any further chemical reaction, space charge layers will form at the interface.

The actual challenge is the determination of $E_{\mathrm{VBM}}^{\mathrm{offset}}$, which can be done in different ways. First, it is possible to align the band edges based on a common electronic reference state. This requires the materials to have a common element with low-lying core states that are not affected by the chemical surrounding. Second, interface calculations can be applied to align the materials.[348] Third, individual slab calculations with vacuum regions can be used to align the materials based on the vacuum level of the local potential (see Equation 3.3).[348] The latter approach is only applicable if net dipoles can be avoided in the simulation. In Section 4.5.2, however, we will briefly show that using charged defects as descriptors for the interface stability is not straightforward if the SEs have complex structures.

3.5.3 Grain Boundaries

GBs are internal interfaces that separate regions of the material with different crystal orientations.[349] The properties of the GB, and how they eventually influence the properties of the material, depend on many aspects such as the the compound, the GBs density, their orientations, their interface terminations, segregation of impurities or defects, and the formation of space charge regions. For example, GBs were found to enable Li dendrite growth in oxide SEs.[350] Furthermore, they influence the ionic transport. In the majority of cases, a deterioration of the transport properties is typically attributed to the presence of GBs in oxide SE,[351] but there are also cases where GBs lead to an increased ionic conductivity in oxide materials.[352] For sulfides SEs, the materials of interest of this thesis, the picture is rather ambiguous and the role of GBs is less clear.[227,228] That is why we have analyzed the effect of GBs on the transport properties in Li_6PS_5Br in Section 5.6.

The degrees of freedom when generating these models, coupled with the size limitations of DFT calculations, result in similar issues as explained in Section 3.4.7 for the explicit treatment of interfaces between two different materials. These are the reasons why usually only experimentally known GBs or rather simple interface models are addressed.[353,354] The latter are commonly generated by relying on the coincident site lattice (CSL) approach, which has also been used in this study.

As the name implies, CSL structures aim to arrange the two GB slabs with respect to each other in such a way that certain lattice sites overlap periodically at the interface plane.[355,356] An example is illustrated in Figure 3.14 for two simple cubic lattices. This configuration is called a $\Sigma 5$ GB because the area A of the lattice that is spanned by the coincident sites is five times larger than the original lattice. GBs can be prepared as pure twist or pure tilt boundaries. For twist boundaries, the crystals are rotated around the axis that is perpendicular to the interface. If the rotation axis is lying within the interface, tilt boundaries will form. This is sketched in Figure 3.15. More complex tilt boundaries are obtained if a second rotation axis perpendicular to the first but still within

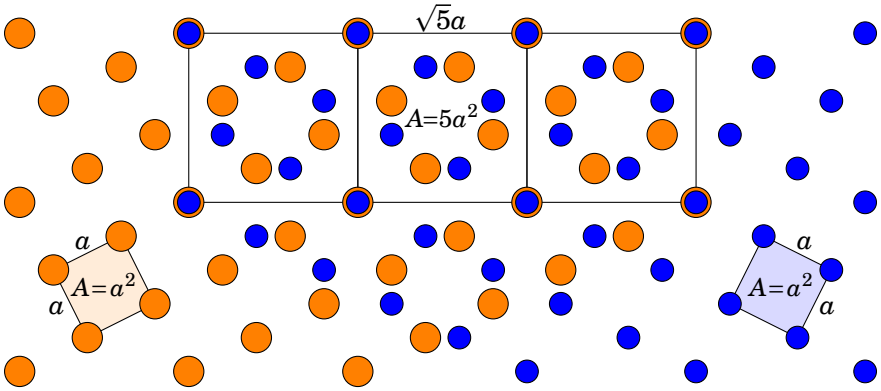

FIGURE 3.14: Illustration of the coincidence site lattice (CSL) of a Σ5 GB for a simple cubic structure.

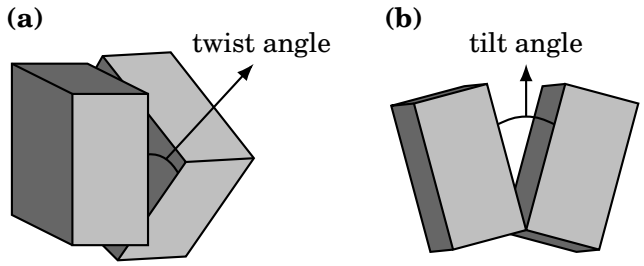

FIGURE 3.15: Two types of grain boundaries: (a) Pure twist boundary and (b) pure tilt boundary. This graphic is adapted from a similar representation of Gokhale *et al.*[357]

the interface plane is added. Naturally, twist and tilt components can also be combined to obtain arbitrarily mixed GBs.

In this work we only took into account pure Σ5 twist and tilt boundaries for Li_6PS_5Br. For the twist boundaries the (100) plane was used as interface plane. Choosing the termination was straightforward in this case because we wanted to avoid the cleavage of PS_4^{3-} units. Therefore, a plane between the structural units was used to terminate the slabs. For the twist boundary the generation was more involved, because cutting of PS_4^{3-} units cannot be avoided for the chosen (102) interface plane. Hence, we decided to construct four interfaces with different terminations. In one case, we merged the cleaved PS_4^{3-} units at the interface to one PS_4^{3-} unit and in another case a $P_2S_7^{4-}$ units was constructed based on the cleaved units. In addition, interfaces with Li_2S excess were generated.

3.6 Ionic Transport Properties

Superionic conductors excel with outstanding ionic transport properties, which are key to deliver a suitable performance in ASSBs. A desirable value for the ionic conductivity σ_{Li} of Li^+ conducting SEs is approximately 1 mS/cm or higher.

The Nernst-Einstein equation is commonly used to access σ_{Li} by feeding the results of atomistic simulations,[105]

$$\sigma(T) = D_\sigma(T)\frac{c\,(Zq)^2}{k_{\mathrm{B}}T}\ , \tag{3.44}$$

where D_σ is the diffusion coefficient of the mobile charge carrier and the parameters c, Z and q are its concentration, its nominal charge, and the elementary charge, respectively. The properties that need to be determined are D_σ and c, and depending on the transport properties of the material at hand, atomistic simulations offer two different approaches to determine them.

3.6.1 Static approach

The first approach employs solely static calculations and we applied it previously to investigate the poor transport properties of $Li_4P_2S_6$.[120] This method is most suitable to treat ionic transport that relies on a simple diffusion mechanism with the characteristic that every local jump can be considered as an independent event. Examples are the motion of point defects such as vacancies or interstitials, whose concentration c is either expected to be the intrinsic defect concentration or fixed by extrinsic means (e.g., doping) as explained in Section 3.5.1. Therefore, D_σ is the only remaining property that needs to be determined and is typically assumed to follow a general Arrhenius dependence,

$$D_\sigma(T) = D_0(T)\exp\left(-\frac{\Delta G_{\mathrm{m}}(T)}{k_{\mathrm{B}}T}\right) \approx D_0\exp\left(-\frac{E_{\mathrm{m}}}{k_{\mathrm{B}}T}\right)\ , \tag{3.45}$$

where the pre-exponential coefficient D_0 is often supposed to be temperature-independent and the Gibbs free energy of activation ΔG_{m} can be approximated by the migration barrier E_{m}. Other commonly used terms for E_{m} are migration energy, activation energy, or activation barrier. High conductivities are obtained if a material exhibits high D_0 and low E_{m} and recent activities, building on initial works by Meyer and Neldel,[358] elaborated on the connection between the transport parameters.[359,360] Experimentally, the transport parameters can be obtained by performing electrochemical impedance spectroscopy measurements at different temperatures and fitting the data to the Arrhenius equation.[361]

Atomistically, E_{m} can be assessed via static NEB calculations as outlined in Section 3.6.2. For the determination of D_0, the diffusion species and mechanism needs to be known. The movement of a vacancy in an isotropic material within the dilute limit, for example, can be assumed to follow a random-walk. The resulting diffusion coefficient of the vacancy D_{V},

$$D_{\mathrm{V}} = D_0\exp\left(-\frac{E_{\mathrm{m}}}{k_{\mathrm{B}}T}\right) = \frac{1}{2d}a_{\mathrm{jump}}^2 v_0\exp\left(-\frac{E_{\mathrm{m}}}{k_{\mathrm{B}}T}\right)\ , \tag{3.46}$$

can be used to determine the tracer diffusion coefficient D^* of the ions/atoms as an approximation to D_σ,

$$D_\sigma \approx D^* = f\,D_{\mathrm{V}}\,c_{\mathrm{V}}\ , \tag{3.47}$$

where f is the correlation factor and c_V the vacancy concentration. The parameter $d = 1,2,3$ accounts for the dimensionality of the diffusion process, a_{jump} is the jump length and v_0 the attempt frequency. The inclusion of the dimensionality d indicates that diffusion coefficients are not necessarily scalars, but actually tensorial parameters for anisotropic materials. If the bulk diffusion is highly anisotropic, it is advisable to analyze the spatial contributions to the diffusion coefficient. For such cases, care needs to be taken that only the projected jump length of a_{jump} along the considered direction is employed.

The attempt frequency v_0 can be calculated by different means,[362] but is often found to be of comparable order as phonon frequencies. In many cases, values of 1-10 THz are used as an estimate.[363] The temperature dependence of v_0 and a_{jump} (e.g., due to thermal expansion) is usually neglected.

The factor f accounts for the correlation of the diffusion mechanism and is connected to the geometry of the jump. In many situations it is approximated as unity but for certain cases it is important to acknowledge the correlation of jumps: Assuming a vacancy-mediated diffusion mechanism, we find that the vacancy itself performs a random-walk. The ions, however, only have the possibility to jump if a vacancy is next to them. After a jump has occurred the vacancy is again adjacent to the same atom and the probability for a subsequent back jump is high (so-called memory effect) and depends on the number of neighbors, i.e., the local geometry of the system.[364,365]

The last ingredient for Equation 3.45 is the migration barrier E_m, that can be calculated based on NEB calculations as outlined in the following section. Once E_m is available, D_σ can be calculated and can be used to predict the ionic conductivity of SEs. Obviously, this only holds true if the considered diffusion mechanism is the only source for diffusion. The majority of SE, however, have more involved structures such that the diffusion is governed by multiple paths with different barriers and jump lengths. The determination of effective diffusion properties from a multitude of paths is a non-trivial task and is only feasible for relatively simply models, such as interstitial diffusion with a two-barrier model.[366]

3.6.2 Excursus 6: Nudged Elastic Band Calculations

The concept of the NEB approach is illustrated in Figure 3.16 for a symmetrical migration path.[367] Typically, the initial and end configuration of an ionic jump are statically optimized beforehand. These local minima are then used as fixed "anchor" images. Next, atomic configurations are prepared that interpolate the positions of the jumping atom between the two anchor points. These intermediate images are virtually connected to the neighboring images. This is done via virtual springs that are applied to every atom and its own image atoms in the neighboring images. All intermediate images are then statically optimized simultaneously while taking into account (i) the real forces acting on the atom of a given image and (ii) the forces resulting from the virtual springs.

Without the virtual springs, the intermediate images would simply relax back into one of the anchor images. By applying the virtual springs, however, the migrating species is constrained to the migration path. Note that there are more technical details concerning how exactly the (projected) spring forces are applied to the atoms to obtain an improved description of the minimum energy pathway.[368] The energies of the intermediate images are then used to characterize the jump. More precisely, the migration barrier E_m can then be calculated as the energy difference between the saddle point of the migration path and the initial position. If the left and right anchor images are dissimilar in energy, the migration path is asymmetrical and E_m will differ for a forward or backward jump.

Within the classical NEB method there is no guarantee that the saddle point is exactly captured. Therefore, a sufficient amount of images is needed to appropriately feature the migration path and to obtain accurate values for E_m, which can demand high computational power. Alternatively, the NEB approach can be extended to the so-called climbing image NEB approach where the highest energy image is able to climb the path toward the saddle point.[369] With that a more accurate description of the path and especially E_m can be

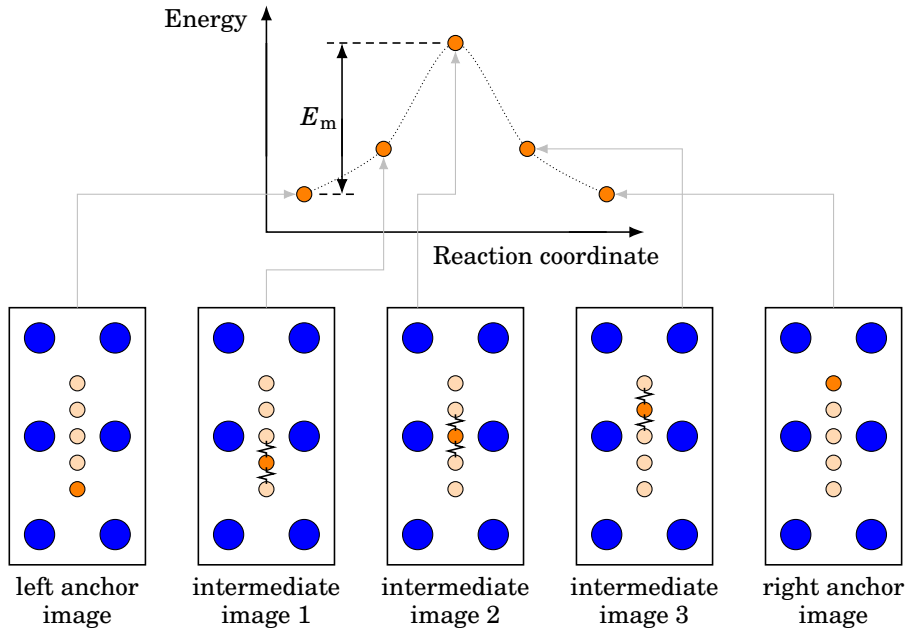

FIGURE 3.16: Illustration of the nudged elastic band (NEB) approach for a symmetrical migration path such as the surface diffusion of an adatom. Blue spheres correspond to the surface atoms and the sphere in full orange to the jumping atom. Spheres in light orange indicate the position of the moving atom in the remaining images. The intermediate images are connected to their neighboring images by virtual springs.

obtained, possibly also reducing the computational effort. For the applied NEB calculations, however, it was not necessary to use the climbing image NEB approach because the path was already sufficiently resolved by relying on the classical NEB method.

3.6.3 Dynamic approach

The static approach explained in the two previous sections is in most cases problematic for superionic conductors. This is because the diffusion mechanism does not correspond to well defined and independent local jumps for most SEs with high ionic conductivities. Instead, the large amount of structural Li^+ vacancies enables highly concerted and correlated Li^+ jumps within an extended volume.[111,207,296,370] Therefore, it becomes virtually impossible to postulate the exact diffusion mechanism and diffusion path, a necessary prerequisite for NEB calculations. We will see such issues in Section 4.4.3 and Section 4.4.4 when comparing the Li^+ diffusion mechanism in LiPS glasses as observed in AIMD simulations with NEB results of single vacancy jumps. Moreover, the definition of a single E_m becomes ill-defined as soon as several Li^+ move simultaneously.

Due to these complications, the transport properties of superionic conductors are commonly determined by executing AIMD simulations. The trajectories of all particles are then evaluated in the spirit of the random-walk methodology.[371] In many cases, the exact calculation of D_σ is omitted (see discussion in Section 3.6.4) and approximated by the tracer diffusion coefficient D^*. According to Einstein and Smoluchowski,[372] D^* is connected to the mean squared displacement (MSD) of all moving species N,

$$D_\sigma \approx D^* = \Theta \lim_{t\to\infty} \frac{1}{2dt}\mathrm{MSD}(t) = \Theta \lim_{t\to\infty} \frac{1}{2dt}\frac{1}{N}\sum_i^N \Big[\mathbf{R}_i(t) - \mathbf{R}_i(t=0)\Big]^2 , \quad (3.48)$$

where d, t and $\mathbf{R}_i$ are the dimensionality of diffusion mechanism, the simulation time, and the atomic coordinates of atom i, respectively. The thermodynamic factor Θ,[105]

$$\Theta = \frac{c}{k_\mathrm{B}T}\frac{\partial\mu}{\partial c} = \frac{\partial\mu/(k_\mathrm{B}T)}{\partial \ln c} , \quad (3.49)$$

takes into account the concentration-dependent chemical potential of the diffusing species and is relevant for understanding the Li^+ (de)intercalation kinetics in electrode materials.[373] For the investigations in this work, however, $\Theta = 1$ can be applied because the composition and Li^+ concentration in all SEs is considered as constant.

For the evaluation of Equation 3.48 in practice, the MSD evolution over time is interpolated with a linear equation and D^* is extracted from its slope.[105,374] Because the MSD is a statistical quantity, its statistical significance needs to be guaranteed by sufficiently long simulations or by averaging over several independent runs.[164] Moreover, it needs to be ensured that the moving species are not trapped in local mega-basins and that indeed long-range transport

occurs. It is therefore advisable to always inspect the atomic trajectories and the MSD plots and examples of common pitfalls in the data evaluation are presented in Section 4.4.1.

In the majority of cases, D^* is too low to be determined directly from AIMD simulations at the temperature of interest. This problem is circumvented by computing D^* at several elevated temperatures at which the kinetics are accelerated. The data is then fitted to an Arrhenius equation (see Equation 3.45) to obtain D_0 and E_m. Both parameters therefore encapsulate the global properties of the material, taking into account all possible migration mechanisms and correlation effects. These values are then typically used to extrapolate D^* to the desired temperature.

In the case of sulfide SEs, it is usually assumed that all Li^+ participate in the ion transport. Therefore, the concentration of the charge carriers is simply expressed as the number of Li^+ ions contained in the cell with volume V, i.e., $c = N/V$. With that, all quantities needed for Equation 3.44 can be obtained based on the AIMD simulations.

3.6.4 Limitations of the Dynamic Approach

Although the method described in the previous subsection is commonly applied to determine the transport properties of SEs[104,106,162,375] the usage of D^* in combination with the Nernst-Einstein equation is actually not an entirely valid approach. The proper calculation of D_σ requires the evaluation of the following equation,[165]

$$D_\sigma = \lim_{t\to\infty} \frac{1}{2dt} \mathrm{MSD}_\mathrm{CoM}(t) = \lim_{t\to\infty} \frac{1}{2dt} \frac{1}{N} \left[\sum_i^N \mathbf{R}_i(t) - \mathbf{R}_i(t=0) \right]^2 , \tag{3.50}$$

which can be understood as the calculation of the MSD of the Li^+ ions' center of mass ($\mathrm{MSD}_\mathrm{CoM}$). But because the convergence of $\mathrm{MSD}_\mathrm{CoM}$ is slow, it's calculation is often omitted as it demands much more extensive statistics and with that much more computational resources. Fortunately, it has been shown that E_m is similar for D^* and D_σ.[163,165] Furthermore, the two diffusion coefficients are connected via the Haven ratio H_R,[376]

$$H_\mathrm{R} = \frac{D^*}{D_\sigma} , \tag{3.51}$$

where $H_\mathrm{R} < 1$ is typically observed. Therefore, the ionic conductivity obtained by utilizing D^* within the Nernst-Einstein equation can be seen as a lower bound to the actual conductivity. For the studies in this work we have constrained most analyses to D^* to keep the computational demands manageable. We will therefore mostly address D^* in the remaining scope of this work. In the case of Li_6PS_5Br, however, we have also computed D_σ and H_R for a selected set of structures at high temperatures in Section 5.3.5.

A second point limits the validity of theoretical transport properties obtained via AIMD simulations. This concerns the extrapolation of D^* to low temperatures, which assumes that the diffusion mechanism and the corresponding E_m is temperature-independent. Recently, however, it was shown that D^* exhibits a pronounced kink in the Arrhenius representation for various SEs.[377] This kink was only observed because the authors generated machine learning potentials for several SEs and used these to conduct AIMD simulations at low temperatures. The position of the kink was found toward the lower end of the temperature range that is typically considered in AIMD simulations. An extrapolation of data that has been obtained exclusively at higher temperatures is therefore likely to overestimate D^* at low temperatures. The authors claim that this is the reason why theoretical predictions of room temperature conductivities of SEs do not match the experimental results in the majority of cases.[377]

3.6.5 Pressure Dependence and the Activation Volume

So far, we have only considered the temperature as an external variable that influences the transport properties. Naturally, other variables can affect the ionic transport, too. One important aspect in this regard is the application of mechanical loadings (i.e., pressure), which is discussed in the context of ASSB to maintain good contact between the materials to improve the cycling stability.[378] The relationships between pressure and the bulk transport properties, however, can be intricate. For example, a compressed material will show reduced jump lengths ($D^*\downarrow$) but an increased concentration of Li^+ due to a reduced volume ($D^*\uparrow$). Most importantly, however, diffusion paths become more narrow, likely leading to increased migration barriers ($D^*\downarrow$).[379]

To capture such effects, the activation volume $\Delta^\ddagger V$ is a useful quantity.[380] It is defined as,

$$\Delta^\ddagger V = -k_\mathrm{B} T \frac{\partial \ln(D^*)}{\partial p} \,, \tag{3.52}$$

and can also be understood as the change in the migration barrier as function of pressure p.[379,381] Under the assumption of constant E_m and $\Delta^\ddagger V$ (i.e., negligible dependence on T and p), the equation for the tracer diffusion coefficient therefore reads as,

$$D^* = D_0 \exp\left(-\frac{E_\mathrm{m} + \Delta^\ddagger V p}{k_\mathrm{B} T}\right) . \tag{3.53}$$

The origin of $\Delta^\ddagger V$ can be understood if its two components are considered,

$$\Delta^\ddagger V = \Delta^\ddagger V^\mathrm{form} + \Delta^\ddagger V^\mathrm{mig} \,, \tag{3.54}$$

where $\Delta^\ddagger V^\mathrm{form}$ is the volume of formation of the moving defect and $\Delta^\ddagger V^\mathrm{mig}$ its activation volume for the migration process. In other words, if diffusion is enabled by a certain defect type, the formed defect interacts with its surrounding. This typically demands a local relaxation of the material that can be expressed

via $\Delta^{\ddagger}V^{\text{form}}$. Similarly, also the defect migration induces lattice relaxations, which are reflected in $\Delta^{\ddagger}V^{\text{mig}}$. In this study, however, we have not decomposed $\Delta^{\ddagger}V$ into the two contributions and only determined its total value. This was done by computing D^{*} via AIMD simulations at different pressures and applying Equation 3.52.

Because AIMD simulations with pressure control are very demanding, however, we have relied on the NVT ensemble and performed calculations at different fixed volumes. The actual pressure was then extracted as the mean pressure acting on the simulation cell over the full simulation. Our calculated values for $\Delta^{\ddagger}V$ might therefore only act as an approximation to the true $\Delta^{\ddagger}V$.

3.7 Elastic Properties

The calculation of the elastic properties via DFT is helpful to understand the response of a material under mechanical loading. We will address this topic in Section 6.3 for Li_7SiPS_8 because it was found that the Li^+ conductivity of pressed pallets strongly depends on the applied pressure. The process was assumed to be of elastic nature and we therefore analyzed the elastic properties of the material. In the following, we will briefly address the necessary aspects of linear elasticity theory that were considered in this work. The interested reader is referred to textbooks for a more thorough introduction to the topic of linear elasticity.[382]

3.7.1 Bulk Modulus

The bulk modulus B is an essential quantity to understand how materials behave if they are subjected to hydrostatic pressures p. B relates the change in p acting on a material as function of the volume V,

$$B_0 = -V\left(\frac{\partial p}{\partial V}\right)_{p=0}, \tag{3.55}$$

where a 0 in the subscripts denotes the quantity at $p = 0$. A relationship between the hydrostatic pressure acting on a cubic material and the volume has been derived by Birch,

$$p(V) = \frac{3B_0}{2}\left[\left(\frac{V_0}{V}\right)^{\frac{7}{3}} - \left(\frac{V_0}{V}\right)^{\frac{5}{3}}\right]\left\{1 + \frac{3}{4}(B_0' - 4)\left[\left(\frac{V_0}{V}\right)^{\frac{2}{3}} - 1\right]\right\}, \tag{3.56}$$

where V_0 is the equilibrium volume and $B_0' = (\partial B/\partial p)_{p=0}$ describes the change of B with pressure.[383] Moreover, Birch established a connection to the energy of the material,

$$E(V) = E_0 + \frac{9V_0B_0}{16}\left\{\left[\left(\frac{V_0}{V}\right) - 1\right]^3 B_0' + \left[\left(\frac{V_0}{V}\right) - 1\right]^2\left[6 - 4\left(\frac{V_0}{V}\right)^{\frac{2}{3}}\right]\right\}. \tag{3.57}$$

Equation 3.57 is commonly called the Birch-Murnaghan equation of state (BM-EOS) to acknowledge the prior work of Murnaghan.[384] Although it was originally derived for cubic materials, it was shown that it can satisfactorily be applied to non-cubic materials as well, if care is taken that the pressure is applied hydrostatically.[385]

In practice, the material of interest is simulated at various fixed volumes around V_0 while allowing for the optimization of the atomic positions and the shape of the simulation cell.[379,386] The simultaneous optimization of the atomic positions and the cell shape at fixed cell volume, a simulation mode that is implemented in may DFT codes, guarantees that hydrostatic conditions are mimicked. The resulting energies as function of volume, so-called energy-volume curves, are then fitted to Equation 3.57 to obtain B_0 and B_0'.

3.7.2 Elastic Constants

In many cases, more information than the mere bulk modulus are needed to understand a material's response to mechanical loading. This is because materials typically exhibit anisotropic elastic bulk properties. As a result, elastic properties such as the Young's modulus Y or shear modulus G become tensorial quantities. It is therefore beneficial to determine the full elasticity tensor $[c]$ whose components c_{ijkl} connect arbitrary strain tensors $[\epsilon]$ and its components ϵ_{kl} to the resulting stress tensor $[\sigma]$ and ts components σ_{ij} in the spirit of Hook's law,

$$[\sigma] = [c][\epsilon] \qquad \text{or} \qquad \sigma_{ij} = c_{ijkl}\,\epsilon_{kl}\ , \tag{3.58}$$

where each $i,j,k,l = 1,2,3$ denotes one of the three cartesian directions. The total number of 81 c_{ijkl} coefficients can be reduced to 21 independent coefficients based on symmetry arguments. The Voigt notation is typically applied to transform the relation into a more comprehensible representation,

$$[c] = \begin{bmatrix} c_{1111} & c_{1122} & c_{1133} & c_{1123} & c_{1113} & c_{1112} \\ c_{2211} & c_{2222} & c_{2233} & c_{2223} & c_{2213} & c_{2212} \\ c_{3311} & c_{3322} & c_{3333} & c_{3323} & c_{3313} & c_{3312} \\ c_{2311} & c_{2322} & c_{2333} & c_{2323} & c_{2313} & c_{2312} \\ c_{1311} & c_{1322} & c_{1333} & c_{1323} & c_{1313} & c_{1312} \\ c_{1211} & c_{1222} & c_{1233} & c_{1223} & c_{1213} & c_{1212} \end{bmatrix} \overset{\text{Voigt}}{=} \ldots$$

$$\ldots \overset{\text{Voigt}}{=} \begin{bmatrix} c_{11} & c_{12} & c_{13} & c_{14} & c_{15} & c_{16} \\ c_{12} & c_{22} & c_{23} & c_{24} & c_{25} & c_{26} \\ c_{13} & c_{23} & c_{33} & c_{34} & c_{35} & c_{36} \\ c_{14} & c_{24} & c_{34} & c_{44} & c_{45} & c_{46} \\ c_{15} & c_{25} & c_{35} & c_{45} & c_{55} & c_{56} \\ c_{16} & c_{26} & c_{36} & c_{46} & c_{56} & c_{66} \end{bmatrix}\ , \tag{3.59}$$

where $[\sigma]$ and $[\epsilon]$ can be expressed as vectors,

$$[\sigma] = \begin{bmatrix} \sigma_{11} \\ \sigma_{22} \\ \sigma_{33} \\ \sigma_{23} \\ \sigma_{13} \\ \sigma_{12} \end{bmatrix} \overset{\text{Voigt}}{=} \begin{bmatrix} \sigma_1 \\ \sigma_2 \\ \sigma_3 \\ \sigma_4 \\ \sigma_5 \\ \sigma_6 \end{bmatrix} \quad , \qquad [\epsilon] = \begin{bmatrix} \epsilon_{11} \\ \epsilon_{22} \\ \epsilon_{33} \\ 2\epsilon_{23} \\ 2\epsilon_{13} \\ 2\epsilon_{12} \end{bmatrix} \overset{\text{Voigt}}{=} \begin{bmatrix} \epsilon_1 \\ \epsilon_2 \\ \epsilon_3 \\ \epsilon_4 \\ \epsilon_5 \\ \epsilon_6 \end{bmatrix} \quad . \tag{3.60}$$

The relation therefore simplifies to

$$\sigma_m = c_{mn}\,\epsilon_n \ . \tag{3.61}$$

The c_{mn} components can be connected to the elastic moduli, for example for cubic systems,

$$Y = c_{11} = c_{22} = c_{33} \ , \ G = c_{44} = c_{55} = c_{66} = (c_{11} - c_{12})/2 \quad , \quad B = (c_{11} + 2c_{12})/3 \ . \tag{3.62}$$

DFT calculations are capable to determine all individual c_{mn} components. Within linear elasticity, c_{mn} depends on the energy change under the application of strain according to

$$c_{mn} = \frac{\partial^2 E}{\partial \epsilon_m \partial \epsilon_n} \ . \tag{3.63}$$

In practice, and as indicated in Equation 3.64, we first applied strain vectors only containing a ϵ_1 component but with different magnitudes to the material and computed the corresponding energies of the structure. This energy-strain data was then fitted with a quadratic equation to obtain a function for $E(\epsilon_1)$. Based on the curvature of the fit we obtained c_{11},

$$\frac{\partial^2 E(\epsilon_1)}{\partial \epsilon_1^2} = c_{11} \ . \tag{3.64}$$

This scheme was repeated for the remaining elements of the main diagonal. Next, the first off-diagonal was treated by applying stress tensors of different magnitude consisting of two components, e.g., ϵ_1 and ϵ_2. Furthermore, the components of the stress tensors were chosen to be of equal magnitude so that the curvature could be easily determined,

$$\frac{\partial^2 E(\epsilon_1, \epsilon_2 = \epsilon)}{\partial \epsilon^2} = c_{11} + c_{22} + 2c_{12} \ . \tag{3.65}$$

Because the main diagonal elements are known from the previous step, the off-diagonal c_{12} element in Equation 3.65 is clearly defined. Similarly, also the remaining components of the first off-diagonal were obtained. In the next step three components were used for $[\epsilon]$ to compute the second off-diagonal and so forth.

3.7.3 Macroscopically Averaged Elastic Moduli

The methods described in the previous section allow us to calculate the elastic bulk properties a material, which can be understood as the properties of a single crystal. For the most common battery applications, however, single crystals are rarely used. Instead, batteries typically consist of polycrystalline materials with non-trivial microstructures.[387,388] A sufficiently large, polycrystalline and non-textured particle will therefore comprise a large amount of arbitrarily orientated crystalline regions that will lead to an averaging of the elastic properties: The particle as a whole effectively appears to be isotropic although the underlying bulk properties are anisotropic.

Different theories have been developed to connect the anisotropic bulk properties with the effective elasticity of macroscopic particles. The following methods as derived by (i) Voigt, (ii) Reuss and (iii) Voigt-Reuss-Hill have been used in this work. For a deeper insight the reader is referred the comprehensibly review by Den Toonder *et al.*[389] and references therin.

Voigt Method

The effective elastic properties within the Voigt approach are obtained if $[c]$ is averaged over all possible rotations. This leads to the effective Young's modulus Y_V, effective shear modulus G_V and effective Poisson's ratio υ_V according to Voigt,

$$Y_\mathrm{V} = \frac{(\alpha-\beta+3\gamma)(\alpha+2\beta)}{2\alpha+3\beta+\gamma} \quad , \quad G_\mathrm{V} = \frac{\alpha-\beta+3\gamma}{5} \quad , \quad \upsilon_\mathrm{V} = \frac{\alpha+4\beta-2\gamma}{4\alpha+6\beta+2\gamma} \, , \tag{3.66}$$

with

$$\alpha = \frac{c_{11}+c_{22}+c_{33}}{3} \quad , \quad \beta = \frac{c_{23}+c_{13}+c_{12}}{3} \quad , \quad \gamma = \frac{c_{44}+c_{55}+c_{66}}{3} \, . \tag{3.67}$$

Reuss Method

The Reuss Method does not rely on $[c]$, but on the compliance tensor $[s]$ instead. $[s]$ is the inverse tensor of $[c]$ and connects $[\sigma]$ and $[\epsilon]$ via

$$[\epsilon] = [s][\sigma] \, . \tag{3.68}$$

The effective elastic properties are then obtained by averaging $[s]$ over all orientations in the same spirit as in the Voigt method. The resulting effective properties according to Reuss are then

$$Y_\mathrm{R} = \frac{5}{3\alpha'+2\beta'+\gamma'} \quad , \quad G_\mathrm{R} = \frac{5}{4\alpha'-4\beta'+3\gamma'} \quad , \quad \upsilon_\mathrm{R} = -\frac{2\alpha'+8\beta'-\gamma'}{6\alpha'+4\beta'+2\gamma'} \, , \tag{3.69}$$

with

$$\alpha' = \frac{s_{11}+s_{22}+s_{33}}{3} \quad , \quad \beta' = \frac{s_{23}+s_{13}+s_{12}}{3} \quad , \quad \gamma' = \frac{s_{44}+s_{55}+s_{66}}{3} \, . \tag{3.70}$$

Voigt-Reuss-Hill Method

Because of the way the Voigt and Reuss method calculate the effective constants, their results represent an upper and lower bound to the true effective elastic constants, respectively.[389] A more reasonable result is obtained by applying the Voigt-Reuss-Hill method,[390] where the effective moduli are obtained as average of the Voigt and Reuss method and the Poisson's constant is calculated based on the averaged moduli,

$$Y_{\mathrm{VRM}} = \frac{Y_{\mathrm{V}} + Y_{\mathrm{R}}}{2} \quad , \quad G_{\mathrm{VRM}} = \frac{G_{\mathrm{V}} + G_{\mathrm{R}}}{2} \quad , \quad \upsilon_{\mathrm{VRM}} = \frac{Y_{\mathrm{VRM}}}{2G_{\mathrm{VRM}}} - 1 \, . \tag{3.71}$$

All effective elastic constants can then be used to determine other effective properties such as the effective bulk modulus via the established relations,

$$B_{\mathrm{VRM}} = \frac{Y_{\mathrm{VRM}}}{3(1-2\upsilon_{\mathrm{VRM}})} = \frac{Y_{\mathrm{VRM}} G_{\mathrm{VRM}}}{9G_{\mathrm{VRM}} - 3Y : q : q_{\mathrm{VRM}}} \, . \tag{3.72}$$

4 Pure Lithium Thiophosphates (LiPS)

Parts of this chapter have been published in:

[1] **M. Sadowski**, S. Sicolo and K. Albe, *Defect thermodynamics and interfacial instability of crystalline $Li_4P_2S_6$*, Solid State Ionics 319, 53-60 (2018).[316]

[2] **M. Sadowski** and K. Albe, *Computational study of crystalline and glassy lithium thiophosphates: Structure, thermodynamic stability and transport properties*, Journal of Power Sources 478, 229041 (2020).[391]

The Li-P-S phase system is of high technological relevance for ASSBs because it comprises promising phases used as SEs. The ternary compounds are typically called lithium thiophosphates and we will refer to them as LiPS phases. A number of crystalline phases (see Figure 2.1) have already been identified. These phases are built from different P_xS_y structural units and a large spread concerning the materials properties is observed. In particular, the Li^+ transport properties can vary by orders of magnitude.

Although these crystalline phases are not the main focus of this chapter, we briefly address them to allow for a valid comparison with LiPS glasses, which are an important characteristic of the Li-P-S system: The majority of synthesis procedures lead to the presence of (residual) glassy phases. As a result, most LiPS materials are actually glass-ceramics, whose properties are determined by the type, ratio and distribution of the underlying phases. The exact influences and properties of the glassy phase, however, have not been fully understood so far. One reason for this is the missing long-range order that complicates an experimental structural analysis. We have therefore used DFT calculations, where the structure of the simulated system is unambiguously defined, to take a closer look on the structure-property relationships of LiPS glasses. To distinguish crystalline from glassy systems when using chemical formulas, we will add the prefixes “c-” and “g-”, respectively. A complete overview of all simulated LiPS systems with their key properties is given in Table 4.1.

TABLE 4.1: Overview of simulated LiPS compounds using the in-text abbreviations. Crystalline and glassy (amorphous) LiPS structures are indicated with a "c-" and "g-" prefix, respectively. Relative stabilities ΔE (normalized per atom) have been determined with respect to the three boundary phases (i) c-Li_3PS_4, (ii) c-$Li_4P_2S_7$ and (iii) c-$Li_4P_2S_6$ ($P321$).

(a) Crystalline compounds (supercell models were used for evaluation of transport properties and RDFs)

Abbreviation	No. of atoms			Volume	Density	ΔE	No. of structural units					E_m	D_0	$\sigma_{300\,K}$
	Li	P	S	[Å^3]	[g/cm^3]	[meV]	PS_4^{3-}	$P_2S_7^{4-}$	$P_2S_6^{4-}$	S^{2-}	$P_2S_6^{2-}$	[meV]	[cm^2/s]	[mS/cm]
c-Li_3PS_4 (β-type)	96	32	128	5310	1.80	-	32	-	-	-	-	354	$5.81\cdot10^{-3}$	0.74
c-$Li_7P_3S_{11}$	168	72	264	10462	1.88	5.1	12	12	-	-	-	164	$4.70\cdot10^{-4}$	83.6
c-$Li_4P_2S_7$	64	32	112	4592	1.82	-	-	16	-	-	-	220	$9.38\cdot10^{-4}$	16.7
c-$Li_2P_2S_6$	72	72	216	7953	2.02	-	-	-	-	-	36	-	-	-
c-Li_7PS_6	336	48	288	11916	1.82	-	48	-	-	96	-	171	$2.91\cdot10^{-4}$	68.8
c-$Li_4P_2S_6$ ($P321$)	96	48	144	5162	2.18	-	-	-	24	-	-	-	-	-
c-$Li_4P_2S_6$ ($P\bar{3}1m$)	72	36	108	3855	2.19	4.1	-	-	18	-	-	-	-	-

(b) Generated glass models using the "soft" melt-quenching scheme

Abbreviation	No. of atoms			Volume	Density	ΔE	No. of structural units				E_m	D_0	$\sigma_{300\,K}$
	Li	P	S	[Å^3]	[g/cm^3]	[meV]	PS_4^{3-}	$P_2S_7^{4-}$	$P_2S_6^{4-}$	$P_3S_{10}^{5-}$	[meV]	[cm^2/s]	[mS/cm]
g-Li_3PS_4	96	32	128	5516	1.73	33.4	32	-	-	-	257	$1.96\cdot10^{-3}$	10.4
g_1-$Li_7P_3S_{11}$	84	36	132	5465	1.80	23.0	12	12	-	-	239	$1.22\cdot10^{-3}$	11.2
g_2-$Li_7P_3S_{11}$	84	36	132	5987	1.65	21.0	13	10	-	1	265	$2.36\cdot10^{-3}$	7.32
g_1-$Li_4P_2S_7$	64	32	112	5313	1.57	18.8	-	16	-	-	251	$1.60\cdot10^{-3}$	7.40
g_2-$Li_4P_2S_7$	64	32	112	5064	1.64	19.9	-	16	-	-	231	$1.13\cdot10^{-3}$	11.6
g-$Li_4P_2S_{6.5}$	64	32	104	4635	1.71	22.7	-	8	8	-	259	$1.68\cdot10^{-3}$	6.51
g-$Li_4P_2S_6$	72	36	108	4716	1.79	40.0	-	-	18	-	239	$9.68\cdot10^{-4}$	8.86
g-$Li_7P_3S_{10}$	84	36	120	5349	1.72	39.7	12	-	12	-	245	$1.69\cdot10^{-3}$	12.6

(c) $Li_4P_2S_7$ glasses obtained via the "brute-force" melt-quenching scheme [preceding work]

Abbreviation	No. of atoms			Volume	Density	ΔE	No. of structural units	E_m	D_0	$\sigma_{300\,K}$
	Li	P	S	[Å^3]	[g/cm^3]	[meV]		[meV]	[cm^2/s]	[mS/cm]
g-quench$^{2000\,K}_{10\,K/ps}$	64	32	112	4850	1.72	40.2	unusual units	274	$2.34\cdot10^{-3}$	4.72
g-quench$^{2000\,K}_{50\,K/ps}$	64	32	112	5000	1.67	62.3	unusual units	256	$2.37\cdot10^{-3}$	9.42
g-quench$^{2000\,K}_{100\,K/ps}$	64	32	112	5049	1.65	96.7	unusual units	235	$1.21\cdot10^{-3}$	10.82
g-quench$^{2500\,K}_{10\,K/ps}$	64	32	112	4934	1.69	33.8	unusual units	287	$2.80\cdot10^{-3}$	3.38
g-quench$^{2500\,K}_{50\,K/ps}$	64	32	112	4825	1.73	59.7	unusual units	261	$1.93\cdot10^{-3}$	6.65
g-quench$^{2500\,K}_{100\,K/ps}$	64	32	112	5001	1.67	78.9	unusual units	178	$4.43\cdot10^{-4}$	35.7

(d) Glass models that contain S–S bonds obtained by idealization of structures from (c) [preceding work]

Abbreviation	No. of atoms			Volume	Density	ΔE	No. of structural units				
	Li	P	S	[Å^3]	[g/cm^3]	[meV]	PS_4^{3-}	$P_2S_7^{4-}$	$P_2S_6^{4-}$	$P_3S_{10}^{5-}$	S–S
g-$Li_4P_2S_7$-mod_1	64	32	112	5008	1.67	18.3	7	8	3	1	3
g-$Li_4P_2S_7$-mod_2	64	32	112	4895	1.71	21.0	12	4	6	-	6
g-$Li_4P_2S_7$-mod_3	64	32	112	4773	1.75	26.7	16	-	8	-	8

(e) Glass models obtained by adding Li to the structures from (d)

Abbreviation	No. of atoms			Volume	Density	ΔE	No. of structural units			E_m	D_0	$\sigma_{300\,K}$
	Li	P	S	[Å^3]	[g/cm^3]	[meV]	PS_4^{3-}	$P_2S_7^{4-}$	$P_2S_6^{4-}$	[meV]	[cm^2/s]	[mS/cm]
g-$Li_{70}P_{32}S_{112}$	70	32	112	4972	1.68	23.9	6	10	3	268	$2.08\cdot10^{-3}$	5.78
g-$Li_{76}P_{32}S_{112}$	76	32	112	4898	1.70	33.6	12	4	6	242	$1.49\cdot10^{-3}$	12.3
g-$Li_{80}P_{32}S_{112}$	80	32	112	5048	1.65	37.9	16	-	8	218	$9.54\cdot10^{-4}$	20.3

(f) Average transport properties of glasses from (b) and (e)

Abbreviation	No. of atoms			Volume	Density	ΔE	No. of structural units	E_m	D_0	
	Li	P	S	[Å^3]	[g/cm^3]	[meV]		[meV]	[cm^2/s]	
⌀ Glasses	varying among all glasses							246	$1.48\cdot10^{-3}$	

4.1 Initial Steps

4.1.1 Structure Generation

The atomic structure of all crystalline LiPS phases, except for the hypothetical c-$Li_4P_2S_7$, has already been solved experimentally (see Section 2.1.2 for illustrations of all structures) and could directly be used as input for the DFT calculations. Only for c-Li_3PS_4 (β-phase) or c-$Li_7P_3S_{11}$ that exhibit a non-trivial Li^+ substructure, the various partially occupied Li^+ sites needed to be preprocessed to obtain initial structural models. The Li^+ ions were distributed among the various sites based on the experimentally reported occupancies by employing the `supercell` program.[392] For comparison, much more care needed to be taken for Li_6PS_5Br (see Section 5.1) and Li_7SiPS_8 (see Section 6.1) because, in addition to a complex Li^+ substructure, they exhibit ionic disorder on further sites.

Speaking of the Li^+ distribution in sulfide SEs, another point is worth noting: Certainly, the actual distribution of the Li^+ ions in the calculations has an important influence on the calculated properties of the material. Hence, a reasonable, initial Li^+ distribution is crucial if structures are used directly for any analyses. With our approach, however, the initially chosen Li^+ distribution is not of utmost importance. This is because AIMD simulations were performed for all structures first. Thus, Li^+ ions were able to migrate to more favorable positions if they were initialized with an unfavorable distribution. Snapshot structures, extracted from the AIMD simulations, were then optimized to ensure an intrinsic and natural Li^+ substructure, adequate for further postprocessing.

The situation for LiPS glasses is even more complicated: Atomistic glass models are not available. This is the reason why such glass models need to be generated as a first step. The procedure is outlined in Section 3.3.8 in more detail and only a brief summary is given here: Starting with crystalline phases, the structures were subjected to elevated temperatures in AIMD simulations and either explicitly quenched in subsequent AIMD simulations or directly optimized in static calculations. Depending on the outcome, the structures were manually modified (e.g., by adding/removing atoms or locally rearranging the atomic structure) and/or annealed again. We limited the generation of glasses to compositions lying in the phase triangle spanned by Li_3PS_4, $Li_4P_2S_7$ and $Li_4P_2S_6$; exemplary structure models for g-Li_3PS_4 and g-$Li_{76}P_{32}S_{112}$ are shown in Figure 4.1.

Our approach by no means guarantees that the most stable LiPS glasses (if such a thing exists at all) have been generated and even more stable models might possibly be generated. Still, relative stabilities in the range of the thermal energy at room temperature (see Section 4.2) supports our approach and indicates that reasonable structural models have been obtained. A structural comparison presented in the following further substantiates our approach and lays the foundations for more involved analyses.

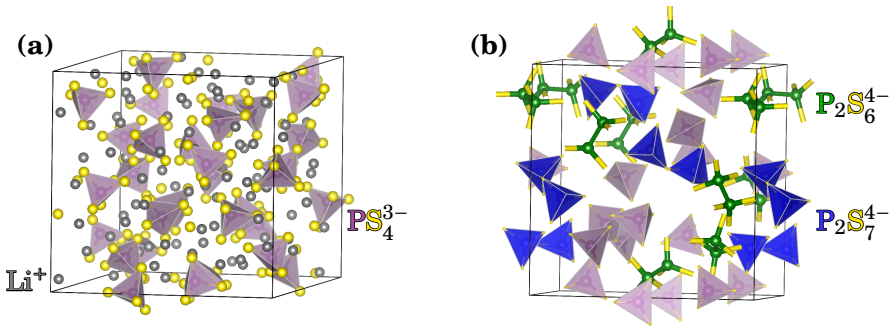

FIGURE 4.1: (a) Structural model of g-Li_3PS_4 that only contains PS_4^{3-} tetrahedra. (b) Structural model of g-$Li_{76}P_{32}S_{112}$ that contains three different types of structural units: PS_4^{3-}, $P_2S_7^{4-}$ and $P_2S_6^{4-}$. For clarity, Li^+ and S^{2-} ions are not shown in part (b).

4.1.2 Structure Validation of LiPS Glasses

Figure 4.2 (a) and (b) show experimentally obtained reduced pair distribution functions $G(r)$ by Stöffler *et al.*[132] and Shiotani *et al.*[393] of crystalline and glassy Li_3PS_4. Their data was used to extract the average particle density of the material ρ_0 based on the slope $m = -4\pi\rho_0$ of the dashed line that runs through the origin and the minimum prior to the first major peak, here shortly before 2 Å.[394]

With the knowledge of ρ_0, $G(r)$ can be converted to tRDFs and the corresponding curves are shown in Figure 4.2 (c) for the crystal and (d) for the glass together with our theoretically calculated data. The experiments, however, relied on X-ray radiation for the determination of $G(r)$. Hence, the intensities of the different pair correlations change with the atom types and should approximately scale with the number of electrons of every species. In contrast, the theoretical tRDFs are obtained from an analysis of the spatial correlations (i.e., bond lengths), where every bond counts equally. To make the data comparable, a weighting of the theoretical data as outlined in Section 3.3.5 was applied.

Notably, the highest peaks in the experimental tRDFs are broader than the ones in the theoretical data. We attribute this to the fact that X-rays are scattered by the diffuse electron clouds around the atoms, leading to a natural smearing of the data, whereas the assessment of theoretical tRDFs is based on the distance between the atomic nuclei. The latter is a precisely defined quantity in the simulations, resulting in sharper peaks with high intensity.

The experimental tRDFs are in line with the theoretical results (see Figure 4.2). In particular, a comparison with the data of Shiotani *et al.* is straightforward. The data of Stöffler *et al.*, on the other hand, suffers from substantial, so-called termination ripples due to a limited maximum scattering vector (typically denoted as Q_{max}), but the main changes between crystalline and glassy Li_3PS_4 are still reproduced:

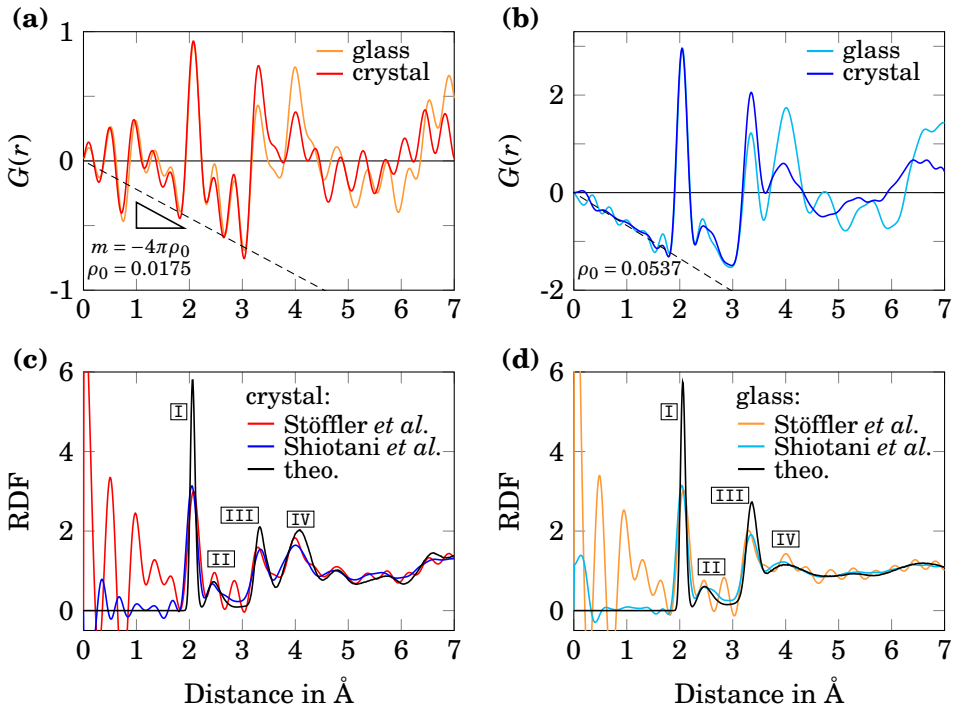

FIGURE 4.2: Experimental $G(r)$ curves of crystalline and glassy Li_3PS_4 as reported by (a) Stöffler *et al.*[132] and (b) Shiotani *et al.*[393]. The experimental data has been converted to tRDFs and is compared to our theoretical tRDFs for (c) the crystalline and (d) the glassy phase. A weighting, described in Section 3.3.5, was applied to make theoretical and experimental data comparable.

- At short distances, the tRDFs in Figure 4.2 (c) of the crystalline phase are virtually identical to those of the glassy phase in Figure 4.2 (d). This can be seen when comparing the height and shape of the first peak (I) at approximately 2 Å due to intramolecular P−S correlations within PS_4^{3-} units and the second, smaller peak (II) around 2.5 Å due to Li−S correlations.
- The third peak (III) due to intramolecular S−S correlations around 3.4 Å increases in the glass, whereas the following peak (IV) around 4.0 Å due to intermolecular S−S correlations is strongly flattened.
- Small P−S and S−S correlations at distances above 4.5 Å become more shallow.

The comparison proves that our generated Li_3PS_4 glasses show the same features observed in the experiment and we believe that this can be transferred to the remaining glasses as well, which enables further analyses. In the analysis above, we anticipated the attribution of specific atomic correlations to certain

TABLE 4.2: Reaction energies $\Delta_f E$ of the crystalline LiPS phases in the $Li_2S-P_2S_5$ system and their energy distance E_{hull} to the convex hull. All energies are given in meV and normalized to the number of atoms.

		P_2S_5 at V_{PBE}		P_2S_5 at $V_{exp.}$	
x	Compound	$\Delta_f E$	E_{hull}	$\Delta_f E$	E_{hull}
0.5	$Li_2P_2S_6$	−49.5	23.6	−66.02	13.94
0.67	$Li_4P_2S_7$	−83.0	14.4	−95.70	10.91
0.70	$Li_7P_3S_{11}$	−88.1	14.2	−99.88	12.06
0.75	Li_3PS_4	−109.6	0.0	−119.94	0.0
0.825	Li_7PS_6	−41.3	13.5	−47.14	12.83

peaks in the RDFs. A more detailed structural analysis and comparison of the crystalline and glassy phases is presented in Section 4.3. But let us first inspect the energetics of the LiPS compounds.

4.2 Stability

4.2.1 Formation Energy of Crystalline LiPS Phases

The stability of the crystalline LiPS phases within the $Li_2S-P_2S_5$ system can be evaluated via the formation energy $\Delta_f E$, normalized to the number of atoms,

$$\Delta_f E = \frac{E(Li_{2a}P_{2b}S_{a+5b}) - [a \cdot E(Li_2S) + b \cdot E(P_2S_5)]}{3a+7b}\,, \tag{4.1}$$

of reactions according to

$$a \cdot Li_2S + b \cdot P_2S_5 \quad \longrightarrow \quad Li_{2a}P_{2b}S_{a+5b}\,, \tag{4.2}$$

where negative values for $\Delta_f E$ indicate an exothermic reaction. The corresponding $\Delta_f E$ is shown in Figure 4.3 as blue squares and proves that every LiPS compound is more stable than the binary phases Li_2S and P_2S_5. The convex hull, however, reveals that only c-Li_3PS_4 is thermodynamically stable. This is despite the fact that the β-phase has been considered, which is known to be less stable than the γ-phase.[174] The γ-phase, in turn, is technologically irrelevant due to its limited Li^+ transport properties, which is the reason why only the β-phase of c-Li_3PS_4 is considered in this work.

With approximately 10 to 20 meV, the energy distance E_{hull} of the remaining phases to the convex hull is in the range of the thermal energy at room temperature. Overall, our results fit to reported Li-P-S phase diagrams[104] and are partly in accordance to calculations by Holzwarth *et al.*:[150] c-Li_7PS_6 is reported to be unstable whereas c-$Li_7P_3S_{11}$ is found to be slightly stable in DFT calculations relying on the local density approximation.

Taking a closer look at the binary phases, we find that P_2S_5, which can be described as a molecular crystal consisting of neutral P_4S_{10} units, is not well

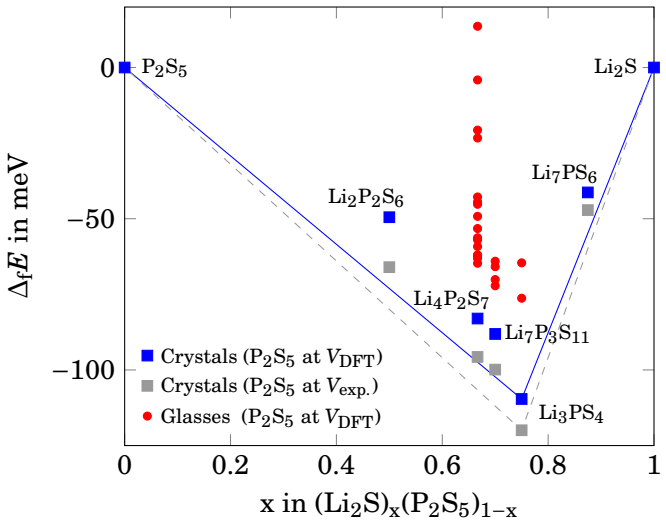

FIGURE 4.3: Reaction energies $\Delta_f E$ of the crystalline LiPS compounds in the $Li_2S-P_2S_5$ system. P_2S_5 has been considered with the calculated equilibrium volume V_{DFT} (using the PBE exchange-correlation functional) and the experimental volume $V_{exp.}$. The lines indicate the convex hull. Exact energy values can be read from Table 4.2. For comparison, $\Delta_f E$ of LiPS glasses have been added.

represented by our DFT calculations. For such systems, the correct description of van der Waals forces is necessary, which is not entirely possible with the applied PBE exchange-correlation potential. As a result, the equilibrium volume V_{DFT} of P_2S_5 is considerably overestimated by 32% compared to the experimental volume $V_{exp.}$. Presumably, this also affects the calculated total energy, which might lead to inaccurate formation energies of the crystalline LiPS phases. A recalculation of $\Delta_f E$ using the energy of P_2S_5 at the fixed experimental volume leads to a shift of all values as can be seen by the gray squares in Figure 4.3 but does not change the results qualitatively: Li_3PS_4 remains the only stable LiPS phase.

One possibility to avoid the aforementioned issues is the inclusion of a dispersion correction in the calculations, but we did not apply it retrospectively to all generated structures. Alternatively, energy corrections based on experimental reaction energies can be applied. This has been done in the course of calculating Li-P-S phase diagrams[104] or analyzing the stability of Na_3PS_4.[395] In both cases, an energy correction for sulfur, which crystallizes as a molecular crystal with S_8 rings, was employed.

As the stability of the crystalline LiPS compounds was not of central importance in the scope of this work, such attempts were not pursued here. For the energy comparison of the LiPS glasses, however, similar issues are faced and we will outline how this was circumvented in the next section.

4.2.2 Relative Stabilities of LiPS Glasses

To circumvent the issues related to the energy comparison we did not reference the energies of the LiPS glasses to any “problematic” compound such as elemental S, elemental P or P_2S_5. Instead, relative stabilities ΔE are obtained by

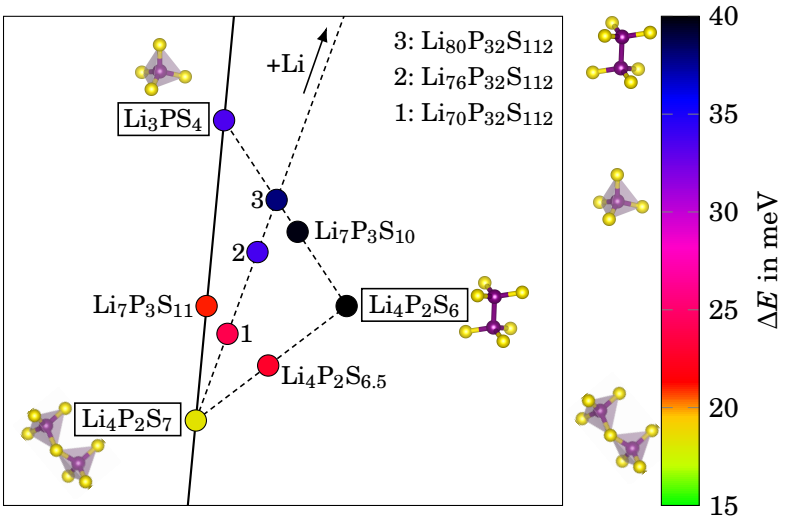

FIGURE 4.4: Relative stabilities ΔE, normalized to the number of atoms, of the generated LiPS glasses with respect to the three crystalline boundary phases c-Li_3PS_4, c-$Li_4P_2S_7$ and c-$Li_4P_2S_6$ ($P321$). Only the most stable glasses at every composition are considered.

comparing the energy of the glasses to the energy of the crystalline compounds that span a triangle in the Li-P-S phase diagram (see inset of Figure 2.1). The three boundary phases that define the triangle are c-Li_3PS_4, c-$Li_4P_2S_7$ and c-$Li_4P_2S_6$ ($P321$ symmetry), and only glasses in this compositional space have been generated. Their calculated ΔE have been normalized to the number of atoms and are illustrated in Figure 4.4. Note that only the most stable glass at every composition is shown. Based on that several conclusions can be drawn:

1. ΔE of all LiPS glasses with respect to the boundary phases is positive and up to 40 meV. For comparison, relative stabilities close to the thermal energy at room temperature of 25 meV per atom are often considered to potentially yield (meta)stable compounds by acknowledging the accuracy of DFT calculations and entropic effects.[396] Considering crystalline materials, it has even been proposed to raise the metastability criteria to approximately 70 meV per atom depending on the material.[397] The calculated ΔE therefore indicates that all LiPS glasses are metastable.

2. The most stable glass (ΔE = 18.3 meV, structure labeled as g-$Li_4P_2S_7$-mod_1 in Table 4.1 (d)) is obtained at a composition of $Li_4P_2S_7$, at x = 0.67 in $(Li_2S)_x(P_2S_5)_{1-x}$. Interestingly, this generated structure does not only contain $P_2S_7^{4-}$ units, but a variety of structural units including several intermolecular S–S bonds, a feature that will be discussed in more detail in Section 4.3.7. Still, two other glasses (g_1- and g_2-$Li_4P_2S_7$, see Table 4.1

(b)) with similar ΔE of 18.8 and 19.9 meV but only containing $P_2S_7^{4-}$ units could be generated. The rather low ΔE of the $Li_4P_2S_7$ glasses might indicate a reason why crystalline $Li_4P_2S_7$ has not been synthesized, yet: The driving force to crystallize is low and entropic contributions might even favor the glass over the crystal. Furthermore, we argue that residual PS_4^{3-} and $P_2S_6^{4-}$ structural units, commonly observed in synthesized $Li_4P_2S_7$ glasses,[115,134] could hinder the crystallization.

3. Glasses at a composition of $Li_7P_3S_{11}$ (x = 0.70) are of high interest because they compete with the superionic c-$Li_7P_3S_{11}$. Two glasses have been prepared: First, g_1-$Li_7P_3S_{11}$ with ΔE = 23.0 meV comprises an equal amount of PS_4^{3-} and $P_2S_7^{4-}$ units, which is exactly the same for the crystalline phase. Second, g_2-$Li_7P_3S_{11}$ is found to be slightly more stable (ΔE = 21.0 meV) despite the fact that one transformation of the structural units according to

$$2\ P_2S_7^{4-} \longrightarrow PS_4^{3-} + P_3S_{10}^{5-}\,, \tag{4.3}$$

was observed. The latter $P_3S_{10}^{5-}$ unit can be understood as a chain of three corner-sharing PS_4 tetrahedra, which have been reported in LiPS glasses at x = 0.60.[115] The slight energy gain of the structural model, however, cannot be exclusively attributed to Reaction 4.3 because also the volume and the remaining arrangement of the structural units differ between the two glass models. Compared to c-$Li_7P_3S_{11}$, the two glasses are 17.9 and 15.9 meV higher in energy.

4. At Li_3PS_4 (x = 0.75) a glass with ΔE = 33.0 meV is obtained. Taking into account the results of the previous two points, a trend can be identified within the considered $(Li_2S)_x(P_2S_5)_{1-x}$ composition space for $0.67 \leq x \leq 0.75$: Higher x leads to higher ΔE, i.e., less stable glasses.[135] who report values that should translate to 8.8, 29.5 and 36.2 meV for g-$Li_4P_2S_7$, g-$Li_7P_3S_{11}$ and g-Li_3PS_4, respectively, when converting their data. Note that they referenced the energy to the slightly more stable γ-phase of Li_3PS_4. The largest difference to our results is found for g-$Li_4P_2S_7$. Most likely, this does not only originate from different glass structures, but also from the underlying energy of the c-$Li_4P_2S_7$ model. In particular, we observed a slight shearing of $P_2S_7^{4-}$ units and the occupation of new Li^+ sites during AIMD simulations, leading to a structure that is 5 meV more stable than the initial model proposed by Holzwarth *et al.*[150]

5. Further trends concerning the stability of S-deficient glasses, which have not been analyzed in such a systematic way before, can be identified: Starting at g-$Li_4P_2S_7$, ΔE constantly increases toward g-$Li_4P_2S_6$ as well as toward $Li_{80}P_{32}S_{112}$ (obtained by adding Li to $Li_4P_2S_7$). Similarly, the glasses become less stable when going from g-Li_3PS_4 toward g-$Li_4P_2S_6$. The latter is found to be the least stable glass with ΔE = 40.0 meV.

6. It appears that the observed trends are related to the structural units contained in the glasses and a hierarchy can be deduced: From more to less stable glasses, the majority of structural units are $P_2S_7^{4-}$ over PS_4^{3-} to $P_2S_6^{4-}$ as indicated next to the color bar in Figure 4.4. Presumably, this is connected to the properties of the structural units. For example, despite their comparably large size, the $P_2S_7^{4-}$ units are rather flexible, as the individual corner-sharing tetrahedra are able to tilt and rotate around their bridging S^{2-} ion. This does not only promote Li^+ diffusion,[104] but might also facilitate structural adjustments according to the surrounding ions and enable favorable structures with low ΔE. In contrast, $P_2S_6^{4-}$ structural units are stiff and therefore only able to rearrange as a whole unit, which might hinder the formation of low energy configurations.

4.2.3 Inclusion of Vibrational Entropy

A computational study by Chu *et al.* has reported that crystalline $Li_7P_3S_{11}$ is metastable at 0 K but becomes thermodynamically stable at elevated temperatures if vibrational contributions to the entropy, S_{vib}, are included.[104] This raises the question of whether S_{vib} is also helpful in stabilizing the LiPS glasses over the crystalline phases. To answer this question, we have calculated S_{vib} by performing phonon calculations for all crystalline phases and a selection of LiPS glasses. Not all glasses could be considered because the required phonon calculations are computationally demanding with such large structure models (N_{atoms} ≈200, $N_{electrons}$ ≈1200) in the absence of any crystal symmetry.

In addition to glasses with the same compositions as the three boundary phases, we considered two additional glasses. First, one glass with $Li_7P_3S_{11}$ composition to inspect also the changes in the relative stability with respect to the superionic phase c-$Li_7P_3S_{11}$. Second, the glass named g-$Li_{76}P_{32}S_{112}$ to include a structure model that comprises the three most important structural units (PS_4^{3-}, $P_2S_6^{4-}$, $P_2S_7^{4-}$). The resulting pDOS plots for a selection of LiPS materials are shown in Figure 4.5 and those of c-Li_3PS_4 and c-$Li_7P_3S_{11}$ fit well to previously reported results.[104,398] All pDOS comprise a peak around 2.5 THz that is mostly resulting from S contributions, followed by a broader region between approximately 4-11 THz governed by mixtures of S and Li. Slightly below frequencies of 15 THz the pDOS exhibit a small gap and above these frequencies a signal from P and S ions presumably results from fast vibrations due to the relatively stiff P–S bonds.

Additionally, imaginary frequencies, here plotted at negative frequencies, are observed for some of the structures. Such imaginary frequencies can result from mostly two issues. First, numerical issues can occur if the reference structure has not been optimized accurately enough and a part of the species are slightly displaced from their local minimum. For the mentioned case of $Li_7P_3S_{11}$, Chu *et al.*[104] attributed small fraction of imaginary frequencies to such numerical issues. Second, imaginary frequencies can indicate a dynamical instability of the

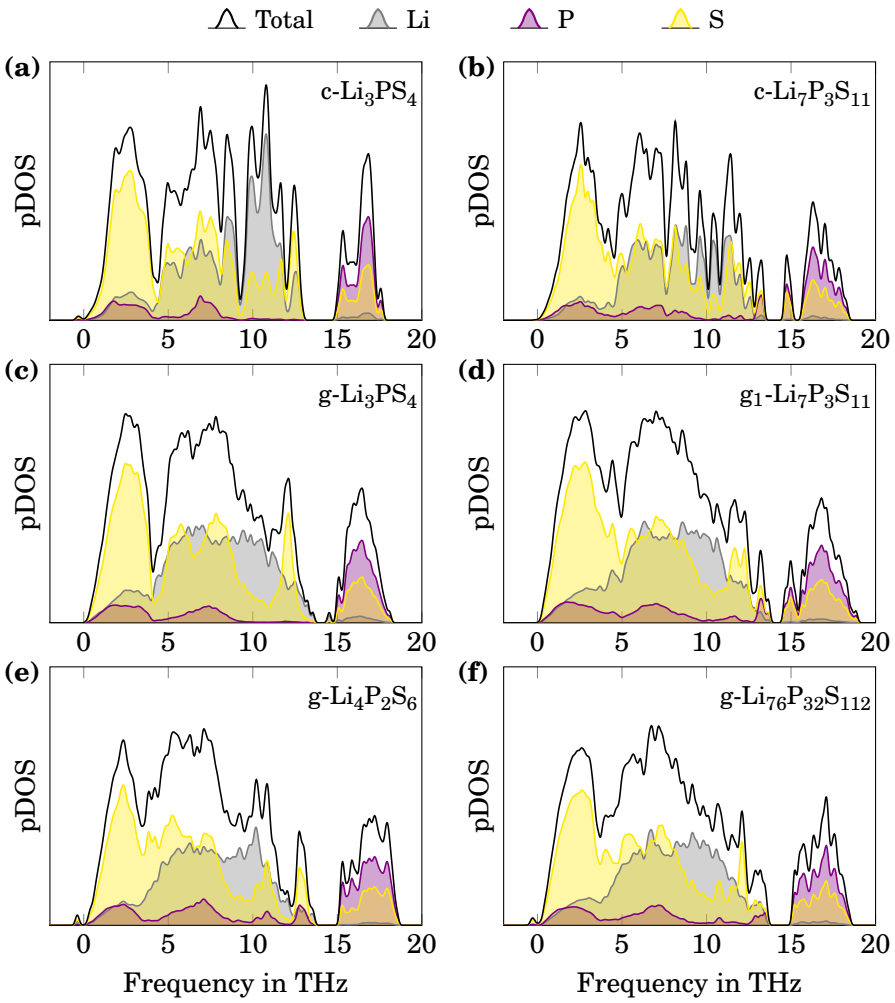

FIGURE 4.5: Phonon density of states (pDOS) for a selection of crystalline and glassy LiPS phases with the individual contributions of the different species.

material. In other words, the structure is able to transform into a more stable state. Given the complicated structure of LiPS glasses and the fast Li^+ diffusion, we can deduce that the Li^+ substructure can be described as a relatively flat potential energy landscape. Therefore, it is likely that the application of small displacements to a fraction of the ions might result in a slightly more stable configuration, i.e., the displacements induce a transition to another local energy minimum close by. It is therefore difficult to distinguish between such cases and purely numerical issues. Fortunately, the overall amount if imaginary frequencies and their magnitudes are low compared to the real frequencies.

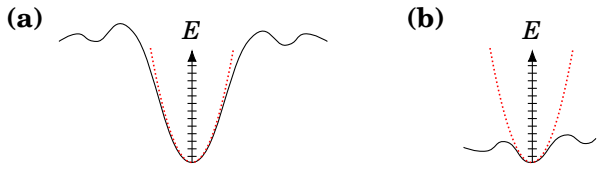

FIGURE 4.6: Illustration of the potential energy landscape for the displacement of an ion. (a) If the ion is located on a low-energy site, it can be properly described within the harmonic approximation even for rather large displacements that occur at high temperatures. (b) For Li^+ ions in SEs, however, it is likely that the harmonic approximation is only valid for low temperatures due to the flat energy potential energy landscape. Extrapolating the results to higher temperatures might lead to artifacts.

Hence, the imaginary frequencies should barely influence the properties derived from the phonon calculations.

However, another issue related to the method itself needs to be kept in mind: If ions are located in a deep minimum, the harmonic approximation is appropriate to describe the potential well even for rather large displacements appearing at high temperatures, as shown in Figure 4.6 (a). This scenario should apply the P and S ions due to their covalent bonds. For the flat potential energy landscape of Li^+ ions that are fast diffusing species, however, it is likely that the harmonic approximation breaks down at high temperatures, as sketched in Figure 4.6 (b). In this regard, several publications make us of the term "Li^+ sublattice melting" in the context of other superionic Li^+ conductors.[399–401] This term nicely depicts the conceptual mismatch between the harmonic approximation and the actual Li^+ motion in superionic conductors, at least at high temperatures. More advanced techniques like thermodynamic integration[402] or an analysis of the velocity-velocity autocorrelation[403] might be necessary to obtain a better description of the vibrational properties of sulfide SEs at high temperature, but this needs to be attempted elsewhere.

Keeping the issues in mind, the results of the phonon calculations have been used to compute S_{vib} for every phase. On this basis, the difference in vibrational entropy ΔS_{vib} with respect to the crystalline boundary phases has been calculated in the same spirit as ΔE. Both quantities can be used to derive relative stabilities ΔF at finite temperature,

$$\Delta F = \Delta E - T\Delta S_{\mathrm{vib}} \,. \tag{4.4}$$

The values obtained for ΔF at temperatures of 300 K, 500 K and 700 K are shown in Figure 4.7 and demonstrate that the relative stability of all LiPS glasses improves with the inclusion of vibrational entropy. The average energy gain amounts to −3.5, −5.8 and −7.9 meV at 300 K, 500 K and 700 K, respectively. Remarkably, the energy gain is not uniform and more strongly pronounced for the less stable glasses. For example, g-$Li_4P_2S_6$ with a compa-

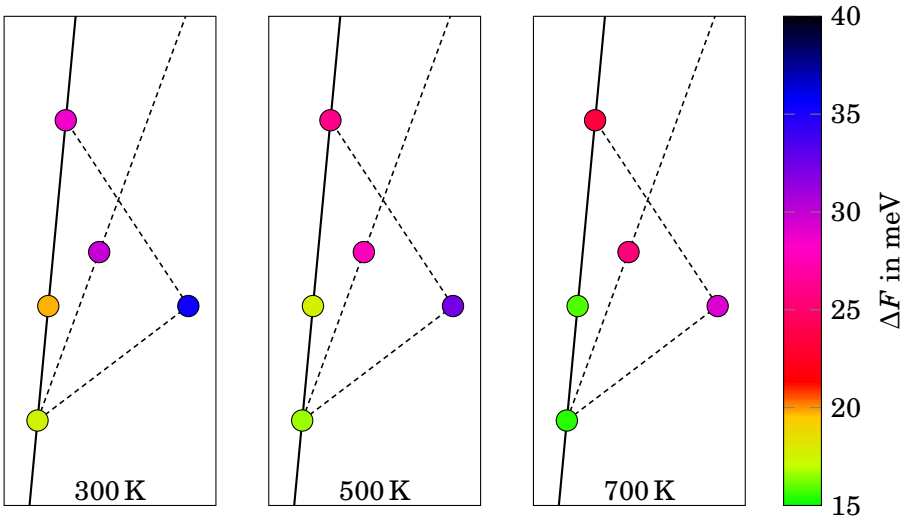

FIGURE 4.7: Relative stability $\Delta F = \Delta E - T\Delta S_{\text{vib}}$ of selected LiPS glasses with respect to the three crystalline boundary phases c-Li_3PS_4, c-$Li_4P_2S_7$ and c-$Li_4P_2S_6$ ($P321$) at (a) 300 K, (b) 500 K and (c) 700 K. The color coding is the same as in Figure 4.4 and the exact values can be read from Table 4.3.

rably poor relative stability of 40.0 meV at 0 K improves by −10.8 meV to 29.2 meV at 700 K. In comparison, the more stable glass g_1-$Li_4P_2S_7$ only gains −3.4 meV over the same temperature interval (from 18.8 to 15.4 meV). These results indicate that LiPS glasses with the considered compositions will never become thermodynamically stable. Instead, the accelerated kinetics at such elevated temperatures will induce crystallization processes or might even lead to decomposition reactions.[115,116,124,125,404,405]

Another interesting observation is made for the superionic crystal c-$Li_7P_3S_{11}$. Please notice that we did not use the same structural model for the calculation of S_{vib} as for the remaining analyses, because the structure was simply too large to conduct feasible phonon calculations. Instead, a $1 \times 2 \times 1$ supercell was used. We find that the relative stability of c-$Li_7P_3S_{11}$ barely changes upon the inclusion of vibrational entropy. It even slightly increases from 5.1 meV at 0 K to 5.4 meV at 700 K, which implies that the decomposition to c-Li_3PS_4 and c-$Li_4P_2S_7$ would be even slightly favored with increasing temperatures. This is in contradiction to the reports by Chu *et al.*,[104] who have predicted that c-$Li_7P_3S_{11}$ would become thermodynamically stable at a temperature of 630 K by relying on a similar approach.

The only difference is that they evaluated the decomposition reaction to crystalline P_2S_5 and Li_3PS_4 and used an energy correction for every S atom in deriving the relative stabilities.[104,395] Unfortunately, they do not comment on the volume issues related to P_2S_5 (see Section 4.2.1) and how they could affect

TABLE 4.3: Relative stability $\Delta F = \Delta E - T\Delta S_{\text{vib}}$ of selected LiPS glasses with respect to the three crystalline boundary phases c-Li_3PS_4, c-$Li_4P_2S_7$ and c-$Li_4P_2S_6$ ($P321$) at the respective temperature. Besides the boundary phases and the selection of LiPS glasses, also c-$Li_7P_3S_{11}$ has been considered. The ΔF values are in meV/atom.

	0 K[†]	300 K	500 K	700 K
g-Li_3PS_4	33.4	28.5	25.9	23.4
g_1-$Li_7P_3S_{11}$	23.0	19.7	17.7	15.8
g_1-$Li_4P_2S_7$	18.8	17.6	16.6	15.4
g-$Li_4P_2S_6$	40.0	35.6	32.2	29.2
g-$Li_{76}P_{32}S_{112}$	33.6	29.8	27.6	25.4
c-$Li_7P_3S_{11}$	5.1	5.3	5.4	5.4

[†]Previous values for ΔE. No inclusion of zero-point energy.

the reliability of phonon calculations and the determination of S_{vib}, although they have used the same exchange-correlation functional as we did. Due to these issues we believe that our results are more trustworthy because they do not require any correction scheme and probe the stability against more comparable phases. Hence, our calculations indicate that c-$Li_7P_3S_{11}$ is a metastable compound at all temperatures, which is supported by the fact that it cannot be synthesized by conventional solid-state methods[153] and already decomposes shortly above 550 K.[160,406] Therefore, the formation of c-$Li_7P_3S_{11}$ from LiPS glasses can only be explained by the kinetics of the crystallization, which seems to be favored over other crystallization routes or phase separations.

4.3 Structural Analysis

4.3.1 Short-Range Order

Figure 4.8 shows the computed RDFs of the crystalline phases and Figure 4.9 those of our generated LiPS glasses that only contain the commonly reported PS_4^{3-}, $P_2S_7^{4-}$ and $P_2S_6^{4-}$ structural units. Glasses comprising other "unusual" structural units or cross-linking S–S bonds between structural units will be discussed in Section 4.3.6 and Section 4.3.7, respectively. All RDFs have been obtained from AIMD simulations at 300 K by averaging over approximately 30 ps with time steps of 1 fs. Note that no weighting has been applied to RDFs presented in the following. Therefore, the shown RDFs reflect the true ratios of the correlations.

The tRDFs of all crystalline and glassy phases, shown in Figure 4.8 (a) and Figure 4.9 (a), respectively, exhibit three common features at short distances (see the three gray boxes in background of the tRDFs):

1. All tRDFs start with a sharp peak at approximately 2 Å, which is attributed to P–S bonds of the underlying structural units as can be seen in

the P–S pRDFs in Figure 4.8 (b) and Figure 4.9 (b). Only for c-$Li_2P_2S_6$ the first peak is split into two peaks due to the shorter bond lengths of the terminal P–S bonds and longer bond lengths of bridging P–S–P bonds within the $P_2S_6^{2-}$ unit (not explicitly marked in Figure 4.8 (b)). Similarly, for all compounds that contain $P_2S_7^{4-}$ units (c- and g-$Li_4P_2S_7$, c- and g-$Li_7P_3S_{11}$, g-$Li_{70}P_{32}S_{112}$, g-$Li_{76}P_{32}S_{112}$, g-$Li_4P_2S_{6.5}$) the bridging P–S–P bonds lead to a small shoulder on the right side of the first peak.[134]

2. A peak around 2.5 Å is attributed to Li–S correlations, as can be seen in Figure 4.8 (e) and Figure 4.9 (e). The exact position and shape of the peak varies between the different crystalline phases and is more uniform for the glasses.

3. Between 3.2 and 3.6 Å a third peak evolves due to S–S correlations, as can be seen in Figure 4.8 (c) and Figure 4.9 (c). Again, the crystalline phases show more distinct characteristics, whereas the pRDFs of the glasses exhibit only subtle differences.

4.3.2 Structural Aspects of Crystalline Phases

The similarities at short distances are expected because all crystalline and glassy phases consist of negatively charged P_xS_y units with comparable short-range order. At distances beyond the third common peak, however, the tRDFs of the crystalline phases start to diverge and the identification of similarities is barely possible. This is reasonable because the different crystal structures determine different long-range orders.

Nevertheless, there are further distinct features besides the three common peaks that are shared between several of the crystalline phases, mostly because they share the same type(s) of structural unit(s). These features become more apparent if the pRDFs are inspected and for specific cases their origin is indicated in Figure 4.8 with red bonds of the responsible structural unit.

For example, the peak around 3.4 Å in the P–S pRDFs in Figure 4.8 (b) can clearly be attributed to intramolecular correlations of $P_2S_6^{4-}$ units. Furthermore, c-$Li_7P_3S_{11}$ and c-$Li_4P_2S_7$ share comparable patterns between 3.7 and 5.1 Å, which belong to intramolecular correlations of $P_2S_7^{4-}$ units as well as superimposed intermolecular P–S correlations expected at such distances.

Also in terms of S–S correlations the different structural units may exhibit characteristic features that are not explicitly marked in Figure 4.8 (c) but are in accordance to the literature.[132] We will have a closer look at the S–S correlations in Section 4.3.5. The P–P pRDFs in Figure 4.8 (d) reveal intramolecular features of $P_2S_6^{4-}$ and $P_2S_7^{4-}$ units at 2.3 and 3.6 Å, respectively. For the sake of completeness, also the unique P–P correlations around 2.9 Å of the $P_2S_6^{2-}$ units from c-$Li_2P_2S_6$ are marked. All P–P signals beyond 4 Å are attributed to intermolecular correlations.

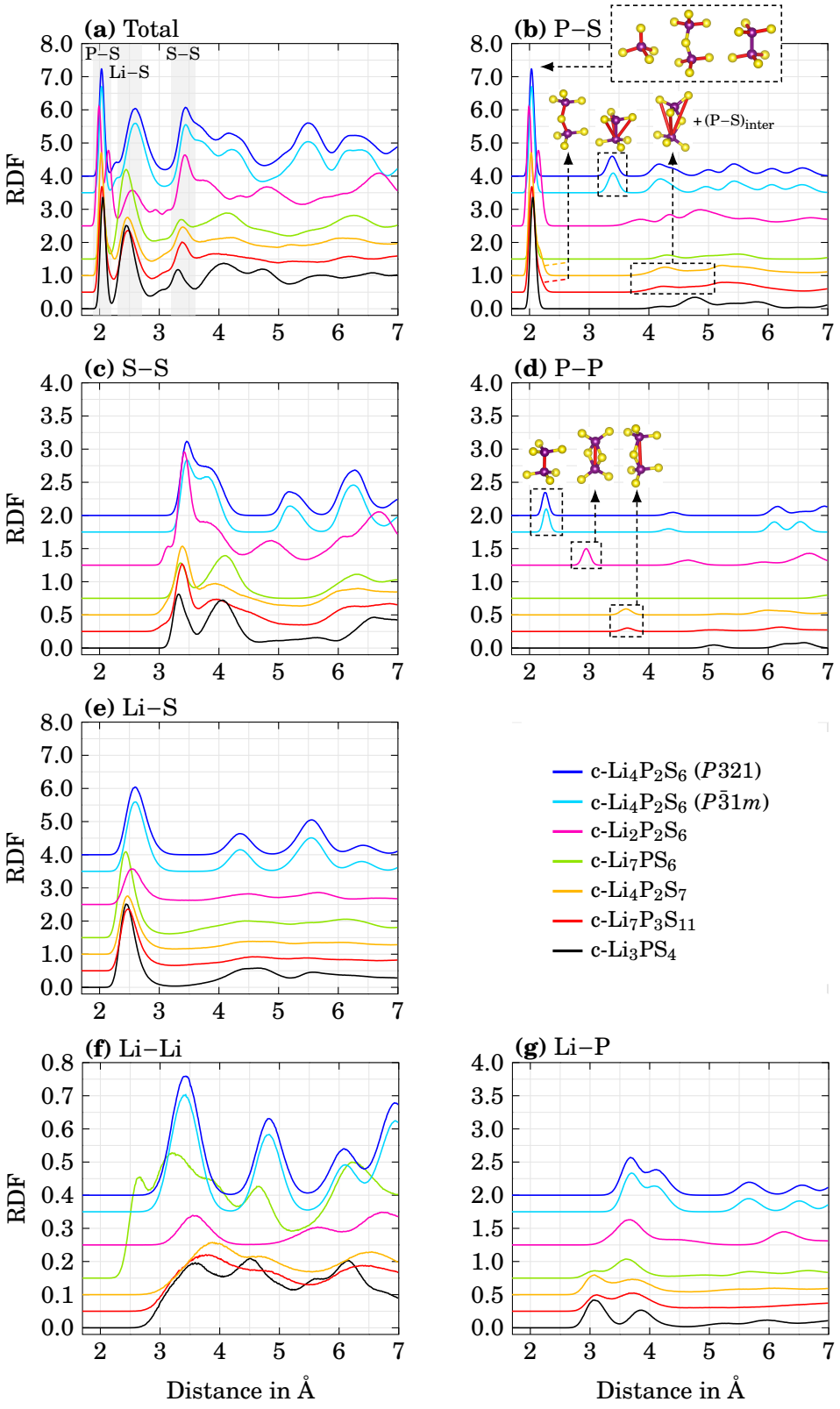

FIGURE 4.8: Illustration of (a) the tRDF and (b)-(g) all pRDFs of various crystalline LiPS phases at 300 K. Features marked with dashed boxes belong to certain correlations as indicated by red bonds in the respective structural units. Note the different scalings on the y axes.

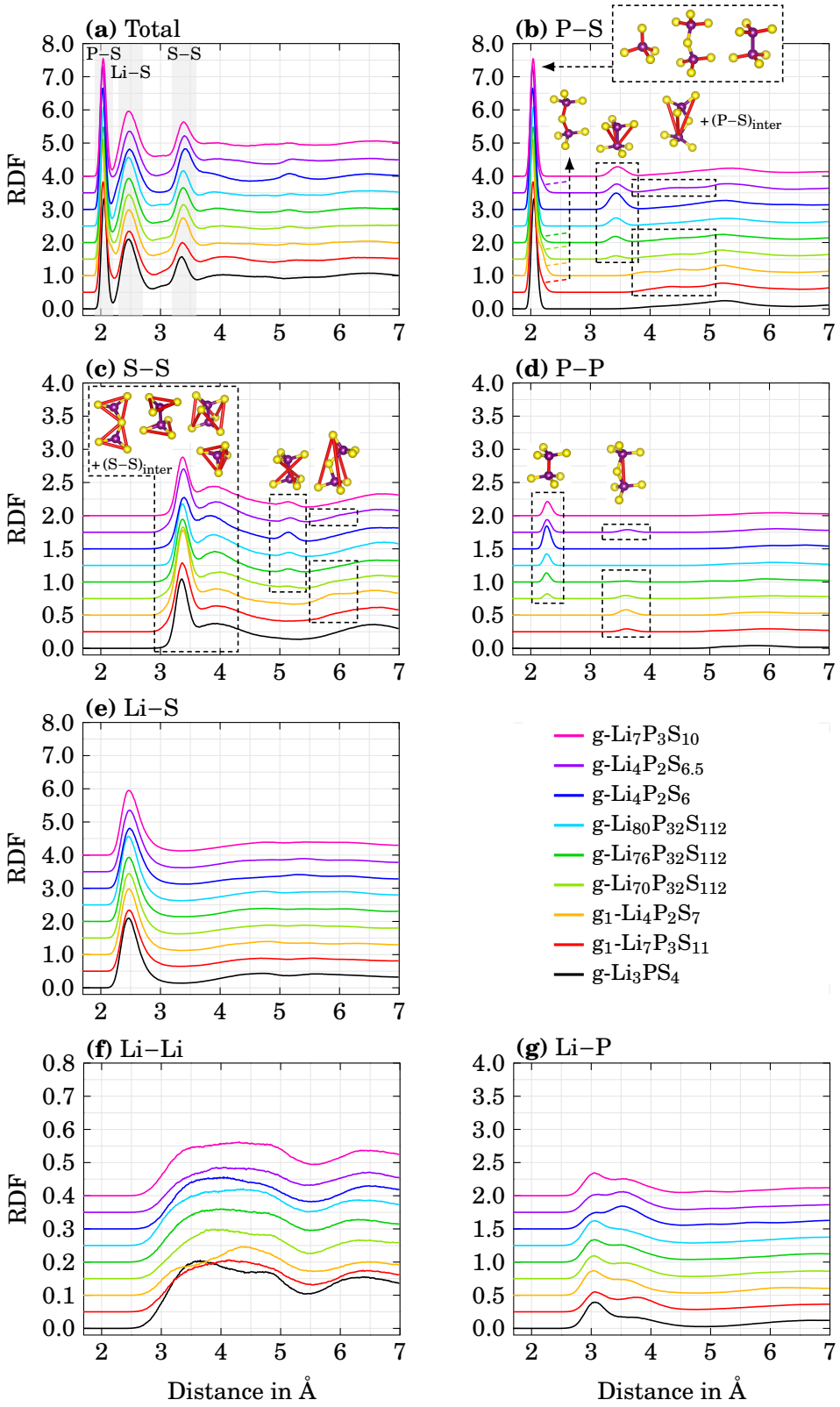

FIGURE 4.9: Illustration of (a) the tRDF and (b)-(g) all pRDFs of various LiPS glasses at 300 K. Features marked with dashed boxes belong to certain correlations as indicated by red bonds in the respective structural units. Note the different scalings on the y-axes.

Notably, the crystalline phases also strongly vary in terms of correlations that involve Li^+ ions. For the two c-$Li_4P_2S_6$ phases and c-$Li_2P_2S_6$ the Li−Li correlations exhibit distinct peaks clearly separated from each other by regions where the RDF drops to nearly zero. This is indicative of an ordered Li^+ substructure with well defined Li^+ sites, which might even hint at poor Li^+ transport properties.[120,123] The Li−Li correlations of the remaining crystalline phases do not drop in such a pronounced manner. Especially, for c-$Li_4P_2S_7$ and c-$Li_7P_3S_{11}$ the correlations are rather smeared, indicating that $P_2S_7^{4-}$ units promote a flat potential energy landscape for Li^+ ions that enhances the ionic conductivity.[107] Presumably, this also facilitates the formation of $P_2S_7^{4-}$-containing glasses and could be one reason for their low ΔE values presented in Section 4.2.2.

Interestingly, all RDFs (except for the P−P contributions above 4 Å) of the $P\bar{3}1m$ and $P321$ phase of c-$Li_4P_2S_6$ are virtually identical despite their different arrangements of the $P_2S_6^{4-}$ units. Although RDFs cannot be used to unambiguously deduce a certain local atomic structure, the high degree of similarity observed for both c-$Li_4P_2S_6$ indicates that the local environment for Li^+ ions is closely related. Therefore, we assume that also the defect thermodynamics, which we have previously analyzed for the $P\bar{3}1m$ structure,[120] can be transferred to the $P321$ structure as well. According to that, high Li^+ Frenkel pair formation energies are responsible for a low density of mobile charge carriers and a poor ionic conductivity. We will revisit the defect thermodynamics of the $P\bar{3}1m$ in Section 4.4.5 and see that the inclusion of sulfur-related defects will not change the conclusion that c-$Li_4P_2S_6$ is a poor ionic conductor.

4.3.3 Distinct Features of LiPS Glasses

The computed RDFs of all glasses are shown in Figure 4.9 and are comparable to results by Ohara *et al.*[134] and Baba *et al.*[135], who also reported calculated RDFs. We notice that the RDFs of all our glass models are very similar, and in particular the tRDFs are hardly distinguishable despite the different ratios of the underlying PS_4^{3-}, $P_2S_7^{4-}$ and $P_2S_6^{4-}$ structural units. The subtle differences can only be recognized in the pRDFs and the origin of characteristic features is indicated with red bonds and the responsible structural unit.

Similarly to the crystalline phases, the P−S correlations in Figure 4.9 (b) show a small shoulder due to P−S−P bonds of $P_2S_7^{4-}$ structural units on the right of the first peak at approximately 2.2 Å in our glass models. Furthermore, $P_2S_6^{4-}$ units lead to a signal around 3.4 Å. Compared to the one of c-$Li_4P_2S_6$, the signal in g-$Li_4P_2S_6$ is slightly broadened and shifted to the larger distances in the sub-Ångström regime. This indicates that the $P_2S_6^{4-}$ slightly expand in glassy LiPS structure, which fits to the lower densities that have been obtained for our generated LiPS glasses (see Table 4.1). Further intramolecular P−S correlations are observed between 3.7 and 5.1 Å. They stem from $P_2S_7^{4-}$ units, but are mostly hidden by superimposed intermolecular $(P-S)_{inter}$ correlations.

Therefore, we believe that such signals are difficult to probe by experimental means.

Distinct features of $P_2S_6^{4-}$ and $P_2S_7^{4-}$ units around 5.2 and 5.9 Å, respectively, can also be found in the S–S pRDFs in Figure 4.9 (c). The peak between 3.3 and 3.6 Å and the more shallow peak around 3.9 Å, however, cannot be unambiguously assigned because the various intramolecular S–S correlations within the different PS_4^{3-}, $P_2S_7^{4-}$ and $P_2S_6^{4-}$ structural units lead to similar signals. The situation is complicated by intermolecular S–S correlations, denoted as $(S–S)_{inter}$, that start to set in at these distances. We will revisit this issue more closely in Section 4.3.5.

Similarly to the crystalline phases, the P–P bond of $P_2S_6^{4-}$ units and the intramolecular P–P correlations of $P_2S_7^{4-}$ units are recognizable in the P–P pRDFs at distances around 2.3 and 3.6 Å, respectively. Owing to the low peak height, however, resolving these signals by experiments will presumably be difficult because the strong P–S signal around 2.2 Å and the more intense S–S correlations will hide the weak P–P contributions. Intermolecular P–P correlations then start to set in at approximately 4.6 Å for all LiPS glasses, independently of the underlying structural unit, but stay at low intensity. Therefore, we disagree with Shiotani *et al.*,[393] who have attributed a signal around 7 Å to intermolecular P–P correlations among PS_4^{3-} units. Such distances are at the limit of our data. Still, our RDFs suggest that the observations of Shiotani *et al.* rather result from S–S correlations.

In summary, distinct features in the S- and P-related RDFs of LiPS glasses could only be attributed to intramolecular correlations of $P_2S_7^{4-}$ and $P_2S_6^{4-}$ units. The PS_4^{3-} unit does not lead to unique patterns in the RDFs. Furthermore, no explicit intermolecular features are observed, indicating that the structural units do not exhibit a preferential ordering and are arranged randomly with respect to each other.

4.3.4 Influence of Structural Units on Li^+ Ions in Glasses

Because LiPS compounds are of interest as SEs, it is of concern how the different structural units influence the Li^+ substructure in the glassy phases. We have already seen that the tRDFs of the various glasses strongly resemble each other. Hence, it is not surprising that also the Li^+-related pRDFs are very similar. This is apparent when comparing the shapes of the peaks around 2.5 Å in the Li–S pRDFs in Figure 4.9 (e). The slight deviations of the peak heights can be attributed to compositional differences.

The similarities suggest that the S^{2-} ions of all structural units (regardless of whether it is PS_4^{3-}, $P_2S_7^{4-}$ or $P_2S_6^{4-}$) are surrounded by Li^+ ions in a rather uniform manner in LiPS glasses. As a result, also the Li–S correlations at higher distances are difficult to distinguish. Only if a high magnification is applied to the data (not shown), subtle differences above 3.5 Å become apparent. These features, however, could not be unambiguously assigned to the different

structural units because several features that are present in glasses with only one type of structural unit appear in some, but not in all glasses with mixed types.

The Li–Li correlations, shown in Figure 4.9 (f), are in good agreement with other theoretical[104] and experimental[157] studies. They start to appear shortly below 3 Å, which has been reported to be the approximate minimum distance between Li^+ ions in sulfide SEs.[134,163] The Li–Li pRDFs further show a plateau between 3.5 and 5.0 Å that might indicate a smeared nearest-neighbor Li^+ shell around every Li^+ ion. The plateaus exhibit slight variations, but these can not be correlated with the structural units. After a minimum at 5.5 Å, the next smeared shell of Li^+ presumably starts.

As shown in Figure 4.9 (g), the Li–P correlations of all glasses start to appear at approximately 2.7 Å and exhibit a first maximum around 3 Å, followed by a second, broader maximum or shoulder between 3.5 and 3.8 Å. In the case of g-$Li_4P_2S_6$ and g-$Li_4P_2S_{6.5}$, which both comprise $P_2S_6^{4-}$ units, the second maximum is even higher than the first. However, also g-$Li_7P_3S_{10}$ and g-$Li_{80}P_{32}S_{112}$ contain $P_2S_6^{4-}$ units but do not show a prominent second maximum. Therefore, the second maximum cannot be explained by the presence of $P_2S_6^{4-}$ units, but rather by the absence of PS_4^{3-} units. This assumption is affirmed by the Li–P pRDF of g-$Li_4P_2S_7$, which exhibits a distinct second maximum and does not contain PS_4^{3-} units. Another evidence is the transition from g-$Li_{80}P_{32}S_{112}$ over g-$Li_{76}P_{32}S_{112}$ to g-$Li_{70}P_{32}S_{112}$, where a decreasing amount of PS_4^{3-} units seems to be correlated to a more perceptible second peak. Beyond 4.5 Å no further differences in the pRDFs are found.

The overall strong resemblance in the Li-related pRDFs reveals that Li^+ ions experience comparable chemical surroundings in all LiPS glasses, independently of the underlying structural units. Moreover, a similar structure suggests that also the Li^+ dynamics is similar. We will see in Section 4.4.2 that this is truly the case: All LiPS glasses seem to exhibit comparable diffusion coefficients.

4.3.5 Resolving Intra- and Intermolecular S–S Correlations

The disentanglement of intra- and intermolecular correlations can be difficult by experimental means and is much easier to assess from our computational data. The following analysis clarifies individual contributions to the RDFs, facilitates any future characterization attempts for LiPS glasses similar to those of Stöffler *et al.*,[132] and might even be helpful for related compounds. Because the assignment of P–S and P–P correlations is straightforward, we have restricted the analysis to the S–S correlations. Let us first concentrate on Figure 4.10 (a) to (d), which show the S–S pRDFs of those LiPS glasses that have a crystalline counterpart.

Interestingly, we find that intermolecular correlations (orange curves) start at lower distances in the glasses. This is best seen for Li_3PS_4 in Figure 4.10 (a), where the onset of the intermolecular S–S correlations is located at ap-

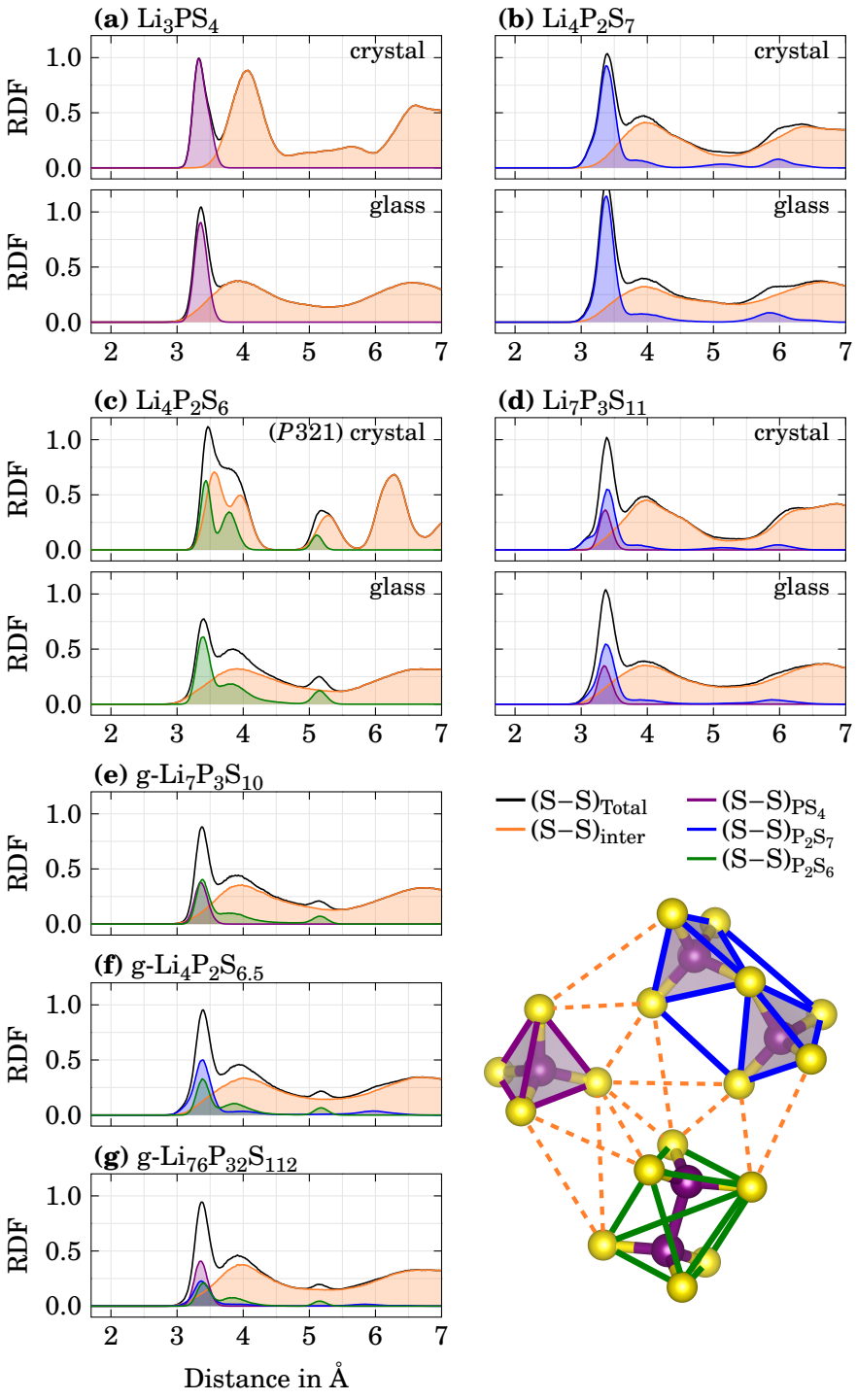

FIGURE 4.10: Partial RDFs of the S–S correlations, partitioned into the different intra- and intermolecular contributions of the structural units.

proximately 3.4 Å in the crystalline phase but at 3 Å in the glass. Likewise, for $Li_4P_2S_6$ in Figure 4.10 (c) it is reduced from 3.2 to 3 Å, and also for $Li_4P_2S_7$ and $Li_7P_3S_{11}$ the intermolecular S−S contributions around 3 Å become slightly more prominent in the glass. This indicates that a portion of the structural units is able to move closer together in the glass, regardless of the structural unit type. Beyond 3.5 Å, most notably for the two peaks of c-$Li_4P_2S_6$ and the peak around 4 Å for the remaining crystalline phases, the intermolecular contributions become more smeared in the glasses. The least changes between crystalline and glassy phase are observed for $Li_4P_2S_7$ and $Li_7P_3S_{11}$.

In terms of intramolecular correlations barely no changes are observed for the PS_4^{3-} units (purple curves), as can be seen in the RDFs of Li_3PS_4 and $Li_7P_3S_{11}$. For $P_2S_7^{4-}$ units (blue curves) minor changes are observed: In $Li_4P_2S_7$ the shallow peak shortly above 5 Å, present in the crystalline phase, disappears in the glass and also the peak around 6 Å shifts to slightly lower distances. Similar changes are also observed in $Li_7P_3S_{11}$, where additionally a shoulder around 3 Å in the crystal becomes more blurred in the glass. We believe that it will be a challenging task in experiments to unambiguously identify such changes in the intramolecular S−S correlations of $P_2S_7^{4-}$ units because (i) they are subtle, (ii) intermolecular S−S contributions show a much stronger intensity at these distances, and (iii) superimposed contributions from P−S correlations and other sources complicate the analysis.

It is noteworthy, however, that the intramolecular S−S correlations of $P_2S_6^{4-}$ units (green curves) shown in Figure 4.10 (c) undergo obvious changes from the crystalline to the glassy phase. The most prominent change involves the peak around 3.8 Å that is significantly reduced in height. Moreover, the flank on the right side of the peak expands up to the signal shortly above 5 Å. The changes of the S−S correlations indicate that the dynamics of $P_2S_6^{4-}$ units is considerably different in an amorphous surrounding. This fits to the observation that also the Li^+ dynamics have changed tremendously: The obtained Li^+ diffusion coefficients have increased by several orders of magnitudes in g-$Li_4P_2S_6$ compared to the crystalline phase, as will be shown throughout Section 4.4.

For completeness, the intra- and intermolecular features just described reappear in Figure 4.10 (e) to (g) for glasses comprising at least two different types of structural units.

4.3.6 Occurrence of “Unusual” Structural Units

Up to this point we have only discussed the structure of LiPS glasses comprising the commonly observed, “usual” structural units: PS_4^{3-}, $P_2S_7^{4-}$ and $P_2S_6^{4-}$. In the course of a preceding work, however, we have noticed the formation of various “unusual” structural units when $Li_4P_2S_7$ glasses have been generated by relying on a brute-force melt-quenching protocol as described in Section 3.3.8 and listed in Table 4.1 (c). We have revisited these glasses in the scope of this work and briefly recap previous results in the following summary. The “unusual” units

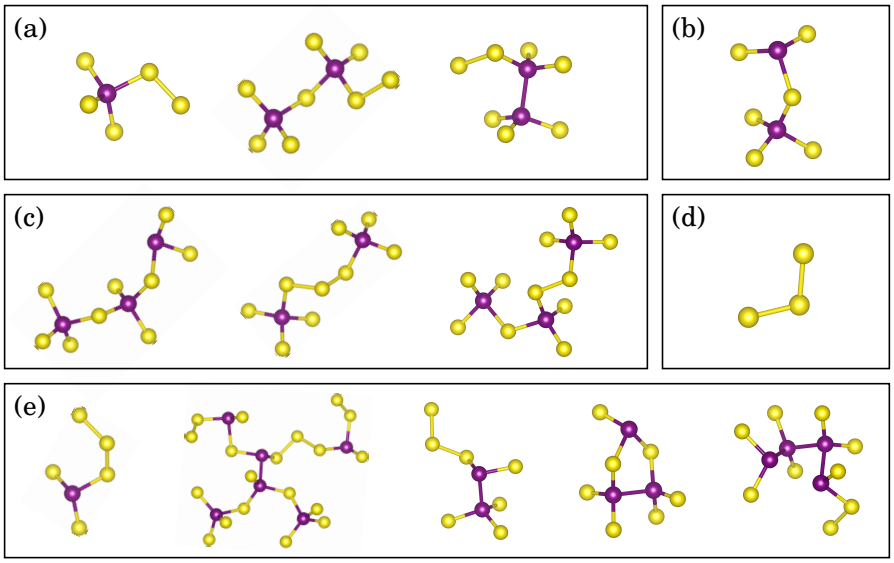

FIGURE 4.11: A selection of unusual P_xS_y units, observed in different melt-quenched LiPS glasses. The subfigure labels (a) to (e) correspond to the in-text description. Color coding: P (purple), S (yellow).

observed in the glasses have been classified according to the following types, and a selection of examples are shown in Figure 4.11 in the corresponding subfigure:

(a) Usual units with additional "sulfur tail(s)"

(b) Usual units with missing terminal sulfur

(c) Usual units cross-linked to other usual/unusual units via atypical P–S or S–S bonds

(d) Free sulfur chains

(e) Others, e.g., large clusters or units containing P–P–P bonds

We have found that glasses containing a large number of unusual structural units, especially if they are considerably different from the usual structural units, are less stable than glasses only containing usual structural units. However, also one glass with comparable low ΔE of 33.8 meV is obtained despite a large number of unusual structural units, indicating that not all unusual units necessarily exhibit high excess energies. Based on this energetic argument we argue that unusual units are actually present in LiPS glasses and further studies need to (dis)prove their existence and how they influence the properties of LiPS glasses.

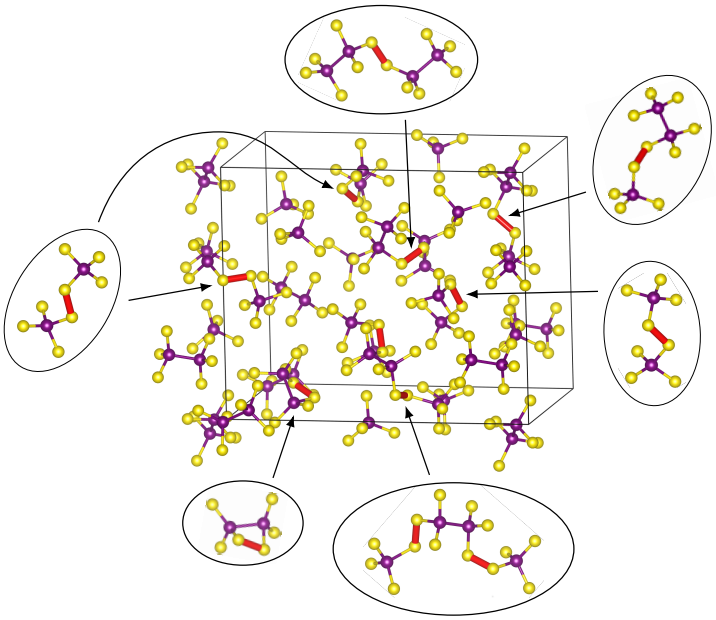

FIGURE 4.12: Structural model of g-$Li_4P_2S_7$-mod$_3$ that only contains 16 PS_4^{3-} and 8 $P_2S_6^{4-}$ structural units. The structure, however, misses 16 Li^+ to compensate the formal charges of the structural units. This Li deficiency leads to the formation of 8 S–S bonds (shown in red), mainly established as cross-linking bonds.

4.3.7 Formation of S–S Bonds

The melt-quenched $Li_4P_2S_7$ glasses, mentioned in the previous section, have been used to generate a set of modified glasses with improved relative stabilities (see g-$Li_4P_2S_7$-mod$_1$, -mod$_2$ and -mod$_3$ in Table 4.1 (d)). To this end, we manually rearranged atoms in such a way that the local structure corresponds to the usual PS_4^{3-}, $P_2S_7^{4-}$ and $P_2S_6^{4-}$ units. Because the composition was not changed, however, the existence of PS_4^{3-} and $P_2S_6^{4-}$ units demands for a charge compensation mechanism: We found that this is achieved by the formation of cross-linking S–S bonds between the structural units.

One example has already been shown in Figure 4.11 (c), where the rightmost structural unit can be understood as a $P_2S_7^{4-}$ units connected to a PS_4^{3-} unit via a S–S bond. Formally, this combined structural unit corresponds to $P_3S_{11}^{5-}$, i.e., two negative charges have been compensated by the S–S bond. Alternatively, the opposite argument can be made: Each cross-linking S–S bond compensates for two missing Li^+ ions.

A more illustrative example is presented in Figure 4.12 for g-$Li_4P_2S_7$-mod$_3$. Due to its 16 PS_4^{3-} and 8 $P_2S_6^{4-}$ structural units, it would require 80 Li^+ ions to achieve charge neutrality. Because the structure only contains 64 Li^+ ions, however, the mismatch of 16 charges is compensated by the formation of 8 S–S

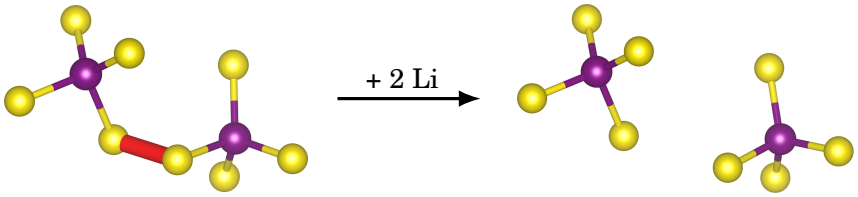

FIGURE 4.13: Upon addition of Li to the structures containing S–S bonds, the dissociation of the S–S bonds was observed during static optimizations. Therefore, their formation and dissociation might be a reversible process triggered by the local Li content.

bonds. These are formed mostly as cross-linking bonds between two structural units. Only in one case the formation of a S–S bond within a P_2S_6 unit was noticed (see bottom left of Figure 4.12).

The three glasses g-$Li_4P_2S_7$-mod_1, -mod_2 and -mod_3 containing cross-linking bonds S–S have been further modified in the course of this work: To counter the Li deficiency we have added two Li to the structures for each occurring S–S bond and optimized their geometry in static calculations. The predominant observation was that the S–S bonds dissociate during the optimization as shown in a schematic illustration in Figure 4.13.

These observations indicate that S–S bonds are considerably weaker than the remaining P–S and P–P bonds and we assume that the formation and dissociation of S–S bonds is a reversible process, presumably triggered by the local Li content. We further propose that the cross-linking between structural units via S–S is not limited to LiPS glasses, but might occur in crystalline LiPS phases as well as in other types of sulfide SEs too. It could therefore be a relevant process especially in the vicinity of the electrodes, where SCLs and a variation of Li content are expected.[176] Other regions of interest could also be GBs or phase boundaries between amorphous and crystalline parts within LiPS glass-ceramics and further efforts are needed to elucidate the relevance of cross-linking S–S bonds.

4.3.8 Electronic Structure

A suitable SE must not only possess good ionic conductivity, which is the topic of Section 4.4, but also requires a negligible electronic conductivity. In this regard, the electronic structure can be analyzed to verify that the material of interest is not an electronic conductor. Therefore, we computed the eDOS for all considered LiPS compounds.

Figure 4.14 shows the eDOS of the crystalline phases, their glassy counterparts and a selection of additional glasses. Note that all these structures only comprise the usual structural units. Generally, the eDOS of the shown crys-

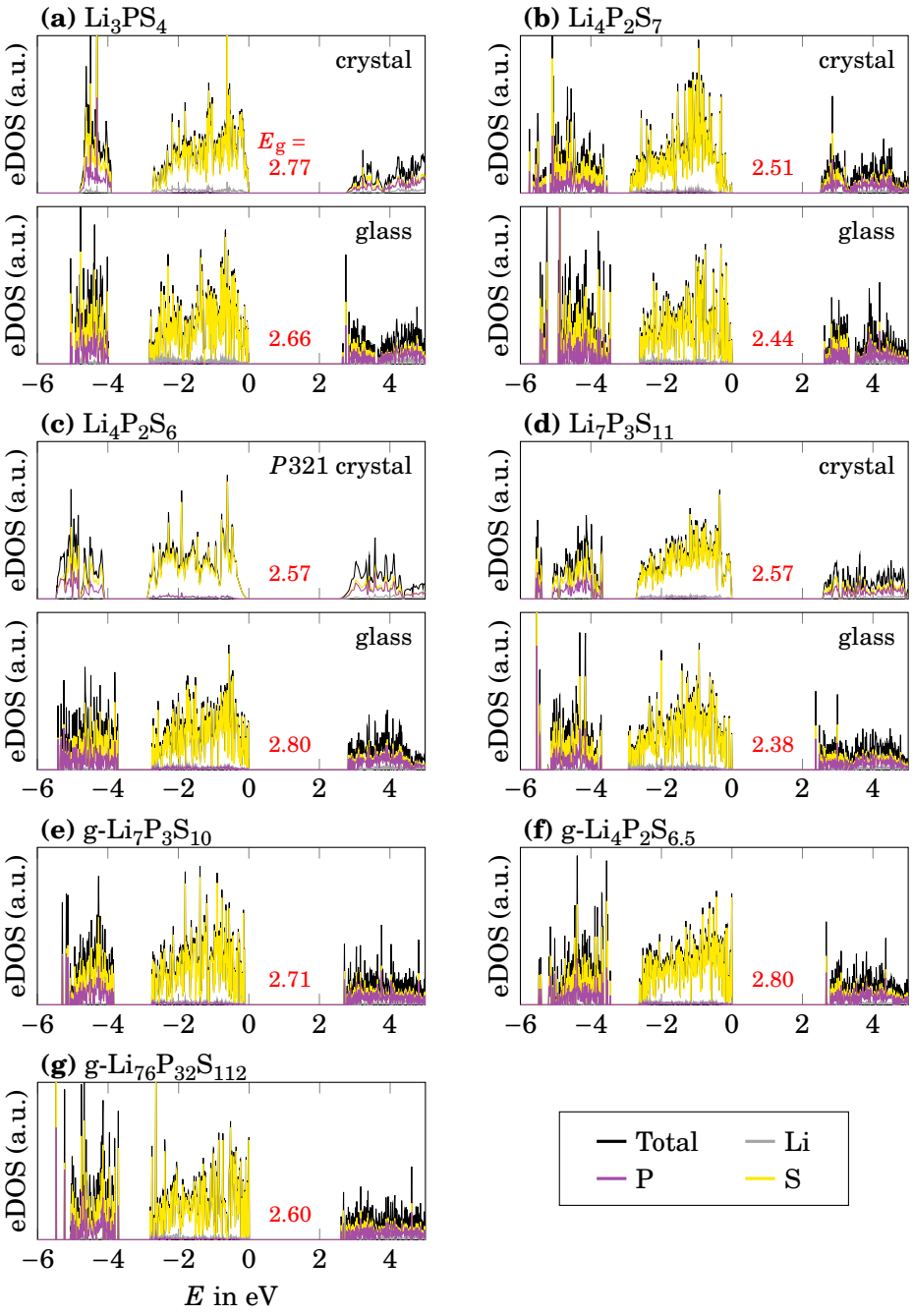

FIGURE 4.14: Computed eDOS of crystalline LiPS phases and their glassy counterparts in (a) to (d) and of additional glasses in (e) to (g). All structures only contain the usual structural units PS_4^{3-}, $P_2S_7^{4-}$ and $P_2S_6^{4-}$. The band gap E_g is indicated in red and the computed E_{VBM} was set to $E = 0$ eV.

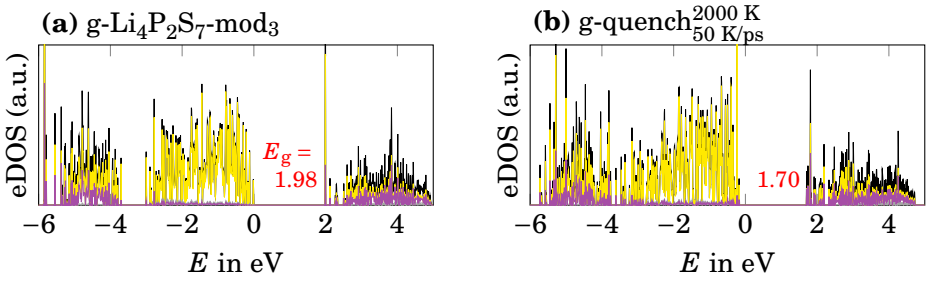

FIGURE 4.15: Computed eDOS for (a) g-$Li_4P_2S_7$-mod_3, the glass with the highest amount of cross-linking S–S, and (b) g-$quench^{2000\,K}_{50\,K/ps}$, one of the glasses obtained via the brute-force melt-quenching scheme comprising a large number of unusual structural units. The same color coding as in Figure 4.14 applies.

talline and glassy phases are very similar and exhibit band gaps of 2.4-2.8 eV. In all cases, the states directly below E_{VBM} (i.e., $E = 0$ eV) to approximately −3 eV are only due to the lone electron pairs of S^{2-} ions. A gap of approximately 1 eV separates them from hybridized contributions of S and P ions between −4 and −5.5 eV that result from P–S bonds within the various structural units. This fits to previous reports for various sulfide SEs that have been treated with similar calculations.[134,150,174,186,318]

Our computed band gaps are certainly underestimated, which is a typical shortcoming of the applied exchange-correlation functional as explained in Section 3.2.1. For c-$Li_7P_3S_{11}$ this was already shown by Chu *et al.*[104] and Xiong *et al.*[407], who obtained values of 2.6 and 2.1 eV, respectively, when using the same PBE exchange-correlation functional as we did. This compares well to our obtained value of 2.57 eV. The two research groups also recalculated the band gap with a hybrid exchange-correlation functional, which is known to describe the electronic properties of materials much more accurately than PBE, and obtained 3.9 and 3.5 eV, respectively Based on these results we expect that also all our band gaps are approximately 50% higher in reality. This substantiates that our generated glasses are indeed electronic insulators, whose ionic transport properties can be analyzed.

Before we do so, however, our previous structural analysis poses another question: How do the observed cross-linking S–S bonds or the various unusual units influence the electronic properties? To answer this question, Figure 4.15 shows the eDOS of (a) g-$Li_4P_2S_7$-mod_3 (containing a comparably large number of S–S bonds) and (b) of g-$quench^{2000\,K}_{50\,K/ps}$ (a glass obtained via the brute-force melt-quenching approach that contains several unusual units). Qualitatively, the eDOS plots are similar as those shown above, but smaller band gaps less than 2 eV are observed.

Particularly, a series of LiPS glasses (g-$Li_4P_2S_7$-mod_1, -mod_2 and -mod_3) indicate that the band gap reduction is related to the number of S–S bonds: the

mentioned glasses contain 3, 6 and 8 S−S bonds and exhibit band gaps of 2.42, 2.25 and 1.98 eV, respectively. Following this line of thought, LiPS compounds could exhibit an increased electronic conductivity if a high concentration of S−S bonds and/or unusual structural units is available. As mentioned in the previous section, S−S bonds might be relevant near the electrodes, at phase boundaries or in the vicinity of GBs. A high concentration of S−S bonds could then lead to a considerable reduction of the band gap and might increase the electronic conductivity on a local scale. In the worst case, the material might locally become a mixed electronic-ionic conductor, accelerating interfacial reactions.[1]

In summary, the bulk phases of all investigated LiPS materials exhibit sufficiently large band gaps to be classified as electronic insulators. This justifies further investigations of their ionic transport properties to better understand LiPS glass-ceramics.

4.4 Transport Properties

Diffusion coefficients were mostly extracted by analyzing MSD plots obtained from AIMD simulations and we will use Section 4.4.1 to comment on the common pitfalls of these analyses. The transport properties of properly analyzed cases are presented in Section 4.4.2. The Li^+ diffusion mechanisms for the LiPS glasses are then presented in Section 4.4.3 and found to be highly concerted. This indicates that NEB approaches cannot be used to reliably represent Li^+ diffusion in the glasses. Still, we tested what insights NEB calculations can deliver for one test case in Section 4.4.4. Instead of treating one of our generated glasses, however, we used c-$Li_4P_2S_7$, which exhibits similar transport properties but decreases the structural complexity of the problem.

4.4.1 Analysis of MSD Plots – Common Pitfalls

The extraction of diffusion coefficients from the MSD evolution is not straightforward in all cases and several pitfalls need to be avoided. Let us start with an obvious case: Figure 4.16 (a) shows the Li^+ MSD evolution of c-$Li_4P_2S_6$ ($P\bar{3}1m$) at 900 K. In the very beginning the MSD abruptly jumps to approximately 0.2 $Å^2$ and, besides some statistical noise due to thermal vibrations, remains constant for the rest of the simulation. Obviously, this indicates that no long-range diffusion occurs.

Technically, however, it is still possible to linearly interpolate the data and the slope of the interpolation may be used to calculate artificial diffusion coefficients. If the interpolation is done without an intercept, the slope will be positive but crucially depends on the covered simulation time. This is shown for various fits according to f(x), where the number in the subscript indicates the included data range, e.g., f_{40} was fitted up to 40 ps. If an intercept is taken into account, see g(x), the interpolation is more representative, but the comparably large statistical noise even leads to a negative slope. A graphical inspection

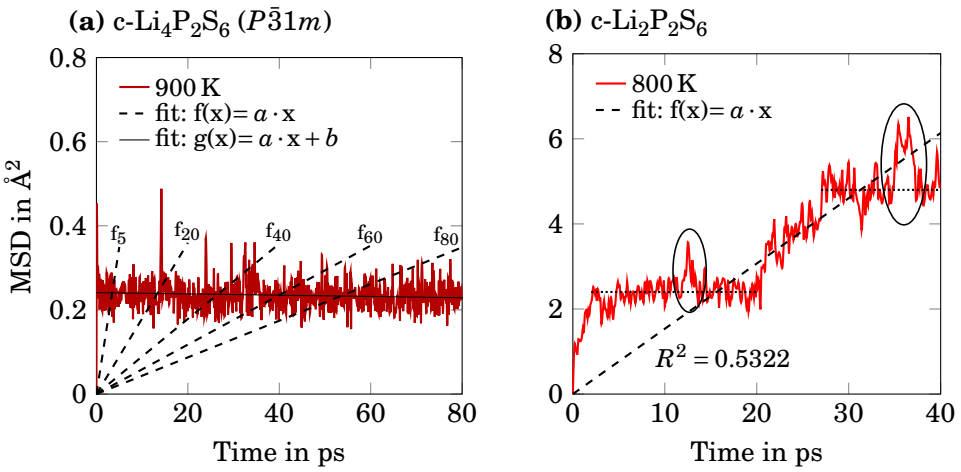

FIGURE 4.16: Two examples of MSD plots that cannot be used to extract proper Li^+ coefficients. (a) Example of c-$Li_4P_2S_6$ ($P\bar{3}1m$) at 900 K with several unsuitable linear interpolations. The corresponding coefficients of determination R^2 are listed in Table 4.4. (b) Simulation of c-$Li_2P_2S_6$ at 800 K. Dashed lines have been added as a guide to the eye and indicate regions with approximately constant MSD. Furthermore, two peaks resulting from unsuccessful Li^+ jumps are marked.

TABLE 4.4: Low or even negative coefficients of determination R^2 indicating that the fits of Figure 4.16 (a) cannot be used to extract Li^+ diffusion coefficients. Good fits should yield $0.9 < R^2 \leq 1.0$.

	$f_5(x)$	$f_{20}(x)$	$f_{40}(x)$	$f_{60}(x)$	$f_{80}(x)$	$g(x)$
R^2	-8.0290	-9.2961	-9.7655	-11.1773	-11.9948	0.0131

of the MSD would not have been necessary in the present case because the obtained coefficients of determination R^2 (see Table 4.4) clearly indicate that all fits fail to appropriately represent the data and are not suitable for an extraction of diffusion coefficients.

A less obvious example that is more appropriate but should also not be used to extract Li^+ diffusion coefficients is shown in Figure 4.16 (b) for c-$Li_2P_2S_6$ at 800 K. The MSD quickly rises in the beginning but settles around 2 $Å^2$ for approximately 20 ps as indicated by a dotted line. The small peak at 12.7 ps marks an unsuccessful attempt of Li^+ ions to jump to a different site. The MSD then rises between 20 and 27 ps but again settles just below 5 $Å^2$, only interrupted by a small peak at 36 ps. The linear interpolation (dashed line) is much more representative of the data than in the first example but still shows a poor R^2. Another reason for not trusting extracted Li^+ diffusion coefficients in this case is the fact that the MSD only reaches a value of approximately 5 $Å^2$ at the end of the simulation. This means that every Li^+ has only moved

$\sqrt{5\ \text{Å}^2} = 2.2$ Å on average, which is less than the closest Li–Li nearest neighbor distance of approximately 3 Å (see Figure 4.8 (f)). In other words, despite the elevated temperature only a few number of Li^+ jumps are featured in the simulations, which fits to the low reported diffusion coefficient of c-$Li_2P_2S_6$.[123] Better statistics (i.e., longer simulation times and/or larger systems) are needed to obtain reliable Li^+ diffusion coefficients.

4.4.2 Li^+ Transport From AIMD Simulations

A collection of MSD plots that are appropriate to extract reliable Li^+ diffusion coefficients are shown in Figure 4.17. Parts (a) to (f) compare the crystalline LiPS phases on the left to their glassy counterpart on the right and the parts (g) and (h) show two further glassy phases. To improve the statistics at low temperatures, the data for temperatures of 500 K and below are obtained by averaging the MSD of three individual simulations. Still, the results of the lower temperatures need to be taken with care. These mostly involve the simulations at 400 and partly also those at 450 K, where only a MSD of 10 Å^2 or below was reached. Longer simulations would be needed to clearly confirm these results. Nevertheless, we added the data to illustrate that more extended AIMD simulations could be used for selected cases to analyze the transport properties of superionic SEs even close to practical operating temperatures.

Li^+ diffusion coefficients D^* are obtained from linear regressions to the MSD curves. To allow for equilibration, the first 5 ps are not included in the fits. The extracted D^* are presented in an Arrhenius plot in Figure 4.18, which was used to extract migration barriers E_m and pre-exponential coefficients D_0. These transport parameters have further been used to extrapolate D^* to 300 K and to calculate the corresponding Li^+ conductivity $\sigma_{300\,\text{K}}$ as described in Section 3.6.3. A compilation of the essential properties of all simulated phases can be found in Table 4.1 .

Li_3PS_4

The comparison for Li_3PS_4 in Figure 4.17 (a) and (b) reveals that the transport properties of the crystalline β-phase cannot be assessed with AIMD simulations for temperatures of 500 K and lower because the MSD hardly rises within the accomplished simulation times. On the contrary, the MSD reaches significantly higher values in the glass even for 400 K. Likewise, also at the higher temperatures the MSD rises faster in the glass and reveals superior Li^+ transport properties, which can also be seen in the Arrhenius plot in Figure 4.18 and extracted transport parameters: Although D_0 is found to be approximately three times larger in the crystalline phase, the reduction of E_m from 354 meV to 257 meV in glass overpowers the transport properties at room temperature. The extrapolated $\sigma_{300\,\text{K}}$ therefore increases from 0.74 to 10.4 mS/cm from the crystalline to the glassy phase, respectively.

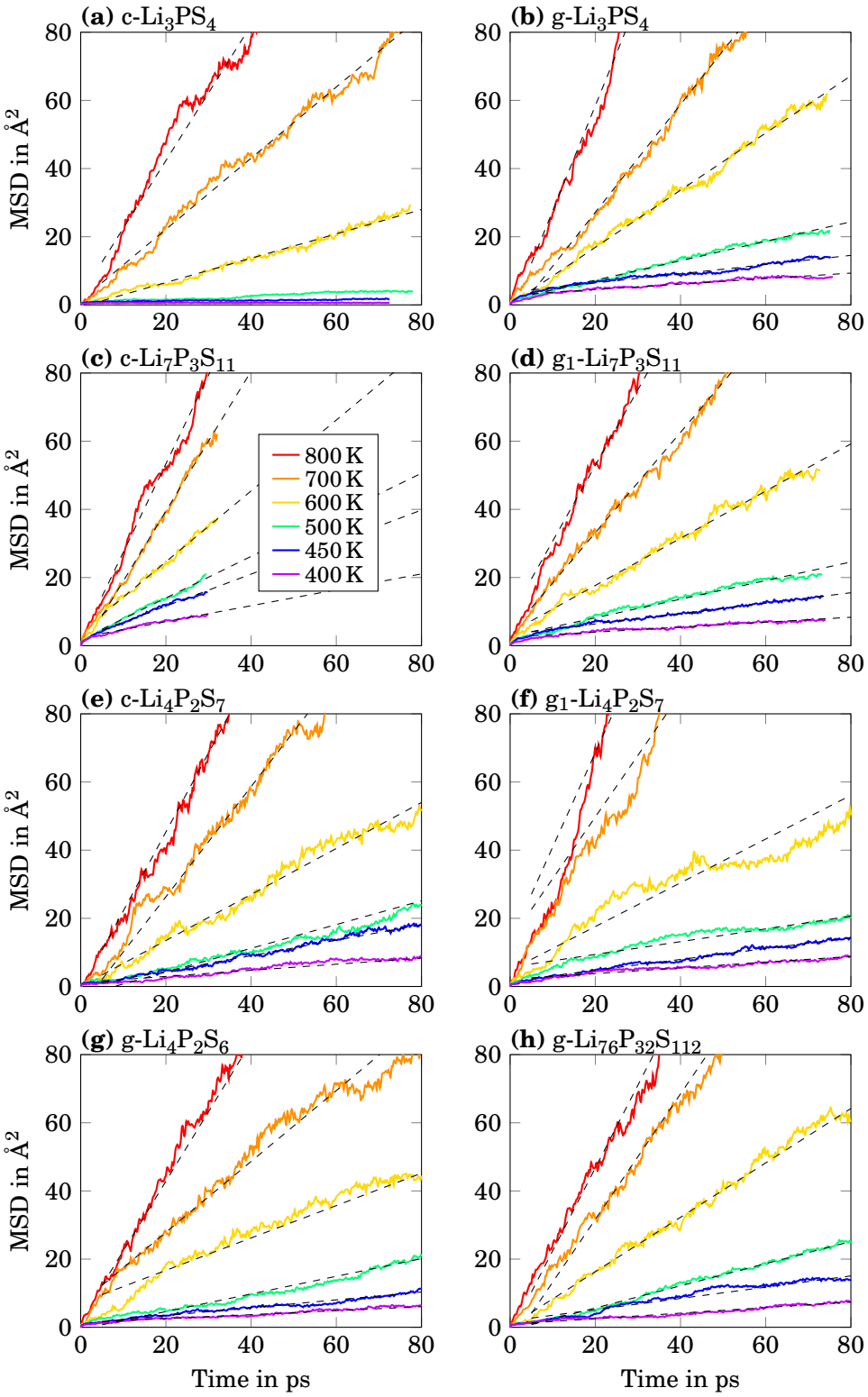

FIGURE 4.17: MSD plots of representative crystalline and glassy LiPS phases. The first 5 ps were excluded from the linear regressions, whose slopes were used to extract Li^+ diffusion coefficients.

Our E_m for the crystalline phase is within the rather broad range of reported barriers,[143,173] but in good agreement to impedance measurements of Stöffler *et al.*,[140] who report 360 meV. For glassy Li_3PS_4, however, such small barriers have never been reported. Instead, barriers typically vary between 330 and 400 meV.[115,132]

Although our computed $\sigma_{300\,K}$ is one to two orders of magnitude significantly higher than any experimental results (see also Section 3.6.4 for a deeper discussion of the origin of related discrepancies), the overall trend is in line with impedance measurements,[132] NMR studies[172] and crystallization experiments[125] that attribute superior transport properties to the amorphous phase of Li_3PS_4. Because the detection of amorphous phases is difficult, we assume that an increased amount of glass might also explain improved ionic conductivity in samples that are claimed to contain nano-porous Li_3PS_4.[139]

$Li_7P_3S_{11}$

In contrast to Li_3PS_4, the MSD plots for $Li_7P_3S_{11}$ in Figure 4.17 (c) and (d) show that the crystalline phase exhibits slightly better transport properties than the glassy phase. Note that shorter simulation times for the crystalline phase were reached because the highly anisotropic unit cell demanded a larger supercell to obtain a uniform structural model. Overall, the size was approximately twice as large than the majority of the remaining models. Consequently, statistics are comparable despite the shorter simulations times because the MSD is averaged over a larger number of Li^+ ions.

Our data shows that c-$Li_7P_3S_{11}$ exhibits the highest Li^+ diffusion coefficients among all LiPS phases treated in this work, fitting to experimental reports.[104,117,137,138] The computed migration barrier of 161 meV for the crystalline phase is in excellent agreement with several experimental reports.[104,117,137] Note, however, that there are considerable discrepancies between experimental studies and also migration barriers of approximately 300 meV have been reported.[160] Again, extrapolated $\sigma_{300\,K}$ seem to be overestimated as our result of 83.6 mS/cm is approximately five times larger than the highest experimental value of 17 mS/cm,[137] but close to the calculated conductivities of 57 and 72 mS/cm obtained via AIMD simulations.[104,107]

The calculated barriers for our glass models g_1- and g_2-$Li_7P_3S_{11}$ are noticeably higher than the crystalline phase and settle around 250 meV. This is considerably lower than experimentally reported barriers, which range between 400 and 450 meV.[115,119,133,160] Extrapolated $\sigma_{300\,K}$ reach approximately 10 mS/cm, which is comparable to g-Li_3PS_4 of the previous subsection, but at least one order of magnitude higher than found experimentally.

In conclusion, the Li^+ transport properties obtained so far do not quantitatively reproduce the experimental findings. More importantly, however, they capture the qualitative trends and we believe the results are helpful to improve the understanding of LiPS phases. Accordingly, the insights suggest that

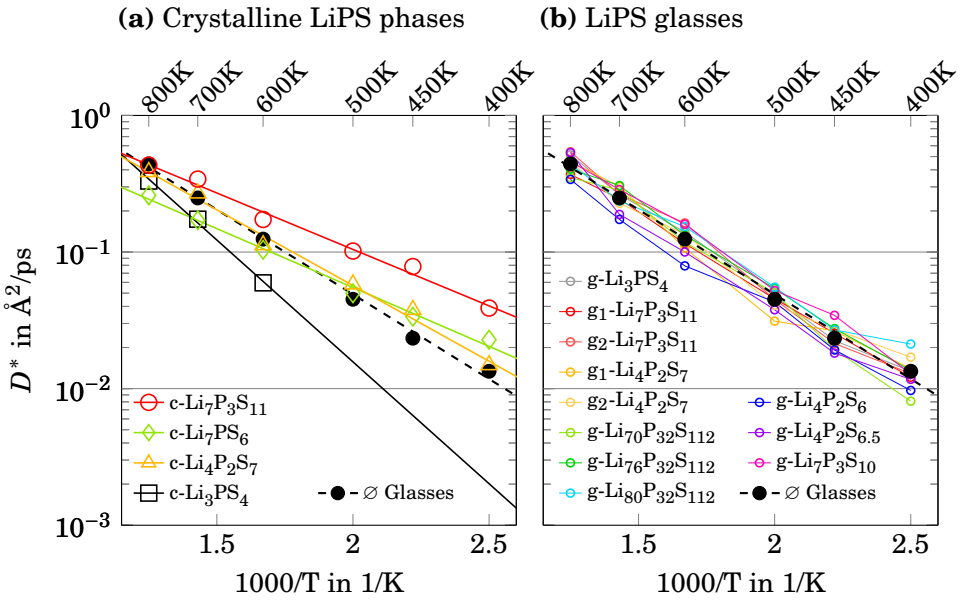

FIGURE 4.18: (a) Arrhenius plot of D^* for various crystalline LiPS phases and their Arrhenius fits. (b) Arrhenius plot for our generated LiPS glasses. Lines that connect data points are a guide to the eye. Full, black circles indicate the average D^* of all glasses with its Arrhenius fit shown as black. The results for the average glass is shown in both diagrams for comparison.

c-$Li_7P_3S_{11}$ is indeed the fastest SE among all LiPS materials. Therefore, the formation of any other phase needs to be avoided for the best Li^+ transport properties to be achieved.

$Li_4P_2S_7$

The MSD plot for c-$Li_4P_2S_7$ in Figure 4.17 (e) is comparable to its glassy counterpart shown in (f) for temperatures of 600 K and below. At 700 and 800 K, however, the glass shows a slightly steeper increase of the MSD. Note that the linear regressions for the 700 and 800 K curves match the data much better than what is implied based on the relatively small section of the shown data.

The obtained migration barriers amount to 220 meV for the crystalline phase and we predict a $\sigma_{300\,\mathrm{K}}$ of 16.7 mS/cm. Because the hypothetical c-$Li_4P_2S_7$ has not yet been synthesized, we cannot compare its properties to any experiments. Interestingly, our glassy structures show similar transport properties to the crystalline phase and barriers of approximately 240 meV and $\sigma_{300\,\mathrm{K}}$ of around 10 mS/cm are found. This again contradicts the experimental findings that report barriers of 440 meV and conductivities that are two orders of magnitude lower for the glass.[115]

Referencing our previous analyses, however, it is not utterly surprising that our crystalline and glassy models for $Li_4P_2S_7$ exhibit similar transport properties: We already saw that the local structure of the crystalline and glassy $Li_4P_2S_7$ resemble each other in the RDFs (see Section 4.3). Therefore, also similar transport properties are expected.

Remaining glasses

The MSD plots in Figure 4.17 (g) and (h) show two further examples of LiPS glasses, g-$Li_4P_2S_6$ and g-$Li_{76}P_{32}S_{112}$. Therefore, a representative selection of glasses with different types and ratios of the PS_4^{3-}, $P_2S_7^{4-}$ and $P_2S_6^{4-}$ structural units is available. In summary, the MSD data already indicates that the Li^+ diffusion is similar in all glasses. This can be seen more clearly in Figure 4.18 (b), where the diffusion coefficients of all glasses are shown. The extracted E_m mostly range between 230 and 260 meV and extrapolated $\sigma_{300\,\mathrm{K}}$ of approximately 10 mS/cm are predicted.

To stress the high degree of similarity, an average tracer diffusion coefficient (thick, black circles) among all glasses and the corresponding regression to the Arrhenius equation (dashed line) have been computed. It can be seen that all glasses are scattered around the average value, which substantiates the fact the Li^+ transport properties are the same in the amorphous LiPS phases and that deviations are likely to be of statistical nature. Why is this the case? In the previous subsection we argued that crystalline $Li_4P_2S_7$ has similar Li^+ transport properties as glassy $Li_4P_2S_7$ because also their local structures (RDFs) are similar. It seems that the same reasoning can be applied to all LiPS glasses.

4.4.3 Li^+ Diffusion Mechanisms in LiPS Glasses

The evolution of the MSD, the extracted D^*, D_0, E_m and the extrapolated $\sigma_{300\,\mathrm{K}}$ of the previous section are helpful quantities to describe the globally averaged Li^+ transport properties. Without any further evaluation, however, these transport parameters typically do not provide insights about the local diffusion mechanisms, which might helpful to improve the material. Therefore, we have analyzed the atomic motion in our generated glasses in more detail and found that the mechanisms of Li^+ diffusion are similar in all glasses. This is not surprising because the transport properties of the previous section as well as the local structures (i.e., the RDFs) in Section 4.3 were found to be comparable as well. We picked g-$Li_{76}P_{32}S_{112}$ as a representative case to illustrate our findings in this section. The presented results have all been obtained from a simulation at 600 K.

Atomic Displacements

Figure 4.19 shows structural models of g-$Li_{76}P_{32}S_{112}$ at several time steps and displacement vectors with respect to the reference structure at $\Delta t = 0$ ps have

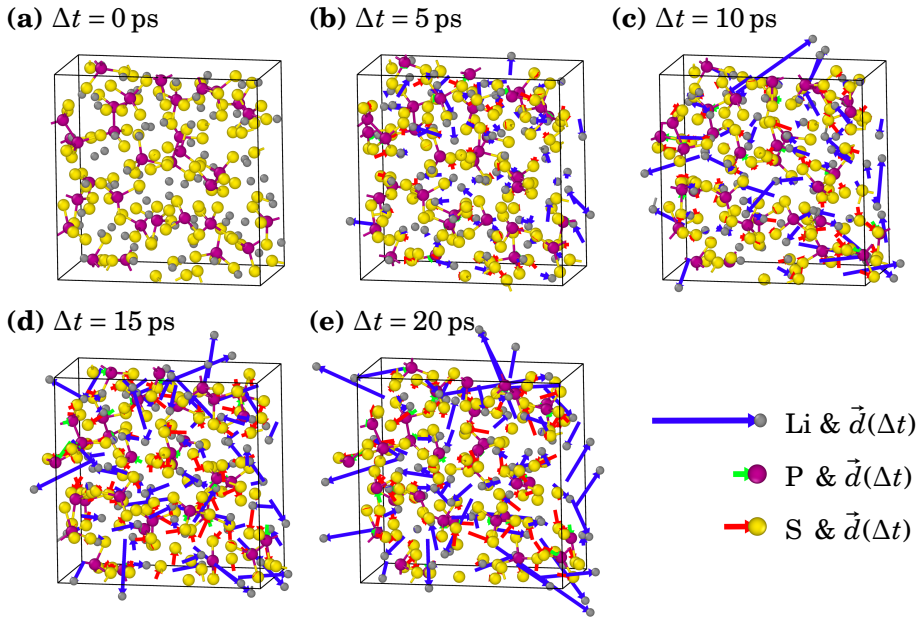

FIGURE 4.19: Snapshots of g-$Li_{76}P_{32}S_{112}$ during a 600 K simulations. The displacement vectors $\vec{d}$ with respect to the structure at $\Delta t = 0$ have been added and reveal that Li^+ is the most mobile species. S^{2-} ions also show noticeable displacements, but these are mostly attributed to local rearrangements of the structural units. Overall, the structural units do not move on a long-range scale as can be seen by the negligible displacements of the P ions.

been added to all particles. Clearly, Li^+ ions are the most mobile species and show the largest displacements after 20 ps, which is the expected result for Li^+ conducting SE. Furthermore, the majority of S^{2-} ions also exhibit noticeable displacements, mostly resulting from local rearrangements (i.e., subtle translations or rotations and tilting) of the structural units. Presumably, such movements are either part of paddlewheel-like mechanisms or of local, thermally activated relaxations.[193] They do not result from any long-range motion of the structural units because P ions exhibit negligible displacements within the covered simulation time.

Inspection of Li^+ Trajectories

In the absence of concentration gradients or any other driving forces, diffusion is a purely stochastic process. It is then expected that the displacement magnitudes of Li^+ ions are not uniform. During the 20 ps illustrated in Figure 4.19, however, several Li^+ ion can be identified that have barely left their initial positions. Hence, the question arises whether this is a purely statistical phenomenon or

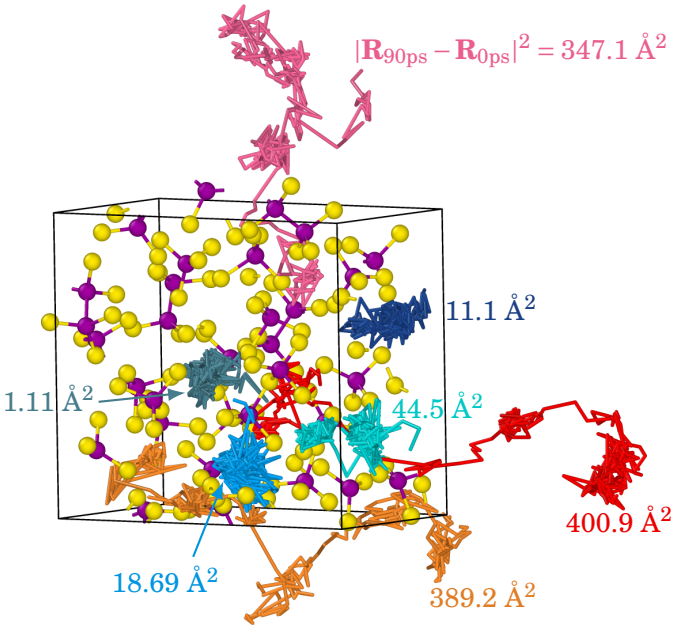

FIGURE 4.20: Selected Li^+ trajectories and their individual squared displacements of the g-$Li_{76}P_{32}S_{112}$ glass after 90 ps at 600 K. Li^+ ions are not shown for clarity.

whether Li^+ ions are trapped in certain local sites and do not contribute to transport.

Because 20 ps is a rather short simulation time, we have extended the analysis to the full course of the simulation (90 ps) and show the trajectories and corresponding squared displacements (i.e., the individual contributions to the MSD) of selected Li^+ ions in Figure 4.20. The Li^+ ion with the largest squared displacement of 400.9 Å^2 is indicated in red and reveals that it has traveled approximately 20 Å during the simulation. Comparably large (squared) displacements are also reached by other Li^+ ions, as for example indicated by the orange and magenta trajectories. The trajectories exhibit several sites, indicated by locally concentrated trajectories clouds, where the Li^+ ion has thermalized for several picoseconds before traveling on. This is reminiscent of a classical jump or hopping mechanism as observed in other ion conducting solids.[298,408,409] Additionally, there are other regions with rather smeared trajectories (e.g., upper part of the magenta trajectory). Hence, parts of the amorphous structure of the LiPS glasses seem to establish a flat and perhaps frustrated energy landscape along the diffusion pathways. Such energy landscapes are known to promote Li^+ diffusion, as has been seen for crystalline compounds with a distorted or irregular structure such as $LiTi_2(PS_4)_3$.[410]

Not all Li^+ ions, however, are similarly mobile. On the contrary, the trajectories illustrated in different shades of blue highlight one intermediately mobile (44.5 Å^2, cyan) and three of the least mobile Li^+ ions with squared displacements below 20 Å^2. One of them has only reached 1.11 Å^2 after 90 ps. Moreover, its trajectories (gray-blue) show that the Li^+ ion has only moved locally and never

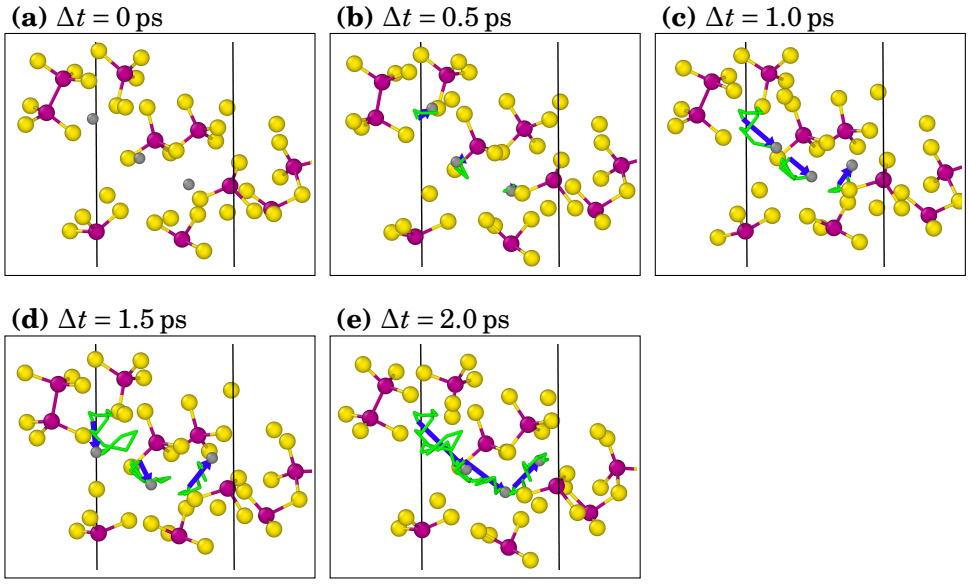

FIGURE 4.21: Example of a concerted jump sequence of three Li^+ ions during a time span of 2 ps in a 600 K simulation of g-$Li_{76}P_{32}S_{112}$. The blue displacement vectors and green trajectory lines of the three Li^+ ions are drawn with respect to $\Delta t = 0$ ps. The majority of the remaining ions are not shown for clarity.

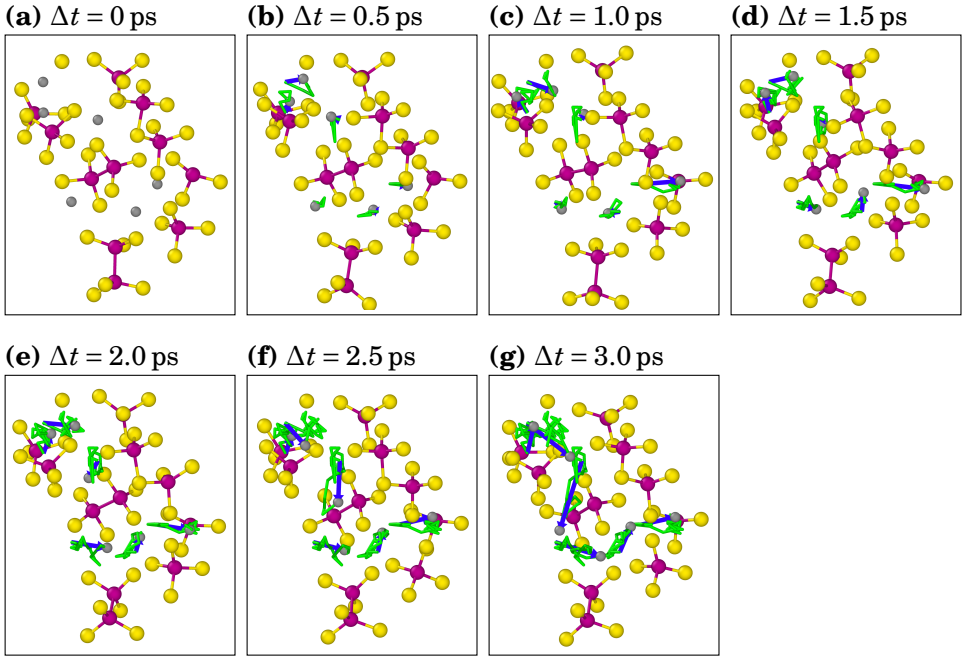

FIGURE 4.22: Example of a highly concerted jump sequence of six Li^+ ions during a time span of 3 ps in a 600 K simulation of g-$Li_{76}P_{32}S_{112}$. The blue displacement vectors and green trajectory lines of the six Li^+ ions are drawn with respect to $\Delta t = 0$ ps. The majority of the remaining ions are not shown for clarity.

left its initial site in the course of the simulation. This indicates that it is either occupying a deep, favorable position or that the barriers for leaving the site are high. The remaining trajectories in shades of blue reveal further Li^+ ions that are mainly trapped in certain sites for a long period of time, indicating that not all Li^+ ions might constantly contribute to long-range transport.

We tried to relate these observations to the local surrounding structure because such knowledge would be helpful to further optimize the amorphous parts of LiPS materials. Unfortunately, we could not derive a clear relation so far and additional studies are needed to tackle this issue.

Observation of Highly Concerted Li^+ Jumps

The diffusion mechanism of many SEs has been reported not to follow a sequence of individual Li^+ jumps. Instead, it is usually described as a sequence of collective or concerted jumps, where several Li^+ ions jointly and simultaneously move into the same direction.[370,411–413] We identified that such jumps substantially contribute to the long-range diffusion processes in LiPS glasses and two examples from the g-$Li_{76}P_{32}S_{112}$ glass are illustrated in the following.

Figure 4.21 shows snapshots of a concerted jump sequence that involves three Li^+ ions and takes place within only 2 ps. An even more illustrative example is shown in Figure 4.22, where six Li^+ ions are found to move in a concerted manner within 3 ps. In light of the comparably high simulation temperature of 600 K, it is likely that such highly concerted and fast jump sequences occur less frequently and on longer time scales at room temperature. Still, we believe that these diffusion mechanisms play a crucial role in the transport properties of LiPS glasses.

4.4.4 NEB-based Migration Barriers in c-$Li_4P_2S_7$

In the past, NEB calculations have often been used to investigate local diffusion events where only the jump of a single mobile species is considered.[150,201,407,414] The knowledge gathered in the previous section, however, questions whether such approaches are able to extract useful information if concerted motion is observed. Such a comparison is rarely done in literature and in the vast majority of cases only one method is applied.

Naturally, it would be most insightful to use NEB simulations to investigate the local transition states in our generated LiPS glasses. Unfortunately, we saw in the previous section that the potential energy landscape of the glasses is rather complicated because it comprises flat parts where Li^+ sites cannot be defined unambiguously. Likewise, also the definition of Li^+ vacancies becomes ill-defined and it was necessary to reduce the structural complexity for further analyses.

This was achieved by relying on c-$Li_4P_2S_7$ as model system for NEB calculations. For simplicity, we did not employ our optimized model as described in

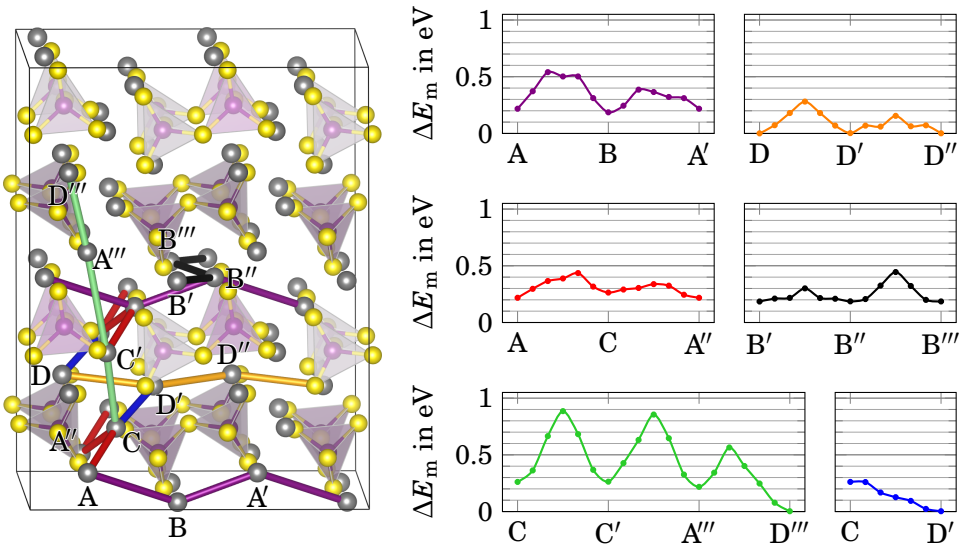

FIGURE 4.23: Li^+ vacancy diffusion in a 2×2×2 supercell of c-$Li_4P_2S_7$. Selected diffusion pathways are indicated with different colors and several pathways are shown multiple times for a more comprehensive representation. Migration barriers E_m have been obtained via NEB calculations. The shown energies of every NEB image i are referenced to the most stable Li^+ vacancy on D positions: $\Delta E_m(i) = E(i) - E(D)$.

Section 4.2.2. Instead, the original structural model as published by Holzwarth *et al.*[150] was used. The decision for c-$Li_4P_2S_7$ is rationalized because this crystalline structure shows a comparable local structure to its glassy counterpart (see RDFs in Section 4.3). Furthermore, c-$Li_4P_2S_7$ also exhibits similar Li^+ transport properties as the averaged glass models. Lastly, it only comprises four symmetrically distinct Li^+ sites, which reduces the number of feasible diffusion paths.

To limit substantial self-interactions from periodic images, we created a 2×2×2 supercell of c-$Li_4P_2S_7$, removed one Li^+ ion to create a Li^+ vacancy and left the system with one negative charge to avoid any oxidation state changes of the remaining ions. Charge compensation was achieved with a homogeneous background charge. The four symmetrically distinct Li^+ sites in the system are referred to as A, B, C, and D and vacancies needed to be created at several symmetrically equivalent sites (such sites are indicated by adding apostrophes, i.e., A′) to construct a representative amount of diffusion paths. In total, 12 NEB calculations were performed and the results are compiled in Figure 4.23.

First, Li^+ vacancies are not equally stable at the four sites and the most stable position was found on site D. The corresponding energy was used as reference energy ($\Delta E_m(D) = 0$) for all migration barriers E_m. Vacancies on the

positions A, B and C are 218, 186 and 264 meV higher in energy, which fits to the results of Holzwarth *et al.*[150]

Our constructed paths enable three-dimensional diffusion, but the barriers for overcoming the transition states vary considerably depending on the path and the jump direction. Several paths show barriers of approximately 200-400 meV and examples are A→B (purple path, 322 meV), D→D′ (orange, 280 meV), A→C (red, 218 meV) or B″ →B‴ (black, 258 meV). Considerably higher barriers of up to 637 meV are observed for the green path along A‴→C′, whereas a C→A″ (red) jump needs to overcome a small barrier of 74 meV and a C→D′ jump (blue) even exhibits a negligibly small barrier. As expected from the $P\bar{1}$ symmetry of the system, paths between symmetrically equivalent sites are symmetric, as can be seen for the orange and black paths.

In summary, NEB calculation with a moving Li^+ vacancy confirm that the energy landscape in c-$Li_4P_2S_7$ is rather complicated despite the fact that c-$Li_4P_2S_7$ is a well defined, crystalline phase. Local migration barriers were found to range from below 100 to more than 600 meV. For comparison, based on the AIMD simulations a global migration barrier of 220 meV was obtained. This example shows that it is non-trivial to connect the results from NEB calculations to the global transport properties of superionic SEs whose ionic transport processes are governed by a variety of pathways and arbitrary diffusion mechanism (e.g., concerted motion of several Li^+ ions). This is also the reason why NEB calculations have not been applied for any other sulfide SE with good Li^+ transport properties in the course of this study.

4.4.5 Li^+ Transport in c-$Li_4P_2S_6$: Revisited Defect Thermodynamics

Let us return to the poor ionic conductor c-$Li_4P_2S_6$, for which we have seen in the MSD plot in Figure 4.16 (a) that the Li^+ kinetics is too slow to be studied with AIMD simulations. In the past we have relied on NEB calculations that assumed intrinsic Li^+ defects (i.e., Frenkel pairs = V'_{Li} + $Li^{\bullet}_i$) as the source of mobile charge carriers.[120] As explained in Section 2.1.2, however, the relatively high Frenkel pair formation energy leads to a low defect concentration and therefore a low ionic conductivity. Other external defect equilibria could offer further charge compensation mechanisms but were not considered so far. Because it would be insightful to see whether they have a profound influence on the defect concentration, we investigate in the following how external, S-related defects interact with the system.

By symmetry, there is only one type of S vacancy, which was investigated with the overall charge states 0, +1 and +2. The singly charged state, however, was found to be irrelevant based on the defect energy diagrams discussed below. In terms of S interstitials we explored several configurations and found the two setups termed $S_{i,a}$ and $S_{i,b}$ to be the most stable. Similarly to the vacancy again only the neutral and doubly charge state −2 were found to be favorable. Their

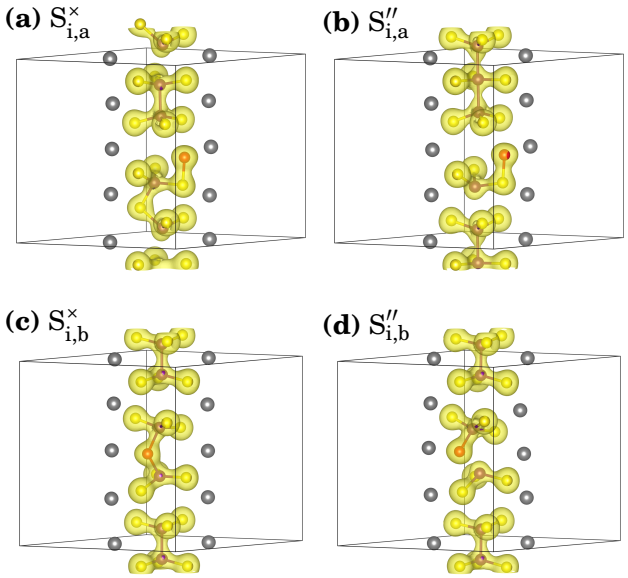

FIGURE 4.24: Relaxed configurations of the sulfur interstitials $S_{i,a}$ and $S_{i,b}$, indicated as red spheres, at different charge states. Charge density isosurfaces have been added to visualize the formation/breaking of bonds depending on the charge state.

relaxed structures are shown in Figure 4.24 together with isosurfaces of the charge density to indicate which bonds form or break depending on the charge state.

For the relaxation of $S_{i,a}$ substantial rearrangements are observed and in the case of the neutral $S^{\times}_{i,a}$ in Figure 4.24 (a) an unusual structural unit is formed and one P–P bond is broken. In the charged state in part (b) of the figure, $S''_{i,a}$ leads to the formation of a larger structural unit comprising a P–P–P bond and a small splintered unit. In the case of the second interstitial, the formation of a regular $P_2S_7^{4-}$ unit is observed in Figure 4.24 (c) for the neutral $S^{\times}_{i,b}$. For the charged interstitial $S''_{i,b}$, however, one of the bridging P–S bonds is broken and leads to the splitting of the $P_2S_7^{4-}$ unit according to,

$$P_2S_7^{4-} + 2e^- \rightarrow PS_4^{3-} + PS_3^{3-} \,. \tag{4.5}$$

The resulting defect formation energy diagram is shown in Figure 4.25. The diagram includes our previous results and we recall that -1 is the most stable charge state Li vacancies across the full band gap ($E_g \approx 2.5$ eV).[120] V'_{Li2} is more stable than V'_{Li1} and shows a formation energy of 2.98 eV at the CBM, which is reduced to 0.50 eV at the VMB. All interstitials prefer the $+1$ state except for Fermi levels just below the CBM and the most stable interstitial is $Li^{\bullet}_{i,3}$ with $E_f = 2.01$ eV at the VMB. It reaches the charge transition level to the neutral defect at a Fermi energy of 2.43 eV and exhibits a formation energy of 0.42 eV.

Except for Fermi levels just above the VBM, the S vacancy is in a neutral charge state with a formation energy of 1.48 eV. In terms of S interstitials, $S^{\times}_{i,a}$ has a formation energy of 2.14 eV until the charge transition level to $S''_{i,a}$ at a Fermi level of 1.18 eV is reached. $S^{\times}_{i,b}$ shows a lower formation energy of 1.38 eV,

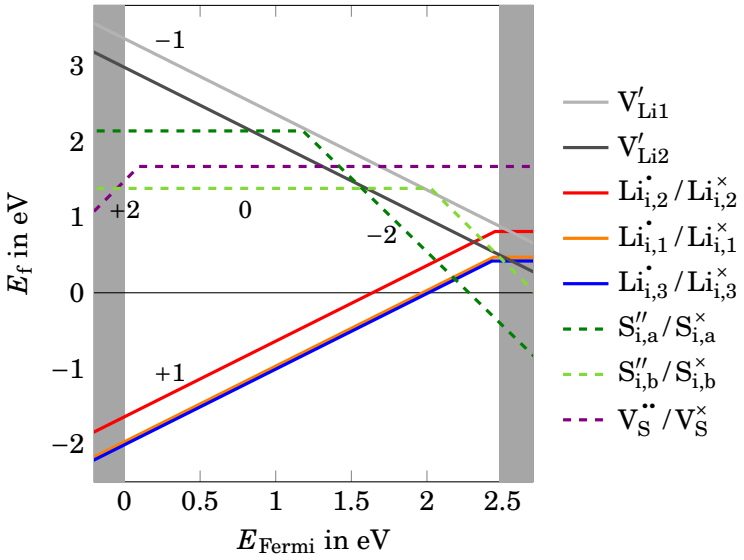

FIGURE 4.25: Defect formation energy diagram of Li and S point defects. The slopes correspond to the charge state q and are indicated in the diagram.

but the charge transition level is reached at a higher Fermi level of 2.02 eV. Both S interstitials then transition to a −2 charge state and $S''_{i,a}$ and $S''_{i,b}$ exhibit formation energies of −0.46 and 0.47 eV at the CBM.

Combining these results, various schemes of how the different defects compensate each other can be constructed. Obviously, the formation energy of $V^{\bullet\bullet}_{S}$ defects is too high to enable a favorable compensation mechanism for Li^+ vacancies. The most evident combination involves two $Li^{\bullet}_{i,3}$ and one $S''_{i,a}$, resulting in a combined formation energy of 0.5 eV, which is half of the Frenkel pair formation energy. Therefore, the concentration of Li^+ interstitials might be increased if the material is in contact to a Li and a S reservoir at the same time. The ionic conductivity, however, will most certainly not increase significantly in this case. First, this is because S interstitials are covalently bound to the P ions and therefore expected to be immobile. Second, the long-range diffusion of Li^+ interstitials involves barriers of approximately 0.5 eV, which is more than twice the Li^+ vacancy migration barrier of 0.2 eV.

In summary, even external defect equilibria that could be enabled by a sulfur reservoir will not substantially change the ionic conductivity of c-$Li_4P_2S_6$. This result is in accordance with literature, which always connects the occurrence of c-$Li_4P_2S_6$ with a worsening of the ionic conductivity, independently of the conditions.[120,154,160,189] Therefore, other strategies need to be applied to mitigate any conductivity decrease due to the presence of c-$Li_4P_2S_6$. Potential schemes could involve the insertion of extrinsic defects to achieve higher conductivities[221] or synthesis procedures to prevent the formation of c-$Li_4P_2S_6$ in the first place.

4.5 Defect Formation Energies: Descriptors for the Interface Stability

Except for model cases, the properties of interfaces are difficult to access, often due to the intricate interplay between interface structure, thermodynamics and kinetics. It is therefore advisable to adopt multiple approaches, so that different aspects of the interface can be investigated depending on the specific problem. We will discuss this first in the context of c-$Li_4P_2S_6$ | Li interfaces and show that they are unstable by employing established methods. More interestingly, however, we will use this showcase to demonstrate the predictive power of defect formation energies as descriptors to assess the interface stability. Further, we present a literature survey that supports the applicability of the approach for several other compounds and their (in)stability against Li metal. Finally, we will also consider the stability of interfaces in LiPS glass-ceramics. In particular, we will discuss c-$Li_4P_2S_6$ | g-$Li_4P_2S_7$ interfaces and see that they are stable.

4.5.1 SE | Li Interfaces

Let us first show that the c-$Li_4P_2S_6$ | Li interface is inherently unstable by relying on (i) a purely thermodynamic approach, (ii) explicit interface calculations and (iii) defect formation energies as valid descriptors for the interface stability.

Thermodynamics

In the present case, a purely thermodynamic consideration can easily be used to show that the c-$Li_4P_2S_6$ | Li is unstable. Based on previous experimental observation it was proved that many LiPS phases are unstable against Li metal and react to Li_2S and Li_3P.[89,90] Hence, the following decomposition reaction can be considered,

$$Li_4P_2S_6 + 14\,Li \longrightarrow 6\,Li_2S + 2\,Li_3P\,, \tag{4.6}$$

which shows a decomposition energy of −19.4 eV (−746 meV/atom). This indicates a highly exothermic reaction and fits to the general observation that sulfide SEs exhibit a poor (electro)chemical stability. The success of the purely thermodynamic consideration has one drawback: the decomposition reaction needs to be known. If this is not the case, all possible decomposition paths have to be considered, but the method might fail if unknown compounds are involved.

Explicit Interface Simulations

One possibility to circumvent the aforementioned issue of unknown reaction phases is the investigation of explicit interface models. This requires the construction of interfaces - a difficult task for low-symmetry crystals with large unit cells due to the size constraints of DFT calculations. Here, we investigate the

(001) and (100) interface of c-$Li_4P_2S_6$ exposed to Li metal. The models were created without cleaving any $P_2S_6^{4-}$ units and slabs of c-$Li_4P_2S_6$ and Li metal have been relaxed in separate calculations beforehand. The corresponding surface energies of the (001) and (100) surfaces of c-$Li_4P_2S_6$ are 14.5 and 20.2 meV/Å^2, respectively. The slabs have then been put into contact and were statically optimized. The initial and relaxed structures are compared in Figure 4.26.

Although we only performed static calculations, substantial atomic rearrangements can be observed at both interfaces indicating that the initial steps of the reaction do not involve significant barriers, similar to what was found for other interface simulations.[186,196] The related reaction energies are approximately −155 meV/Å^2 for both interfaces. This indicates a strong driving force for the reaction and fits to the previous thermodynamic analysis. Changes in the local charge states have been used to monitor local reactions. For comparison, the charge states in the pristine c-$Li_4P_2S_6$ are found to be $Li^{1.00+}$, $P^{1.81+}$ and $S^{1.27-}$ using the Bader charge analysis.[415] In the case of sulfur and phosphorus the charge states deviate substantially from the formal P^{4+} and S^{2-}, which is attributed to covalent character of P−S bonds.

For the (001) interface in Figure 4.26 (a) the beginning of interdiffusion of Li species between Li metal and c-$Li_4P_2S_6$ is observed. Moreover, the $P_2S_6^{4-}$ units that are in contact to Li metal partly dissociate and the released S^{2-} ions are

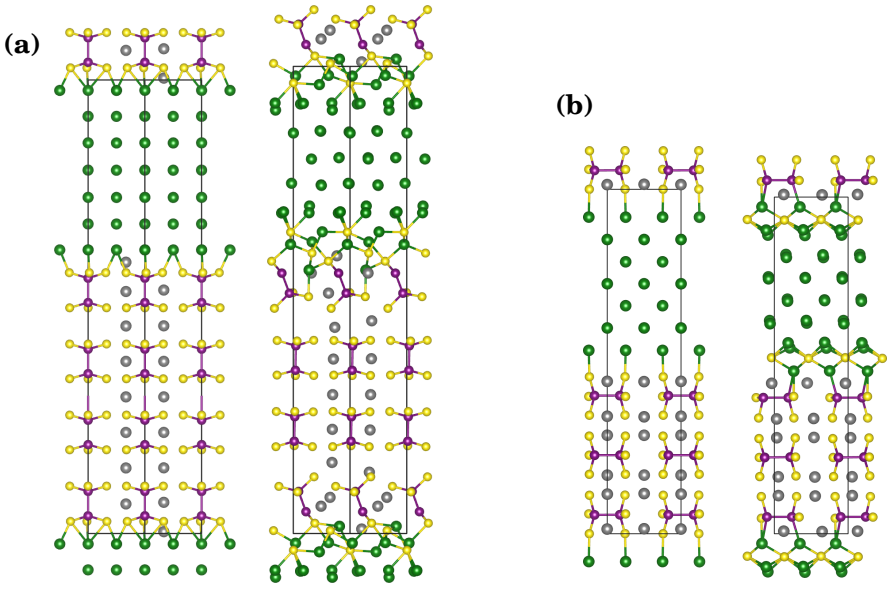

FIGURE 4.26: Initial and relaxed structures of the investigated c-$Li_4P_2S_6$ | Li interface models with (a) the (001) plane and (b) the (100) plane of c-$Li_4P_2S_6$ exposed to Li metal. The atoms that initially belong the Li metal layer are indicated in green, whereas the Li^+ ions of the c-$Li_4P_2S_6$ are shown in gray.

incorporated into the Li metal slab, which might be considered as the onset for the formation of Li_2S. This can also be monitored based on the bond lengths to the surrounding Li: The average length of 2.50 Å compares well to the one in Li_2S (2.45 Å) and is significantly lower than the bond lengths in the pristine c-$Li_4P_2S_6$ (2.62-2.66 Å). Likewise, Li−P bond lengths decrease from 3.71-4.14 Å in the bulk to 2.55-3.00 Å at the interface, which is close to the ones observed in Li_3P (2.45-2.53). The onset of the interface reduction can also be detected based on oxidation state changes as $P^{0.5+}$ is found at the reacted interface. Overall, approximately 9 electrons are transfered from Li metal to c-$Li_4P_2S_6$ during the static relaxation.

For the (100) interface in Figure 4.26 (b) a comparable reaction is monitored, but the formation of a more ordered interphase in observed. This is reminiscent of what was found for LiPON: Depending on the orientation of the SE an ordered or more disordered interface is formed.[196] We note, however, that the interface dimensions of the c-$Li_4P_2S_6$ | Li interfaces are relatively small, so that every formed interphase appears to be ordered due to its periodic images. Still, the interphase formed at the (100) interface resembles Li_2S in the way S^{2-} is coordinated with Li^+. This might be of relevance for the further stability of the interface because Li_2S has been proposed as a metastable buffer layer in sulfide SEs.[174] The changes in bond lengths, charge states and transfered electrons are comparable to the (001) interface.

In summary, these results are in good agreement with previous interface calculations between sulfide SEs and Li metal,[186,318] and confirm that the c-$Li_4P_2S_6$ | Li interface is unstable. Presumably, an ongoing interface reaction is observed if the relaxed structural models are subjected to finite temperatures in AIMD simulations, similarly to our results shown for Li_7SiPS_8 | Li interfaces in Section 6.4. Nevertheless, the generation of interface models is quite involved and can therefore only be applied to selected cases.

Defect Formation Energies as Descriptors

As we have explained in Section 3.5.2, point defects may be used as an alternative approach to evaluate the stability of interfaces. Let us recall the defect formation energy diagram shown in Figure 4.25, which reveals that $Li_i^\bullet$ exhibit negative formation energies over a wide range of Fermi levels. Starting with a formation energy of approximately −2 eV at the VMB, the formation energy is −0.75 eV in the middle of the band gap and reaches 0 eV at $E_{\mathrm{Fermi}} = 2$ eV close to the CBM. This means that there is a driving force for the incorporation of $Li_i^\bullet$ into c-$Li_4P_2S_6$ for given values of E_{Fermi}. However, $Li_i^\bullet$ will not form intrinsically because a compensating V'_{Li} is too expensive in the pristine material.

The situation can change if the material is connected to an external Li reservoir. In this regard, it is important how the defect formation energy is calculated, i.e., which reservoir for Li is chosen. With Li metal as the Li reservoir, we can use resulting defect formation energies to directly probe the stability of the

c-$Li_4P_2S_6$ | Li interface. The mostly negative $E_f(Li_i^{\bullet})$ represents a strong indicator that c-$Li_4P_2S_6$ is unstable against Li metal. Naturally, a single interface like the c-$Li_4P_2S_6$ | Li interface does not suffice to confirm the applicability of defect formation energies as descriptors for the interface stability. Therefore, let us review existing literature to see if previously published results are in line with our approach.

The first case resembles our analysis of c-$Li_4P_2S_6$ and concerns c-$Li_7P_3S_{11}$, which is also found to be unstable against Li metal in experiments.[89] This is in line with results from Xiong *et al.*,[407] who report negative formation energies for $Li_i^{\bullet}$ over the whole band gap. The instability is even more obvious because also neutral Li interstitials show negative formation energies. Similar results are reported by Chang *et al.*,[107] although they did not use the same Li reservoir. Still, at chemical potentials that correspond result in a phase equilibrium of $Li_7P_3S_{11}$ with Li_3P and Li_2S, a negative $E_f(Li_i^{\bullet})$ up to a Fermi level of approximately 1.4 eV has been found. In this regard it would be insightful to know the defect thermodynamics of these compounds (i.e., the defect formation energy of V'_{Li}) to further evaluate the stability.

Let us also have a look at LLZO, which is often stated to exhibit high stability against Li metal.[82–84] According to our descriptor approach, $E_f(Li_i^{\bullet})$ should be positive. A thorough computational study, however, shows that $E_f(Li_i^{\bullet})$ is negative for a broad range of the Fermi energies under reducing (i.e., Li-rich) conditions.[416] This apparent contradiction with the known stability of the material was resolved by revealing the presence of a kinetic barrier that hinders the reduction of the material.[85,417] This kinetic barrier seems to be overcome at elevated temperatures.[418]

So far we only identified cases where negative $E_f(Li_i^{\bullet})$ indicate unstable interfaces. Li_2S represents a nice example of the opposite case: The defect thermodynamics shows that all Li defects exhibit positive formation energies,[419] indicating that there are no driving forces for a reaction with Li metal. This is reasonable because the S^{2-} ion is already fully reduced and Li_2S is yielded as final product in Li–S sulfur batteries after complete lithiation.[420]

In conclusion, we argue that negative defect formation energies may be used as descriptors for the interfacial (in)stability. The given examples demonstrate this tendency for formation energies of charged interstitials, $Li_i^{\bullet}$, in the context of interfaces between SEs and Li metal. The model, however, lacks the ability to predict which reaction phases form and how the interfaces evolve after a reaction is initiated. Furthermore, it cannot assess the related kinetics and might predict unstable interfaces that, as in the case of LLZO, are metastable due to slow reaction kinetics. Nevertheless, the approach could be applied, possibly supported by other methods and descriptors, to screen for stable material combinations via established high-throughput calculations of defect formation energies.[396,421]

4.5.2 SE | SE Interfaces in LiPS Glass-Ceramics

In the previous sections we only considered E_f as a descriptor for the interface stability between the material of interest and Li metal, which simultaneously constitutes the Li reservoir. The approach, however, can be extended to analyze the stability of interfaces between two arbitrary, Li-containing compounds.[309] The basic idea is to use a common chemical reservoir as a mediator for the calculation of defect formation energies for all compounds of interest. Hence, the common reservoir allows us to combine defect formation energies of different materials consistently and use the concept of Frenkel pairs "across material boundaries" as introduced in Section 3.5.2. This is exemplarily shown for c-$Li_4P_2S_6$ | g-$Li_4P_2S_7$ interfaces, which we believe are representative for interfaces in LiPS glass-ceramics.

Explicit Interface Simulations

Let us first check the stability of c-$Li_4P_2S_6$ | g-$Li_4P_2S_7$ interfaces via explicit interface simulations. Again, we have considered interfaces parallel to the (001) and (100) planes of c-$Li_4P_2S_6$. For the amorphous part, g-$Li_4P_2S_7$ glasses were obtained using the melt-quenching approach described in Section 3.3.8. To obtain matching interfaces, the corresponding dimensions of the c-$Li_4P_2S_6$ cell were directly used for the generation of the g-$Li_4P_2S_7$ glasses.

After creating the interfaces, the structures were optimized statically and no interface reactions were observed. To exclude an artificial stability due to the inability to overcome barriers in static calculations, we additionally performed AIMD simulations at elevated temperature. Figure 4.27 shows that the interfaces remain stable after approximately 30 ps at 600 K. For the (100) interface, we observed that the Li^+ ions directly at the interface keep their original crystalline sites, indicating that the interface does not induce Li^+ vacancies in c-$Li_4P_2S_6$. Therefore, the Li^+ transport properties of c-$Li_4P_2S_6$ are expected to remain unchanged.

Interestingly, crystal and glass seem to be separated by a thin layer of Li^+ ions that might be indicative of the formation of a thin space charge layer. Possibly, this layer might exhibit Li^+ transport properties along the interface that differ from the bulk crystal or bulk glass. Unfortunately, a proper investigation is not possible because longer AIMD simulations were not feasible for the present case.

Defect Formation Energies as Descriptors

The c-$Li_4P_2S_6$ | g-$Li_4P_2S_7$ structures exemplify the challenge of generating interface models, and defect formation energies appear as an attractive alternative to assess the interface stability. The approach can be interpreted as computing defect formation energies E_{FP}^{across} of Frenkel pairs "across material boundaries" and has been introduced in Section 3.5.2. In a nutshell: We want to probe whether

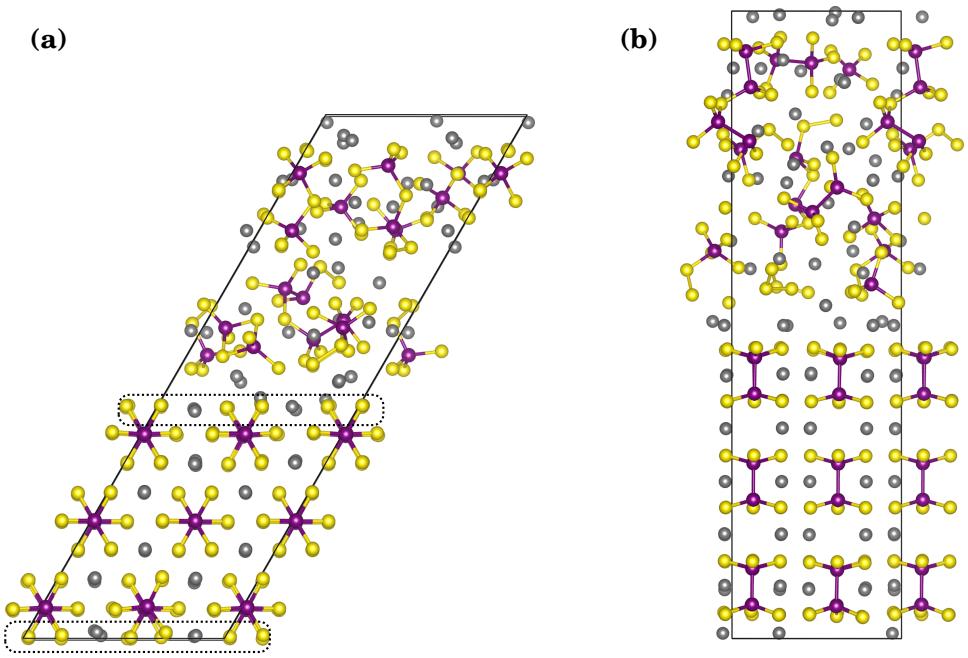

FIGURE 4.27: c-$Li_4P_2S_6$ | g-$Li_4P_2S_7$ interface models using (a) the (100) and (b) the (001) plane of c-$Li_4P_2S_6$ after 30 ps at 600 K. The initial g-$Li_4P_2S_7$ glass models were generated relying on the "brute-force" melt-quenching scheme and contain several unusual units. The dashed boxes in (a) indicate Li^+ at the (100) interface that remained on their initial sites during the AIMD simulation.

the transfer of Li from one material to the other is preferential, which can be achieved by calculating the defect formation energies of a vacancy in material A and an interstitial in material B, as illustrated in Figure 4.28. The combined formation energy $E_{\mathrm{FP}}^{\mathrm{across}}$ can be understood as a measure for the driving force of the transfer of Li from material A to B.

To this end, we took the bulk glass models that were generated for the explicit interfaces and computed the defect formation energies of various Li vacancies and interstitials in their neutral and charged states. Together with the most stable defect formation energies of c-$Li_4P_2S_6$, the most stable defect formation energies of the glasses are shown in Section 4.5.1 (a) and (b), respectively. Note that the CBM of the glasses is not displayed because the CBM positions differ for the (001) and (100) models, most likely due to the large amount of unusual units that lead to comparably low-lying bands. We can neglect this issue for now because we are only interested in the defect formation energies of neutral defects that do not depend on the Fermi level. By following the approaches illustrated in Section 4.5.1 (c) and (d), both combinations of $E_{\mathrm{FP}}^{\mathrm{across}}$ are calculated and

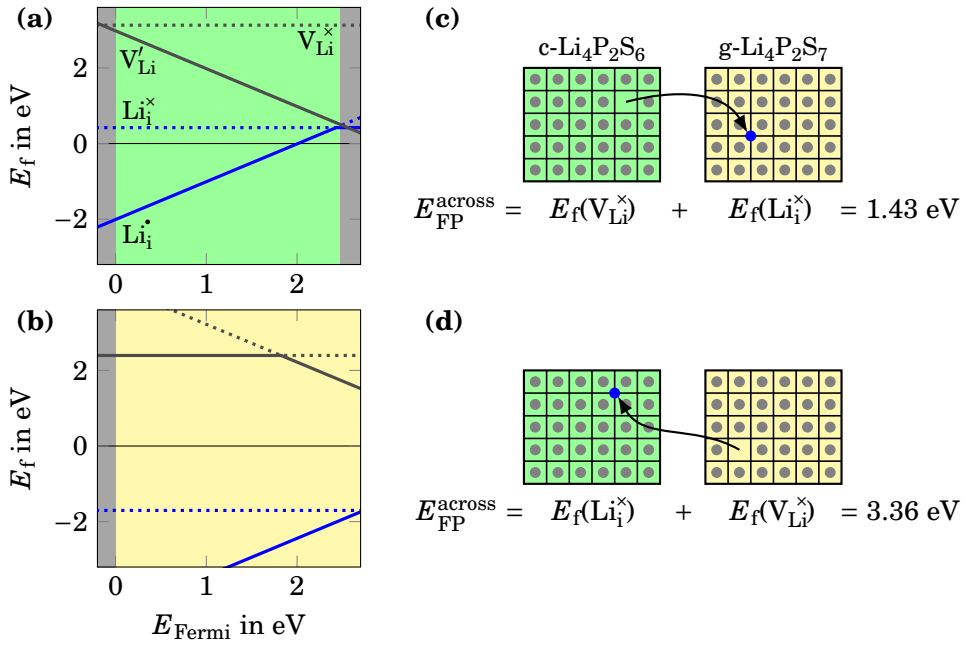

FIGURE 4.28: Defect formation energy diagram of (a) c-$Li_4P_2S_6$ and (b) the $Li_4P_2S_7$ glasses used for the explicit interface simulations. Only the defects with the lowest formation energies are shown. Frenkel pair formation energies "across material boundaries", E^{across}_{FP}, of the two phases are calculated for both directions as shown in (c) and (d). The positive values indicate that there is no driving force for a reaction that involves the transfer of Li from one material to the other.

formation energies of 1.43 and 3.36 eV are obtained. This reveals that, in both directions, the transfer of a neutral Li from one material to the other is not favorable. Hence, the interface is classified as a stable interface, which is in agreement with the explicit interface simulations.

As mentioned above, the glasses that were prepared for the interface simulations contain several unusual units (see Figure 4.27). Furthermore, we know from Section 4.3.6 that such glasses tend to be less stable than glasses containing the usual units. This is also the case here and relative stabilities of 44.4 and 46.2 eV are obtained for the glasses used for the construction of the (100) and (001) interfaces, respectively. Therefore, we have reason to use a more stable glass for the same approach, and we chose g_1-$Li_4P_2S_7$ because it is the most stable glass (relative stability of 18.8 eV) that was generated at the same composition. The calculated defect formation energies are shown in Figure 4.29. The corresponding E^{across}_{FP} of the neutral defects amounts to 1.88 eV for the transfer of one Li from c-$Li_4P_2S_6$ to g_1-$Li_4P_2S_7$ and 3.47 eV for the opposite transfer. These values suggest again a stable interface, as there is no driving force for Li

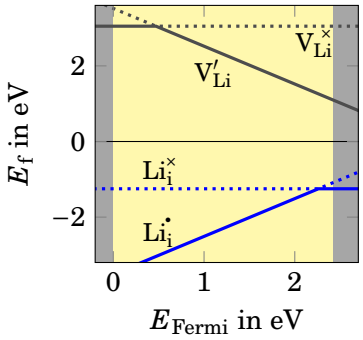

FIGURE 4.29: Defect formation energy diagram of g_1-$Li_4P_2S_7$. Only the defects with the lowest formation energies are shown. For neutral defects, E_{FP}^{across} amounts to 1.88 eV for the transfer of one Li from c-$Li_4P_2S_6$ to g_1-$Li_4P_2S_7$. The opposite transfer yields a value of 3.47 eV.

transfer across the c-$Li_4P_2S_6$ | g-$Li_4P_2S_7$ interface, which is consistent with the variety of reported LiPS glass-ceramics.[8,116–119]

First Attempts: Charged Defects as Descriptors

So far, we have only used neutral defects to compute E_{FP}^{across}. As outlined in Section 3.5.2, the approach can be extended to charged defects if the valence band offset E_{VBM}^{offset} of the interfaced materials is known. Unfortunately, the determination of E_{VBM}^{offset} via low-lying electronic states is not possible because the explicitly treated electrons within the available pseudopotentials of Li, P and S are not able to represent true core states. Instead, we used slab calculations with vacuum regions to align the vacuum levels of the local potentials (see Equation 3.3 for the definition of the local potential). The chosen compounds were again c-$Li_4P_2S_6$ and g_1-$Li_4P_2S_7$.

However, there are several caveats to this approach. First, any net dipole in the cell needs to be avoided because it would cause a slope in the vacuum potential and prohibit a proper alignment. This is a straightforward task for c-$Li_4P_2S_6$ because it shows inversion symmetry and the Li coverage on the (001) surface can be chosen such that a symmetric slab is obtained. The amorphous g_1-$Li_4P_2S_7$, on the other hand, does not exhibit any symmetry by definition. Nevertheless, we prepared several slab structures without cutting any $P_2S_7^{4-}$ units. For one case, the local potential only exhibited a small slope, and by slightly displacing surface-near Li^+ ions away from the surface we could achieve a flat vacuum potential.

The structural models are shown in Figure 4.30 together with the aligned, plane-averaged potentials. The potentials of the bulk systems have been overlaid in black and show good agreement with the slab calculations. The required shifts have been used to align the band edges of the two materials, indicated with dashed lines. Surprisingly, we find that the VBM of c-$Li_4P_2S_6$ is located above the CBM of g_1-$Li_4P_2S_7$, which would result in a E_{VBM}^{offset} larger than 2 eV. According to the HOMO-LUMO method (see Section 3.4.8), this situation implies an unstable interface and electron transfer from the VMB of c-$Li_4P_2S_6$ to the CBM of g_1-

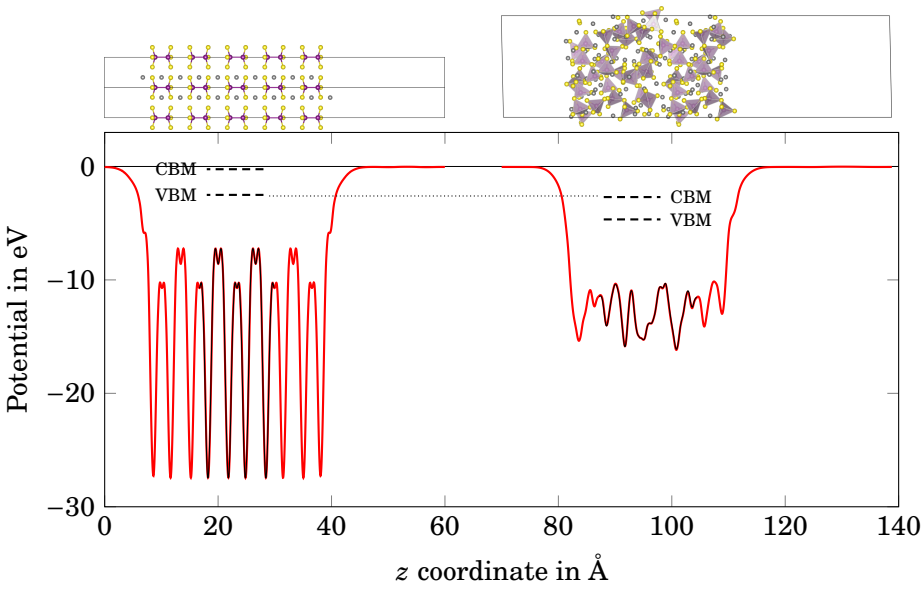

FIGURE 4.30: Electrostatic potentials of the slab models of c-$Li_4P_2S_6$ (left) and g_1-$Li_4P_2S_7$ (right), shown in red, where the vacuum potentials have been aligned to 0 eV. The electrostatic potentials of the bulk systems are overlaid in black and show excellent agreement. Based on the alignment, the absolute positions of E_{VBM} and E_{CBM} can be determined and are indicated. The dotted line serves as visual guide for a comparison of the relative positions of the band edges.

$Li_4P_2S_7$ if we assume that the Fermi level is not below the VMB of c-$Li_4P_2S_6$. This, however, will likely lead to further reactions that were not observed in the explicit interface simulations.

We can attempt to understand this unexpected behavior, following the reasoning of Conesa.[348] First, the underestimation of band gaps within the used PBE exchange-correlation functional might prevent a proper alignment of the band edges. Second, our approach to flatten the vacuum potential of the g_1-$Li_4P_2S_7$ glass by displacing several surface-near Li^+ might induce an artificial dipole close to the surface, which shifts the vacuum level and also compromises the alignment. In summary, extending the approach to use charged defects as a descriptor for the interface stability between two compounds seems to be challenging, at least with such complex structures. We recommend to thoroughly test the applicability of the approach with simpler systems first.

4.6 Summary

Pure LiPS phases are of high technological relevance and different aspects have been investigated to improve the understanding of their structure-properties

relationships. This especially concerns amorphous LiPS glasses that are difficult to analyze experimentally. To this end, melt-quenching schemes were applied to generate various glass models within the compositional triangle Li_3PS_4–$Li_4P_2S_7$–$Li_4P_2S_6$ and their structures were validated on the basis of available experimental data.

A thermodynamic analysis reveals that, among the considered phases, only c-Li_3PS_4 is stable within the Li_2S–P_2S_5 system. All glasses are found to be metastable and the most stable glasses exhibit relative stabilities of 20-40 meV (per atom) with respect to the crystalline boundary phases. The relative stability follows certain trends and more stable glasses tend to contain $P_2S_7^{4-}$ units, whereas less stable glasses comprise $P_2S_6^{4-}$ units. The inclusion of vibrational entropy improves the stability of the glasses by approximately 3-10 meV without changing their metastability.

The structures of the compounds were mostly analyzed my means of RDF plots and certain common features at short ranges were identified. These include a sharp peak around distances of 2 Å due to P–S bonds, a broader peak at 2.5 Å due to Li–S correlations and signals between 3.2 and 3.6 Å due to S–S correlations. Other subtle distinct features in the RDF are attributed to certain intramolecular correlations within the structural units. A disentanglement of the intra- and intermolecular S–S correlations is presented and might be helpful for a future structural characterization of LiPS materials. Interestingly, the RDFs of all glasses are very similar despite the fact that they comprise different ratios of the underlying structural units PS_4^{3-}, $P_2S_6^{4-}$ and $P_2S_6^{4-}$.

These units, however, are not the only ones that might appear: The utilization of a “brute-force” melt-quenching scheme leads to the formation of a variety of “unusual” structural units. Such unusual units have not been considered in the literature so far, but our data suggest that they involve only small excess energies. Therefore, we assume that a small amount of such units is present in LiPS compounds, and further characterization attempts would be insightful to assess their relevance for the properties of the material.

Furthermore, it is found that structural units are able to cross-link via S–S bonds under Li-deficient conditions, which could be an important mechanism near the interface toward the electrodes or at GBs. Calculations of the eDOS indicate that all considered LiPS compounds are electronic insulators, but the mentioned unusual and cross-linked units can lower the band gap. Potentially, this might locally turn the materials into mixed electronic-ionic conductors under certain conditions, which, for instance, could have a negative influence on the interface stability.

An analysis of the ionic transport properties reveals that Li^+ diffusion differs by orders of magnitudes among the crystalline phases. The LiPS glasses, on the other hand, exhibit very similar transport properties despite their different structural units, which is in line with the structural analysis. Their Li^+ diffusion coefficients surpass c-Li_3PS_4, are similar to the hypothetical phase c-$Li_4P_2S_7$, but cannot reach c-$Li_7P_3S_{11}$. A detailed analysis of the transport properties in

the glasses shows that the motion of the structural units is negligible, making Li^+ by far the most mobile charge carrier.

There are, however, certain regions or sites in the material that are able to trap Li^+ ions and prevent their participation in long-range transport. Hence, an optimization strategy to improve the transport properties of LiPS glasses should aim at the elimination of such trapping sites to mobilize all Li^+ ions. Furthermore, AIMD simulations at elevated temperature indicate that correlated jumps involving several Li^+ ions strongly contribute to the long-range diffusion. Such diffusion mechanisms can hardly be assessed by static simulations, as exemplarily shown by applying NEB calculations to c-$Li_4P_2S_7$.

For the poor ionic conductors, such as c-$Li_4P_2S_6$ whose Li^+ transport is mostly governed by the jumps of point defects, however, static calculations proved to be more effective than AIMD simulations. Therefore, we investigated if external defect equilibria can be used to increase the defect concentration, but found that this is not the case even if S-related defect equilibria are considered. Moreover, the defect thermodynamics proved to provide helpful descriptors to estimate the stability of sulfide SEs against Li metal: By using Li metal as the chemical reservoir, we reason that negative formation energies of Li^+ interstitials in SEs can indicate a chemical instability against Li metal. This is substantiated by a literature survey. Moreover, the approach to use Frenkel pairs "across material boundaries" with neutral defect species correctly predicts the stability of LiPS glass-ceramic interfaces as demonstrated for c-$Li_4P_2S_6$ | g-$Li_4P_2S_7$ interfaces. An extension of the approach that makes use of charged defects is introduced, but needs further testing.

5 Influence of Br^-/S^{2-} Site-Exchange on the Properties of Li_6PS_5Br

Parts of this chapter have been published in:

[3] A. Gautam, **M. Sadowski**, N. Prinz, H. Eickhoff, N. Minafra, M. Ghidiu, S. Culver, K. Albe, T. Fässler, M. Zobel, and W. Zeier, *Rapid Crystallization and Kinetic Freezing of Site-Disorder in the Lithium Superionic Argyrodite Li_6PS_5Br*, Chemistry of Materials 31, 24, 10178-10185 (2019).[9]

[4] A. Gautam, **M. Sadowski** [Gautam and **Sadowski** contributed equally], M. Ghidiu, N. Minafra, A. Senyshyn, K. Albe, and W. Zeier, *Engineering the Site-Disorder and Lithium Distribution in the Lithium Superionic Argyrodite Li_6PS_5Br*, Advanced Energy Materials 11, 5, 2003369 (2021).[10]

[5] **M. Sadowski**, and K. Albe, *Influence of Br^-/S^{2-} site-exchange on Li diffusion mechanism in Li_6PS_5Br: a computational study*, Philosophical Transaction of the Royal Society A 379, 20190458 (2021).[422]

Sulfide materials with argyrodite-type structure have shown high promise as SEs due to their favorable transport properties. In most studies, however, high ionic conductivities have only been reached if the composition was modified, e.g., toward $Li_{6-x}PS_{5-x}Br_{1+x}$.[212,216,225,226] Even within this rather simple composition scheme the reasons for the conductivity increase are not fully understood because at least two effects act at the same time: First, halide excess leads to structural site-disorder among the anions. Therefore, S^{2-} ions on sites on $4d$ are replaced with Br^-. Second, structural Li^+ vacancies are introduced.

Fortunately, the Br^-/S^{2-} site-exchange can also be adjusted in stoichiometric Li_6PS_5Br. This was realized by Zeier *et al.*,[9,10] via careful control of the synthesis conditions: Quenching the material from high temperatures kinetically freezes the equilibrium Br^-/S^{2-} site-exchange that is present at high temperatures. This opens the opportunity to investigate the mere effect of Br^-/S^{2-} site-exchange on the properties of Li_6PS_5Br without changing the Li content. The results of our simulations have corroborated these investigations and delivered interesting insights as presented in the following.

5.1 General Approach

Li_6PS_5Br exhibits a rather complex structure as it contains a variety of partially occupied Li^+ sites and the possibility to introduce Br^-/S^{2-} site-exchange, as introduced in Section 2.2.1. Therefore, the computational treatment of this material is not trivial and will be shortly outlined. An illustrated of the investigated properties of Li_6PS_5Br with some aspects of the workflow are shown Figure 5.1.

The experimentally determined structure, a cubic cell containing four formula units of Li_6PS_5Br, was taken as basis. As a first step, an idealized structure was considered. To this end, we simplified the complicated structural model and prepared it with 0% Br^-/S^{2-} site-exchange, i.e., all Br^- were placed on their 4*a* sites and all S^{2-} on their 4*d* sites. Additionally, the Li^+ substructure was simplified by initially placing all Li^+ on the T5a sites. These sites form Li^+ octahedra around the 4*d* sites and can be considered as Li^+ cages. This initial choice is certainly far from a reasonable Li^+ distribution. However, it avoids dealing with the vast combinatorics of distributing Li^+ among its various sites. The atomic coordinates and cell of this idealized model were then statically optimized. During this process, all Li^+ remained on the T5a sites and a lattice constant of 10.2855 Å was obtained. This idealized model was used as basis for the generation of all further structures.

Next, a $\sqrt{2}\times\sqrt{2}\times2$ was constructed and the `supercell` program[392] was used to generate supercells with various degrees of Br^-/S^{2-} site-exchange. The supercells contain 16 formula units of Li_6PS_5Br, which enable the adjustment of the Br^-/S^{2-} site-exhange in steps of 6.25% (= 1/16). Overall, supercells with 0.00% (1), 6.25% (4), 12.5% (6), 25% (6), 37.5% (6), 50% (9), 75% (6) and 100% (1) site-exchange were analyzed. The numbers in brackets indicate how many explicit arrangements of the Br^-/S^{2-} ions were taken into account for the following calculations. All these structures were used as initial models to conduct AIMD simulations in the NVT ensemble at different temperatures. Five snapshots of every AIMD simulation at 500 K were extracted and their atomic coordinates and cell were statically relaxed. This was done to obtain optimized structural models with a reasonable Li^+ distribution to properly analyze the effect of the Br^-/S^{2-} site-exchange on the relative stability and lattice constant of Li_6PS_5Br. Furthermore, entropy contributions were considered to assess the stability at finite temperatures. For the assessment of the vibrational entropy, phonon calculations of smaller structural models were conducted. The approach is explained in more detail in Section 5.2.2.

The AIMD simulations were further used to study the Li^+ transport properties. The MSD was calculated, diffusion coefficients were determined, and other transport properties were extracted. This analysis was repeated for compressed cells to evaluate the effect of mechanical loading on the bulk transport properties. For a deeper understanding of the long-range diffusion mechanism, anion defects (S'_{Br} and $Br^{\bullet}_{S}$) were introduced into the structure and the Li^+ intercage jumps were monitored. The atomic trajectories of the AIMD simulations were

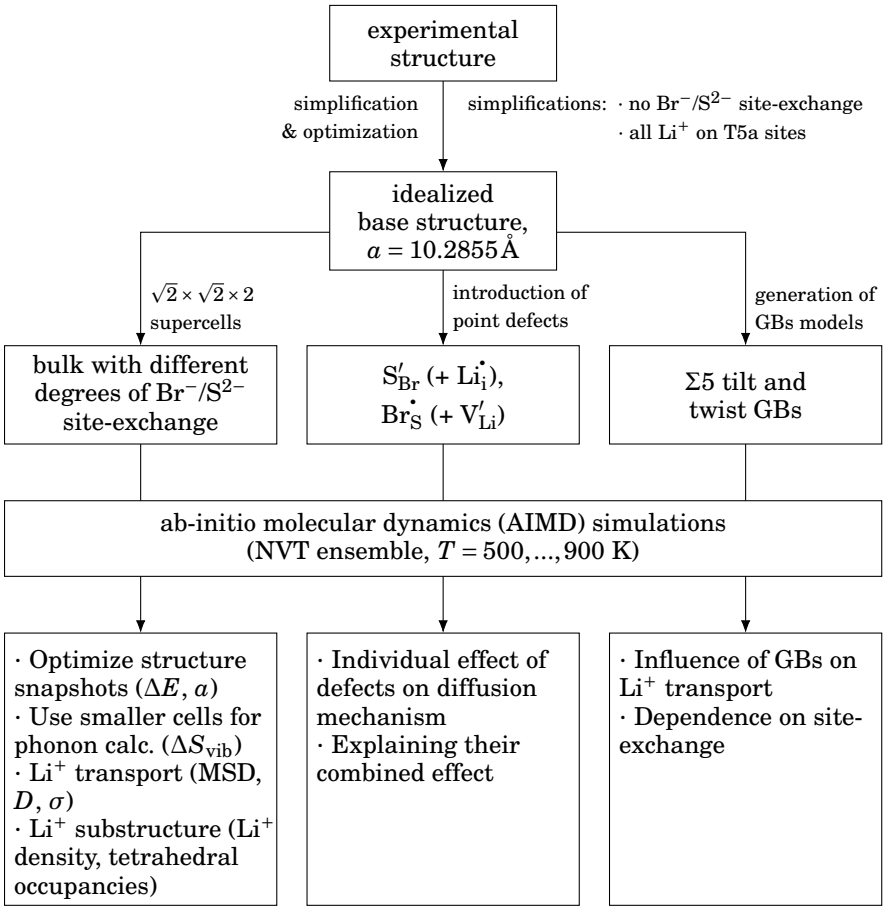

FIGURE 5.1: Summary of the investigated properties of Li_6PS_5Br together with aspects of the workflow.

also used to analyze the Li^+ substructure. Therefore, globally averaged Li^+ densities were calculated and compared to experiment. The Li^+ density was further used to compute occupancies of the tetrahedral Li^+ sites (T1, T2, T3, T4, T5). Finally, symmetric tilt and twist GBs models with different degrees of site-exchange were constructed and their influence on the Li^+ transport was investigated.

5.2 Stability and Structure

5.2.1 Relative Stability and Lattice Constant at 0 K

After optimizing snapshot structures extracted from the AIMD simulations, relative stabilities ΔE and lattice constants a at realistic Li^+ distributions have been determined. They are presented in Figure 5.2 and show that the most

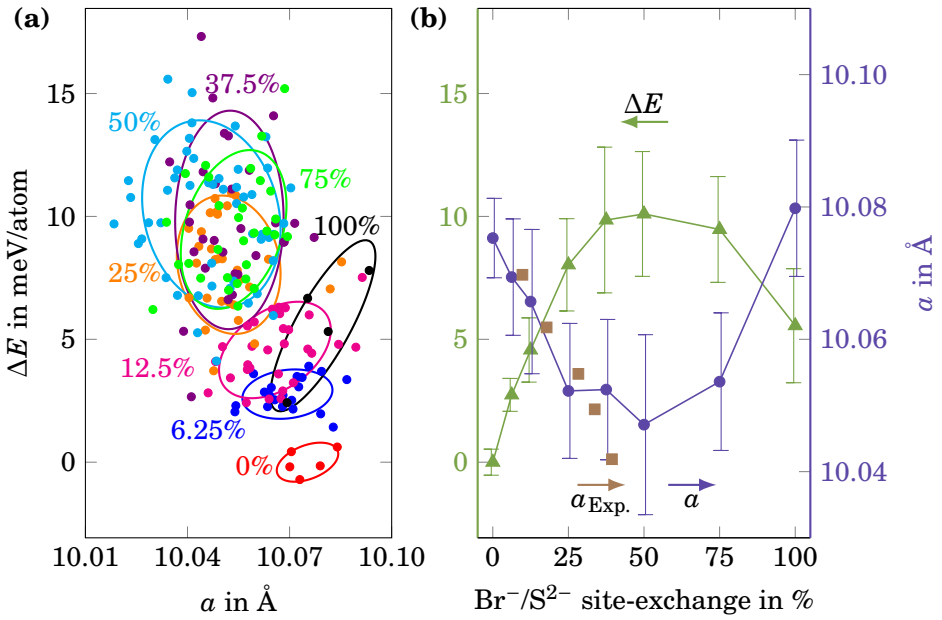

FIGURE 5.2: (a) Correlation between calculated relative stability ΔE and lattice constant a of optimized snapshots structures extracted from AIMD simulations. Assuming a normal distribution of the data points, the ellipses show a confidence interval of 1.5σ and are meant as a guide to the eye. Where possible, the color coding of the different degrees of Br^-/S^{2-} site-exchanges is retained in the remaining pictures. (b) Average values of ΔE and a as a function of Br^-/S^{2-} site-exchange. Shown experimental lattice constants $a_{Exp.}$ are shifted by an absolute offset of +0.075 Å.[10]

stable structures are obtained with 0% Br^-/S^{2-} site-exchange. Hence, all values of ΔE are calculated as the energy difference with respect to the average energy of the 0% structures and are normalized per atom. The average value of ΔE constantly increases up to 10.1 meV/atom at 50% site-exchange indicating a loss of stability with increasing site-exchange. Beyond 50%, ΔE decreases again down to 5.6 meV/atom at 100% site-exchange. By comparing the energies of the 6.25% to the 0% model on an absolute scale, the formation energy of one Br^-/S^{2-} antisite can be calculated. The obtained value of 576 meV is in good agreement with the previously reported value of 530 meV.[221]

The average a was found to be 10.0753 Å in the fully ordered case. It generally decreases with increasing site-exchange until the minimum of 10.0471 Å is reached at 50%. This depicts a decrease of 0.028 Å (0.28%). Toward 100% site-exchange, a rises again and the lattice constant of 10.0798 Å at 100% site-exchange slightly surpasses the one at 0%. All optimized lattice constants are much lower than the lattice constant of our initial model (10.2855 Å) where only the T5a sites were occupied with Li^+. Moreover, the optimizations of the

snapshots revealed that the initial model exhibits a ΔE of 37.4 meV/atom. It is therefore obvious that the distribution of Li^+ plays an important role for the energies and lattice constants in Li_6PS_5Br obtained via static DFT calculations.

This observation is especially prominent for one snapshot structure at 100% Br^-/S^{2-} site-exchange. This optimized snapshot was extracted after only approximately 2 ps of AIMD simulation and resulted in comparably large a and ΔE of 10.1074 Å and 17.4 meV/atom, respectively. Apparently, the short simulation time was not enough to allow for a reasonable rearrangement of the Li^+ ions, initially placed on the T5a sites, to adjust to the inversed Br^-/S^{2-} arrangement. The resulting unfavorable Li^+ distribution then leads to a high ΔE and large a. These observations highlight the fact that sufficient equilibration times are necessary to properly analyze superionic conductors with intricate Li^+ distributions such as Li_6PS_5Br.

The experimental lattice constants[10] $a_{Exp.}$ have been added to Figure 5.2 with an absolute offset +0.075 Å to superimpose $a_{Exp.}$ on our calculated a. In this regard, it is not surprising that the theoretical values exceed the experimental ones. This is because of the applied PBE exchange-correlation functional that commonly overestimates bond lengths.[423] Similarly, also a in Li_6PS_5Cl has been overestimated in a previous theoretical study.[220] What is more meaningful than an absolute agreement of a, in this regard, is that experimental and theoretical trends coincide. The reason for the decreasing a toward 50% site-exchange is most likely related to a more homogeneous Li^+ distribution, which will be discussed in more detail in Section 5.5.

The experimental data shows another interesting point here: It seems that the accessible range of Br^-/S^{2-} site-exchange is limited. On the one hand, it cannot fall below approximately 10% even if a slow cooling protocol is used. On the other hand, quenching from the highest temperature (550°C) only leads to 40% site-exchange. Higher degrees of site-exchange have only been achieved for Cl-containing argyrodites.[225] At this point, it is noteworthy that our theoretical studies are capable to address an arbitrary Br^-/S^{2-} site-exchange, which is helpful for the systematic analysis of the relationships between the site-exchange and the properties of Li_6PS_5Br.

5.2.2 Assessment of Entropy Contributions at Finite Temperatures

The ability to predict the equilibrium degree of site-exchange in Li_6PS_5Br would be helpful in order to formulate optimized synthesis recipes. Moreover, if such an approach was transferable to systems with comparable structural features, it could allow for a computational pre-screening of materials, potentially reducing experimental efforts. To this end, the difference in Free Energy ΔF needs to be considered,

$$\Delta F = \Delta E - T\Delta S \ , \tag{5.1}$$

which requires the inclusion of entropy changes ΔS.

Configurational Entropy due to Br^-/S^{2-} Site-Exchange

Obviously, the Br^-/S^{2-} site-exchange brings a contribution to the configurational entropy, as Br^- and S^{2-} ions can be distributed among the $4a$ and $4d$ sites in various ways. This contribution can be accounted for by using Gibbs Entropy,

$$S = -k_B \sum_i p_i \ln(p_i) \,, \tag{5.2}$$

where p_i is the probability of finding a particle in a state i. In our case we distinguish between four different states: Br on $4a$, Br on $4d$, S on $4a$, and S on $4d$. Because the composition is fixed and each $4a$ and $4d$ site can only be occupied by one anion at a time, Equation 5.2 can be reduced to

$$S_{Br/S} = -2k_B[x\ln(x) + (1-x)\ln(1-x)] \,, \tag{5.3}$$

where x represents the degree of Br^-/S^{2-} site-exchange. In this representation, $S_{Br/S}$ is an extensive quantity. Therefore, the factor of 2 accounts for the two available sites, namely one $4a$ and one $4d$ site, if one formula unit of Li_6PS_5Br is considered. The fully ordered structures at 0% and 100% site-exchange result in $S_{Br/S} = 0$ and we therefore omit the "Δ" prefix. Figure 5.3 (a) shows ΔE and a fit to the data that we refer to as ΔE_{fit}. The remaining curves are obtained as $\Delta F = \Delta E_{fit} - S_{Br/S}T$. The position of the global minimum in every ΔF curve indicates the equilibrium site-exchange at the respective temperature. Based

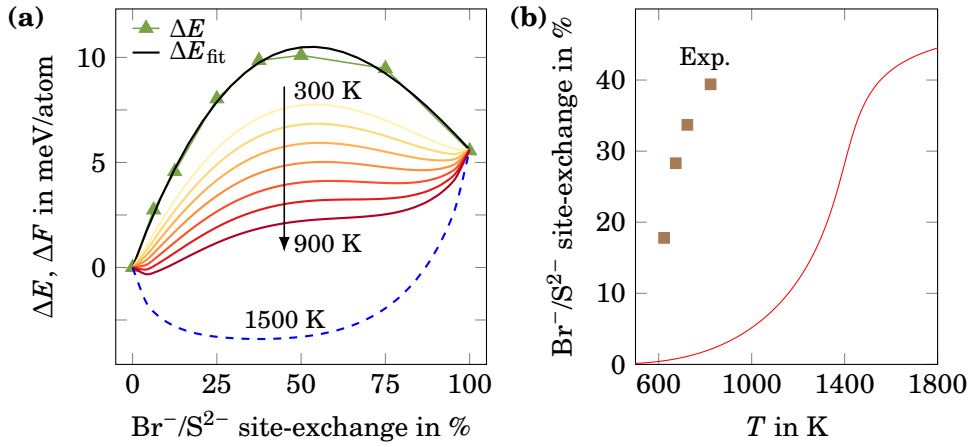

FIGURE 5.3: (a) Relative stability ΔE and an analytical fit, ΔE_{fit} as a function of site-exchange. The remaining curves correspond to $\Delta F = \Delta E_{fit} - TS_{Br/S}$ for temperatures between 300 K and 900 K. Exemplarily, also one curve for a high temperature of 1500 K has been added. (b) Predicted equilibrium Br^-/S^{2-} site-exchange, determined by the minimum in ΔF of part (a), as a function of temperature and observed site-exchange from quenching experiments (Exp.).

on this information, the calculated equilibrium site-exchange is honplotted as a function of temperature in Figure 5.3 (b).

We find that even a comparably high temperature of 900 K only leads to a low predicted site-exchange of 3%. According to our data, much higher temperatures are needed to yield a Br^-/S^{2-} site-exchange comparable to the experiment. Based on these results we conclude that $S_{Br/S}$ alone cannot be responsible for Br^-/S^{2-} site-exchange in Li_6PS_5Br. Therefore, other entropic contributions must be considered, too.

Vibrational Entropy

The second entropic contribution is the vibrational entropy S_{vib}. The applied workflow to compute properties derived from phonons is sketched in Figure 5.4. In order to reduce the computational effort, we only considered structural models containing one unit cell (4 formula units). Due to the reduced system size, only one symmetrically distinct arrangement of the Br^- and S^{2-} ions exists for 0%, 25%, 75% and 100% site-exchange. For 50% site-exchange two different arrangements exist. These six configurations were used as starting structures for AIMD simulations at 800 K to allow for a structural equilibration of Li^+. Five snapshot structures have been extracted from each AIMD simulation at different times and their atomic positions and simulation cell were optimized until forces fell below 5×10^{-4}eV/Å. The snapshots have been used to obtain an average S_{vib} based on different Li^+ distributions. Finite displacement calculations, as implemented in `VASP`, were then conducted for every snapshot. The individual force constant matrices, pDOS, zero-point energies E_{ZP} and S_{vib} were then calculated using `Phonopy` within the harmonic approximation.

The calculated pDOS curves are shown in Figure 5.5 and reveal the individual contributions of the different ionic species. It is not surprising that the contributions of Br^- are found at low frequencies (≈2 THz) because they are

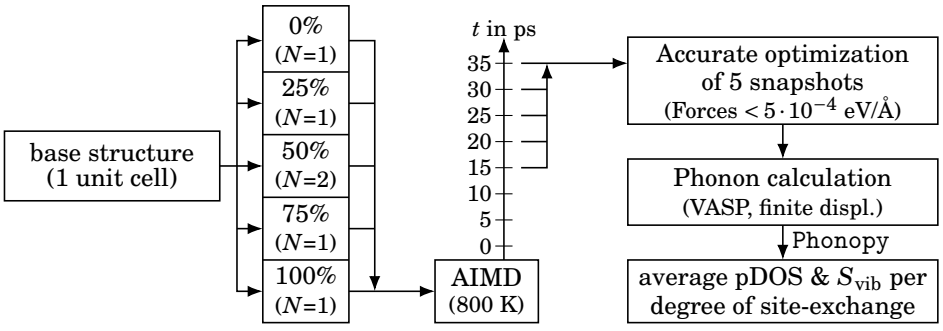

FIGURE 5.4: Workflow for the calculation of phonons and thereof derived properties for Li_6PS_5Br with different degrees of Br^-/S^{2-} site-exchange.

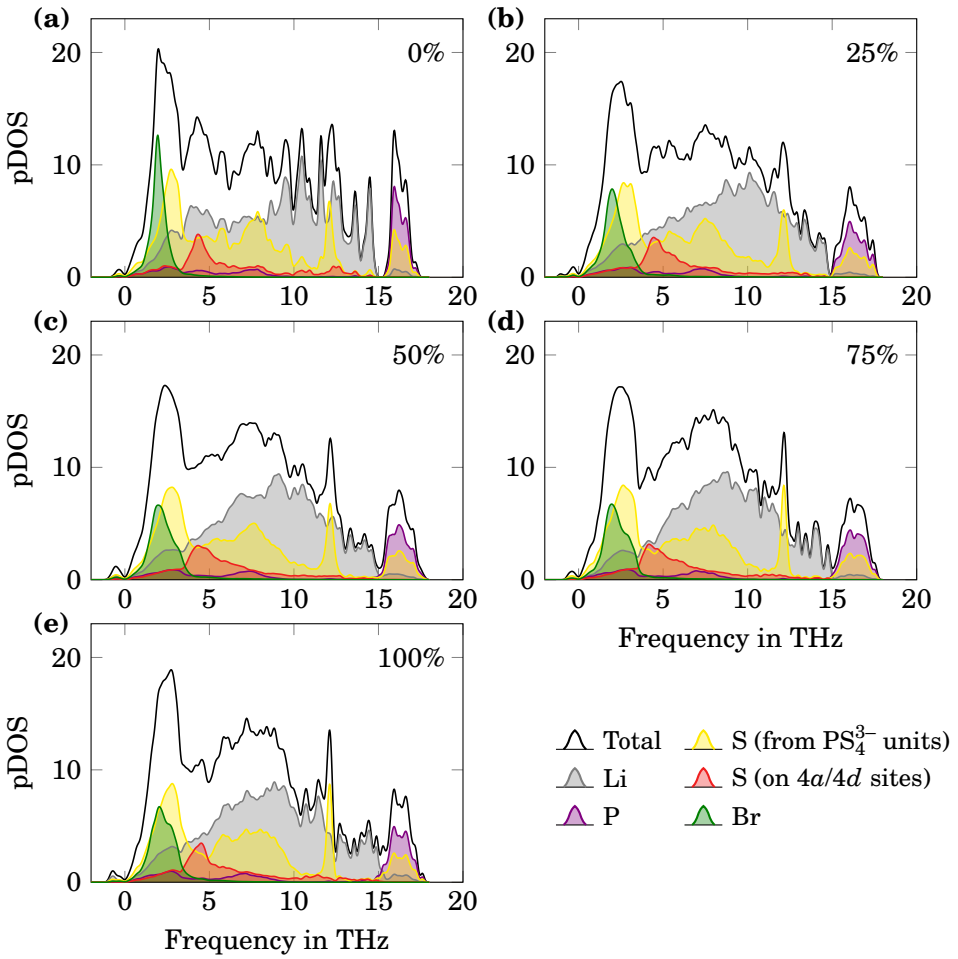

FIGURE 5.5: Calculated pDOS for Li_6PS_5Br at different degrees of Br^-/S^{2-} site-exchange as indicated in the upper right corner of every diagram. At a given site-exchange, every pDOS has been obtained as the average of five structures with different Li^+ distributions. In the case of 50% site-exchange the averaging was additionally performed over two different distributions of the Br^-/S^{2-} ions.

the heaviest ions and not strongly bound to any other species. The same holds true for the S^{2-} ions on 4*a*/4*d* sites that are found at slightly higher frequencies (≈4-5 THz) due to their lower mass. The first peak furthermore comprises significant contributions from S ions that are part of PS_4^{3-} units. This fits to previously computed pDOS of Li_3PS_4 that contain the same type of structural unit,[398] but also to $Li_7P_3S_{11}$ that additionally contains $P_2S_7^{4-}$ units.[104] Intermediate frequencies between 5 and 15 THz are mostly governed by contributions of Li^+ ions and S ions from PS_4^{3-} units. The latter type of ions furthermore exhibits a broad maximum at around 7.5 THz and a sharp peak around 12 THz. The signals at

high frequencies between 15 and 16.5 THz stem from P and S ions, presumably due to fast vibrations resulting from the stiff P–S bonds within PS_4^{3-} units.

We find that the pDOS plots of the different degrees of Br^-/S^{2-} site-exchange are very comparable. There are, however, some differences: The pDOS of the 0% structures exhibits much more pronounced peaks, whereas the pDOS of the remaining degrees of site-exchange are considerably smoother. We believe that this is related to the fact that at 0% site-exchange also the Li^+ substructure shows the highest order, as discussed in Section 5.5. Hence, there is not much variety in the local environment and certain signals should appear more often. With the introduction of Br^-/S^{2-} site-exchange both the changes in the anion and Li^+ substructure lead to more diverse local structures that presumably broadens the signals. The broadening might also be responsible for the disappearance of the small gap at 15 THz.

Notably, all pDOS curves comprise a small fraction of imaginary phonon frequencies, here plotted at negative frequencies. We already discussed the origin of such frequencies in Section 4.2.3 in the context of phonon calculations of LiPS glasses. Fortunately, the small fraction of imaginary frequencies should barely affect any further properties.

Therefore, we continued our analysis and computed S_{vib} for all structures and the averaged curves are shown in Figure 5.6. Because the curves can be hardly distinguished, the inset shows ΔS_{vib}, the difference between S_{vib} of the various degrees of site-exchange with respect to the 0% structure. We find that within the relevant temperature range of ≈500-900 K, positive values for ΔS_{vib} are only obtained for the 100% structure. In the remaining cases ΔS_{vib} is negative, indicating that the relative stability of these structures decreases with increasing temperature. Although this trend does not fit to explain the experimental findings, it qualitatively fits to the changing lattice constants as described above: Toward 50% site-exchange, the lattice constant shrinks. The material should therefore become stiffer and exhibit a decreased vibrational entropy.

For a complete assessment, the zero-point energies E_{ZP} have also been determined and the table in Figure 5.6 shows ΔE_{ZP}, the difference of the zero-point energy with respect to the 0% structure. The overall negative values of ΔE_{ZP} indicate that Br^-/S^{2-} site-exchange is favored over the 0% structure in terms of E_{ZP}. The magnitude of ΔE_{ZP}, however, is rather low and only has little effect on the stability. For instance, in the case of the 50% structure, the small stability advantage due to ΔE_{ZP} is surpassed by the $-\Delta S_{\mathrm{vib}} T$ term already at approximately 100 K.

In summary, we find that vibrational entropy contributions are not able to explain the experimentally observed dependence of Br^-/S^{2-} site-exchange on synthesis temperature. We recall, however, that similar issues as for the LiPS glasses (see Section 4.2.3) are faced: Li^+ ions experience a flat potential energy landscape and diffuse fast, as we will explain throughout Section 5.3. Therefore, the harmonic approximation is likely to break down at elevated temperatures,

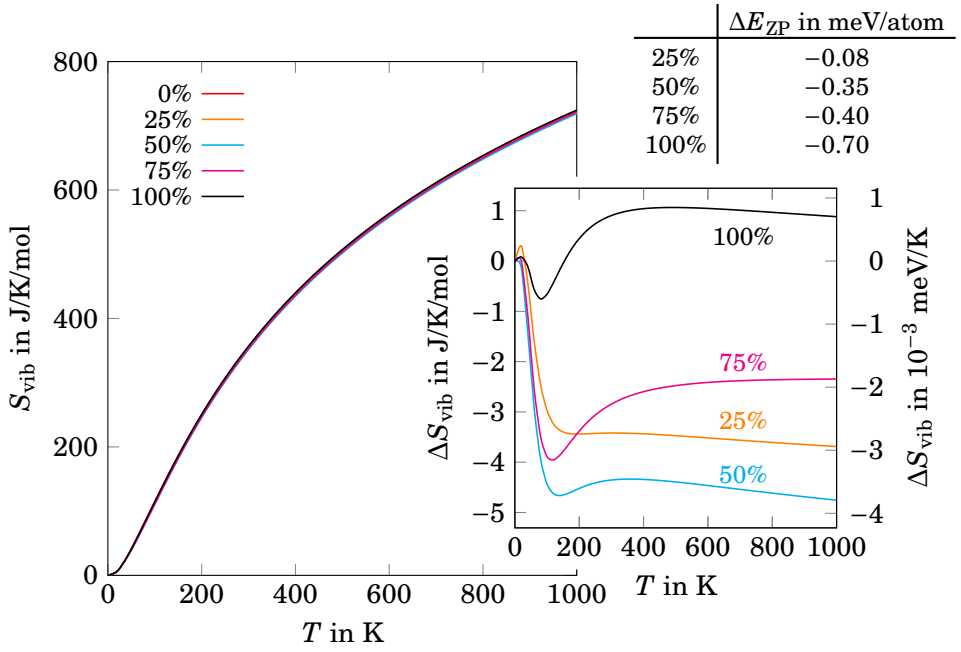

FIGURE 5.6: Vibrational entropy S_{vib} per mol Li_6PS_5Br as a function of temperature for different degrees of Br^-/S^{2-} site-exchange. For a better comparison the difference of the vibrational entropy with respect to the 0% structure, e.g., $\Delta S_{vib}(50\%) = S_{vib}(50\%) - S_{vib}(0\%)$, is shown in the inset. Furthermore, the table in the upper right corner lists the difference in zero-point energies, ΔE_{ZP}, with respect to the 0% structure.

potentially leading to artifacts in S_{vib}. However, it should still be applicable for Br^-, the isolated S^{2-} ions and the ions within the PS_4^{3-} units that are confined to specific sites.

Configurational Entropy due to Li^+

Although $S_{Br/S}$ helps in approaching the experimental observations, it does not suffice to reproduce it correctly. On the other hand, S_{vib} determined within the harmonic approximation is likely not a good measure for superionic conductors. We suppose that the gap between our results and the experimental results can be overcome by including structural contributions of the Li^+ ions. This is because, as we see in Section 5.5, Li^+ becomes more homogeneously distributed within the simulation cell as the site-exchange approaches 50%. As a result, an increased configurational entropy is expected.

A simple approach for calculating the Li^+ configurational entropy was attempted for $Li_{6+x}Sb_{1-x}Si_xS_5I$, but only considered the average occupancies of T5 and T5a sites.[424] As we will see in Section 5.5, however, the Li^+ substructure is much more complicated and varies locally based on the anion arrangement.

Therefore, the development of a more thorough model for assessing the Li^+ configurational entropy, which is out of the scope of this work, is needed. Presumably, a cluster expansion would be an appropriate approach, but certainly represents a challenging task due to the intricate Li^+ substructure.

5.3 Bulk Transport Properties

As we will see in the following, the Br^-/S^{2-} site-exchange has a strong influence on the transport properties and is key for turning Li_6PS_5Br into a superionic conductor. To demonstrate this, we will first examine Li_6PS_5Br without any Br^-/S^{2-} site-exchange. In this case the Li^+ motion is mostly confined to the Li^+ cages around the 4*d* sites. Intercage jumps, necessary for long-range transport, are barely observed and likely to be followed by an immediate back-jump. As soon as Br^-/S^{2-} site-exchange is introduced, the situation changes and long-range transport is enabled. Furthermore, we will investigate how Li^+ diffusion is affected if the material is strained.

5.3.1 Local Li^+ Motion at 0% Site-Exchange

In the absence of Br^-/S^{2-} site-exchange, the Li^+ transport is strongly limited to a local scale at moderate temperatures. Specifically, the Li^+ ions move within the Li^+ cages that encase the S^{2-} ions on the 4*d* sites. This can be seen based on the Li^+ MSD evolution and Li^+ trajectories shown in Figure 5.7.

For 500 K, 600 K and 700 K the MSD initially rises but flattens out already after few ps. It finally converges to approximately 11.5 $Å^2$, which is indicated with a dashed line in Figure 5.7 (a). This fits to the Li^+ trajectories, shown in

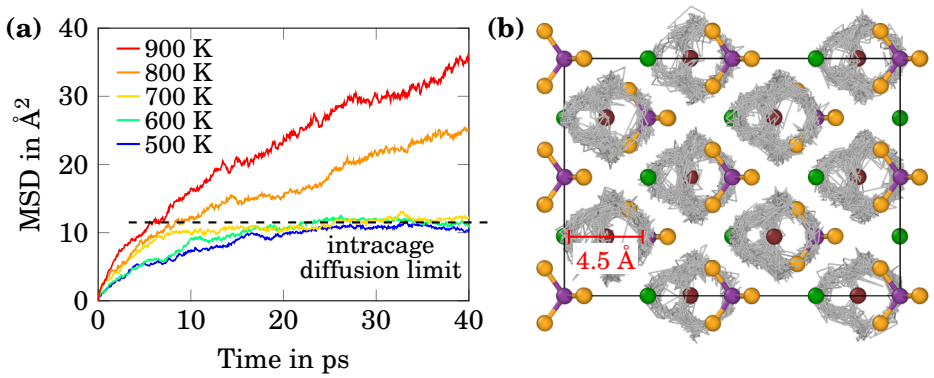

FIGURE 5.7: (a) Evolution of the Li^+ MSD at 0% site-exchange. Each of the curves is obtained by averaging the MSD of two independent simulations. The dashed line at 11.5 $Å^2$ marks the apparent intracage diffusion limit. (b) Exemplary Li^+ trajectories (gray) after 35 ps at 700 K.

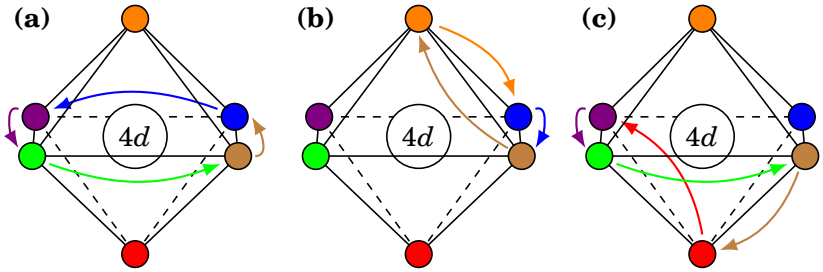

FIGURE 5.8: Sketches of the (a) rigid rotation and (b) trigonal-prismatic internal reorganization mechanism within the Li^+ cages centered around the 4*d* site as reported by Morgan.[207] (c) Newly discovered reorganization mechanism that cannot be described by one single rotation axis. For clarity, the six Li^+ are shown as differently colored spheres.

part (b) of the figure. The trajectories show that no intercage jump occurred and that the Li^+ motion is confined to the cages, as similarly observed in previous studies.[207,221] An approximate cage diameter of 4.5 Å can be deduced from the trajectories and an upper limit for the MSD can be estimated: Assuming all Li^+ have moved to the opposite side of their cage, a MSD of $(4.5\ \text{Å})^2 \approx 20\ \text{Å}^2$ is expected. This situation, however, is very unlikely and, on average, Li^+ will be randomly distributed in the cage leading to the apparent intracage diffusion limit of $11.5\ \text{Å}^2$.

The following question arises: Which atomic diffusion mechanisms govern the redistribution of Li^+ within the cages? Similarly to other studies, we observe that doublet jumps within the T5-T5a-T5 triplets occur frequently.[184,207,219] Therefore, we believe that this triplet can be rather understood as a megabasin of sites separated by negligible migration barriers. Two different mechanisms for intracage jumps, i.e., the jumps between different T5-T5a-T5 triplets within same Li^+ cage, have been reported by Morgan[207] and are sketched in Figure 5.8 (a) and (b). The rigid rotation and the trigonal prismatic internal reorganization mechanisms involve four and three Li^+, respectively, and reveal a highly concerted motion for Li^+. Both mechanisms can be described by only one rotation axis. By analyzing the Li^+ motion in our simulations we can confirm these two mechanisms. Additionally, we have identified a third mechanism that is shown in Figure 5.8 (c). This newly discovered reorganization mechanism involves four Li^+ and cannot be described by a single rotation axis. At 600 K, such a Li^+ reordering is completed within approximately 2 ps, which emphasizes the concerted character of the diffusion process. Our findings corroborate that the dominant Li^+ motion in the absence of Br^-/S^{2-} site-exchange occur within the Li^+ cages and belong to doublet and intracage jumps.

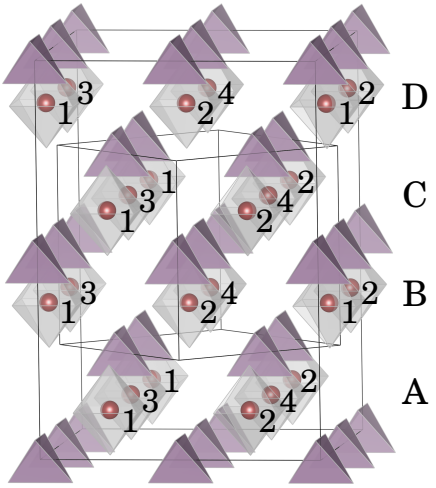

FIGURE 5.9: Illustration of the used supercell model with the labels A1, A2, ..., D4 that have been given to the 4*d* sites and the respective Li^+ cages. For clarity, the majority of ions is not shown. The S^{2-} ions on the 4*d* sites are indicated as red spheres. They are surrounded by the Li^+ octahedra (gray) spanned by the T5a sites. The remaining, purple tetrahdra indicate the positions of the PS_4^{3-} units.

5.3.2 Intercage Jumps at 0% Site-Exchange

Contrary to doublet and intracage jumps, the occurrence of intercage jumps between two different Li^+ cages at 0% site-exchange is rare. The low tendency for long-range transport is underlined by the fact that during two independent simulations of approximately 60 ps length at 600 K only one single intercage jump was observed. In order to characterize such intercage jumps, the 4*d* sites of the supercell model have been labeled as A1, A2, ..., D4 as shown in Figure 5.9. These labels are interchangeably used in the following to refer to the 4*d* site itself or its surrounding Li^+ cage.

The mentioned intercage jump at 600 K is illustrated in Figure 5.10 with the corresponding simulation time in ps in the respective upper left corner. The jumping Li^+ is depicted as a blue sphere and its trajectory line is shown in light blue. After having performed only doublet jumps for 12.5 ps (see the clustered trajectory lines in the 12.500 ps subfigure), the marked Li^+ jumps from its initial cage at C4 to the neighboring cage D2. Until this point of the simulation, every cage in the simulation cell was comprised of exactly six Li^+. Once the jump has been completed at 12.875 ps, the cage at C4 is left with only five Li^+, while the destination cage D2 contains seven Li^+. This situation is similar to the formation of a Li^+ Frenkel pair[207] with a Li^+ vacancy (V'_{Li}) at C4 and a Li^+ interstitial ($Li^{\bullet}_i$) at D2.

Apparently, this imbalanced situation is not very stable and a back-jump of the same Li^+ is observed only 2 ps later, which reinstalls the initial distribution with six Li^+ in each cage. The fact that it is the same Li^+ ion that performs the back-jump, together with the short time between the jumps, indicates a high correlation for Li^+ intercage jumps in the absence of Br^-/S^{2-} site-exchange.

Based on the MSD evolution in Figure 5.7 (a) we have seen that the intracage diffusion limit is overcome within reasonable simulation times only at

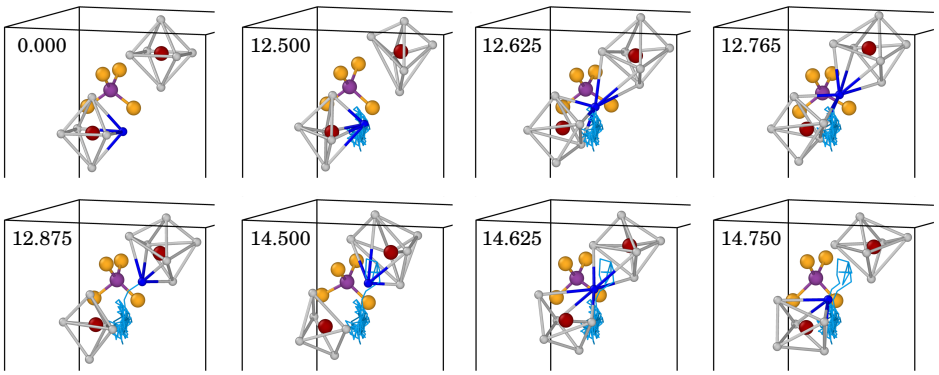

FIGURE 5.10: Structural models documenting the only successful intercage jump in Li_6PS_5Br with 0% Br^-/S^{2-} site-exchange observed during a 60 ps simulation at 600 K. The hopping Li^+ jumps from the cage at C4 to the cage at D2. After only approximately 2 ps the jump is followed by a back-jump. The simulation time in ps is shown in the upper left corner of every snapshot. The majority of ions are not shown for clarity.

temperatures of 800 K or above. Therefore, we have also analyzed the intercage jumps for such simulations in a similar way as in Figure 5.10. Instead of showing multiple series of atomic structures, the information have been condensed into a flowchart representation as shown in Figure 5.11. Similar flowcharts will also be used to illustrate intercage jumps observed in other simulations in the course of this chapter. They show the time of the simulation on the x-axis and every dashed, horizontal line belongs to one of the Li^+ cages. The bare, dashed lines are used as a guide to the eye and indicate that the corresponding cage contains its regular six Li^+ ions. Actual Li^+ intercage jumps are indicated with arrows. As a result of an intercage jump, the number of Li^+ in the two involved cages changes. This is visualized with colored bars.

As an example, let us consider Figure 5.11 (a). At the beginning of the simulation no intercage jumps are observed. The first intercage jump happens after approximately 15 ps and involves a Li^+ jump from cage B3 to B4. Therefore, a Frenkel pair with a V'_{Li} on B3 (yellow bar) and a $Li^{\bullet}_i$ on B4 (blue bar) is created. The V'_{Li} on B3 is filled by a Li^+ from A2 at approximately 16.5 ps, which itself is refilled by a Li^+ from B1 shortly afterward. This process can be considered as a vacancy-mediated diffusion process. The $Li^{\bullet}_i$ remains on B4 for approximately 3 ps until a Li^+ jump from B4 to C2 is initiated. Virtually simultaneously, a Li^+ ion jumps from C2 to B1. In this last jump, the $Li^{\bullet}_i$ recombines with the V'_{Li}, and the Frenkel pair is annihilated again.

The flowchart continues in part (b) of Figure 5.11 and shows that the simulation does not record any intercage jump for several ps. At approximately 27 ps a more complicated sequence of jumps is initiated. This time, also a chain of jumps triggered by interstitials is observed. One example is the jump sequence

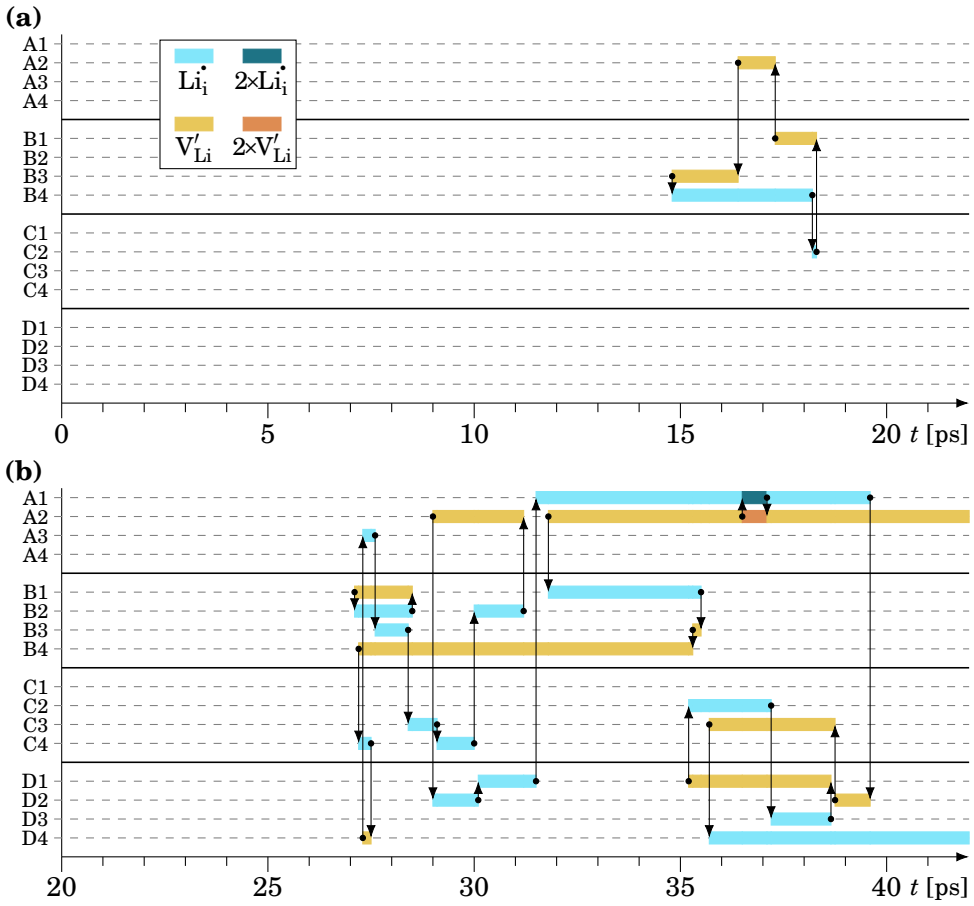

FIGURE 5.11: (a) Flowchart illustrating all observed Li^+ intercage jumps during a simulation at 800 K and 0% Br^-/S^{2-} site-exchange. Arrows indicate the jump of a Li^+ ion from one cage to another. Colored bars indicate the presence and number of $Li_i^{\bullet}$ and V'_{Li} in the respective cages. (b) Continuation of the simulation shown in (a). Note that the remaining flowcharts in this work illustrate simulations at a reduced temperature of 600 K.

observed shortly after 27 ps: A3→B3→C3→C4→B2→A2. Notably, between 36 and 37 ps even two $Li_i^{\bullet}$ and two V'_{Li} are present at A1 and A2, respectively, for a short period of time.

In summary, at a high temperature of 800 K Li^+ diffusion is governed by the spontaneous formation of Li^+ Frenkel pairs even in the absence of Br^-/S^{2-} site-exchange. Once the Frenkel pairs have formed, a cascade of Li^+ jumps is initiated and both the $Li_i^{\bullet}$ and the V'_{Li} can be considered as mobile species. In contrast to that, the simulation at 600 K showed that Li^+ diffusion is prevented because Frenkel pairs rarely form and their immediate recombination is likely.

5.3.3 Enhanced Li^+ Motion due to Site-Exchange

As soon as Br^-/S^{2-} site-exchange is introduced in Li_6PS_5Br, Li^+ transport is greatly improved. This can be seen in Figure 5.12, which shows the MSD evolution at different degrees of Br^-/S^{2-} site-exchange together with a representative illustration of the Li^+ trajectories. The MSD is obtained as the average of all distinct Br^-/S^{2-} arrangements that have been simulated at the respective degree of site-exchange. The transparent areas around the MSD indicate one standard deviation. Because only two independent simulations have been performed for the 0% and 100% structures, the standard deviation is omitted in these cases. The overall trend of the MSD is in line with reports by Morgan for Li_6PS_5Cl and Li_6PS_5I.[207]

The trajectory lines of the 25% model in Figure 5.12 (b) show that the cage structure is partially kept intact, as can be seen in the left part of the structural representation. In the right part, however, the local cage structure is considerably disturbed and the Li^+ trajectories become more diffuse, indicating an increased number of intercage jumps and improved long-range Li^+ transport. This is reflected in the MSD evolution: The intracage diffusion limit, which is still observed for the 0% structure at 700 K, is already overcome at 500 K in the presence of 25% site-exchange.

Figure 5.12 (c) shows that the cage structure is completely dissolved at 50% site-exchange. The corresponding MSD evolution exhibits the steepest increase, i.e., the highest diffusion coefficients, among all investigated degrees of site-exchange. Once the site-exchange exceeds 50%, the transport properties deteriorate as can be seen in Figure 5.12 (d) for 75%. The Li^+ trajectories start to manifest cage like-structures around the 4*a* sites, but plenty of intracage jumps still take place and long-range transport is observed. The situation is comparable to the 25% structure with shifted cage positions.

The structural model shown in Figure 5.12 (e) reveals that at 100% site-exchange the cage shift is completed (compare the position f the dashed circle to the 0% structure). The few trajectory lines in the 100% structure that are visible between the cages do not depict true intercage jumps. Instead, they merely result from the starting geometry where the Li^+ ions were initially placed on the T5a sites that are located exactly between the shifted cages. The cage structure indicates that Li^+ transport becomes again locally confined, which is also proved by the MSD: The MSD converges similarly as observed for the 0% structure at temperatures of 700 K and below. Only at higher temperatures successful long-range transport is observed in the simulations.

For all cases where the MSD could be reasonably interpolated using a linear equation, the tracer diffusion coefficients D^* have been calculated from the fitted slopes. This was not possible for low temperature simulations with low or 100% site-exchange. We note that slightly longer simulations than those shown in the MSD plots have been performed and that the full simulation time has been used to obtain D^* in all cases. The results are shown in an Arrhenius representation

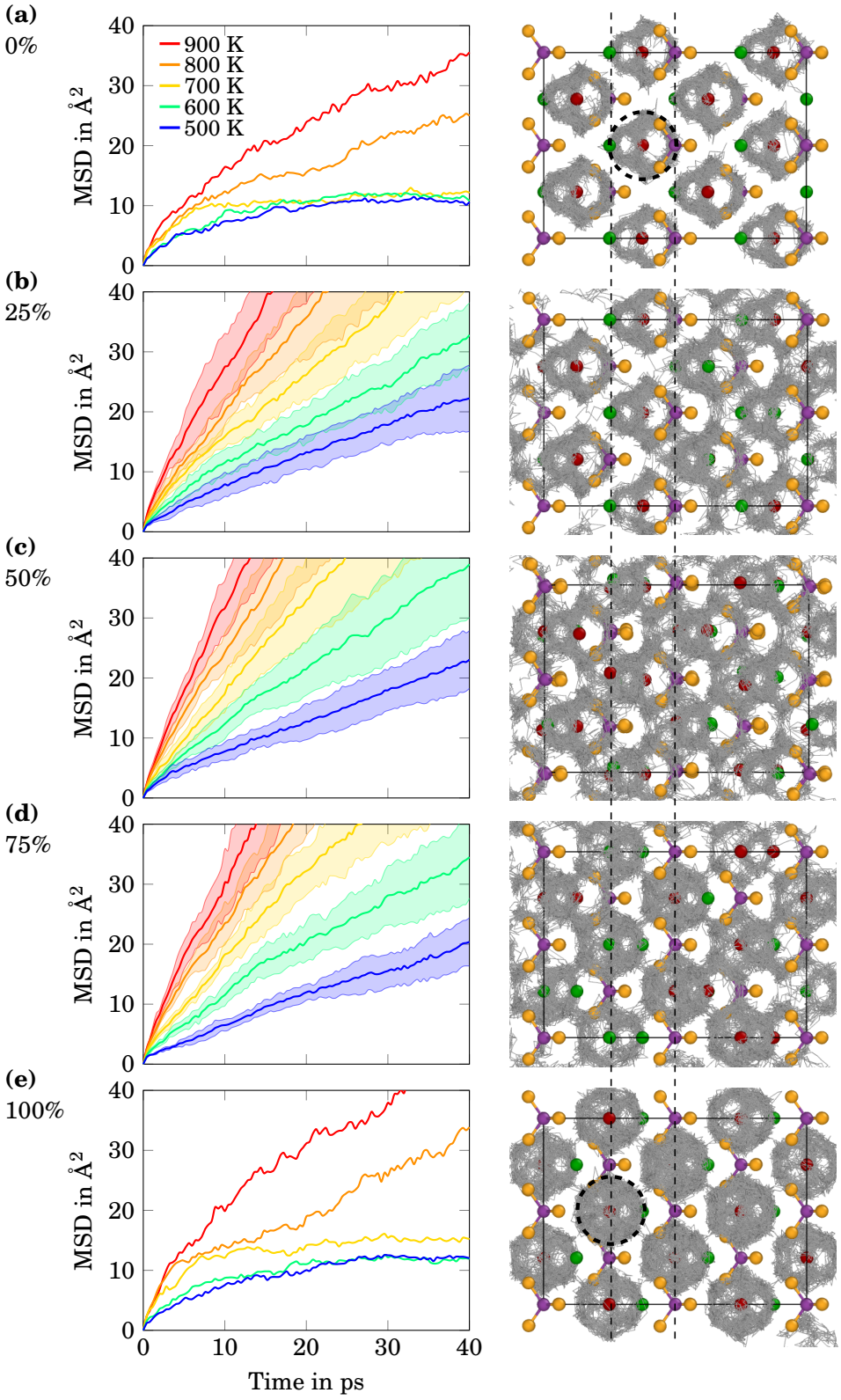

FIGURE 5.12: Evolution of the MSD for different degrees of Br^-/S^{2-} site-exchange. The MSDs at 0% and 100% are averaged over two independent runs. For 25%, 50%, and 75% the MSDs is averaged over 6, 9, and 6 structures with different Br^-/S^{2-} arrangements, respectively. The corresponding standard deviation is indicated by the transparent region surrounding the MSD. Next to every MSD plot an exemplary structural model with Li^+ trajectories (gray) after 35 ps at 700 K is shown. Dashed lines and circles are added as a guide to the eye to indicate the shifting of the cage positions.

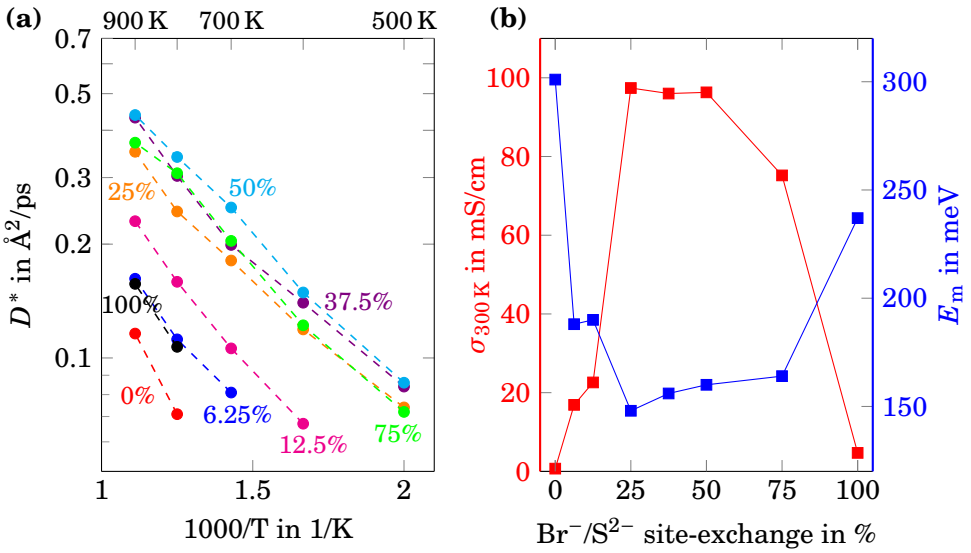

FIGURE 5.13: (a) Arrhenius representation of D^* at various degrees of site-exchange. (b) Extrapolated Li^+ conductivity $\sigma_{300\,K}$ at 300 K and migration barrier E_m.

in Figure 5.13 (a) together with the extracted transport coefficients in (b). The exact values can be read from Table 5.1, but note that especially low D^* might be strongly affected by the statistics, as we will see in Section 5.3.4.

Figure 5.13 (a) indicates that 50% site-exchange delivers the highest diffusion coefficients in the AIMD simulations. Also for 25%, 37.5% and 75% comparably high values for D^* are obtained, whereas it is significantly reduced for a site-exchange of 12.5% and below. This is reflected in the extracted transport parameters. Most notably, the migration barrier E_m in Figure 5.13 (b) drops from approximately 300 meV at 0% to 148-164 meV for site-exchanges between 25% and 75%. A similar drop in E_m is observed for $Li_{6+x}P_{1-x}M_xS_5I$ (M=Si, Sn, Ge) at $x \approx$ 20%-25%.[225,226] In addition to small contribution from an increasing lattice constants and a higher Li^+ content, the reasons for the decrease in E_m are mainly attributed to a flattened potential energy landscape due to I^-/S^{2-} site-exchange that starts to set in at $x \approx$ 20%.[226] This reasoning fits to our results as all AIMD simulations have been performed with constant compositions and at the same volume.

We note that our extracted values for E_m should be interpreted with a certain amount of skepticism. This is because subtle changes in D^* due to statistical noise may induce noticeable changes in E_m.[164] The same holds true for the extracted D_0 (see Table 5.1). Still, a comparison of the obtained values for E_m and D_0 indicates that E_m dominates the change of the transport properties for extrapolated diffusion coefficients $D^*_{300\,K}$ and ionic conductivities $\sigma_{300\,K}$ at 300 K: $\sigma_{300\,K}$ at 50% site-exchange is two orders of magnitude higher than at 0%.

TABLE 5.1: Determined transport parameters for different degrees of Br^-/S^{2-} site-exchange x. Several values have been omitted because no or insufficient long-range transport was observed at these temperatures. The Li^+ number density, needed to calculate σ based on Equation 3.44, corresponds to $c = N/V = 96/4352.4\,Å^3$. Note for the conversion of D^*: 1 $Å^2/ps$ = 10^{-4} cm^2/s.

x	D^* [$Å^2$/ps]					E_m	D_0	$D^*_{300\,K}$	$\sigma_{300\,K}$
	500 K	600 K	700 K	800 K	900 K	[meV]	[$Å^2$/ps]	[$Å^2$/ps]	[mS/cm]
0%	-	-	-	0.0712	0.1156	301	5.60	$4.93{\cdot}10^{-5}$	0.7
6.25%	-	-	0.0806	0.1125	0.1620	188	1.79	$1.24{\cdot}10^{-3}$	16.9
12.5%	-	0.0670	0.1061	0.1593	0.2295	190	2.57	$1.65{\cdot}10^{-3}$	22.6
25%	0.0741	0.1186	0.1810	0.2441	0.3507	148	2.18	$7.13{\cdot}10^{-3}$	97.4
37.5%	0.0836	0.1397	0.1988	0.3034	0.4315	156	2.95	$7.02{\cdot}10^{-3}$	96.0
50%	0.0858	0.1490	0.2505	0.3404	0.4385	160	3.47	$7.05{\cdot}10^{-3}$	96.3
75%	0.0723	0.1224	0.2043	0.3080	0.3711	164	3.13	$5.50{\cdot}10^{-3}$	75.2
100%	-	-	-	0.1069	0.1567	237	3.33	$3.47{\cdot}10^{-4}$	4.7

Similarly to E_m, also the values for $\sigma_{300\,K}$ should not be compared quantitatively with experimental results due to the reasons explained in Section 3.6.4.

5.3.4 Diffusion Under Mechanical Loading

In the previous sections we saw that effective Li^+ transport in Li_6PS_5Br demands the presence of Br^-/S^{2-} site-exchange. Experimental studies have also analyzed the influence of pressure during fabrication and during measurements on the transport properties of the closely related material Li_6PS_5Cl.[378] The authors conclude that the application of pressure during fabrication is necessary to reduce the porosity and enable high conductivity. Using suitable electrode contacts, however, only a weak improvement of the conductivity with increasing pressure during electrochemical impedance spectroscopy (EIS) measurements was observed. The reason for this observation can most likely be attributed to improved particle-particle contact, as NMR measurements indicate a reduced bulk diffusion under compression.[425]

To obtain a better understanding of related issues, we investigate how the bulk transport properties of Li_6PS_5Br are altered if mechanical loading is applied. For this purpose, performing AIMD simulations with pressure control would be an ideal approach. However, this demands accurate calculation settings (i.e., high energy cutoff of the plane wave basis set) that considerably limit the affordable time scales. Instead, we relied on the NVT ensemble and executed the simulations at different constant volumes. The volume was adjusted via a lattice scaling factor f, used to isotropically rescale the lattice constant of the simulation cell according to $a = f \cdot a_0$, where a_0 corresponds to the base lattice constant of the idealized Li_6PS_5Br model with ordered Li^+ sites as described in Section 5.1. A similar approach will be used in Section 6.2.4, where the influence of mechanical loading on the transport properties of Li_7SiPS_8 is discussed.

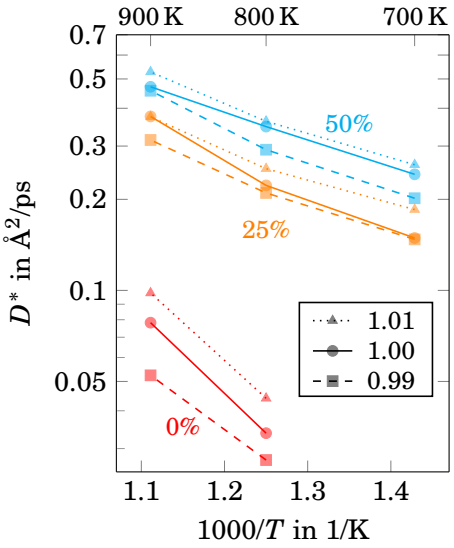

FIGURE 5.14: Arrhenius representation of D^* extracted from extended AIMD simulations (> 200 ps) for different lattice scaling factors $f = 0.99, 1.00, 1.01$ at 0%, 25% and 50% Br^-/S^{2-} site-exchange in Li_6PS_5Br. At 0% site-exchange, every data point is obtained as the average of three independent runs. For both 25% and 50%, D^* is obtained as the average from four different Br^-/S^{2-} arrangements. The exact values of D^* can be read from Table 5.2.

For the present analysis, we restricted the analysis to temperatures of 700 K, 800 K and 900 K at scaling factors of 0.99, 1.00 and 1.01, and only considered structures with 0%, 25% and 50% site-exchange to keep the computational effort manageable. Reasonable statistics were ensured by performing long AIMD simulations (> 200 ps). Furthermore, three independent runs for every volume-temperature setting at 0% site-exchange and four different arrangements of the Br^-/S^{2-} ions for both the 25% and 50% structures were used. Nevertheless, all datasets at 700 K with 0% site-exchange were disregarded due to insufficient Li^+ diffusion. The obtained MSD curves were averaged and then fitted to a linear regression to extract D^* as described previously. The results are shown in Figure 5.14 and the individual values can be read from Table 5.2.

First, we note that the values of D^* for the 0% structure, obtained from the extended AIMD runs at $f = 1.00$, deviate considerably from the ones mentioned in Section 5.3.3 obtained with the same simulation settings. Here, only half and two-thirds of the previously mentioned values at 800 and 900 K are reached, respectively. For the structures with 25% and 50% Br^-/S^{2-} site-exchange, however, D^* is in agreement with our previous values and differs by less than 20%. This indicates that the previous AIMD simulations for the 0% structure might be too short to deliver statistically accurate results. In other words, structures with low diffusion coefficients need extended AIMD simulations to extract reliable properties.[164] Therefore, also the reported D^* in Table 5.1 for the structures with 6.25%, 12.5%, and 100% site-exchange might be subjected to considerable statistical deviations.

The data in Figure 5.14 shows that $D^*_{1.01} > D^*_{1.00} > D^*_{0.99}$ in almost all cases. Hence, higher volume results in faster diffusion, which fits to the NMR measurements of Adeli *et al.*,[425] reporting decreasing diffusion coefficients under

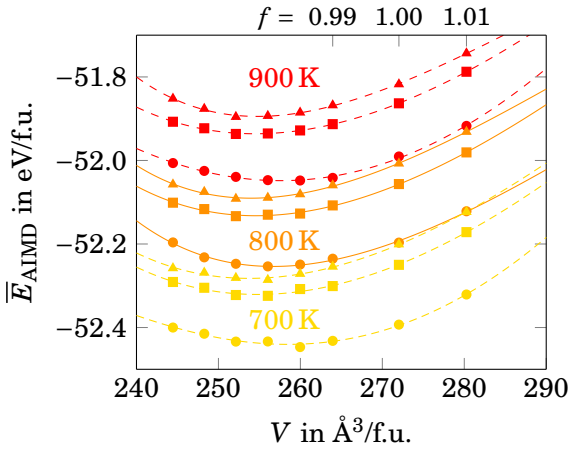

FIGURE 5.15: Energy-volume curves of Li_6PS_5Br. Data points at $f < 0.99$ have been obtained from shorter AIMD simulations (≈ 5 ps), sufficient to determine an averaged $\overline{E}_{\mathrm{AIMD}}$, but too short to extract D^*. The average bulk modulus B amounts to 23.6 GPa. Spheres, squares and triangles correspond to the structures with 0%, 25% and 50% site-exchange, respectively.

compression. Most likely, this dependence stems from the fact that the diffusion pathways can broaden under tensile strain or dopant-induced lattice expansion.[426,427] On the contrary, the pathways narrow if the material is compressed.

An alternative reason for this dependence could be related to the Li^+ cages: Under compression, the size of the Li^+ cages shrinks and offers less space to accommodate an additional Li^+ in the cage. This might be critical for the success rate of intercage jumps, similarly to the one shown in Figure 5.10. With less space available, an incoming Li^+ will experience an increased electrostatic repulsion that raises the likelihood of an immediate back-jump and prevents successful intercage jumps.

For a better quantification of the influence of mechanical loading on the Li^+ transport properties, activation volumes $\Delta^{\ddagger}V$, as introduced in Section 3.6.5, can be calculated. This requires the knowledge of the pressure p for the individual calculations, which can be extracted in two different ways: First, $\overline{p}_{\mathrm{AIMD}}$ is obtained as the time-average of the pressure output at every time step. However, the accuracy of $\overline{p}_{\mathrm{AIMD}}$ is expected to suffer due to the reduced energy cutoff. Second, $\overline{E}_{\mathrm{AIMD}}$ is obtained as the time-average of the energy output at every time step. The Birch-Murnaghan equation of state (see Section 3.7) can then be fitted to the energy-volume data to determine the bulk modulus B, which in turn is used to calculate the pressure $p_{\mathrm{BM\text{-}EOS}}$ at a given volume.

Both approaches have been applied and Figure 5.15 shows the energy-volume curves used to calculate B. Note that data points at $f < 0.99$ have been obtained from short AIMD simulations (≈ 5 ps) that are too short to determine D^*, but sufficient for a calculation of $\overline{E}_{\mathrm{AIMD}}$. These additional data points are required to obtain a reliable fit to the Birch-Murnaghan equation of state. The average bulk modulus according to the energy-volume curves is 23.6 GPa, which compares well to the bulk moduli of other sulfide SEs.[428] The individual bulk moduli have been used to calculate $p_{\mathrm{BM\text{-}EOS}}$.

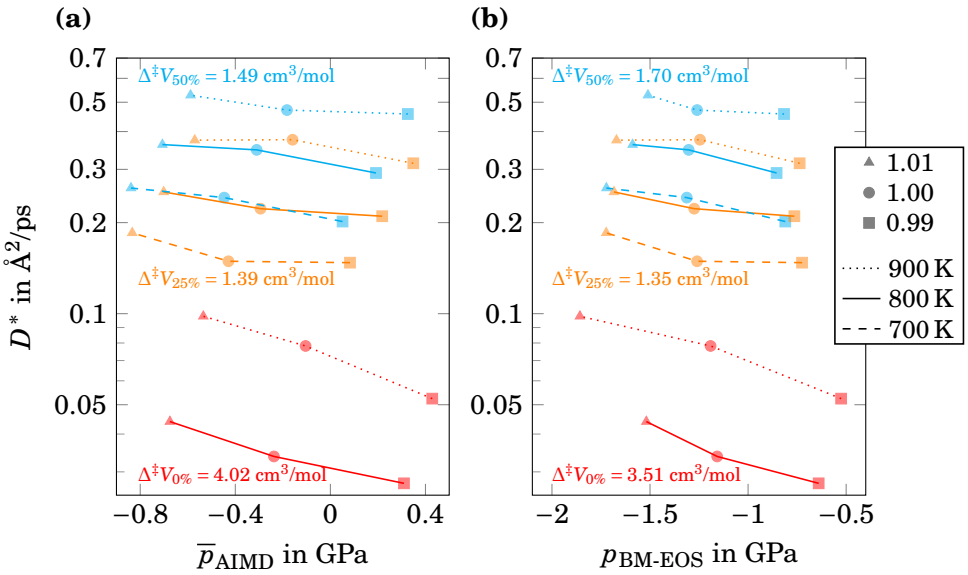

FIGURE 5.16: D^* as function of (a) $\overline{p}_{\text{AIMD}}$ and (b) $p_{\text{BM-EOS}}$, where negative and positive values indicate tensile and compressive conditions, respectively. The exact pressure values can be read from Table 5.3. The color coding corresponds to the degree of Br^-/S^{2-} site-exchange and is the same as in Figure 5.14, i.e., 0%=red, 25%=orange, and 50%=blue. The labeled activation volumes $\Delta^\ddagger V$ have been extracted by data interpolation and are averaged for each degree of Br^-/S^{2-} site-exchange.

Figure 5.16 (a) and (b) show the dependence of D^* on $\overline{p}_{\text{AIMD}}$ and $p_{\text{BM-EOS}}$ as well as average activation volumes. The two approaches lead to considerably different pressures, but the overall dependence is similar and positive activation volumes $\Delta^\ddagger V$ are obtained. Our data suggests a weak dependence of $\Delta^\ddagger V$ on temperature, i.e., $\Delta^\ddagger V_{700\text{K}} \approx \Delta^\ddagger V_{800\text{K}} \approx \Delta^\ddagger V_{900\text{K}}$. Therefore, the values labeled in the diagrams for each degree of Br^-/S^{2-} site-exchange are calculated as the average over the three different temperatures and are comparable to other SEs.[379]

Regardless of the approach to determine the pressure, the data reveals a two- to threefold increase of the activation volumes at 0% compared to 25% and 50% site-exchange. This indicates that the relative change in the transport properties for the 0% structure is more sensitive to the application of mechanical loadings than structures with Br^-/S^{2-} site-exchange. We believe that the reason for an increased $\Delta^\ddagger V$ is that Li^+ transport at 0% site-exchange demands the formation of Li^+ Frenkel pairs to begin with. Such a behavior was presented in Figure 5.11 for a simulation at 800 K. Even at such high temperatures, the formation of Frenkel pairs was only observed after a considerable amount of time. Moreover, the first Frenkel pair survives only few ps before being annihilated. Only at a later point of the simulation a cascade of intercage jumps is observed, leading to

up to three Frenkel pairs at the same time. Toward the end of the simulation, however, the system remains with only one Frenkel pair.

If we recall that the total activation volume consists of two contributions related to (i) the formation and (ii) the migration of the defect (see Section 3.6.5), we can expect that $\Delta^{\ddagger}V$ of the 0% structures exhibits a considerable contribution of the activation volume of formation $\Delta^{\ddagger}V^{\text{form}}$. In contrast, we will see in Section 5.4 that Li^+ Frenkel pairs are a natural consequence of Br^-/S^{2-} site-exchange: At 6.25% site-exchange and a moderate temperature of 600 K, one Frenkel pair forms already at the very beginning of the simulation and is not annihilated over the full simulated timespan. This implies that the mobile defects are not required to be generated repeatedly and should result in a decreased contribution of the activation volume of formation $\Delta^{\ddagger}V^{\text{form}}$, leading to a decreased $\Delta^{\ddagger}V$.

The energy-volume curves in Figure 5.15 as well as the pressure dependence of D^* shown in Figure 5.16 reveal another interesting fact: Apparently, the AIMD simulations for extracting D^* have been simulated under tensile conditions, if we neglect the few positive pressures from the less accurate $\overline{p}_{\text{AIMD}}$. This also fits to the observation of Section 5.2.1, where our initially obtained lattice constant of $a = 10.2855$ Å (corresponding to $f = 1.00$) for the idealized model of Li_6PS_5Br was found to be artificially high due to the simplified Li^+ distribution. After optimizations of the AIMD snapshots, the lattice constant shrank to approximately 10.05-10.08 Å, depending on the degree of Br^-/S^{2-} site-exchange. Therefore, all D^* reported in this section and in Section 5.3.3 are slightly overestimated because they have been obtained under tensile conditions. It should be noted that such effects are rarely addressed in literature, although it is likely that comparable issues are regularly encountered if materials with a complex Li substructures are approximated with simplistic orderings.

TABLE 5.2: Tracer diffusion coefficients D^* as a function of the degree of Br^-/S^{2-} site-exchange x, temperature T, and lattice scaling factors f. 1 Å^2/ps = 10^{-4} cm^2/s.

x	T [K]	$D^*_{0.99}$ [Å^2/ps]	$D^*_{1.00}$ [Å^2/ps]	$D^*_{1.01}$ [Å^2/ps]
0%	700	-	-	-
	800	0.0275	0.0337	0.0440
	900	0.0524	0.0782	0.0980
25%	700	0.1475	0.1490	0.1850
	800	0.2100	0.2224	0.2526
	900	0.3142	0.3759	0.3747
50%	700	0.2016	0.2420	0.2603
	800	0.2918	0.3480	0.3622
	900	0.4572	0.4711	0.5276

TABLE 5.3: Average pressures during the AIMD simulations at the given degree of Br^-/S^{2-} site-exchange x, temperature T, and lattice scaling factors f. $\overline{p}_{\mathrm{AIMD}}$ has been obtained from the output of the AIMD simulations, whereas $p_{\mathrm{BM\text{-}EOS}}$ is obtained via the Birch-Murnaghan equation of state. All pressures are given in GPa.

x	T [K]	$f = 0.99$		$f = 1.00$		$f = 1.01$	
		$\overline{p}_{\mathrm{AIMD}}$	$p_{\mathrm{BM\text{-}EOS}}$	$\overline{p}_{\mathrm{AIMD}}$	$p_{\mathrm{BM\text{-}EOS}}$	$\overline{p}_{\mathrm{AIMD}}$	$p_{\mathrm{BM\text{-}EOS}}$
0%	700	0.18	−0.42	−0.36	−1.10	−0.81	−1.81
	800	0.31	−0.64	−0.24	−1.16	−0.68	−1.52
	900	0.43	−0.53	−0.10	−1.19	−0.53	−1.85
25%	700	0.08	−0.72	−0.43	−1.26	−0.83	−1.72
	800	0.22	−0.76	−0.29	−1.27	−0.70	−1.68
	900	0.35	−0.74	−0.16	−1.25	−0.57	−1.67
50%	700	0.05	−0.81	−0.45	−1.31	−0.84	−1.72
	800	0.19	−0.85	−0.31	−1.30	−0.71	−1.59
	900	0.32	−0.82	−0.18	−1.26	−0.59	−1.51

5.3.5 Haven Ratio

Another aspect which is commonly neglected is the Haven ratio H that connects the tracer diffusion coefficient D^* with the conductivity diffusion coefficient D_σ, as discussed in more detailed in Section 3.6.4. This is because D_σ can only be reasonably calculated if good statistics are available, which requires the calculation of long and/or many trajectories and the extended AIMD simulations, mentioned in the previous section, qualify for the calculation of D_σ. Because the conditions for the simulations with $f = 0.99$ have been found to be correspond to the most reasonable pressure, we omit the analysis for the even more tensile conditions at $f = 1.00, 1.01$ in the following. Furthermore, the 0% structures were disregarded because insufficient Li^+ diffusion for a proper calculation of D_σ was reached.

For improved statistics, the AIMD simulations of the 25% and 50% structures were evaluated using a moving average approach: Each extended AIMD run was first segmented into smaller intervals. The interval length was chosen to be 75 ps and the starting points of the intervals were chosen to increment with 25 ps steps. Therefore, intervals according to [0:75], [25:100], [50:125], ... were obtained. Next, the mean squared displacement of the center of mass of all Li^+ ions, $\mathrm{MSD}_{\mathrm{CoM}}$, was calculated for every interval, while taking into account the relative shift of the center of mass of the anion matrix. Finally, the $\mathrm{MSD}_{\mathrm{CoM}}$ of all corresponding intervals were averaged and are shown in Figure 5.17. The slopes of linear regressions (dashed lines) were used to determine D_σ. They are listed in Table 5.4 together with the resulting Haven ratios, which amount to 0.5 – 0.8. These are typical values observed for SEs.[410,429]

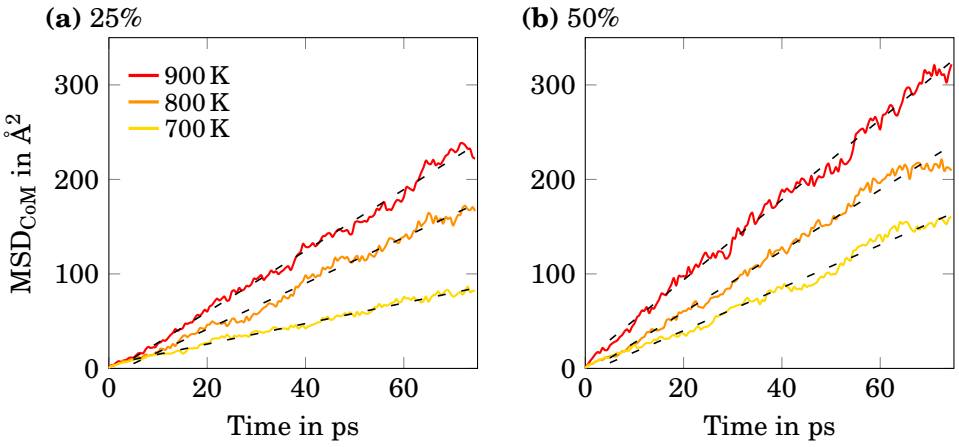

FIGURE 5.17: Evolution of the Li^+ MSD_{CoM} in Li_6PS_5Br with (a) 25% and (b) 50% Br^-/S^{2-} site-exchange. Every curve represents an average MSD_{CoM} computed based on several intervals of the AIMD simulation.

x	T [K]	D_σ [Å^2/ps]	H
25%	700	0.1809	0.815
	800	0.4046	0.519
	900	0.5401	0.582
50%	700	0.3781	0.533
	800	0.5395	0.541
	900	0.7066	0.647

TABLE 5.4: Charge diffusion coefficients D^σ obtained from the extended AIMD simulations and resulting Haven ratios H at 25% and 50% Br^-/S^{2-} site-exchange x and temperatures T. 1 Å^2/ps $= 10^{-4}$ cm^2/s.

Note that we omitted the depiction of the statistical deviations to keep Figure 5.17 clear. Still, the MSD_{CoM} for the individual intervals fluctuates heavily: We estimate that our calculated values for MSD_{CoM} and H might be subjected to errors of up to 50%. Even more rigorous calculations, that could not be afforded here, would be needed to lower the statistical uncertainties.

5.4 Diffusion Mechanism at Low Degrees of Site-Exchange

Based on the previous sections we clearly see that improved Li^+ transport can be achieved solely by the introduction of Br^-/S^{2-} site-exchange. The exact atomistic mechanism behind the improvement, however, remained unclear so far. Therefore, we thoroughly analyzed the Li^+ motion around the anion sites where Br^-/S^{2-} have been exchanged by conducting AIMD simulations at 600 K. More specifically, and to approach this issue step by step, the problem has been divided into individual sub-problems first: (i) a S^{2-} occupying a Br^- site on

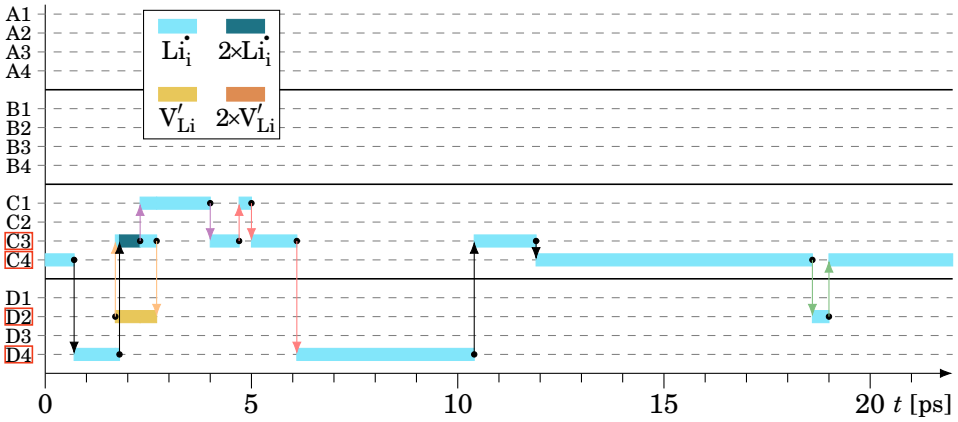

FIGURE 5.18: Flowchart illustrating all observed Li^+ intercage jumps during a simulation at 600 K containing a S'_{Br} defect compensated with a $Li_i^\bullet$. Arrows indicate the jump of a Li^+ ion from one cage to another. Arrows of the same (non-black) color indicate subsequent jumps of the same Li^+ ion. Colored bars indicate the presence and number of $Li_i^\bullet$ and V'_{Li} in the respective cages. The cage labels framed in red indicate the neighboring cages of the S'_{Br} defect.

4*a* (in Kröger-Vink notation: S'_{Br}); (ii) a Br^- occupying a S^{2-} site on 4*d* ($Br_S^\bullet$); (iii) both defects simultaneously. Charge compensation for the individual anion defects was ensured by adjusting the Li^+ content.

5.4.1 S'_{Br} – A Sink for Interstitials

To analyze the influence of a single S'_{Br} defect, we prepared a $\sqrt{2}\times\sqrt{2}\times2$ supercell, removed one Br^- from a 4*a* site and replaced it with S^{2-}. In the following, we will again refer to labels A1, A2, ..., D4 for the various 4*d* site as introduced in Figure 5.9. According to this notation, the chosen 4*a* site that hosts the S'_{Br} defect is located in the center of the tetrahedron spanned by its neighboring 4*d* sites on C3, C4, D2 and D4. To not deal with a charged system, a $Li_i^\bullet$ was added in the vicinity of S'_{Br}. Strictly speaking, this changes the stoichiometry of Li_6PS_5Br to $Li_{6+x}PS_{5+x}Br_{1-x}$ with $x = 0.0625$.

Next, AIMD simulations were executed and the movements of all Li^+ ions were inspected. To only focus on the long-range transport, intercage jumps have exclusively been monitored for the following analysis and doublet and intracage jumps have been disregarded. Nevertheless, doublet and intracage jumps are observed throughout all simulations and occur simultaneously with intercage jumps, permanently leading to a highly concerted Li^+ motion.

The monitored intercage jumps for a simulation containing a S'_{Br} defect are summarized in Figure 5.18. A second, independent simulation delivers similar results. The labels framed in red indicated the 4*d* positions next to the S'_{Br} defect.

The additional Li^+, which was placed close to the S'_{Br} in the initial configuration as charge compensation, can be considered as a $Li_i^{\bullet}$ and immediately jumps to C4 at the start of the simulation. Only in the early stages of the simulation, after approximately 2 ps, the formation of an additional Frenkel pair is observed for less than 1 ps.

In the rest of the simulation, all Li^+ intercage jumps are governed by an interstitial-mediated diffusion mechanism and a more detailed analysis reveals the following conclusion: With one $Li_i^{\bullet}$ present, seven Li^+ can be attributed to the respective cage. One of these Li^+ then jumps to a neighboring cage. This is illustrated as jump *A* with a blue arrow in Figure 5.19 (a). As next the step, different possibilities have then been observed in the simulations:

1. The jumping Li^+ does not truly complete jump *A*. Instead, it immediately performs a back-jump to its originating cage. Such a jump typically happens within fractions of ps. An example of such a jump can be seen at approximately 19 ps in Figure 5.18 for the jump sequence C4→D2→C4.

2. The jumping Li^+ manages to complete jump *A* to a new cage. The new cage now comprises the $Li_i^{\bullet}$ and serves as origin for the following interstitial jump. Such a jump is indicated as jump *B* in Figure 5.19 (a). Depending on the time between jump *A* and *B*, the diffusion mechanism can be further divided:

    a) If the time between jump *A* and *B* is comparably long (more than a few ps), both jumps can be considered as independent events. An example of such a jump is the jump sequence C3→D4→C3 starting at a simulation time of approximately 6 ps in Figure 5.18. In this case, the $Li_i^{\bullet}$ remains for more than 4 ps on D4 before further jumps are initiated. For such independent events, jump *B* can then also be performed by the same Li^+ that performed jump *A*.

    b) If the time between following jumps is short (up to few ps) and jump *B* is performed by a different Li^+, this sequence resembles an interstitialcy mechanism, where the arriving Li^+ displaces another Li^+ to an interstitial site. The interstitialcy mechanism was reported as an important diffusion mechanism in other SEs[430–432] and examples of such jumps are found especially in the early stages of the simulation in Figure 5.18.

3. The jumping Li^+ does not properly thermalize in the new cage and, instead of performing a back-jump, directly travels to a further cage as illustrated in Figure 5.19 (b). For such an event, the residence time in the intermediate cage is typically in the range of 1 ps. An example of such a jump is observed for the jump sequence C1→C3→D4 starting at approximately 5 ps.

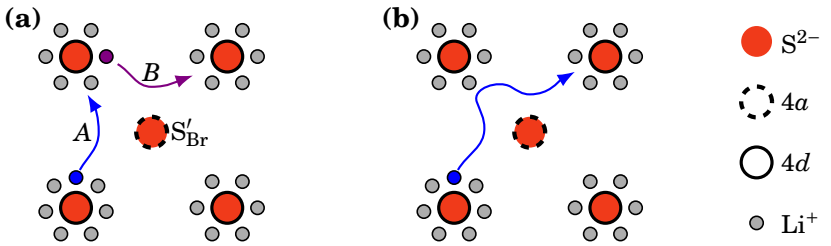

FIGURE 5.19: Illustration of the main jump sequences for successful intercage jumps. (a) Interstitial jumps that, depending on the time between jump *A* and *B*, can be considered as individual interstitial jumps or an interstitialcy mechanism. (b) Consecutive interstitial jumps (also back-jumps possible) of the same Li^+. Note that the real configuration of the structure, where the 4*a* site is actually tetrahedrally coordinated by the 4*d* sites, is strongly simplified in this two-dimensional representation.

Notably, the $Li_i^\bullet$ is predominantly present in the cages C3, C4, D2 and D4. These are directly adjacent to the S'_{Br} defect and we conclude that the S'_{Br} defect can be considered as a sink for Li^+ interstitials. This can be easily understood, as the S'_{Br} defect represents an additional negative charge on the 4*a* site compared to its original Br^-. The $Li_i^\bullet$, on the contrary, contributes an additional positive charge and will be attracted by the S'_{Br} defect, preferentially staying in its orbit. Still, also intercage jumps involving cages not directly adjacent to the S'_{Br} defect have been observed. For the simulation represented in Figure 5.18 this involved C1.

Finally, we note that the tendency for a spontaneous Frenkel pair formation, compared to the 0% structure at the same temperature, seems to be increased. One such example can be seen in the very beginning of Figure 5.18. Also in a second, independent simulation that confirms the aforementioned results, the spontaneous formation of Li^+ Frenkel pairs was observed occasionally. In most cases, their lifetime is short and they are annihilated by a back-jump or another traveling $Li_i^\bullet$ after few picoseconds. Still, this leads to the conclusion that the formation of Li^+ Frenkel pairs is slightly facilitated in the presence of a S'_{Br} defect.

5.4.2 $Br_S^\bullet$ – The Initiator of Li^+ Frenkel Pairs

Let us now turn to $Br_S^\bullet$, the counterpart of a S'_{Br} defect. A $Br_S^\bullet$ defect was created by replacing one S^{2-} on a 4*d* site with Br^-. Specifically, we chose the C3 site for the location of the $Br_S^\bullet$ defect. Charge compensation was ensured by removing one Li^+ from the C3 cage, i.e., by creating a V'_{Li} in the cage that belongs to the $Br_S^\bullet$ defect. The same analysis as described for the S'_{Br} defect was then performed and the obtained flowcharts of two independent simulations are shown in Figure 5.20.

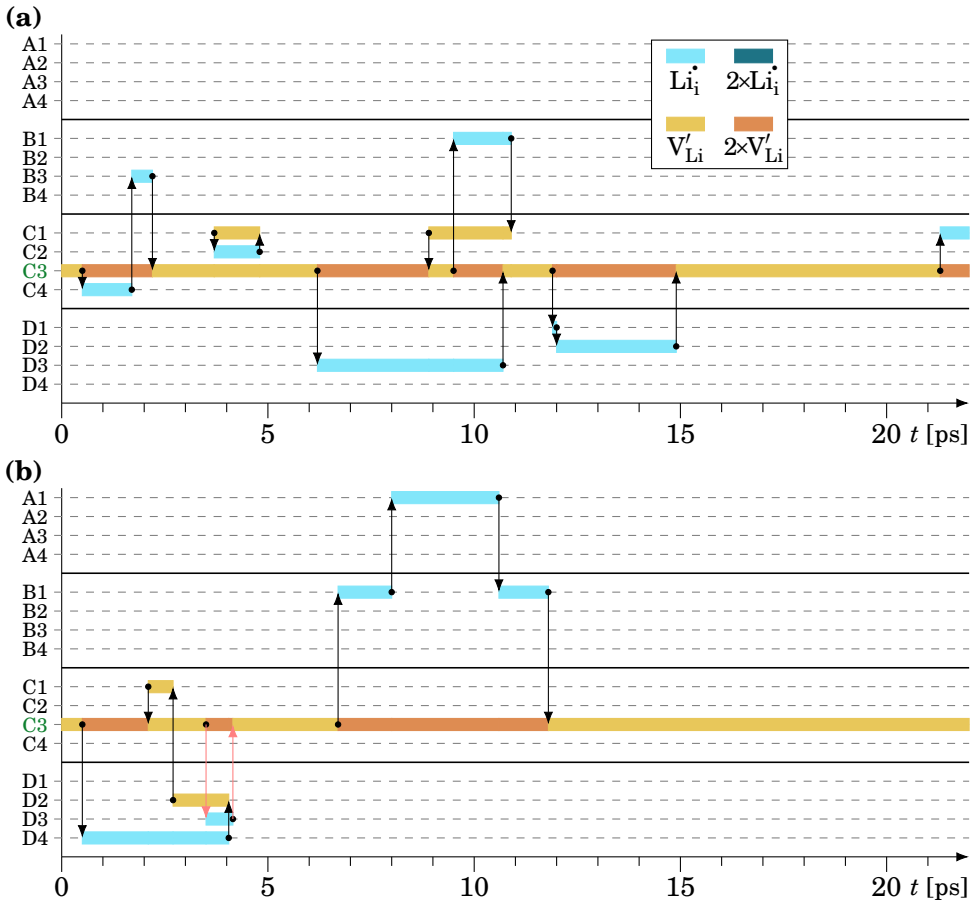

FIGURE 5.20: (a) Flowchart illustrating all observed Li^+ intercage jumps during a simulation at 600 K containing a $Br_S^{\bullet}$ defect, compensated with a V'_{Li}. Arrows indicate the jump of a Li^+ ion from one cage to another. Arrows of the same (non-black) color indicate subsequent jumps of the same Li^+ ion. Colored bars indicate the presence and number of $Li_i^{\bullet}$ and V'_{Li} in the respective cages. The cage label C3 is shown in green and marks the location of the $Br_S^{\bullet}$ defect. (b) Flowchart of a second, independent run.

Interestingly, we find that the $Br_S^{\bullet}$ defect leads to the generation of a Li^+ Frenkel pair. As examples, such processes are observed directly at the beginning in both flowcharts: The C3 cage, belonging to $Br_S^{\bullet}$ defect, donates one of its Li^+ to one of its 12 neighboring cages. This happens despite the fact that charge compensation has already been ensured by the creation of one V'_{Li} in C3. As a result, the cage around $Br_S^{\bullet}$ is left with only four Li^+, i.e., it contains two V'_{Li}, and a $Li_i^{\bullet}$ is formed in one of the neighboring cages. Once a Frenkel pair has been generated, three different processes concerning the $Li_i^{\bullet}$ have been observed:

1. As frequently observed, it can perform a back-jump and return to the cage around $Br_S^{\bullet}$ to recombine with one of the two V_{Li}'. In the majority of cases, the Li^+ ion that performs the back-jump is not the same as the initially generated $Li_i^{\bullet}$. This is most likely due to the high mobility of Li^+ within the cages: The Li^+ ions have rearranged their positions within the cage before a back-jump happens.

2. It can jump to a different neighboring cage. Such jumps are mostly governed by an interstitialcy mechanisms. Examples are the jump sequences C3→C4→B3→C3 and C3→D1→D2 at the beginning and at approximately 12 ps in Figure 5.20 (a), respectively. Similarly, also in Figure 5.20 (b) the sequence C3→B1→A1→B1→C3 contains interstitialcy jumps. Because the residence time of the $Li_i^{\bullet}$ on A1 is comparably long (> 3 ps) in this case, the A1→B1 jump is considered as an independent event and assigned to an interstitial mechanism.

3. It can fill a different cage than one around the Br^-/S^{2-} defect containing a V_{Li}'. Such cages are formed if the two V_{Li}' around the $Br_S^{\bullet}$ defect are able to attract a Li^+ from a pristine, neighboring cage. This diffusion process can also be considered as a vacancy-mediated mechanism. Cages with a V_{Li}' other than the one around the $Br_S^{\bullet}$ defect, however, are hardly present during the simulation, leading to the conclusion that V_{Li}' represents a rather immobile defect compared to $Li_i^{\bullet}$.

Figure 5.21 graphically summarizes the observed diffusion mechanisms. In conclusion, the $Br_S^{\bullet}$ defect is able to frequently generate Li^+ Frenkel pairs with a rather mobile $Li_i^{\bullet}$ mainly jumping between the 12 nearest-neighbor cages, while the V_{Li}' is rather immobile and mostly remains adjacent to the $Br_S^{\bullet}$ defect. The S_{Br}' defect, for comparison, mainly only enabled Li^+ transport among its four surrounding cages, which was only possible via the addition of a $Li_i^{\bullet}$. Therefore, Li^+ transport over an extended spatial area is enabled with the introduction of only one $Br_S^{\bullet}$ defect.

These observations fit to reports of Wang *et al.*,[214] who showed that improved ionic conductivities are achieved when increasing x in $Li_{6-x}PS_{5-x}Br_{1+x}$. Naturally, these Br-rich argyrodites will comprise more $Br_S^{\bullet}$ defects with rising x. According to our findings, this will lead to improved Li^+ diffusion via the generation of Frenkel pairs with mobile $Li_i^{\bullet}$ and is likely to explain the increased ionic conductivities at least for small x. At larger x the increasing amount of structural Li^+ vacancies may change the dominating diffusion mechanism.

5.4.3 Combining S_{Br}' and $Br_S^{\bullet}$

In the previous sections, the individual effects of S_{Br}' and $Br_S^{\bullet}$ defects have been studied. For reasons of charge neutrality, however, the Li content needed to be adjusted, which could have influenced the diffusion mechanism. To eliminate

this uncertainty, we combined one S'_{Br} and one $Br^{\bullet}_{S}$ defect in the same structural model. This preserves the Li_6PS_5Br stoichiometry and does not require compensation schemes. For the used supercell size, the combination of one S'_{Br} and one $Br^{\bullet}_{S}$ defect corresponds to a Br^{-}/S^{2-} site-exchange of 6.25% and can be realized in four symmetrically inequivalent defect configurations. All four of them have been analyzed and consistent results have been obtained.

The flowchart of one representative simulation is shown in Figure 5.22. Here, the $Br^{\bullet}_{S}$ defect was placed on A2 and S'_{Br} is located in the center of the tetrahedron delimited by C3, C4, D1 and D3 sites. The initial Li^{+} distribution started with six Li^{+} around every 4*d* site. Apparently, this distribution is unfavorable, as after only 1.5 ps the $Br^{\bullet}_{S}$ defect initiates the formation of a Frenkel pair. Remarkably, the cage associated to the $Br^{\bullet}_{S}$ defect retains at least one V'_{Li} over the entire course of the remaining simulation.

The generated $Li^{\bullet}_{i}$ performs a few intercage jumps and reaches the neighborhood of the S'_{Br} defect at a simulation time of approximately 14 ps. Form this point on, the $Li^{\bullet}_{i}$ remains in the vicinity of the S'_{Br} defect and the intracage jumps are restricted to the cages C3, C4, D1 and D3. Meanwhile, a second Frenkel pair is occasionally initiated by the $Br^{\bullet}_{S}$ defect, but is annihilated only shortly afterward. Similarly, also in the vicinity of the S'_{Br} defect additional Frenkel pairs with short lifetimes are observed.

As indicated with arrows of the same color, several jump events are performed by the same Li^{+} ion within a short timespan. In many cases, these

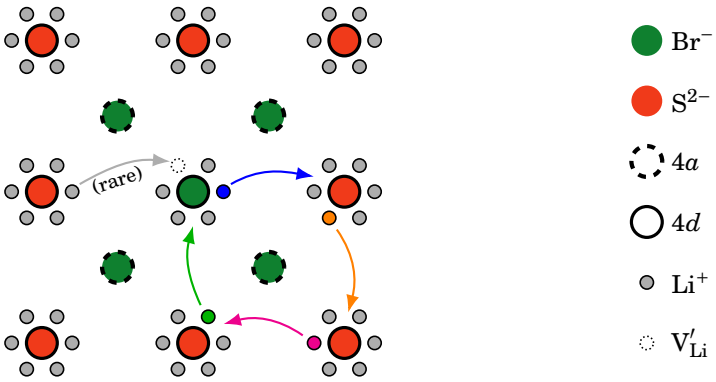

FIGURE 5.21: Main diffusion mechanism of intercage jumps initiated by a $Br^{\bullet}_{S}$ defect (center). The $Br^{\bullet}_{S}$ defect leads to the generation of Li^{+} Frenkel pairs. As a result, one Li^{+} (blue) is donated to the surrounding. This generated $Li^{\bullet}_{i}$ can either perform a back-jump (not shown) or travels further to another cage. In this regard, mostly interstitialcy jumps, but also interstitial jumps, have been observed (colored arrows and Li^{+}). The V'_{Li} left in the cage around the $Br^{\bullet}_{S}$ defect is rather immobile. Only when two V'_{Li} are present around the $Br^{\bullet}_{S}$ defect, a Li^{+} from a pristine, neighboring cage is attracted and fills one of the two V'_{Li} (gray arrow).

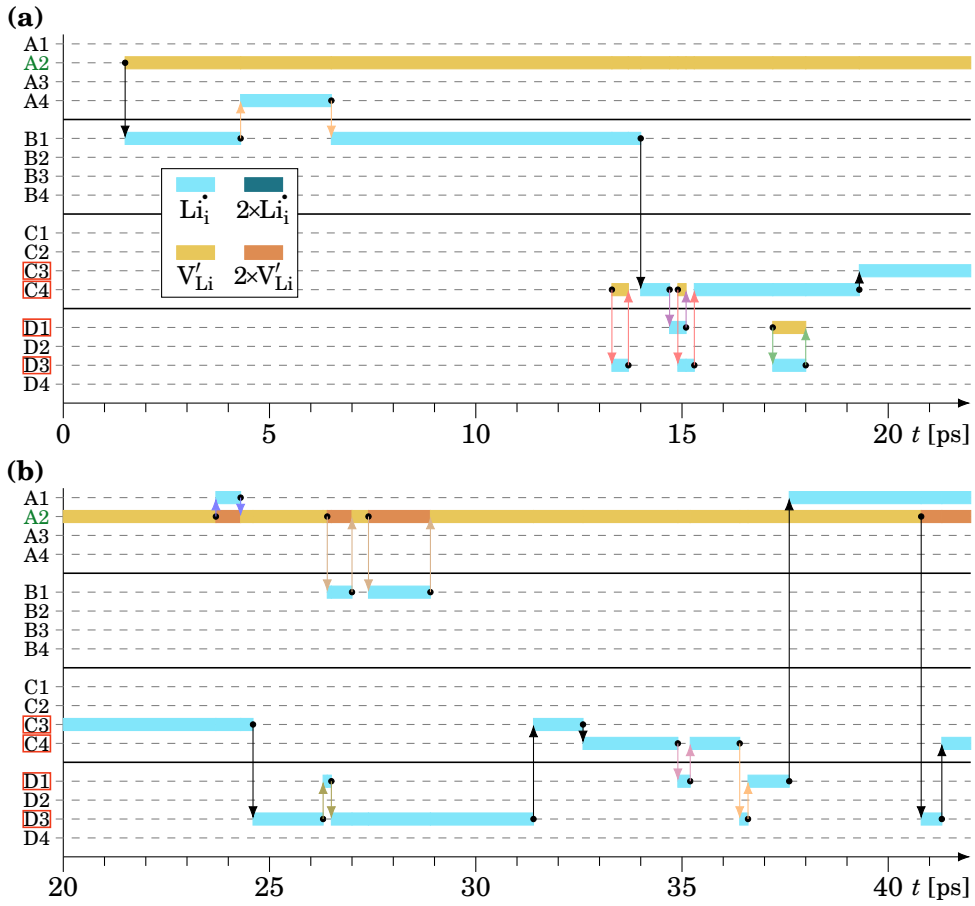

FIGURE 5.22: (a) Flowchart illustrating all observed Li^+ intercage jumps during a simulation at 600 K containing both a S'_{Br} and a $Br_S^\bullet$ defect. Arrows indicate the jump of a Li^+ ion from one cage to another. Arrows of the same (non-black) color indicate subsequent jumps of the same Li^+ ion. Colored bars indicate the presence and number of $Li_i^\bullet$ and V'_{Li} in the respective cages. The cage label A2 is shown in green and marks the location of the $Br_S^\bullet$ defect. The labels framed in red indicate the neighboring cages of the S'_{Br} defect. (b) Flowchart of a second, independent run.

are related to jumps followed by an immediate back-jump, indicating that the diffusion of interstitials is considerably correlated.

In summary, the observations for the combined S'_{Br} and $Br_S^\bullet$ defects corroborate the conclusions that have been drawn when analyzing the individual anion defects in the previous sections: The $Br_S^\bullet$ defect is the main source of Li^+ Frenkel pairs with mobile $Li_i^\bullet$. Frequently, the $Br_S^\bullet$ defect even initiates a second, typically short-lived, Li^+ Frenkel pair. The S'_{Br} defects acts as sink for $Li_i^\bullet$, confining the intercage jumps mostly to its vicinity. Occasionally, the S'_{Br} defect also seems to disturb its surrounding and leads to further, short-lived Li^+ Frenkel pairs.

There is one additional aspect that for clarity is not included in the flowcharts. This concerns the allocation of jumping Li^+ ions to our labeled cages: Occasionally, when a Li^+ jump was registered, we could not clearly assign the jumping Li^+ ion to one of the cages. Instead, the Li^+ stopped halfway between two cages on an interstitial position for a short but non-negligible time. Because such jumps always occurred in the vicinity of the S'_{Br} defect, they mark the onset of the cage shifting toward the 4*a* site. Therefore, our approach to follow the movements of the Li^+ defects from cage to cage is only meaningful at low degrees of Br^-/S^{2-} site-exchange, where the cages are well defined and centered around the 4*d* sites.

5.5 Changes in the Li^+ Substructure

At the end of the previous section, we mentioned interstitial sites that were observed to get occupied in the vicinity of S'_{Br} defects. Naturally, this raises the question of how the Li^+ substructure is influenced by Br^-/S^{2-} site-exchange. Such an analysis can be done in several ways. Our approach, and the outline of this section, is as follows: First, we analyzed how the occupancies of the tetrahedral Li^+ sites change for the structural models that contain the individual and combined S'_{Br} and $Br^{\bullet}_{S}$ defects. Next, the analysis is extended to higher degrees of Br^-/S^{2-} site-exchange. Finally, we discuss how the globally averaged Li^+ density, which is a suitable quantity for the comparison with the experiment, changes as a function of the site-exchange.

5.5.1 Influence of S'_{Br} and $Br^{\bullet}_{S}$ on Tetrahedral Occupancies

For the calculation of tetrahedral occupancies, `OVITO` was used to computed time-averaged Li^+ densities using the full course of every simulation. The Li^+ density was then mapped to the tetrahedral sites to obtain their occupancies. We furthermore selectively inspected the 4*a* and 4*d* sites: For every 4*a* and 4*d* site we tracked the average number of Li^+ ions N_{Li} on only their adjacent tetrahedral sites. Additionally, we further distinguish the 4*a* and 4*d* sites based on their occupying anion, Br^- or S^{2-}. This enables us to draw conclusion about the local changes in the Li^+ substructure.

There is, however, one complication in our approach that needs to be noted: Both the T2 and the T5 tetrahedral sites are adjacent to both the 4*a* and 4*d* sites (see Section 2.2.1 for a revision of the tetrahedral sites). As such, the corresponding site occupancies are counted twice – once from the 4*a* perspective and once from the 4*d* perspective.

The determined values of N_{Li} for the defect-free system, the systems with individual anion defects (and their compensating Li^+ defects), and the combined defects (corresponding to a site-exchange of 6.25%) are shown in Figure 5.23. First, we find that the T1 and T3 sites do not play a role in the occupancy of tetrahedral Li^+ sites for the shown structure models at 600 K. Second, for the

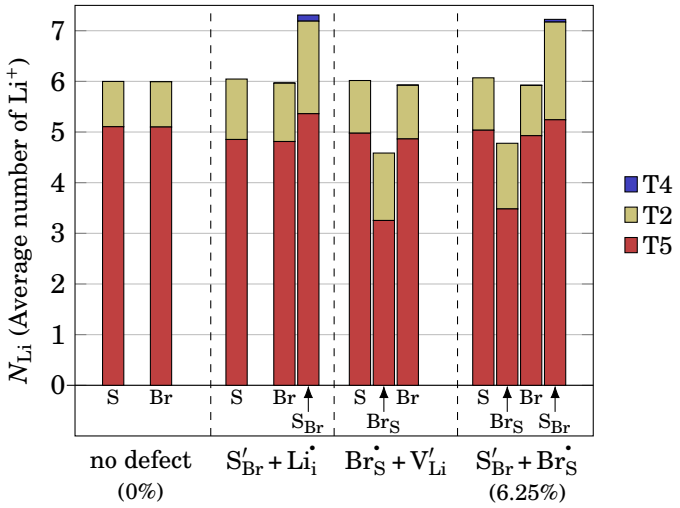

FIGURE 5.23: The average number of Li^+ ions N_{Li} present in the tetrahedral T2, T4 and T5 sites adjacent to the specified anion-site-combination at 600 K. Note that the Kröger-Vink notation for the charge states in the labels directly below the bar plots has been omitted for improved readability. The abbreviations are: S = $S^{\times}_S$ (regular S^{2-} on 4*d* sites); Br = $Br^{\times}_{Br}$ (regular Br^- on 4*a* sites); S_{Br} = S'_{Br} ; Br_S = $Br^{\bullet}_S$.

0% structures there are exactly 6.0 Li^+ around each regular $S^{\times}_S$ site (S^{2-} on 4*d*, labeled as S in Figure 5.23). This fits perfectly to the picture of well defined Li^+ cages around 4*d*, composed of six Li^+ as described in Section 5.3.1. The majority of time, the Li^+ ions reside in the T5-T5a-T5 triplets ($N^{T5}_{Li} \approx 5.1$). However, also T2 sites become occupied ($N^{T2}_{Li} \approx 0.9$), which either happens due to extended thermal displacement at 600 K or in the course of intracage jumps.

The tetrahedral occupancies, accounted to the regular $Br^{\times}_{Br}$ sites (Br^- on 4*a*, labeled as Br in Section 5.3.1), deliver exactly the same results as for the $S^{\times}_S$ sites. This is reasonable because the regular anion arrangement in the 0% structure lead to well defined and uniform Li^+ cages. Only with the introduction of defects, the regular anion arrangement is disturbed and local changes in N_{Li} are induced.

Most notably, the introduction of a S'_{Br} defect leads to an increase of its N_{Li} to 7.3. This reflects its behavior as a sink for $Li^{\bullet}_i$. Because the value is larger than 7, S'_{Br} does not only attract the one $Li^{\bullet}_i$ that has been added to the system to ensure charge neutrality: It is able to attract additional Li^+ ions from the surrounding. Furthermore, we see that T4 sites, which are only adjacent to the 4*a* sites, become slightly occupied ($N^{T4}_{Li} = 0.12$) in the vicinity of the S'_{Br} defect. Presumably, this is because the S'_{Br} defect is able to attract the Li^+ ions more closely to the 4*a* sites than the Br^- can.

The local changes to the Li^+ substructure introduced by the S'_{Br} defect also slightly affect the average N_{Li} for the ordinary $S^{\times}_{S}$ and $Br^{\times}_{Br}$ sites. Notably, the occupancy of T2 sites increase. There are two contributions to that. First, the increased occupancies of T2 sites around the S'_{Br} defect, due to the attracted $Li^{\cdot}_{i}$ which also leads to increased occupancies of T2 sites for the adjacent Li^+ cages. Second, the increased number of intercage jumps that involve the T2 site.[183,207,208]

Similarly, generally increased T2 occupancies are also observed in the presence of a $Br^{\cdot}_{S}$ defect and its compensating V'_{Li}. The reasons are likely the same: The $Br^{\cdot}_{S}$ initiates a Li^+ Frenkel pair with a mobile $Li^{\cdot}_{i}$ and the presence of the $Li^{\cdot}_{i}$ in the cages and the increased number of intercage jumps lead to an overall increase of T2 occupancies. The generation of a Frenkel pair, despite the introduction of a compensating V'_{Li}, is reflected in $N_{Li} \approx 4.6$ for the cage around the $Br^{\cdot}_{S}$ defect.

Finally, the results for N_{Li} from combining $S'_{Br} + Br^{\cdot}_{S}$ in one simulation cell fit to the results of the individual defects. This fact again corroborates that our conclusions, drawn from analyzing the individual defects, are applicable to the combined system. Our approach proved that even rather complex relationships between structure and Li^+ transport can be understood if the problem is separated into its individual sub-problems.

5.5.2 Tetrahedral Occupancies at Increased Site-Exchange

Let us now compare how higher degrees of Br^-/S^{2-} site-exchange influence the occupancies of the tetrahedral site. These are shown in Figure 5.24 for all four combinations of the anions and sites. The variation of the occupancies of a certain anion-site combination can in all cases be explained based on the previous knowledge and depends on the changing environment as a function of the site-exchange.

In Figure 5.24 (a) the change of the occupancies adjacent to regular $S^{\times}_{S}$ sites on 4*d* is shown. Despite decreasing occupancies of the T5 sites, the large increase related to T2 sites leads to an overall increase of N_{Li} with increasing site-exchange. This is reasonable because increasing site-exchange leads to an increasing number of S'_{Br} defects (accompanied by a high N_{Li}) adjacent to the $S^{\times}_{S}$ sites. Therefore, the $S^{\times}_{S}$ profits from the increased number of Li^+ ions in its surrounding.

In contrast, Figure 5.24 (b) shows a decreasing N_{Li} around $Br^{\times}_{Br}$. The explanation is similar: With increasing site-exchange, the number of $Br^{\cdot}_{S}$ defects (accompanied by a low N_{Li}) increases in the vicinity of $Br^{\times}_{Br}$, leading to an overall decrease in its N_{Li}. Moreover, the neighboring $Br^{\cdot}_{S}$ defects on the 4*d* sites are less competitive than S'_{Br} defects with respect to the attraction of Li^+ ions. Despite a decreased N_{Li}, the $Br^{\times}_{Br}$ therefore manages to attract the surrounding Li^+ more closely, so that T4 sites become noticeably occupied.

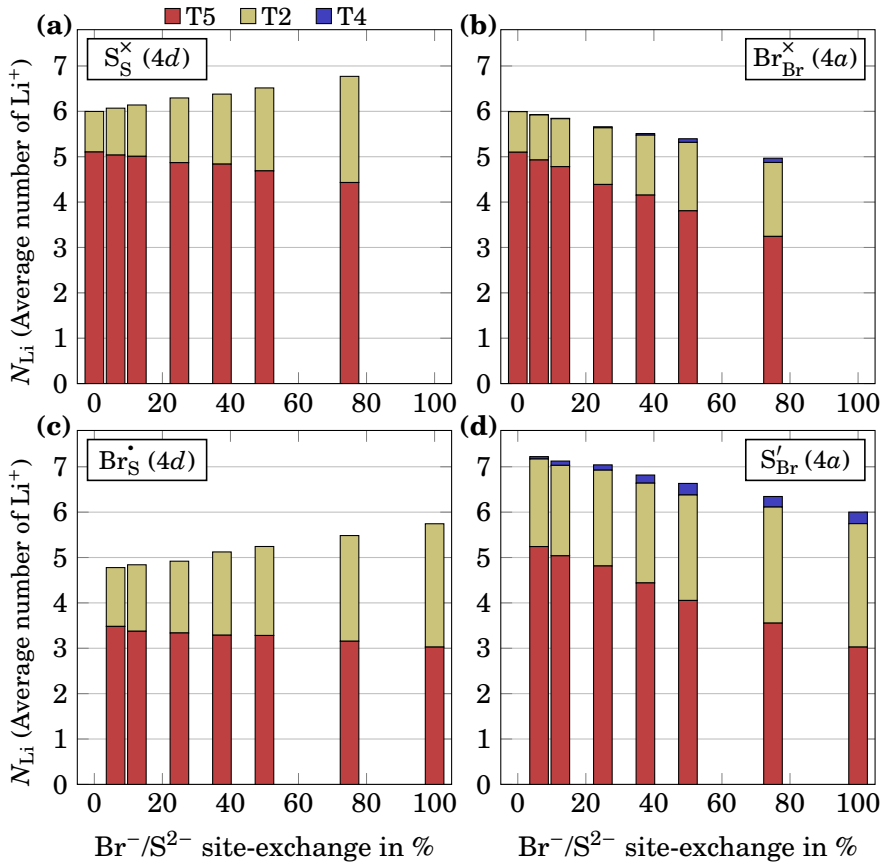

FIGURE 5.24: The average number of Li^+ ions N_{Li} present in the tetrahedral T2, T4 and T5 sites adjacent to the specified anion-site-combination at 600 K. Note that the absolute number of $S_S^{\times}$ and $Br_{Br}^{\times}$ sites decreases with increasing site-exchange, whereas the absolute number of $Br_S^{\bullet}$ and S'_{Br} defects increases with increasing site-exchange.

In Figure 5.24 (c) the occupancies in the vicinity of $Br_S^{\bullet}$ defects are shown. The trend is comparable to $S_S^{\times}$ and the same reasoning as above applies. The only difference is the generally lower extent of N_{Li}. This is due to the -1 charge of Br^-, which leads to a weaker attraction of Li^+ compared to the -2 charge of S^{2-}.

Likewise, the situation of the occupancies adjacent to S'_{Br} defects, shown in Figure 5.24 (d), is comparable to $Br_{Br}^{\times}$ with the difference of an overall increased N_{Li}. At 100% site-exchange, $N_{Li} = 6$ indicates that the cage shift toward the 4*a* is complete and that the cages around 4*a* involve T4 sites.

Our calculated occupancies of the T2 and T5 sites at 12.5% are in good agreement with measurements of Minafra *et al.* for Li_6PS_5Br at approximately 15% site-exchange. The trends of decreasing T5 and increasing T2 occupancies

are in line with calculations for Li_6PS_5Cl and Li_6PS_5I.[207] However, such clear trends could not be confirmed with neutron diffraction experiments at room temperature,[10] which presumably might be due to the elevated temperature of 600 K used for our analysis. Despite these small discrepancies, our results clearly prove that it is indeed the Br^-/S^{2-} site-exchange that not only regulates the transport properties of the Li_6PS_5Br but also has a profound influence on the Li^+ distribution.

5.5.3 Connection between Li^+ Distribution and Lattice Constants

At the beginning of this chapter, in Section 5.2.1, we have shown that the lattice constant depends on the Br^-/S^{2-} site-exchange and that the lowest lattice constant is obtained at 50% site-exchange. With the knowledge gathered in the previous sections, it is plausible to assume that the changing Li^+ distribution is connected to the lattice constant. In this regard, however, no obvious relation could be established during the analysis of the tetrahedral occupancies.

Experimentally, a change in the Li^+ substructure was found as well: The experimentally solved structures of Li_6PS_5Br, available with site-exchanges between 9.8% and 39.4%, mainly hint at shifting positions of the Li^+ sites together with slight variations in the occupancies.[9,10] To compare our data to the experiments, time-averaged Li^+ densities of all simulated supercell models were computed. Our plain Li^+ density, however, depends on the local structure as explained in the previous section, whereas common diffraction experiments are only able to solve structures in terms of the global average. Therefore, every time-averaged Li^+ density was used to calculate the spatial average by making use of the nominal cubic symmetry of Li_6PS_5Br and a representative Li^+ density was finally obtained as the average of the spatially averaged Li^+ densities of all structures with the same degree of Br^-/S^{2-} site-exchange.

A structural model of the 0% structure and its Li^+ density are shown in the left part of Figure 5.25. Gray spheres mark the position of the T5a sites and the T5-T5a-T5 triplets can be clearly identified. As indicated, the Li^+ density of the central slice is shown as a top view projection. The Li^+ density at the locations of the T2 sites is considerably lower than that of the T5 sites, which fits to the observations made during the analysis of the tetrahedral occupancies. This changes with increasing site-exchange: The occupancies of the T2 sites increase and, as indicated with arrows in Figure 5.25, the gap between the Li^+ densities of two neighboring 4*d* sites becomes smaller. This fits perfectly to the experimental results that show a decreasing distance between the T2 sites of neighboring cages.[10]

Moreover, the T5-T5a-T5 triplets, and with them also the cages around the 4*d* sites, start to dissolve with increasing site-exchange. Toward 100%, which lies outside of the experimentally accessible Br^-/S^{2-} site-exchange, a connected Li^+ density is formed between the 4*d* sites. This Li^+ density belongs to the

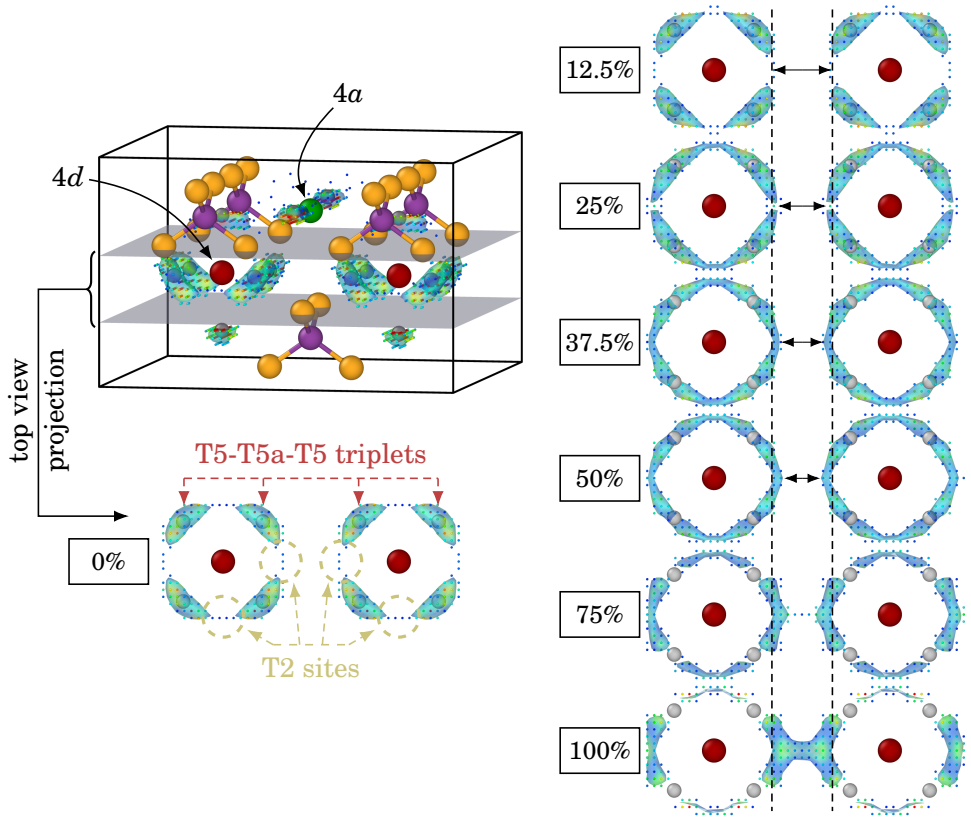

FIGURE 5.25: Projected Li^+ densities at different degrees of Br^-/S^{2-} site-exchange.

cages that are now formed around the 4*a* site. In analogy to the T5-T5a-T5 triplets, one could consider this as T2-T2a-T2 triplets or even extend the picture to T5-T2-T2a-T2-T5 quintuplets.

Let us return to the question of how the lattice constant is connected to the Li^+ substructure. To this end, it is best to compare the Li^+ density of the 0% structure to the 50% one. Whereas the Li^+ density is strongly localized to specific sites at 0%, it is more homogeneous at 50%. In other words, the Li^+ ions are able to spread to previously unoccupied sites. The more homogeneous distribution of Li^+ then leads to a reduced lattice constant.[10] Toward 100%, the lattice constant increases again because a localized Li^+ density is recovered.

There is, however, one apparent mismatch between the calculated Li^+ density and our previous data: The obtained values for N_{Li} during the analysis of the occupancies of the tetrahedral sites showed that the number of Li^+ ions strongly varies on a local scale. N_{Li} therefore depends on the type of the anion, its site, and the surrounding anions. The latter are dictated by the extent of the Br^-/S^{2-} site-exchange. During the spatial averaging of the Li^+ densities,

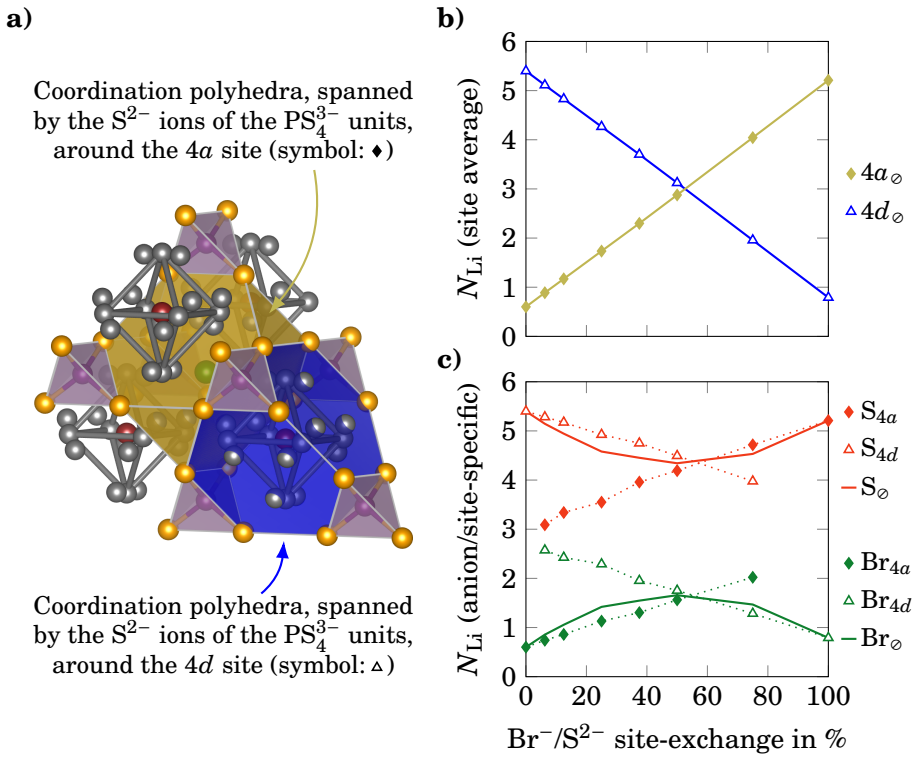

FIGURE 5.26: (a) Structural model of Li_6PS_5Br that indicated the coordination polyhedra around the 4*a* and 4*d* sites. (b) Average N_{Li} inside the respective coordination polyhedra. (c) Anion- and site-specific contributions to N_{Li}.

however, such localized regions with increased or depleted Li^+ densities cancel each other out and a homogeneous Li^+ density is obtained. What is the reason for this mismatch and how can we connect these two views?

To answer these questions, we have tackled the Li^+ distribution from another perspective and compartmented the regions around the 4*a* and 4*d* sites as shown in Figure 5.26 (a). The shown coordination polyhedra are spanned by the S^{2-} ions of the PS_4^{3-} units. We then counted the number of Li^+ ions, N_{Li}, within the coordination polyhedra. This approach avoids the double counting of Li^+ ions located on the T2 and T5 sites as explained in Section 5.5.1.

Figure 5.26 (b) illustrates the averaged N_{Li} around the 4*a* and 4*d* sites. Clearly, a linear trend is observed. On the 4*d* sites the average N_{Li} decreases from 5.4 at 0% to 0.8 at 100%. In contrast, it increases from 0.6 at 0% to 5.2 at 100% for the 4*a* sites. The crossing point is located slightly above 50% site-exchange. At a first glance, this data proves the more homogeneous distribution of the Li^+ ions toward 50% site-exchange: on average, half of the Li^+ ions reside

in the coordination polyhedra around the 4*a* sites, the other half around the 4*d* site.

Still, the average N_{Li} shown in Figure 5.26 (b) neglects the local inhomogeneities of the Li^+ distribution. Therefore, we disentangled N_{Li} further and show the different contributions of the anions and sites in Figure 5.26 (c). Indeed, the data reveals that the Li^+ density is not as homogeneous as the average N_{Li} implies. This is because, due to the -2 charge state, the S^{2-} ions will inherently attract more Li^+ ions than the Br^- ions. Nevertheless, the site-exchange truly leads to a more homogeneous distribution of the Li^+ ions as $N_{\mathrm{Li}}^{\mathrm{S}_{4a}} \approx N_{\mathrm{Li}}^{\mathrm{S}_{4d}} \approx 4.3$ and $N_{\mathrm{Li}}^{\mathrm{Br}_{4a}} \approx N_{\mathrm{Li}}^{\mathrm{Br}_{4d}} \approx 1.7$ at 50% site-exchange. Based on these results we can confidently connect a Br^-/S^{2-} site-exchange toward 50% to a more homogeneous Li^+ substructure among the 4*a* and 4*d* site, which leads to a shrinking lattice constant of Li_6PS_5Br.

5.6 Influence of Grain Boundaries on Li^+ Diffusion

In this last section, the influence of GBs on the Li^+ transport properties of Li_6PS_5Br is analyzed. We restrict the analysis to a small set of Σ5 twist and tilt GBs that could be reasonably handled with DFT calculations and even allow for the treatment of Br^-/S^{2-} site-exchange. We will first address stoichiometric twist GBs with 0% and 50% site-exchange. Afterward, tilt GBs will be discussed. For these models, site-exchanges of 0%, 25% and 50% site-exchange were realized and off-stoichiometric GBs were treated. Finally, we present the attempts to characterize the anisotropy

5.6.1 Σ5 Twist Grain Boundaries

Figure 5.27 shows the basic setup of the modeled Σ5 twist GBs. For clarity, the figure only shows a model with 0% site-exchange, but also seven other structures with 50% site-exchange have been treated. AIMD simulations were performed to analyze the Li^+ diffusion at different temperatures. Moreover, the atomic positions after approximately 100 ps at 500 K were statically optimized to determine the total energies based on a more reasonable Li^+ distribution. These energies have been used to calculate GB energies γ_{GB} in two different ways: First, we used the ground state of the bulk material with 0% site-exchange and obtain $\gamma_{\mathrm{GB}}^{0\%} = 262\ \mathrm{mJ/m^2}$ and $\gamma_{\mathrm{GB}}^{50\%} = 274\ \mathrm{mJ/m^2}$ for the 0% and 50% structures, respectively. Interestingly, if $\gamma_{\mathrm{GB}}^{50\%}$ is calculated with respect to bulk Li_6PS_5Br at 50% site-exchange, a reduced value of $190\ \mathrm{mJ/m^2}$ results. This might indicate that the formation of GBs is facilitated, if Br^-/S^{2-} site-exchange is present in Li_6PS_5Br. For comparison, low-energy Σ3 and Σ5 tilt GBs in LLZO[433] and Li_3OCl[354] yield $520-730\ \mathrm{mJ/m^2}$ and $340-1040\ \mathrm{mJ/m^2}$, respectively, indicating that GBs in sulfide SEs are energetically less costly than in oxides.

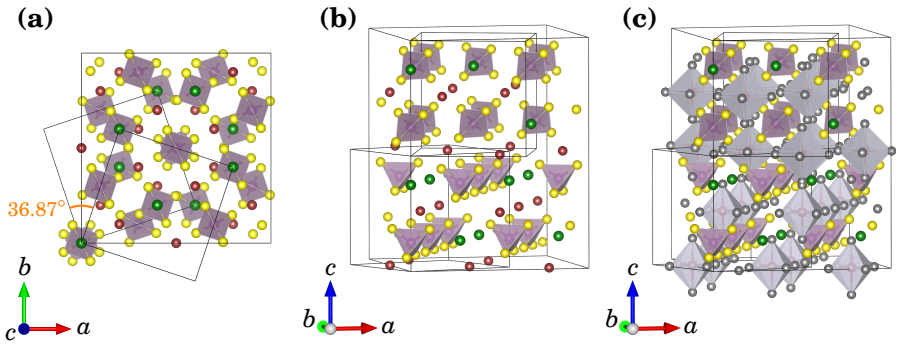

FIGURE 5.27: Basic structure of the modeled Σ5 twist GBs at 0% site-exchange. Additionally, seven models with 50% site-exchange were considered. (a) Top view with the underlying unit cells of the two slabs and their rotation angle. (b) Side view, where Li^+ ions are not shown for clarity. (c) The same structure as in (b) but including the Li^+ ions on the T5a sites. Li^+ ions that were close to each other have been merged prior to the calculations. The composition remained stoichiometric Li_6PS_5Br in all cases.

In terms of transport properties, Li^+ diffusion can be affected differently along or across GBs, leading to anisotropic diffusion coefficients that differ from the bulk. Such effects, however, are difficult to quantify for the present case as will be discussed in Section 5.6.3. Still, insights can be obtained by analyzing how the diffusion changes globally in the system and Figure 5.28 compares the MSD evolutions of the GB models to the ones of bulk Li_6PS_5Br. In part (a) and (b) the comparison of the 0% structures is shown. For temperatures of 500 and 600 K, the MSD appear to be rather similar. However, the MSD of the GB does not converge to the intracage diffusion limit as the bulk does. Instead, it constantly rises over the full simulated time span of approximately 100 ps (not shown). Based on the 700 K structure, the same trend can be observed already within 40 ps: the intracage diffusion limit is overcome in the presence of the GB. Likewise, the diffusion of Li^+ at 800 and 900 K is enhanced.

Contrary to the 0% structures, the comparison at 50% site-exchange in Figure 5.28 (c) and (d) shows that the twist GB leads to a slightly reduced MSD compared to the bulk. This trend does not change beyond the shown simulation time and indicates that the Σ5 twist boundary represents a slight obstacle to the Li^+ diffusion at 50% site-exchange.

We conclude that the Σ5 twist GB has an ambivalent character that depends on the extent of the Br^-/S^{2-} site-exchange: The twist GB improves the Li^+ transport at low degrees of site-exchange and slightly hinders it at higher values. Figure 5.29 indicates the reasons for the improved transport at 0% site-exchange. The figure depicts the individual Li^+ trajectories of only those seven Li^+ ions that were found to travel farther than 7 Å during the simulation at 600 K. Six of these seven trajectories involve the GB regions. This leads

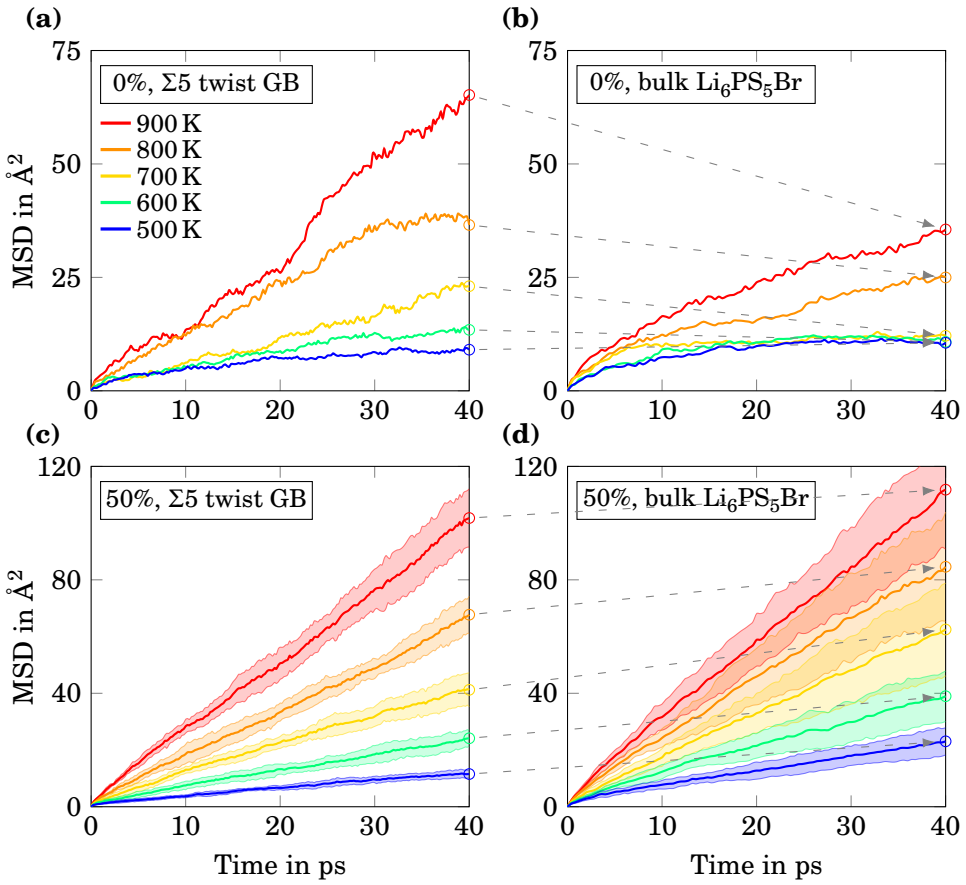

FIGURE 5.28: Comparison of the MSD evolution of the tilt GB models (left plots) with bulk Li_6PS_5Br (right plots). Plots in the same row exhibit the same degree of Br^-/S^{2-} site-exchange as labeled in the upper left corners. Dashed arrows are used as a guide to the eye to compare the reached MSD at a simulation time of 40 ps.

to the explanation that the GB locally disturbs the environment of Li^+ cages. These disturbances are likely to initiate Li^+ jumps, presumably again due to a facilitation of the formation of Li^+ Frenkel pairs, close to the GB.

The explanation for the slightly decreased Li^+ diffusion at 50% is less straightforward. Possibly, the connection of Li^+ pathways are less favorable across the GB compared to the bulk material, as computationally shown for LLZO.[433] Most likely, this leads to higher migration barriers for the diffusion across the GB as measured for different sulfide SEs.[137,425,434]

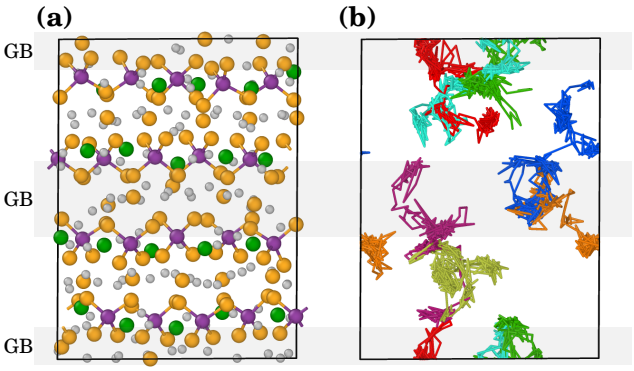

FIGURE 5.29: (a) Structural model of the Σ5 twist GB at 0% site-exchange. The GB region is indicated with a gray, transparent overlay. (b) Individual Li^+ trajectories of the seven Li^+ ions that have traveled farther than 7 Å during a simulation of approximately 100 ps at 600 K. All trajectories, except for the one shown in yellow, traverse the GB regions.

5.6.2 Σ5 Tilt Grain Boundaries

The basic structure of the Σ5 tilt GBs is illustrated in Figure 5.30. As can be seen at the interface in the center of the simulation cell, the two grains do not fit naturally in this setup. Instead, several ions are located close to each other and especially the PS_4^{3-} units overlap at the interface of the two grains. A simple, automated GB generation algorithm would certainly not be able to produce reasonable GB models based on such a complicated structure as for Li_6PS_5Br.

TABLE 5.5: Composition of the four GB models shown in Table 5.5 (a)–(d). The last column represents an alternative way of specifying the composition, motivated by the specific GB structure of the individual models.

GB model	Composition	Stoichiometric?	Alternative composition interpretation
(a) GB-1	$Li_{144}P_{24}S_{120}Br_{24}$	24 Li_6PS_5Br ✓	20 Li_6PS_5Br + 2 $Li_4P_2S_7$ + 6 Li_2S + 4 LiBr
(b) GB-2	$Li_{140}P_{24}S_{118}Br_{24}$	×	20 Li_6PS_5Br + 2 $Li_4P_2S_7$ + 4 Li_2S + 4 LiBr
(c) GB-3	$Li_{164}P_{20}S_{122}Br_{20}$	×	20 Li_6PS_5Br + 22 Li_2S
(d) GB-4	$Li_{160}P_{24}S_{120}Br_{20}$	×	20 Li_6PS_5Br + 20 Li_2S

We manually modified the basic GB structure to obtain a more reasonable interfaces. The resulting four GB models are shown in Figure 5.31. GB-1 is stoichiometric in the sense that the overall composition of the system matches Li_6PS_5Br. Based on the local structure, however, an alternative way of specifying the composition might also be meaningful and is listed in Table 5.5. This is because the two PS_4^{3-} units that overlapped with one of their corners (blue box in Figure 5.30) in the basic structure were combined to form a $P_2S_7^{4-}$ unit. As such, the interface may seem to contain traces of $Li_4P_2S_7$. Moreover, the two completely overlapping PS_4^{3-} units (red box in Figure 5.30) were merged into one single PS_4^{3-} unit at the interface. By removing one formula unit of Li_2S at each interface the structural model for GB-2 was generated. The structures of

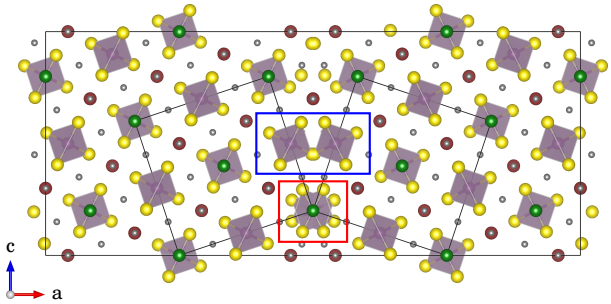

FIGURE 5.30: Basic structure of the Σ5 tilt GBs. The underlying tilted unit cells are indicated. In this basic structure, several ions are very close to each other. Moreover, PS_4^{3-} units overlap at their corners (blue box) or overlap completely (red box). Note that the interface is mirrored at the borders of the simulation box.

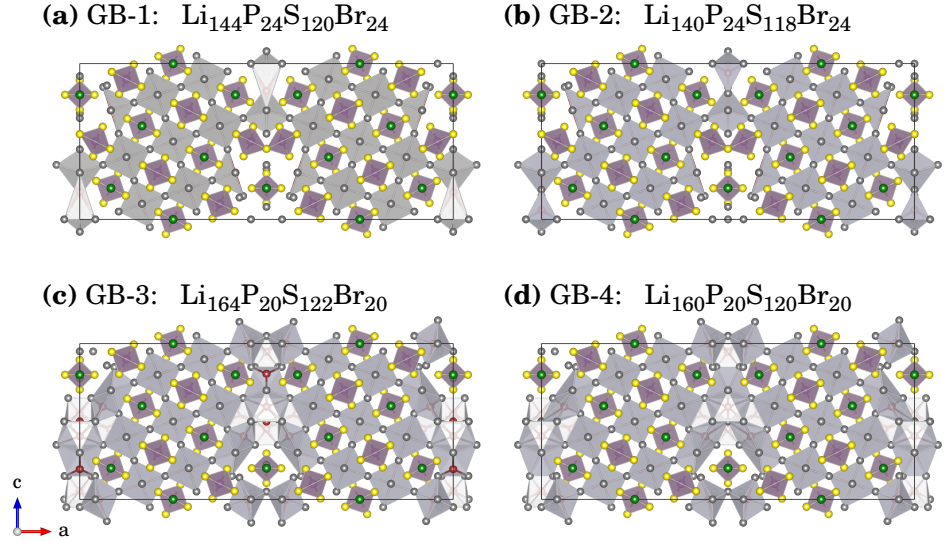

FIGURE 5.31: The four different Σ5 tilt GBs that have been modeled explicitly. The individual interfaces have been modified in several ways. For a better comparison, Li^+ coordination polyhedra (gray) around S^{2-} ions are visualized. More information concerning the composition of the models can be found in Table 5.5. All four GBs were treated with 0%, 25% and 50% Br^-/S^{2-} site-exchange.

GB-3 and GB-4, on the other hand, were prepared with additional Li_2S at the interface and without $P_2S_7^{4-}$ units.

In addition to the differently modified interfaces, all four models were considered with a Br^-/S^{2-} site-exchange of 0%, 25% and 50%. AIMD simulations were performed on these structures at various temperatures to compute the Li^+ MSD. Interestingly, when compared among the same extent of site-exchange, the Li^+ diffusion was found to barely depend on the specific interface modification, At a first glance, this is somewhat surprising as GB-3 and GB-4 contain a

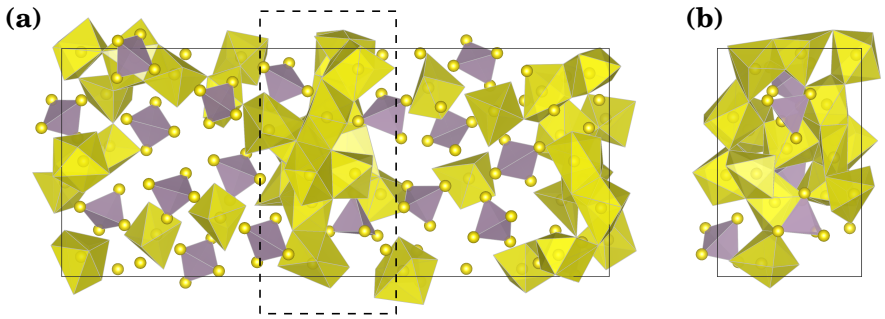

FIGURE 5.32: (a) Structure of the GB shown in Figure 5.31 with 25% site-exchange after approximately 100 ps at 700 K. Only the PS_4^{3-} units (purple) and Li_xS polyhedra (yellow) are shown. (b) Side view of the section that is marked with a dashed box in part (a).

considerable amount of additional Li_2S, which is known to be a rather poor ionic conductor.[435,436] Therefore, deteriorated transport properties are to be expected.

The fact that the presence of additional Li_2S does not influence Li^+ diffusion in the present cases is ascribed to the fact that Li_2S does not homogeneously crystallize at the GB interface – at least not within the considered time and length scales of our simulations. An example of this observation is shown in Figure 5.32 for GB-3 with 25% site-exchange after approximately 100 ps at 700 K. The interface comprises a thin, amorphous layer of Li_2S, which still seems to be permeable to Li^+. This fits to the increased ionic conductivity observed for Li_2S nanoparticles or thin Li_2S layers on Li metal.[436,437]

Because the Li^+ diffusion was comparable in all four GB models, we computed an average MSD. A comparison of this averaged MSD with the MSD of bulk Li_6PS_5Br is shown in Figure 5.33. The results are similar to the ones obtained for the twist GB: Also the tilt GB improves the Li^+ transport at 0% site-exchange, as can be seen in Figure 5.33 (a) and (b). The intracage diffusion limit is again overcome at temperatures of 500 K and 600 K toward advanced simulation times (not shown), but this circumstance can be seen for the data set at 700 K within 40 ps.

Figure 5.33 (c) and (d) reveal that the Li^+ diffusion in bulk Li_6PS_5Br surpasses the diffusion of the models containing a tilt GB already at 25% Br^-/S^{2-} site-exchange. Similarly, also at 50% (Figure 5.33 (e) and (f)) the MSD increases faster for bulk Li_6PS_5Br. This is the same trend as found for the twist GBs in the previous section. Presumably, the explanations for these observations are then similar: The slight worsening of Li^+ transport properties compared to the bulk Li_6PS_5Br in the presence of Br^-/S^{2-} site-exchange is attributed to disturbed diffusion pathways as well as impurity phases.

At 0%, on the other hand, the GB enhances the Li^+ transport properties. This is clearly visible in Figure 5.34 that shows the Li^+ trajectories in all four

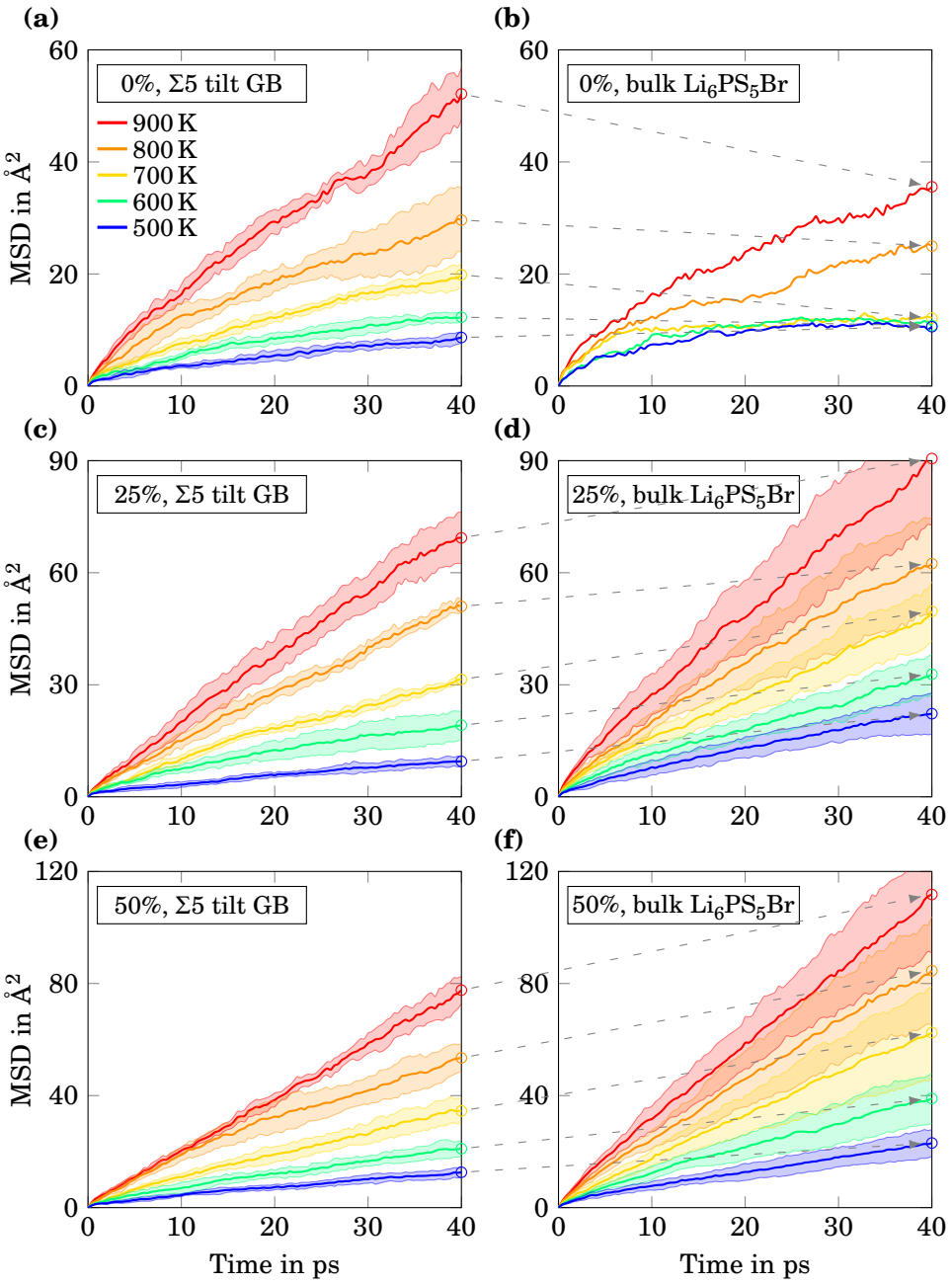

FIGURE 5.33: Comparison of the averaged MSD of the tilt GB models (left plots) with bulk Li_6PS_5Br (right plots). Plots in the same row exhibit the same degree of Br^-/S^{2-} site-exchange as labeled in the respective upper left corners. Dashed arrows are used as a guide to the eye to compare the reached MSD at a simulation time of 40 ps.

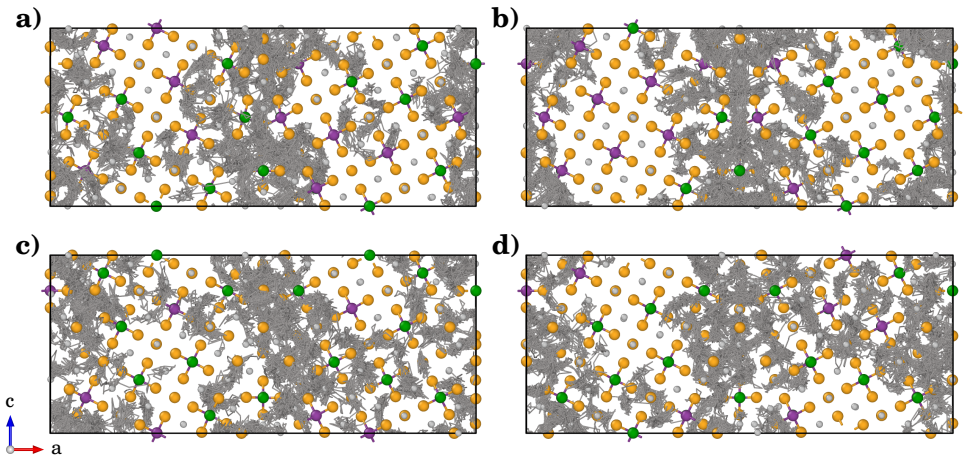

FIGURE 5.34: Observed Li^+ trajectories (gray lines) in the four tilt GB models with 0% site-exchange after approximately 120 ps at 600 K. Only the trajectories of the Li^+ ions that reached an atomic displacements of 5 Å or more at the end of the simulations have been visualized.

GB models exhibiting 0% site-exchange at the end of a 120 ps simulation at 600 K. Trajectories of Li^+ ions that did not reach a displacement of 5 Å at the end of the simulation, however, are omitted in the visualization to highlight the Li^+ pathways that are involved in enhanced diffusion. The remaining trajectories indicate that long-range Li^+ diffusion predominantly involves regions close to the vicinity of the GB interfaces. Opposed to this, many regions inside the bulk grains are not involved in long-range transport at all.

5.6.3 Anisotropic Diffusion due to Grain Boundaries

So far, we only considered the overall diffusion of Li^+ assuming an isotropic material when analyzing the effects of GBs in the transport properties in the previous sections. As a two-dimensional defect, however, it is likely that a GB transforms the isotropic diffusion of the cubic Li_6PS_5Br bulk material to an anisotropic feature. This assumption is supported by a visual inspection of the Li^+ trajectories in Figure 5.34. For a more quantitative analysis, we split the total MSD into its spatial contributions to see if anisotropic diffusion can be identified. We did not consider the twist GBs because their structural models are rather small and it is unclear if the thin regions between the GBs exhibit a true Li_6PS_5Br bulk character. This seems to be less of a problem in the larger models of the tilt GBs.

The evolution of the individual spatial components of the MSD, obtained as the average over all tilt GBs, is shown in Figure 5.35 for a Br^-/S^{2-} site-exchange of 0%, 25% and 50% at temperatures of 500, 700 and 900 K. The x, y and z

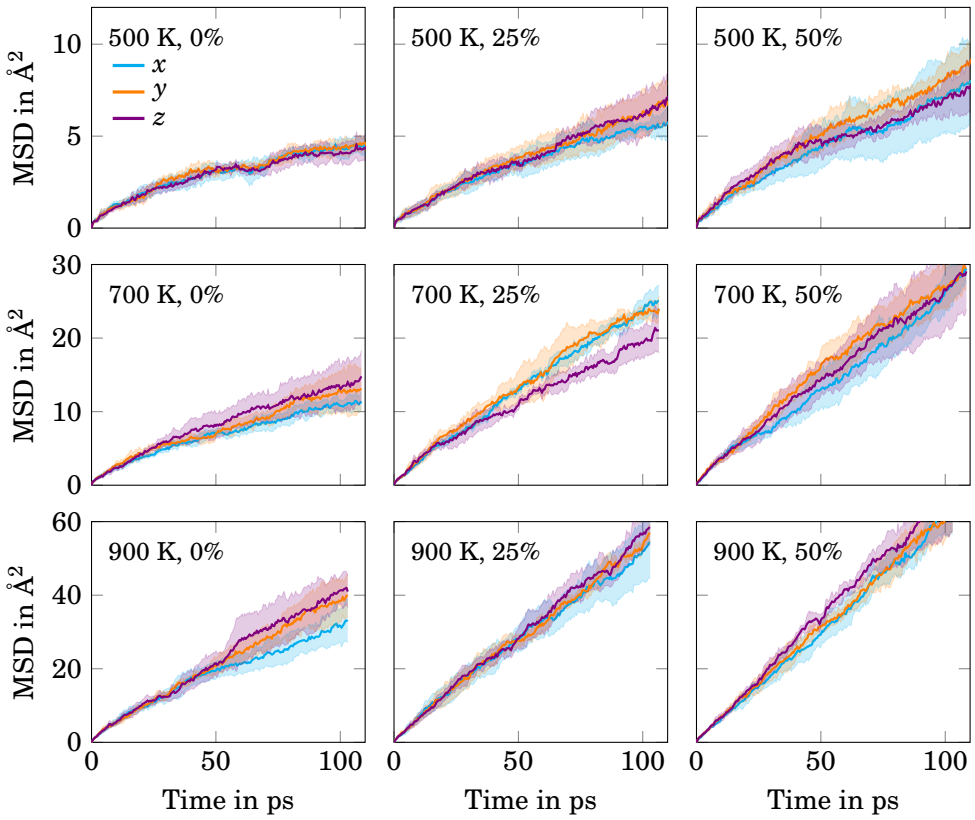

FIGURE 5.35: Evolution of the three spatial components of the averaged MSD of the tilt GB models. The x component corresponds to displacements along the a-axis of the simulation cell (perpendicular to the GB).

components of the MSD correspond to the a-, b- and c-axis of the simulation box, respectively (see coordinate axes in one of the previous structural models). Hence, the the MSD along $_x$ characterizes displacements perpendicular to GB, whereas the y and z components are parallel to the GB. Overall, the evolution of the x, y and z components appears to be rather uniform and the deviations from this trend seem to be consistent with the statistical fluctuations.

These results imply that the diffusion is still isotropic despite the presence of the GBs. This is somewhat counter-intuitive for a two-dimensional defect that was proven to affect the total MSD. At least for the models with 0% site-exchange this discrepancy could be related to the comparably large region of influence of the GB. This can be seen in Figure 5.34: Several of the long trajectories involve Li^+ cages located directly adjacent to the GBs. In relation to the dimensions of the simulation cell, these cages extend far into the part of the model that should represent the bulk Li_6PS_5Br where only local diffusion is expected to

occur. Apparently, this is not the case and might only be realized by using larger models, presumably exceeding the capabilities of DFT calculations. Hence, the apparent isotropy of the diffusion could be an artifact from the small system size.

Notably, however, there a selected cases in the MSD evolution where the deviations of the three spatial components are relatively large. One such example is encountered at 700 K with 25% Br^-/S^{2-} site-exchange, which exhibits a slightly reduced MSD along z. As this tendency is not recognizable at the remaining temperatures with 25% site-exchange, it is likely that it is still a purely statistical effect. But another interesting deviation concerns the 0% structures, whose x contribution is found to be the lowest at 700 as well as at 900 K. This could indeed hint at an improved diffusion along the GB. To confirm any of these hypotheses, longer simulations and/or larger system sizes are needed to tighten the statistics and to identify real trends. Such involved simulations need to be done elsewhere but could deliver interesting and detailed insights for the GB properties of argyrodite-type materials.

5.7 Summary

In this chapter we analyzed the effect of Br^-/S^{2-} site-exchange on various properties of the argyrodite-type solid electrolyte Li_6PS_5Br. The experimental trend of decreasing lattice constants with increasing site-exchange is confirmed and the smallest lattice constants are obtained at 50% site-exchange. Moreover, static calculations with reasonable Li^+ distributions prove that Li_6PS_5Br is most stable in the absence of Br^-/S^{2-} site-exchange and least stable at 50% site-exchange. Hence, entropic effects are likely to stabilize structures with Br^-/S^{2-} site-exchange at finite temperature. The configurational entropy due to the Br^-/S^{2-} site-exchange itself, however, does not suffice to explain the achieved degrees of site-exchange of experimental quenching studies. Likewise, also vibrational entropy contributions cannot explain this issue and we speculate that the configurational entropy of the Li^+ sublattice needs to be included to predict the equilibrium site-exchange.

The Li^+ transport properties are found to critically depend on the Br^-/S^{2-} site-exchange. In the absence of site-exchange, diffusion is mainly confined to the motion of Li^+ ions within the Li^+ cages around the S^{2-} ions ($4d$ sites) and a new internal reorganization mechanism for the intracage diffusion is reported. Only at high temperatures of 800 K or above, the intracage diffusion limit is overcome and long-range Li^+ transport is observed within feasible simulation times. The mechanism involves the intercage jump of a Li^+, which can be interpreted as the spontaneous formation of a Li^+ Frenkel pair. At lower temperatures, however, such Frenkel pairs are likely to be annihilated shortly after their formation due to immediate back-jumps.

The introduction of Br^-/S^{2-} site-exchange greatly improves the Li^+ transport properties and enables the observation of long-range diffusion already at 500 K. The highest calculated D^* are obtained at 50% site-exchange and the corresponding extrapolated ionic conductivity at room temperature is two orders of magnitude higher than the one for the 0% structure. The Haven ratio for structures with 25% and 50% site-exchange are in the range of $0.5-0.8$. For degrees of site-exchange higher than 50%, D^* decreases again and at 100% the Li^+ diffusion is again a local phenomena: The Li^+ cages have followed the S^{2-} ions and are now centered around the $4a$ sites.

AIMD simulations at different volumes have been used to extract activation volumes $\Delta^\ddagger V$. These were found to be positive such that the bulk D^* is expected to decrease under compression. Notably, $\Delta^\ddagger V$ of the 0% structure is $2-3$ times larger than the ones of the 25% and 50% structures. The reason for this is presumably related to the diffusion mechanism: In structures with Br^-/S^{2-} site-exchange Li^+ Frenkel pairs form naturally and at least one Frenkel pair is constantly present in the simulation cell. At 0%, however, every Frenkel pair needs to form spontaneously, which adds to $\Delta^\ddagger V^{\text{form}}$, the activation volume related to the defect formation.

To grasp the exact effect of the Br^-/S^{2-} site-exchange on the atomic diffusion mechanism, its individual underlying defects, namely a S^{2-} ion on a Br^- site (S'_{Br}) and its counterpart $Br^{\bullet}_{S}$, have been at first studied independently. The analysis shows that $Br^{\bullet}_{S}$ defects are responsible for the facilitation of Li^+ Frenkel pairs with mobile Li^+ interstitials ($Li^{\bullet}_{i}$). Occasionally, even two Frenkel pairs are initiated by one $Br^{\bullet}_{S}$ defect. The corresponding Li^+ vacancy (V'_{Li}) of the Frenkel pair mainly remains bound to the $Br^{\bullet}_{S}$ defect and is considered rather immobile. The $Li^{\bullet}_{i}$, on the other hand, is able to perform intercage jumps via an interstitial or interstitialcy mechanism. In this regard, S'_{Br} defects act as a sink for $Li^{\bullet}_{i}$. Additionally, they strongly attract Li^+ ions in their vicinity, so that local disturbances in the Li^+ distributions are induced that support the overall Li^+ transport.

The local disturbances of the Li^+ distributions are recognizable in changing occupancies of the tetrahedral Li^+ sites that are in line with the insights of the diffusion mechanism analysis. Globally averaged, the Li^+ density reproduces the experimental trends of shifting positions and occupancies of Li^+ sites. Moreover, our analysis shows that the Li^+ density toward 50% site-exchange indeed becomes more homogeneous, which in turns explains the observed dependence of the lattice constants.

Finally, $\Sigma 5$ twist and tilt grain boundaries (GBs) are found to have an ambivalent character: At 0%, they enhance the Li^+ diffusion because they locally disturb the strict structure of the Li^+ cages such that Li^+ diffusion in the vicinity of the GB is facilitated. At 25% and 50%, however, the Li^+ transport is slightly reduced compared to the bulk material, most likely because Li^+ diffusion pathways are less favorable along and across the GB. The fact that the diffusion

seems to be isotropic in the presence of GBs is attributed to the rather small model sizes and the limited statistics due to the feasible simulation times.

In conclusion, the generated knowledge of the intricate interplay between Br^{-}/S^{2-} site-exchange and the properties of Li_6PS_5Br is certainly helpful for the further development and optimization of argyrodite-type materials and other SEs whose properties are influenced to a large degree by ionic disorder.

6 Properties of Li_7SiPS_8

Parts of this chapter have been published in:

[6] L. Riegger, , S.-K. Otto, **M. Sadowski**, S. Jovanovic, S. Harm, L. Balzat, S. Merz, O. Kötz, S. Burkhardt, F. H. Richter, J. Sann, B. V. Lotsch, J. Granwehr, K. Albe and J. Janek, *New insights into the reduction stability of thiophosphate electrolytes containing metal ions: Li_7SiPS_8 in contact with a Lithium Metal Anode*, Chemistry of Materials 34, 8, 3659-3669 (2022).[438]

Li_7SiPS_8 is a rather novel material and, as a matter of fact, not much about its properties is known, yet.[11,439] We have therefore analyzed this compound and focused on several aspects which have been of interest in the scope of the "FestBatt" project.[440] We will first present how a material with such a complicated structure as Li_7SiPS_8 can be treated within electronic structure calculations. To this end, we will present in Section 6.1 how representative structural models of its orthorhombic phase (ortho-Li_7SiPS_8) and its tetragonal phase (tetra-Li_7SiPS_8) have been generated and analyzed with respect to their relative stability. Afterwards, we will compare their Li^+ transport properties in Section 6.2 and see that tetra-Li_7SiPS_8 indeed shows high promise as SE. Furthermore, we will consider how the bulk transport properties are influenced by mechanical loading. The latter point is a bridge to Section 6.3 where we will present the elastic properties of tetra-Li_7SiPS_8. Finally, the (in)stability of tetra-Li_7SiPS_8 against Li metal is analyzed in Section 6.4 by means of explicit interface models.

6.1 Structure and Stability

The ortho- and the tetra-phase of Li_7SiPS_8 exhibit a rather complicated atomic structure due to partial disorder among the Si/P sites in combination with various partially occupied Li^+ sites (see Section 2.2.2 for a detailed description). Therefore, the structure generation is not trivial and deserves a short mentioning in the following. Afterwards, the generated structures are compared based on their relative stabilities.

TABLE 6.1: Experimental (Exp.) and approximated (Theo.) occupancies of the various Li^+ sites of ortho- and tetra-Li_7SiPS_8. The numbers in brackets indicate the actual number of Li^+ that needs to be distributed among the respective number of available sites in the supercell models of Li_7SiPS_8.

ortho-Li_7SiPS_8			tetra-Li_7SiPS_8		
Site	Exp.	Theo.	Site	Exp.	Theo.
Li1	0.764	0.750 (24/32)	Li1	0.50	0.500 (32/64)
Li2	0.433	0.438 (14/32)	Li2	0.88	0.875 (14/16)
Li3	0.34	0.375 (6/16)	Li3	0.86	0.875 (28/32)
Li4	0.24	0.250 (4/16)	Li4	0.63	0.625 (10/16)
Li5	0.264	0.250 (8/32)			

6.1.1 Structure generation

For all structures the shared Si/P sites have been populated first. To this end, we relied on the `supercell` program to produce random Si/P distributions and to sample structures according to their electrostatic energies.[392] At this stage, the partial occupancies of the Li^+ sites were still retained and we obtained several structural models with different Si/P distributions for both phases of Li_7SiPS_8. Afterward, the `supercell` program was used to occupy the Li^+ sites for every model while keeping the respective Si/P distribution fixed. Note that the experimental occupancies needed to be slightly adjusted to guarantee an uncharged and stoichiometric supercell. The experimental and approximated occupancies of the various Li^+ sites are summarized in Table 6.1. It also shows the number of Li^+ that needed to be distributed among the available sites. Based on these numbers it is clear that the vast combinatorics of this issue cannot be handled in one single step. For example, only distributing 24 Li^+ ions among the 32 available Li1 sites results in approximately 10^7 configurations without taking the symmetry of the system into account. We therefore split the occupation of Li^+ sites into various steps. After each step the structure with the lowest electrostatic energy was used as basis for the next step until all Li^+ sites have been occupied.

Relying on this procedure will most certainly not result in the optimal Li^+ distribution. That is, if such a thing exists at all for superionic conductors like Li_7SiPS_8. The aim is rather to obtain a reasonable starting structure for our further purposes. During AIMD simulations, for example, the Li^+ distribution will equilibrate eventually. In the following we will outline the detailed procedures for generating initial structures for the ortho- and tetra-phase of Li_7SiPS_8.

Generation of Ortho-Li_7SiPS_8 Structure Models

The utilized $1\times2\times2$ supercell of ortho-Li_7SiPS_8 contains 8 formula units. Because all Si/P sites are occupied with either Si or P with the same probability, we need to distribute 8 Si and 8 P on 16 sites. This alone results in 12870 possibilities

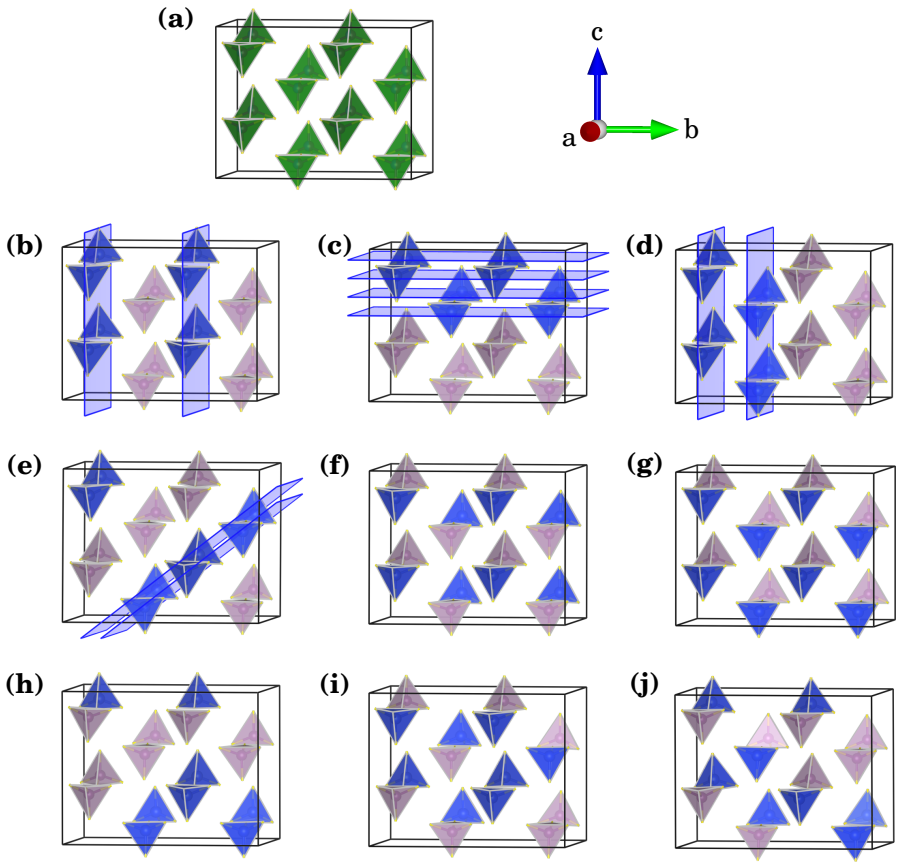

FIGURE 6.1: (a) Base structure of the tetrahedra in ortho-Li_7SiPS_8 and the corresponding axis system. Green tetrahedra indicate that the central sites are occupied either with Si or P in a 50:50 ratio. (b)-(j) Explicit Si/P distributions that have been modeled in this work. Blue tetrahedra indicate that they are occupied with Si and purple tetrahedra are occupied with P. Planes have been added only as a guide to the eye where the perspective allowed for it. Li and S ions are not shown for improved clarity.

which can be reduced to 482 due to the symmetry of the system. Out of these, we have considered 9 structures with different Si/P distributions. These 9 structures are shown in Figure 6.1. They comprise 6 ordered arrangements (b-g) that have been produced manually and 3 random structures (h-j). The structures with the lowest and highest electrostatic energies (still considering all partially occupied Li^+ sites for the Ewald summation) are structures (b) and (d), respectively. For every structure, the Li^+ ions then needed to be subsequently distributed.

Distributing Li^+ in ortho-Li_7SiPS_8 is challenging because several sites occur in pairs with short distances: Li3–Li4 (0.92 Å), Li2–Li2 (0.97 Å), and Li1–Li5 (0.14 Å). A purely random distribution could therefore result in ions that are unreasonably close to each other. We circumvented this issue as follows. First, Li3

and Li4 sites were occupied simultaneously. By only taking the structure with the lowest electrostatic energy we automatically exclude that any neighboring Li3 and Li4 sites are occupied at the same time. This is repeated in the next step for occupying Li2 sites. Unfortunately, Li1 and Li5 sites could not be distributed simultaneously because it exceeded the capabilities of the `supercell` program. We therefore first distributed the Li1 sites followed by the Li5 sites as last step.

Generation of Tetra-Li_7SiPS_8 Structure Models

For the tetra-phase of Li_7SiPS_8 we used a $2 \times 2 \times 1$ supercell corresponding to 12 formula units. The supercell comprises 8 sites that are only occupied by P and 16 sites that are occupied by Si/P with a 3:1 ratio, i.e., 12 Si and 4 P need to be distributed among 16 sites. Accounting for symmetry operations, this can be realized in 58 ways. Again, we have constructed various structures with ordered and random arrangements of Si/P. The resulting 7 structures are shown in Figure 6.2 and similarly to what was done for the ortho-phase, Li^+ needed to be distributed for every individual Si/P arrangement.

First, an approximation to the Li1 sites needed to be introduced because the distribution of 32 Li^+ among 64 sites results in approximately 10^{17} possibilities. As Li1 sites are always arranged in pairs (distance below 1.5 Å), it is unlikely that both sites are occupied at the same time. Therefore, we treated every Li1–Li1 pair as a single site located in the midpoint in order to simplify the configurational problem. Next, Li2 and Li4 sites were occupied simultaneously. Finally, the remaining Li3 sites were populated.

6.1.2 Stability

As a first step, the atomic positions and the cell geometry of all generated structures were statically optimized. This enables us to compare the energies of the structures in order to evaluate if the Si/P ordering has a pronounced influence on the relative stability. However, we need to keep in mind that our initially chosen Li^+ distribution is most probably not optimal and contributes to energy differences as well.

The relative energies ΔE of all structures are shown in Figure 6.3 and their averages $\overline{E}$ are indicated with dashed lines. The average energy of the ortho-phase $\overline{E}_{\text{ortho}}$ has been set as reference energy, i.e., $E = 0$. The decomposition energy $E_{\text{decomp.}}$ refers to the decomposition reaction,

$$Li_7SiPS_8 \longrightarrow Li_3PS_4 + Li_4SiS_4 \,, \tag{6.1}$$

and amounts to −131 meV/f.u. (−7.7 meV/atom), indicating that both phases of Li_7SiPS_8 are only meta-stable at 0 K. In contrast to this, the decomposition reaction of $Li_{10}SiP_2S_{12}$, a compound comparable to Li_7SiPS_8, into Li_3PS_4 and Li_4SiS_4 has been reported to be unfavorable by DFT calculations.[296] Furthermore, the same study mentions other decomposition reactions leading to more

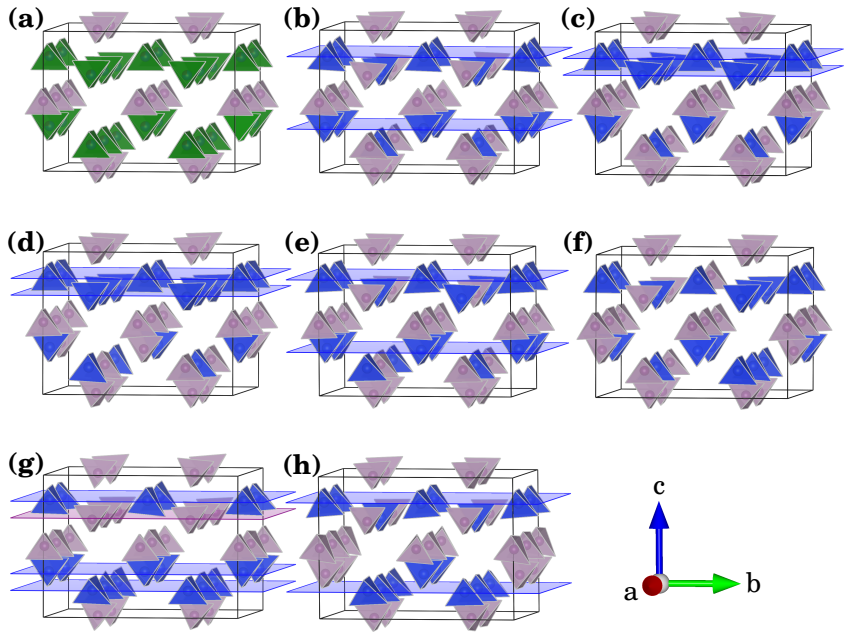

FIGURE 6.2: (a) Base structure of the tetrahedra in tetra-Li_7SiPS_8. Green tetrahedra indicate that their central sites are occupied either with Si or P in a 3:1 ratio. Purple tetrahedra are fixed with P in their centers. (b)-(h) Explicit Si/P distributions that have been modeled in this work. Blue tetrahedra indicate that they are occupied with Si and purple tetrahedra are occupied with P. Planes have been added only as a guide to the eye where the perspective allowed for it. Li and S ions are not shown for improved clarity.

favorable $E_{\text{decomp.}}$. Therefore, it is possible that Reaction 6.1 does not include the most favorable reaction products, which would lower the stability further. To prove this, the calculation of the full phase diagram would be necessary and was not attempted here. Assuming that the decomposition energy does not change dramatically for other reactions, we find that relative energy differences are small. Therefore, it is likely that Li_7SiPS_8 is stabilized by entropic contributions or that a decomposition is kinetically hindered.

Let us now compare the energetic differences between ortho- and tetra-Li_7SiPS_8. Clearly, the ortho-phase of Li_7SiPS_8 is more stable than the tetra-phase and the energy difference $\Delta\overline{E}$ between the average values of the two phases corresponds to 200 meV/f.u. (11.8 meV/atom). This value agrees to the energy difference between Li_6PS_5Br with 50% and 0% site-disorder (see Section 5.2.1). Therefore, it is reasonable to assume that tetra-Li_7SiPS_8 can be stabilized kinetically over ortho-Li_7SiPS_8. The fact that it can be synthesized corroborates this assumption.

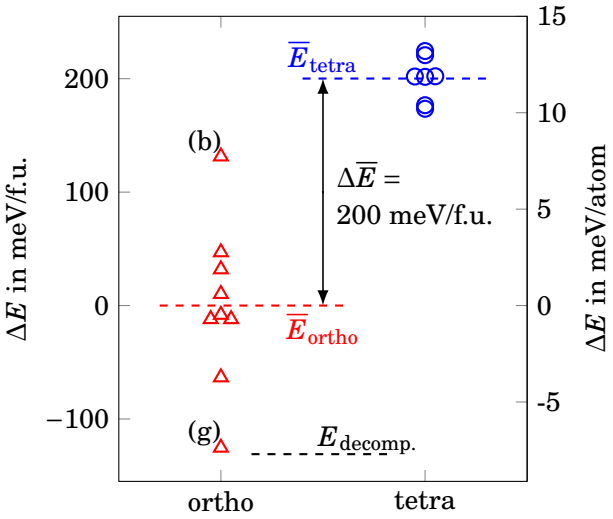

FIGURE 6.3: Relative stabilities of all optimized Li_7SiPS_8 structural models with respect to the average energy of the ortho-phase. Data points that lie on top of each other have been shifted horizontally to be better distinguishable. The labels (b) and (g) for the ortho-phase refer to the corresponding structures shown in Figure 6.1. $E_{\text{decomp.}}$ refers to the decomposition energy according to Reaction 6.1.

Based on the shown energy values in Figure 6.3 another fact becomes apparent: The spread of the energy values for the ortho-phase around its average (approximately ±130 meV/f.u.) is larger compared to that of the tetra-phase (approximately ±25 meV/f.u.). Furthermore, among the structures of the ortho-phase, structure (b) turns out to be the least stable despite the fact that it exhibited the lowest electrostatic energy after having distributed the Si and P ions. This highlights again that a mere electrostatic consideration for estimating the stability of superionic conductors may lead to wrong conclusions because local relaxations are neglected, as previously pointed out.[163] Structure g) was found to be the most stable structure and exhibits a (100) ordering of the Si/P ions. Its relative stability of −125 meV/f.u., however, is not exceedingly large and likely to be compensated by entropic contributions at ambient or elevated temperatures. Therefore, a pronounced ordering of the SiS_4^{4-} and PS_4^{3-} units is not expected. This fits to the experimental results that, on average, found a random arrangement of the two tetrahedra types.[11]

The situation is similar for the tetra-phase. The comparably small spread of the relative stabilities makes an ordering of the tetrahedral units even less likely. As a result, also for tetra-Li_7SiPS_8 no distinct ordering among the shared Si/P sites is expected, again fitting to the results of the experimental structural characterization.[11] Still, in order to get a better overview of whether the Si/P order has an influence on the Li^+ transport, we took all generated structures into account for the following analyses of the transport properties.

6.2 Transport Properties: Ortho- vs. Tetra-Li_7SiPS_8

There are several questions we will shed light on in this section:

Q1 Does the Si/P arrangement have a critical influence on the Li^+ diffusion, as for example recently observed in $Na_3Zr_2Si_2PO_{12}$?[441]

Q2 Do the orthorhombic and tetragonal symmetries of the two phases lead to distinct anisotropy for the Li^+ diffusion?

Q3 How does the bulk diffusion of the ortho- and the tetra-phase compare to each other?

Q4 What is the influence of pressure on the diffusion within tetra-Li_7SiPS_8? Does it explain the experimentally observed conductivity increase upon compression?

Let us start with the first and second question and answer them separately for ortho-Li_7SiPS_8 and tetra-Li_7SiPS_8.

6.2.1 Bulk Diffusion of Ortho-Li_7SiPS_8

The transport properties of ortho-Li_7SiPS_8 have been analyzed in a similar way as reported for the other materials mentioned in this work. All 9 structural models of Figure 6.1 have therefore been used to conduct AIMD simulations at various temperatures and the corresponding MSD of Li^+ has been computed after allowing for 5 ps of equilibration. At every temperature the MSD of all structures has been averaged and is shown in Figure 6.4. The transparent area surrounding the average MSD indicates the resulting standard deviation obtained from the averaging. It is apparent that the standard deviation is not excessively large and falls within the expected statistical noise. This means that the MSD evolution does not critically depend on the Si/P ordering for the investigated structural models. As a result, also the derived diffusion coefficients D^* will have a negligible dependence on the Si/P arrangement (Q1✓).

A linear regression was fitted to the average MSD over the interval starting at 10 ps until the end of the available data. All regressions achieved high coefficients of determination close to unity, as labeled in the figure. Based on their slopes, the diffusion coefficients have been determined and are listed in Table 6.2. Despite the good quality of the fit, the data at 500 K should only be taken as a very crude approximation because of the limited mobility of Li^+ at low temperature. At 500 K, the value of the MSD after 80 ps amounts to approximately 6 $Å^2$. Translating this into average particle displacements results in $\sqrt{6\ Å^2} = 2.44$ Å. Such a displacement can be seen as a typical estimate for a common Li^+ jump, neglecting the close neighboring pairs of Li^+ sites that show a separation of less than 1 Å, as explained above. Therefore, every Li^+ has, on average, performed only one jump during the simulation. Hence, no true

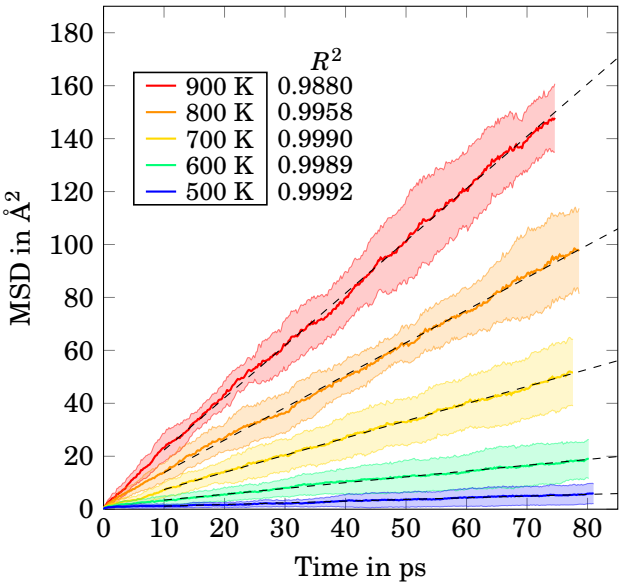

FIGURE 6.4: Evolution of the Li^+ MSD for ortho-Li_7SiPS_8. The shown MSD (thick line) is averaged from all 9 structures with different Si/P orderings. The transparent areas indicate one standard deviation. Linear regressions (dashed lines) and their coefficients of determination R^2 are added. Prior to the shown data the system was allowed to equilibrate for 5 ps. The scaling is the same as shown in Figure 6.6 for a better comparison.

TABLE 6.2: Total Li^+ tracer diffusion coefficients D^* of ortho-Li_7SiPS_8 and the diffusion coefficients along the three crystallographic directions. All D^* are given in Å^2/ps, or equivalently 10^{-4} cm^2/s. Note that for 500 K no true long-range transport was observed during the simulations, yet. Therefore, the extracted D^* for 500 K should only be taken as an approximate result.

T in K	D^*	D^*_a	D^*_b	D^*_c
500	0.0106	0.0073	0.0114	0.0131
600	0.0365	0.0330	0.0325	0.0440
700	0.1082	0.0900	0.1105	0.1240
800	0.2046	0.1773	0.1773	0.2591
900	0.3292	0.2962	0.3290	0.3626

long-range transport has been observed at 500 K, yet. Much longer simulations, which could not be afforded here, would be needed to extract a proper value for D^* at such low temperatures. At 600 K, the MSD reached approximately 20 Å^2 after 80 ps and can be used as the first valid data to extract D^*. The extracted values and estimated conductivities will be discussed in more detail in Section 6.2.3 where they are also compared to tetra-Li_7SiPS_8.

Let us now inspect the degree of anisotropy in ortho-Li_7SiPS_8 with regard to the Li^+ diffusion. To this end the x, y and z contributions to the MSD have been calculated and are plotted in Figure 6.5 for temperatures of 600 K and above. Fortunately, the x, y and z contributions can be directly used to compute diffusion coefficients along the crystallographic a, b and c directions, respectively. The extracted D^* are listed in Table 6.2. First, the MSD of all three contributions increases constantly and the slopes for the x-, y-, and z-MSD fall within the

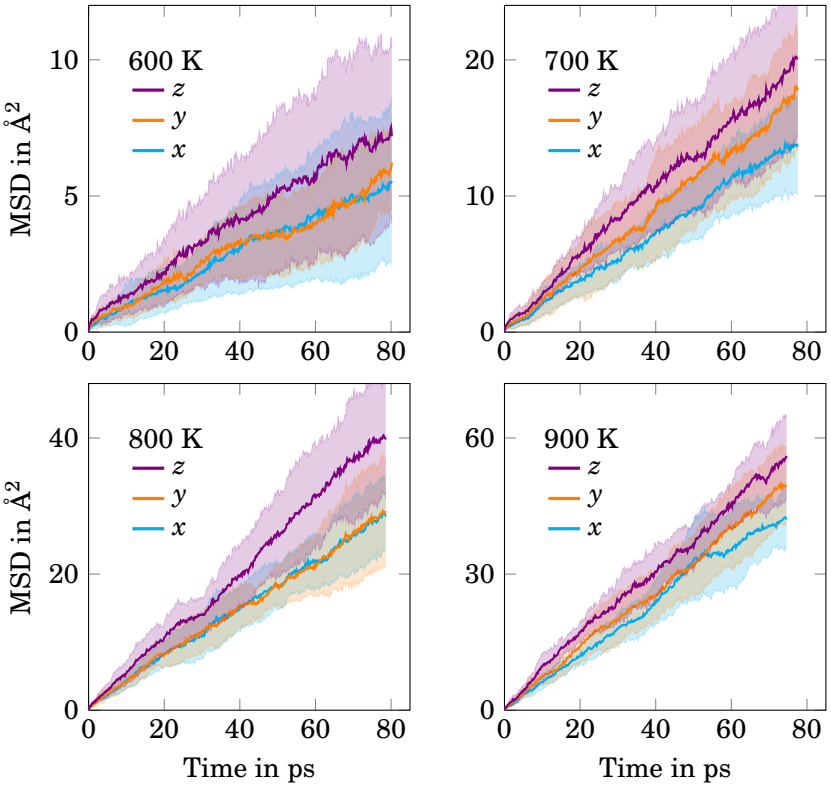

FIGURE 6.5: Evolution of the x, y and z components of the MSD in ortho-Li_7SiPS_8 for temperatures of 600-900 K.

same order of magnitude for the individual temperatures. Therefore, we can deduce that ortho-Li_7SiPS_8 does not exhibit a blocking direction.

Second, no distinct correlations between the Li^+ transport in the various directions and the ordering of the Si/P ions was observed (Q1✓). Naturally, the MSD varies for the different simulations/structural models. The extent of these deviations, however, can be attributed to the statistic nature of the MSD evolution and is not sufficient to justify any other conclusions.

Third, the z component of the MSD seems to be generally faster compared to the other two directions. Therefore, the diffusion along the c direction dominates the Li^+ transport. The hierarchy between the a and b direction is less distinct. Whereas the corresponding MSD evolution is virtually identical at 600 and 800 K, diffusion along the b direction slightly exceeds the a direction at 700 and 900 K. Based on the present data we can therefore conclude that the diffusion exhibits a slight anisotropy with $D_c^* > D_b^* \gtrsim D_a^*$, which is in line with an orthorhombic structure (Q2✓). Improved statistics, however, are needed to ascertain the exact hierarchy of the D^* along the a and b direction.

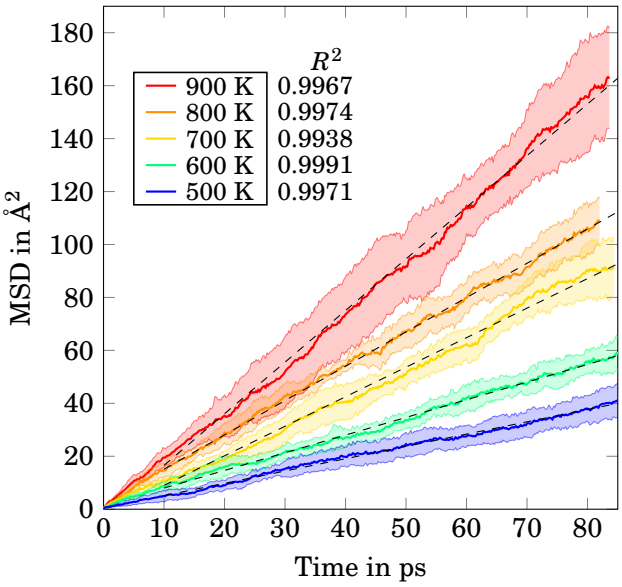

FIGURE 6.6: Evolution of the Li^+ MSD for tetra-Li_7SiPS_8. The shown MSD (thick line) is averaged from all 7 structures with different Si/P orderings. The transparent areas indicate one standard deviation. Linear regressions (dashed lines) and their coefficients of determination R^2 are added. Prior to the shown data the system was allowed to equilibrate for 5 ps. The scaling is the same as shown in Figure 6.4 for a better comparison.

6.2.2 Bulk Diffusion of Tetra-Li_7SiPS_8

The evolution of the averaged MSD and its standard deviation for all treated structures of tetra-Li_7SiPS_8 is shown in Figure 6.6. All fitted linear regressions to the average MSD show high coefficients of determination and the extracted D^+ are listed in Table 6.3. Most notably, this time the MSD at 500 K can also be used to extract valid diffusion coefficients for the tetra-phase. For example, with approximately 40 Å^2 the MSD corresponds to more than six times the one of the ortho-phase after 80 ps. Likewise, also at 600 K the MSD reaches a value three times larger than ortho-Li_7SiPS_8. We can therefore conclude that tetra-Li_7SiPS_8 clearly surpasses ortho-Li_7SiPS_8 in terms of transport properties especially at lower temperatures. A detailed comparison with the ortho-phase follows in the subsequent Section 6.2.3.

Again, no distinct correlation between the Si/P ordering and the transport properties is found (Q1✓). All observed deviations for the Li^+ diffusion fall within the expected range of statistical noise. Despite the lack of correlation between transport properties and Si/P distribution, however, the diffusion is more anisotropic for tetra-Li_7SiPS_8 when compared to the ortho-phase. This can be seen based on Figure 6.7 which shows the spatial components of the MSD for tetra-Li_7SiPS_8. At all temperatures, the z component dominates the contributions to the total MSD. As a result, diffusion along the c direction is three to four times higher compared to the a and b direction. The latter two are approximately equal, as expected for a structure with tetragonal symmetry. The exact values for D^* and its spatial components can be read from Table 6.3.

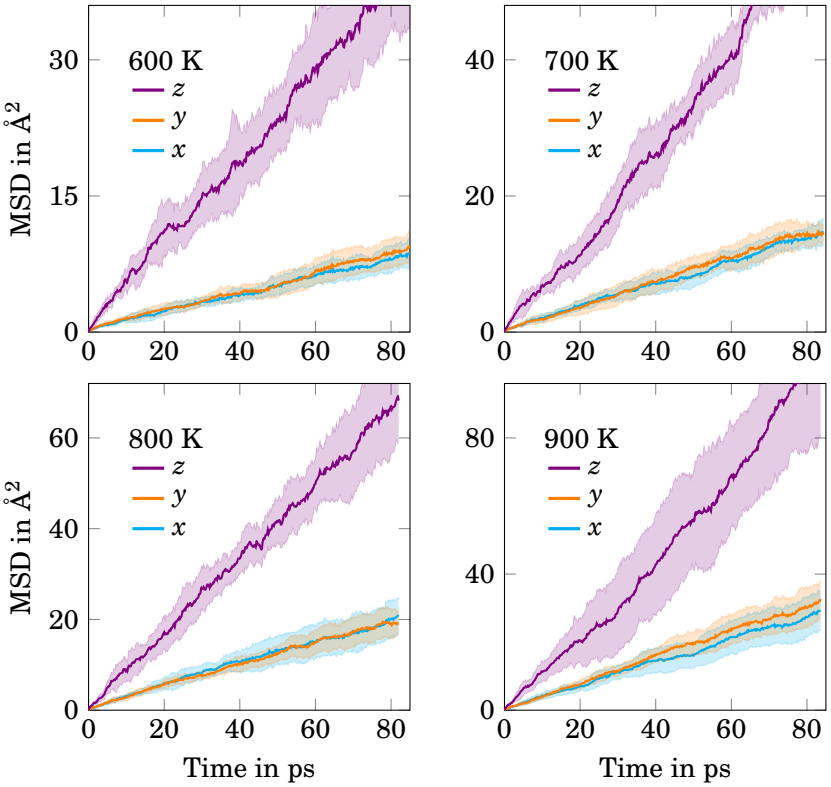

FIGURE 6.7: Evolution of the x, y and z components of the MSD in tetra-Li_7SiPS_8 for temperatures of 600-900 K.

Based on these observations we can conclude that the hierarchy of the diffusion for tetra-Li_7SiPS_8 is as follows: $D_c^* \gg D_a^* \approx D_b^*$ (Q2✓). These observations fit to results reported for $Li_{10}SiP_2S_{12}$ which also crystallizes in a tetragonal structure similar to LGPS and also contains Si.[296] Because the c direction delivers the fastest pathway for the Li^+ transport, it would be helpful to tune the material towards improved transport along the a and b directions. Alternatively, a texturing of the material when used as SE in batteries could be beneficial. If possible, the c axis should be parallel to the line that virtually connects cathode and anode. For a material with randomly distributed orientations of the grains, however, the apparent macroscopic diffusion coefficients will amount to an average value of D_a^*, D_b^* and D_c^*. For simplicity, we will therefore use the average D^* and neglect its anisotropy for tetra-Li_7SiPS_8 for any further considerations.

6.2.3 Diffusion and Conductivity Comparison

For a better comparison, D^* of the ortho- and tetra-Li_7SiPS_8 are plotted as an Arrhenius representation in Figure 6.8. The value of 500 K for the ortho-phase

TABLE 6.3: Total Li^+ tracer diffusion coefficients of tetra-Li_7SiPS_8 and the diffusion coefficients along the three crystallographic directions. All D^* are given in $Å^2$/ps, or equivalently 10^{-4} cm^2/s.

T in K	D^*	D^*_a	D^*_b	D^*_c
500	0.0774	0.0384	0.0336	0.1603
600	0.1113	0.0481	0.0518	0.2338
700	0.1860	0.0840	0.0905	0.3836
800	0.2161	0.1178	0.1181	0.4124
900	0.3250	0.1681	0.1902	0.6169

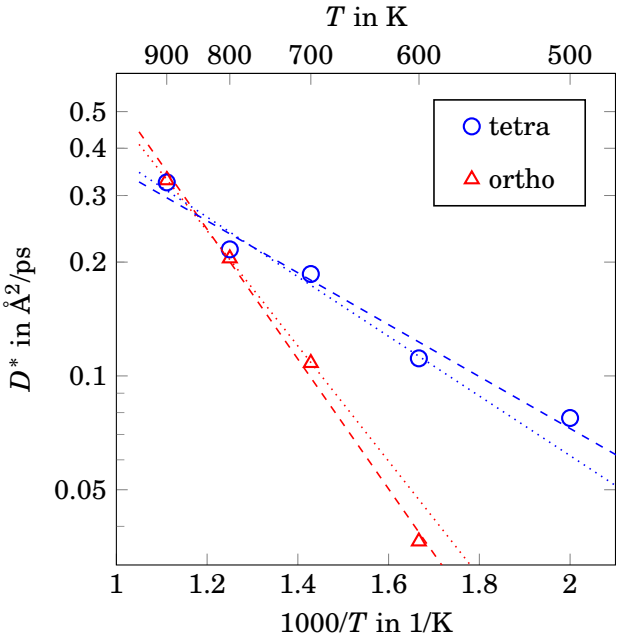

FIGURE 6.8: Arrhenius plot for ortho- and tetra-Li_7SiPS_8. The dashed and dotted lines correspond to Arrhenius fits based on different sets of data points. More details are found in the main text and Table 6.4.

has been discarded, as already mentioned. The Arrhenius plot highlights the fact that tetra-Li_7SiPS_8 is a better Li^+ conductor than ortho-Li_7SiPS_8 especially at lower temperatures up to 700 K. At higher temperatures of 800 K and 900 K, however, the two phases show approximately equal diffusion coefficients.

The data sets shown in the Arrhenius plot have been fitted to an Arrhenius equation in order to extract the transport parameters E_m and D_0. To this end, different data sets have been used to estimate how sensible the fitted parameters are with regard to including or disregarding data points at low temperatures. The characteristics of the shown fits are presented in Table 6.4 together with further properties needed to calculate the ionic conductivity via the Nernst-Einstein relation (Equation 3.44). The volume has simply been calculated as the average volume of all statically optimized structural models.

TABLE 6.4: Properties of the Arrhenius fits shown in Figure 6.8. The fits are based on different data sets, i.e., temperature intervals spanned by the listed lowest temperature T_l and the highest temperature T_h. The resulting transport parameters (E_m, D_0) and extrapolated ionic conductivity $\sigma_{300\,\mathrm{K}}$ at 300 K together with the remaining variables (cell volume V, number of Li^+ in the simulation cell N_Li) needed for calculating the conductivity are summarized.

Li_7SiPS_8 phase	Fit illustration	Data set [T_l:T_h]	V [Å^3]	N_Li	E_m [meV]	D_0 [Å^2/ps]	$\sigma_{300\,\mathrm{K}}$ [mS/cm]
ortho	dashed	[600:900]	2657	56	329	28.1	0.718
	dotted	[700:900]			292	16.3	1.84
tetra	dashed	[500:900]	3883	84	131	1.71	123
	dotted	[600:900]			151	2.33	75.9

Despite the deviations of the different fits depending on the data sets, it is clear that the migration barrier of the ortho-phase is two to three times larger than the one of the tetra-phase. This cannot be compensated by D_0, which is one order of magnitude higher for the ortho-phase. In terms of extrapolated ionic conductivities at 300 K a value of 0.718 mS/cm is obtained for the ortho-phase if the data point at 600 K is included for the interpolation. Without this data point, a 2.5-fold increased conductivity of 1.84 mS/cm is obtained theoretically. This observation emphasizes the strong influence of the fitting procedure on the extrapolated values. We can furthermore deduce that also a (statistical) deviation in the data will lead to some degree of uncertainty. Similarly, also for tetra-Li_7SiPS_8 the extrapolated conductivity at 300 K was calculated to be 75.9 or 123 mS/cm depending on the included data. As stressed before, the calculated conductivities should therefore only be seen as a careful estimate helpful for qualitative comparisons. They should not be mistaken for quantitative predictions of the true conductivity. Keeping this in mind, our data proves that tetra-Li_7SiPS_8 is the superior SE (Q3✓). Therefore, the formation of the ortho-phase should be avoided during synthesis when aiming for high ionic conductivities.

6.2.4 Transport Properties of Tetra-Li_7SiPS_8 Under Mechanical Loading

The elastic properties of SEs are important to understand how mechanical constraints, as they occur in batteries, affect the battery materials. Here, we focus on how the conductivity of tetra-Li_7SiPS_8 is influenced, because experimental partners found increasing conductivities under applied pressure and the reasons for this observation were not clear. The bulk transport properties under mechanical loading were investigated by employing AIMD simulations. Because pressure control requires the accurate computation of the stress tensor, which becomes prohibitive for molecular dynamics simulations, we restrained

ourselves to the NVT ensemble, where mechanical loading is applied through an appropriate strain acting on the cell lattice parameters. For simplicity we applied isotropic strain as illustrated in Figure 6.9 (a) by applying a uniform lattice scaling factor f. If both the elastic properties of the material and the applied pressure are known, f can be calculated according to

$$f = \sqrt[3]{1 - \frac{\Delta p}{B}}\,, \tag{6.2}$$

under the approximation that a material exhibits an isotropic bulk modulus B and neglecting any temperature dependence. Based on speed of sound measurements, performed by experimental partners, the shear modulus G and Young's modulus Y were determined to be 3.22 and 6.93 GPa, respectively. They have been used to calculate a bulk modulus B of 2.73 GPa via Equation 3.72. Aiming for a pressure of approximately 0.4 GPa, as applied in the pressure experiments, the Birch-Murnaghan equation of state yields $f = 0.97$. Both the elastic moduli and f, however, appear to be too small as other sulfide SEs show bulk moduli in the range of 20-30 GPa.[428] We have therefore calculated the elastic properties of tetra-Li_7SiPS_8, which will be discussed in the following section, and adapted our scaling factors accordingly to $f = 0.99, 0.98$. Furthermore, in order keep the computational effort reasonable, we restricted the AIMD simulations to only one Si/P arrangements (the one shown in Figure 6.2 (h)) and only considered temperatures of 500, 700 and 900 K.

The obtained results of AIMD simulations are shown in Figure 6.9 (b)-(d). It shows the MSD evolutions at different temperatures and for different values of f. At all temperatures, the MSD after 80 ps is largest for the standard cell with $f = 1.00$. The structures with $f = 0.99, 0.98$ generally show a slower increase of the MSD. We can therefore assume that the bulk transport properties deteriorate upon the application of compressive mechanical loading. This is in agreement with AIMD simulation on the structurally related material LGPS, for which a reduction of the diffusion coefficients is mostly attributed to the squeezed diffusion pathways.[442]

Here, the limited statistics do not allow for the calculation of activation volumes, but the MSD indicates that the diffusion reduction under pressure is only modest for tetra-Li_7SiPS_8. A reduced D^* might be partly compensated by the reduced volume of the cell that effectively leads to an increased number density of Li^+. Therefore, the effect of mechanical loading on the bulk ionic conductivity is assumed to be of only secondary importance as long as the pressure is not excessively high. In conclusion, these findings indicate that the observed conductivity increase within the experimental pressure up to 0.4 GPa cannot be attributed to the bulk properties of tetra-Li_7SiPS_8 (Q4✓). Presumably, pressure leads to improved contact between particles such that more diffusion pathways are established, effectively increasing the ionic conductivity.

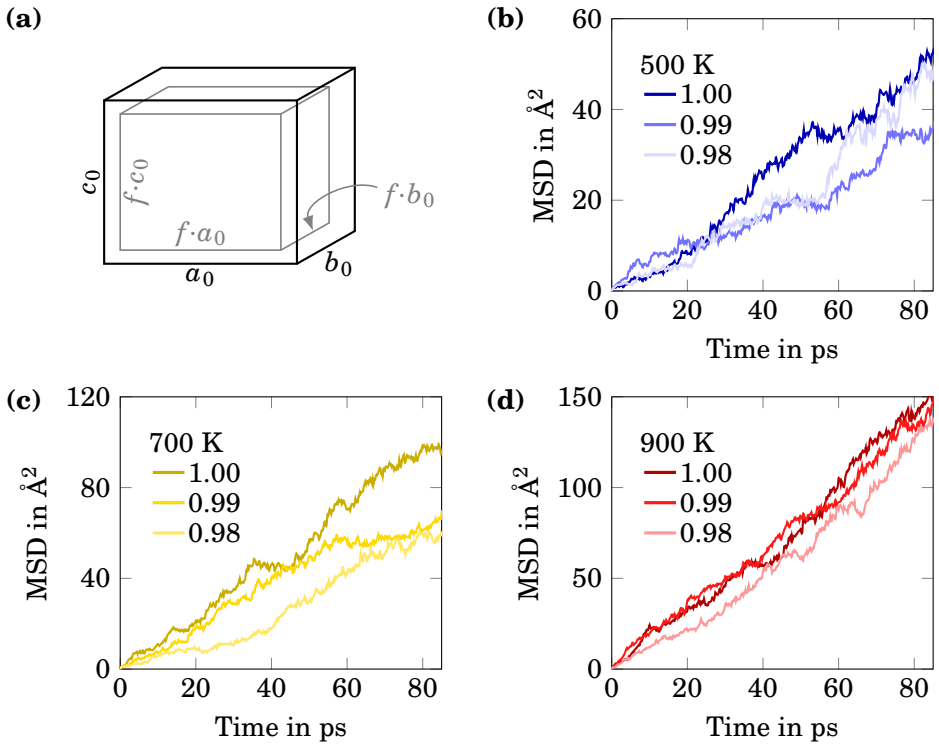

FIGURE 6.9: (a) Schematic representation of the isotropic rescaling of a simulation cell by a lattice scaling factor f. (b)-(d) MSD evolution at different temperatures and lattice scaling factors for the structure shown in Figure 6.2 (h). For $f = 1.00$ the equilibrium structure as obtained at 0 K is utilized. For $f = 0.99, 0.98$ the simulation cell is compressed.

6.3 Elastic Properties

Because the above mentioned elastic properties determined via speed of sound measurements were suspiciously low, we recalculated them based on static calculations. According to our experimental partners, the individual particles of the compressed powder samples are polycrystalline. Furthermore, there are no signs of texturing or preferential crystal orientations of the grains inside the particles. Therefore, the particles should possess isotropic elastic properties even if the underlying crystal phase of Li_7SiPS_8 is actually anisotropic due to its tetragonal symmetry. For the calculation of a reasonable, macroscopically averaged Young's modulus, however, the full elastic tensor needs to be calculated, which is a rather demanding task. We therefore first computed the bulk modulus, as explained in the following section, in order to verify if the elastic properties obtained by the speed of sound measurements are actually erroneous.

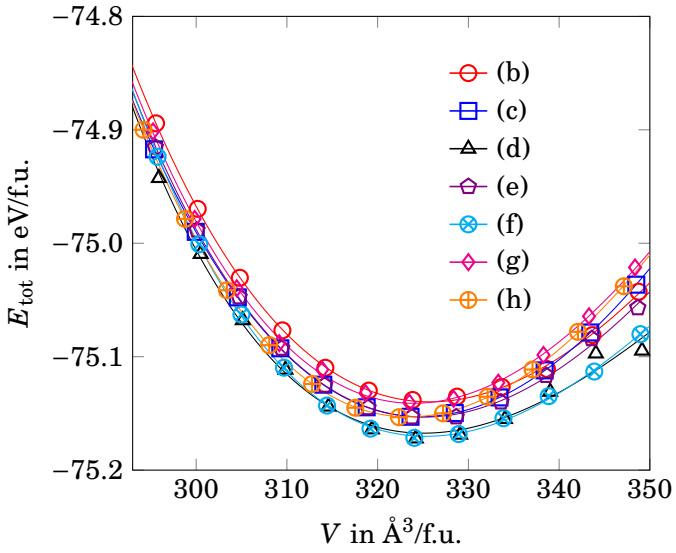

FIGURE 6.10: Energy-volume curves of all generated structural models for tetra-Li_7SiPS_8 and the corresponding fits according to the Birch-Murnaghan equation of state (Equation 3.57). The labels (b)-(h) in the legend refer to the structures shown in Figure 6.2.

TABLE 6.5: Bulk modulus B and its derivative with respect to pressure as obtained from the Birch-Murnaghan fits for all generated structural models of tetra-Li_7SiPS_8. The labels (b)-(h) refer to the structures shown in Figure 6.2.

	(b)	(c)	(d)	(e)	(f)	(g)	(h)	average
B [GPa]	22.2	24.2	19.9	22.4	21.5	24.4	24.9	22.8
B'	6.29	4.19	10.4	6.48	9.18	5.78	5.76	6.9

6.3.1 Bulk Modulus via Equation of State

As a first step to determine the elastic properties we statically optimized the atomic positions and cell geometry of all generated structural models for tetra-Li_7SiPS_8 at different volumes V. The resulting total energies as function of V were then fitted to the Birch-Murnaghan equation of state (Equation 3.57) to extract the bulk modulus B. The energy-volume curves and fits are shown in Figure 6.10 and the extracted elastic properties are listed in Table 6.5.

Our data return an average bulk modulus of 22.8 GPa, which fits to the bulk modulus of the structurally related LGPS of 20.4 GPa that was calculated with comparable simulation settings.[443] Hence, the calculated bulk modulus is one order of magnitude higher than the bulk modulus of 2.73 GPa obtained via the speed of sound measurements. The large mismatch and comparably low experimental value presumably originates from insufficient densification of the sample or other issues during the measurements. As a result, the speed of sound measurements are likely to deliver decreased elastic moduli.[444] For comparison, by using the Birch-Murnaghan equation of state with our computed values, the scaling factors of 0.99 and 0.98 result in pressures of 0.76 and 1.70 GPa, respectively, and a scaling factor of 0.9945 would be needed to reach

the experimental pressure of 0.4 GPa. If also thermal expansion during the finite temperature AIMD simulations is considered, the pressure might be even higher in the simulations discussed above. Still, the bulk transport properties were not found to change excessively, corroborating a weak correlation of the bulk transport properties to compressive mechanical loading. Because our calculated bulk moduli did not match the experimental results, we continued the analysis and calculated the full elastic tensor.

6.3.2 Full Elastic Tensor

In order to obtain the full elastic tensor, needed to determine macroscopically averaged elastic properties of polycrystalline material, we used the approach outlined in Section 3.7.2. Because the calculation of the full elastic tensor is computationally demanding, we only considered 5 of the 7 generated structures. These are the structures shown in Figure 6.2 (b)-(f). For the structure shown in part (e) of the figure, however, the calculation of the elastic constants was not possible. This is because the straining of the cell occasionally led to local rearrangements of individual Li^+ ions. Such a Li^+ rearrangement induces an energy drop in the energy-strain curves. These discontinuous curves cannot be fitted reasonably, preventing the calculation of the elastic constants. Comparable Li^+ rearrangements also occurred infrequently for the remaining structures due to the imposed strain. For these structures, however, the Li^+ rearrangements fortunately only occurred at higher strains, such that the fitting could be restricted to the data obtained at low strain values and the elastic constants could be determined.

The calculated elastic constants c_{ij} are listed in Table 6.6. For a system with true tetragonal symmetry the only six unique elements are c_{11}, c_{12}, c_{13}, c_{33}, c_{44}, and c_{66}. Furthermore, the following relations hold:

$$c_{11} = c_{22} \quad , \quad c_{13} = c_{23} \quad , \quad c_{44} = c_{55} \; . \tag{6.3}$$

All remaining elements should vanish. Table 6.6 shows that the remaining elements take values close to zero. There are two reasons why the values do not exactly equal zero and may be even negative. First, both the accuracy of the simulations and the fitting of the energy-strain data lead to small numeric variations. Second, the base tetragonal symmetry of tetra-Li_7SiPS_8 is broken in most cases as soon as the Si/P ions are explicitly distributed. Similarly, also the occupation of the Li^+ sites violates the tetragonal symmetry in the majority of cases. Therefore, it is reasonable that also elements of the elastic tensor different from the once mentioned above do not vanish. Because only small values are obtained, however, this effect seems to be mostly negligible. The same reasons also explain why the non-vanishing elements do not exactly comply with the relations given in Equation 6.3. We find that our calculated elastic constants are in line with those of other sulfide SEs.[428,443] However, the choice of the exchange-correlation functional has an influence and the PBEsol functional as

well as including Van-der-Waals interactions seem to yield slightly increased values.[428,443]

TABLE 6.6: Elastic constants of the investigated structures for tetra-Li_7SiPS_8. The labels (b), (c), (d), and (f) refer to the structures shown in Figure 6.2.

	Structures					Structures			
c_{ij}	(b)	(c)	(d)	(f)	c_{ij}	(b)	(c)	(d)	(f)
c_{11}	39.2	37.4	38.3	39.3	c_{13}	17.0	11.1	12.1	13.9
c_{22}	39.6	44.2	43.1	40.0	c_{24}	−0.3	0.0	−0.2	0.0
c_{33}	40.5	40.5	39.7	41.4	c_{35}	0.1	0.5	−0.6	−0.3
c_{44}	9.6	11.6	13.1	11.3	c_{46}	0.7	0.0	−0.2	0.3
c_{55}	10.6	8.5	9.0	10.4	c_{14}	0.9	1.6	0.2	0.1
c_{66}	16.8	17.8	18.0	18.4	c_{25}	−0.8	0.3	−0.8	−0.2
c_{12}	26.5	26.5	26.1	26.3	c_{36}	−0.3	−1.0	0.0	0.5
c_{23}	15.9	16.7	15.7	13.2	c_{15}	−0.8	−0.3	−0.1	−0.3
c_{34}	1.9	1.2	0.3	0.2	c_{26}	−0.0	0.6	−0.1	0.7
c_{45}	−0.5	0.9	0.1	0.5	c_{16}	−0.9	−0.7	0.2	0.5
c_{56}	1.1	0.9	0.0	0.6					

6.3.3 Macroscopically Averaged Mechanical Properties

Based on the individual elastic tensors, the elastic moduli were then calculated according to the Voigt, Reuss and Voigt-Reuss-Hill (VRH) approaches as introduced in Section 3.7.3. The results are shown in Table 6.7 and an average VRH bulk modulus of 25.3 GPa is obtained. It is slightly larger than the average value of 22.8 GPa obtained from the fits to the Birch-Murnaghan equation of state. Whereas the first value reflects the effective elastic properties of a polycrystalline material, the latter corresponds to a single crystal under hydrostatic pressure. It is therefore expected that the values differ and the same trend is also observed in other materials.[445]

The average Young's modulus Y_{VRH} based on the VRH approach amounts to 29.7 GPa. It is considerably larger than the measured Young's moduli of 18-25 GPa of pure Li_2S–P_2S_5 glasses and glasses containing halides.[114,387,446]. Values comparable to our calculated moduli, however, are obtained for glasses containing Ge or Si and for other crystalline sulfide SEs.[192,428]

TABLE 6.7: Effective elastic moduli of the investigated tetra-Li_7SiPS_8 structures according to the Voigt, Reuss, and Voigt-Reuss-Hill (VRH) approaches. The labels (b), (c), (d), and (f) refer to the structures shown in Figure 6.2.

(b)	Voigt	Reuss	VRH
Y [GPa]	29.9	26.9	28.4
G [GPa]	11.4	10.1	10.8
υ	0.31	0.33	0.32
B [GPa]	26.5	26.1	26.2

(c)	Voigt	Reuss	VRH
Y [GPa]	31.4	27.5	29.4
G [GPa]	12.1	10.5	11.3
υ	0.30	0.31	0.30
B [GPa]	25.6	24.5	25.0

(d)	Voigt	Reuss	VRH
Y [GPa]	32.2	29.0	30.6
G [GPa]	12.5	11.1	11.8
υ	0.29	0.30	0.30
B [GPa]	25.4	24.7	25.0

(f)	Voigt	Reuss	VRH
Y [GPa]	32.2	28.8	30.5
G [GPa]	12.5	11.0	11.8
υ	0.29	0.31	0.30
B [GPa]	25.2	25.0	25.1

6.4 Interfacial Instability of Tetra-Li_7SiPS_8 Against Li Metal

The stability of tetra-Li_7SiPS_8 against Li metal is of general interest with regard to the utilization of Li metal anodes. We first estimated the stability based on the following reaction,

$$Li_7SiPS_8 + 12\,Li \longrightarrow 8\,Li_2S + Li_3P + Si\,. \tag{6.4}$$

Indeed, this is an exothermic reaction with a reaction energy of −17.34 eV, corresponding to −1672 kJ/mol or −597 meV/atom. For an exact prediction of the equilibrium phases and the corresponding reaction energy the full calculation of the Li−Si−P−S phase diagram would be necessary. This has been done for similar compounds such as Li_4SiS_4 and $Li_{10}SiP_2S_{12}$.[111,296,322] The calculated equilibrium phases strongly vary with the Li chemical potential and comprise various Li_xSi_y phases. Because we did not determine the full phase diagram, Reaction 6.4 and the corresponding reaction energy need to be considered only as an approximation. Regardless of the true equilibrium phases, the highly negative reaction energy of our assumed reaction already indicates that tetra-Li_7SiPS_8 is thermodynamically unstable against Li metal. For a deeper analysis of the stability, explicit interface calculations, as outlined in the following, were conducted.

6.4.1 Setup of Explicit Interface Simulations and Reactivity during Static Calculations

For the construction of tetra-Li_7SiPS_8 | Li interfaces the individual materials were first prepared as slabs. These are shown in Figure 6.11 (a).

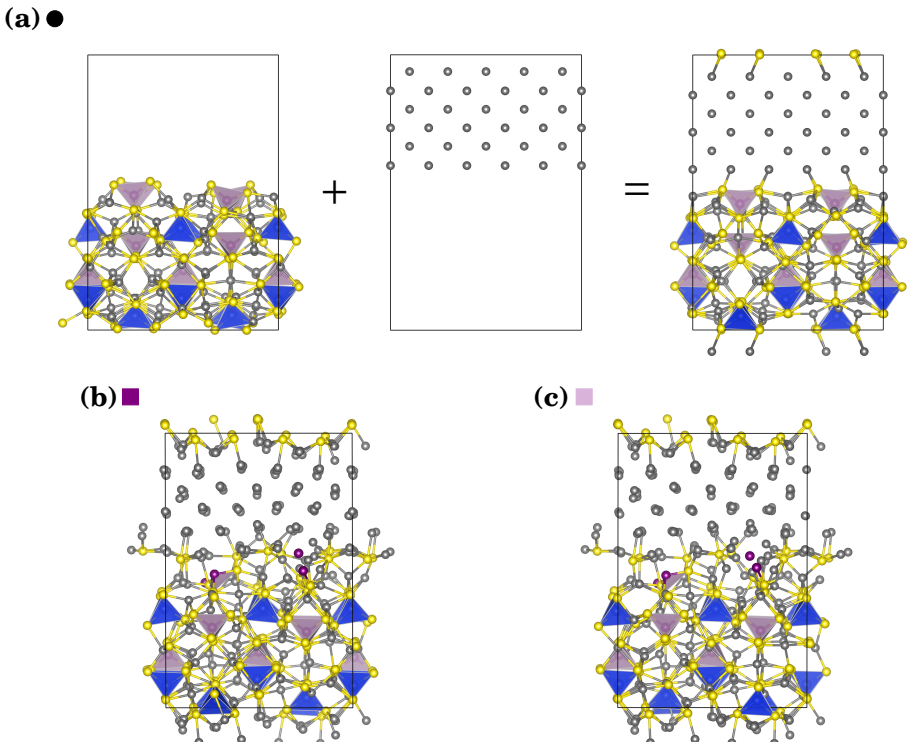

FIGURE 6.11: (a) Individual slabs of Li_7SiPS_8 (left) and Li metal (center) and the resulting interface model (right). Additionally, a second interface model (not shown) with a slightly increased slab distance was created. During static calculations the first and second interface model relaxed into the structures shown in (b) and (c), respectively. The labels (black sphere, colored squares) correspond to those shown in Figure 6.12.

In order to keep the computational effort manageable we only took into account 1 of the 7 generated Si/P ordering. Therefore, we arbitrarily chose the structure shown in Figure 6.2 (g). The slab of tetra-Li_7SiPS_8 was cut along the (001) plane in such a way that all SiS_4^{4-} or PS_4^{3-} units stayed intact and that the composition with 12 formula units remained stoichiometric. In fact, the slab exhibits a SiS_4^{4-}-rich surface at the bottom and a PS_4^{3-}-rich surface at the top. The slab was then statically optimized, which only resulted in negligible atomic rearrangements.

The dimensions of a 5×5×3 Li slab (150 Li atoms, body-centered cubic) were then adopted to the optimized tetra-Li_7SiPS_8 slab. To this end the lattice constants of the Li slab needed to be increased by 1.14% and 2.82% in the basal plane. The Li slab was statically optimized keeping the new dimensions in the basal plane fixed in order to allow for a relaxation in the remaining direction. Next, the two slabs were merged as shown in the right part of Figure 6.11 (a). Similarly, also a second interface model with a slightly increased initial slab

distance between the Li slab and the PS_4^{3-}-rich surface of the tetra-Li_7SiPS_8 slab was constructed. We note that the total composition of the interface model fits very well to the assumed Reaction 6.4. If the interface reacted according to this reaction, only a slight Li excess would remain,

$$12\,Li_7SiPS_8 + 150\,Li \longrightarrow 96\,Li_2S + 12\,Li_3P + 12\,Si + 6\,Li\,. \tag{6.5}$$

The atomic positions and cell geometry of both interface models were then statically optimized and the resulting structures are shown in Figure 6.11 (b) and (c). Interestingly, a reaction at the interface is observed. Similar interface reactions between Li metal and sulfide SEs have been observed in the past.[316,318,447] Such an extensive reaction as observed here, however, is rather unexpected because the static nature of the calculations is not able to overcome energy barriers. For the reaction between amorphous LiPON and Li metal, however, also a substantial atomic rearrangement during static calculations was observed.[196]

Despite allowing for more than 500 ionic optimization steps both interface models did not result in a well-converged structure. This indicates the existence of an extended, barrierless reaction path. Because the static calculations seemed to not reach a local energy minima we stopped them at this point and analyzed the resulting structures.

Most notably, we find that the reaction mainly takes place on the PS_4^{3-}-rich interface and leads to the dissociation of the PS_4^{3-} units. Similar reactions have been observed for interface simulations of other sulfide SEs against Li metal.[318,448] Correspondingly, the structure of the Li metal is disturbed at the interface but the overall body-centered cubic can still be identified. In contrast to the PS_4^{3-} units, all SiS_4^{4-} tetrahedra remain intact, hinting at their preferential stability. In order to exclude that the reaction is an artifact of the initial distance between the two slabs, the second interface model with increased slab distance was generated. The resulting optimized models shown in Figure 6.11 (b) and (c), however, are virtually identical. Therefore, the initial interslab distance seems to only have a negligible influence on the resulting structure and the reaction will proceed regardless. We note that also other studies hint at the instability of PS_4^{3-} units. Based on explicit interface reactions between LGPS and Li metal conducted by Chen et al. a similar case can be identified.[449] In their interface structure, the PS_4^{3-} termination of the LGPS slab is more reactive than the GeS_4^{4-}-termination.

The reactive nature of the interface does not allow for the definition of a proper interface energy. Nevertheless, in order to estimate an approximate reaction energy we referenced the energy of the reacted interface against the summed energies of the individual tetra-Li_7SiPS_8 and Li slabs. According to this both interfaces gained approximately −110 meV/atom during the static optimizations. Incited by the high reactivity we deceided to perform AIMD simulations to study the further evolution of the interface.

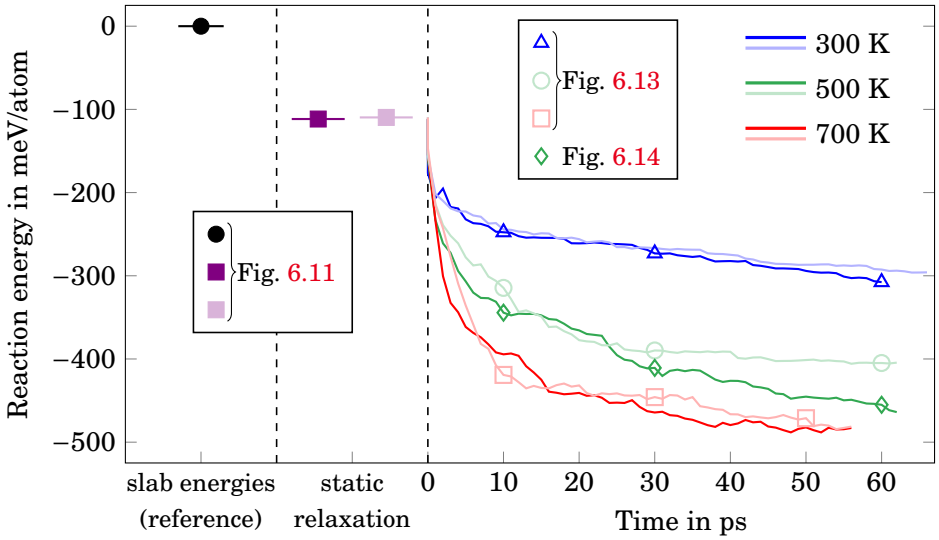

FIGURE 6.12: Reaction energies of the tetra-Li_7SiPS_8 | Li slab at the respective stages of computation. Left, the reference energy (black) is indicated. It is obtained as sum of the individual tetra-Li_7SiPS_8 and Li slabs in vacuum and has is been set to zero. Next, the energies after static relaxation of the initial slab models is shown. In the right part of the diagram the energy change during the AIMD simulations is monitored. The shown energies are obtained by taking snapshot structures of the AIMD and performing a full static optimization. The two color sets indicate that the data sets correspond to the first interface setup (deep, full colors) and the second setup with an initially increased slab distance (whitish, pale colors). Exemplary structures, as marked with different symbols in the diagram, are shown in Figure 6.11, 6.13, and 6.14.

6.4.2 Interface Evolution During AIMD Simulations

The statically relaxed interface models shown in Figure 6.11 (b) and (c) were used as initial structures to conduct AIMD simulations at 300, 500 and 700 K for approximately 60 ps. In order to monitor the ongoing reaction we extracted snapshot structures every 1 ps from the AIMD runs. These snapshots were then statically optimized. The static optimizations allow us to remove any thermal contributions to the total energy. Therefore, the energies between simulations of different temperatures can be compared. The only drawback of this approach is that the reaction may proceed even during the static optimizations, thereby misrepresenting the chronological order of the MD snapshots. Still, it allows an approximate monitoring of the energetic evolution of the interface.

Together with the reaction energies obtained at the end of the static optimization described in the previous section, the evolution of the interface energies during the AIMD simulation is shown in Figure 6.12. The overall trends are clear: First, over the simulated time span the reaction obviously proceeds continuously as the reaction energy decreases in the course of the simulation.

Especially in the very beginning the reaction energy quickly drops. Second, the higher the temperature is set during the AIMD simulations, the faster the reaction proceeds. Moreover, it can be speculated that the reaction energy, especially for the simulations at higher temperatures, is gradually converging as the curves seem to flatten during the end of the simulations. Indeed, a reaction energy of approximately −480 meV/atom was reached at 700 K after 55 ps, close to the calculated reaction energy of −597 meV/atom of Reaction 6.4. Let us now inspect the structural evolution of the interface. To this end, three relaxed snapshots for every temperature, as marked in Figure 6.12 with empty triangles, circles, and squares, are exemplarily shown in Figure 6.13.

At 300 K three structures belonging to the data set indicated with a deep blue line and marked with blue empty triangles in Figure 6.12 are shown in Figure 6.13 (a). The other data set at 300 K delivered comparable results and is therefore not explicitly shown. Remarkably, we find that no single PS_4^{3-} unit stayed intact after only 10 ps. They have all released at least one S^{2-}, the majority even two or more. This even holds true for the PS_4^{3-} units originally located in the central part of the tetra-Li_7SiPS_8 slab not directly adjacent to Li metal. Most likely, the dissociation of PS_4^{3-} units within the tetra-Li_7SiPS_8 slab is initiated by diffusion of Li from the Li metal slab into the tetra-Li_7SiPS_8 slab leading to a reduction of the PS_4^{3-} units.

With its melting point slightly above 450 K, Li metal should still be in its solid phase at 300 K. Nevertheless, the extent of the interface reaction annihilates the body-centered cubic structure of the Li metal and leads to an amorphization of the remaining Li slab. Not only the Li slab is affected by the reaction. Also the tetra-Li_7SiPS_8 slab is heavily disturbed and left with an amorphous structure. This is probably due to the dissociated PS_4^{3-} units and the additional Li that diffused into the SE making the formerly crystalline structure of tetra-Li_7SiPS_8 unrecognizable. At 10 ps also one SiS_4^{4-} unit has already fully dissociated whereas the remaining units are still intact. After 30 ps a second SiS_4^{4-} unit has fully dissociated, the remaining PS_x units decomposed further and the reaction has consumed more Li of the Li slab.

Until the end of the simulation at 60 ps no further SiS_4^{4-} unit has dissociated, several residual PS_x units with $x \leq 3$ are present in the simulation cell and an overall amorphous structure of the interphase remains. The reaction energy has reached approximately −300 meV/atom. At this stage of the reaction all S^{2-} that remain without bonds to P or Si are surrounded by 6 to 8 Li^+. For comparison, in Li_2S the S^{2-} ions are surrounded by exactly 8 Li^+ arranged as cube. The Li_xS coordination polyhedra in the amorphous interphase, however, are considerably distorted, so that only the formation of an amorphous Li_2S can be speculated. Similarly, also the fully disconnected P ions are surrounded by 8 or 9 Li^+ and have therefore undergone a severe coordination change alongside a reduction during the reaction. As described previously for the reaction of other sulfide SEs with Li metal this might be assigned to an early stage of Li_3P formation.[448] In crystalline Li_3P, however, the P ions are surrounded by 11 Li^+.

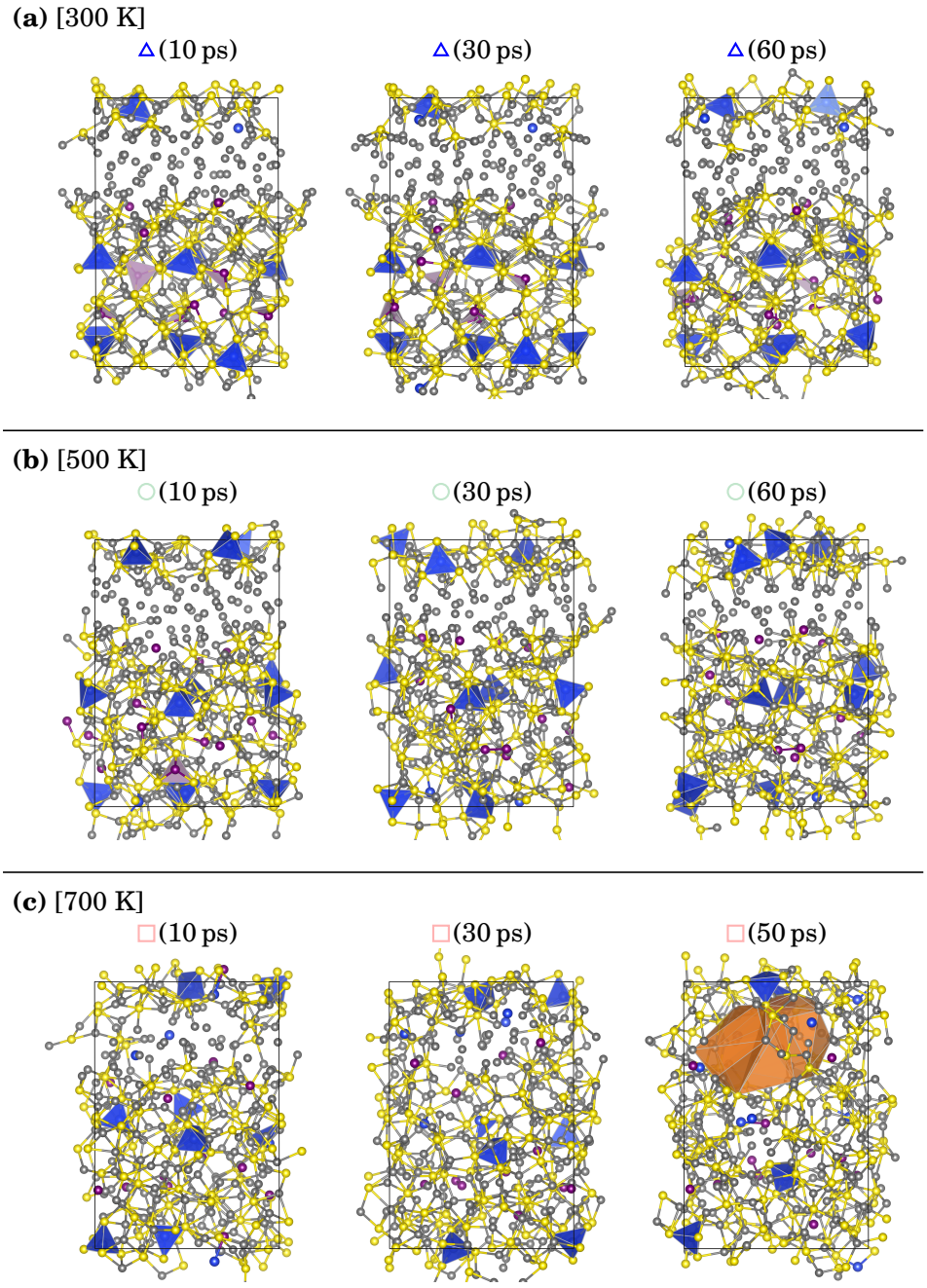

FIGURE 6.13: Relaxed snapshot structures of the tetra-Li_7SiPS_8 | Li interface at different temperatures and simulation times as labeled above the structures. The various symbols (triangle, circle, square) refer to the points marked in Figure 6.12. The orange object in the rightmost structure in (c) is a void with a volume of approximately 400 $Å^3$.

Similar observations as made for the simulations at 300 K can be made for one of the two data sets obtained at 500 K. The corresponding structures shown in Figure 6.13 (b) belong to the data set plotted with a pale green line and marked with pale green circles in Figure 6.12. The main difference to the simulations at 300 K is that the increased temperature of 500 K has accelerated the reaction. All PS_4^{3-} units are again dissociated after only 10 ps to PS_x units with $x \leq 3$ whereas the majority of SiS_4^{4-} units stays intact. At the end of the simulation after 60 ps hardly any P–S bonds remain, but 10 of the former 12 SiS_4^{4-} units survived and one P–P unit is observed. The structure of the interphase is again amorphous and only a thin layer of Li metal remains. For the shown structure in Figure 6.13 (b) the reaction energy amounts to approximately −400 meV/atom after 60 ps. The other data set at 500 K (deep green curve, structures indicated with diamond markers) even reached approximately −460 meV/atom within the same time. This will be discussed separately in the following sections in more detail because, differently from all other simulations, the formation of an ordered interphase has been observed. Let us first consider the remaining results obtained at 700 K.

As it is expected, at 700 K (Figure 6.13 (c)) the reaction is even faster compared to 500 K. Just as observed for 300 K the two data sets at 700 K qualitatively deliver similar results: After 10 ps the Li metal layer is almost depleted already. Furthermore, several SiS_4^{4-} units are already dissociated, no P–S bonds remain and an amorphous interphase has formed. After 50 ps the structure is left with only 4 intact SiS_4^{4-} units and one P–P and Si–P bond is observed. An extended network of Li_xS coordination polyhedra (x equal to 7 or 8, rarely also 6) is found and corroborates the formation of an amorphous Li_2S phase. Fully dissociated P ions are coordinated by 7 to 10 Li^+. Likewise, also fully dissociated Si is surrounded by 9 to 10 Li^+. This observation confirms that the assumed Reaction 6.5 is only an approximation with regard to the formation of a pure Si phase. Instead it would be more reasonable to include one or multiple of the many Li_xSi_y phases. Because (i) the inclusion of such phases complicates the reaction considerably and (ii) the amount of Si is low, we will keep referring to Reaction 6.5 for the following considerations, keeping in mind that it only represents an approximation to the true reaction.

Interestingly, an extended pore close to the initial position of the Li slab has formed during the reaction. The pore is shown as an orange object that is delimited by its surrounding atoms. Its volume is approximately 400 $Å^3$. The volume reduction of the material during the reaction is not surprising. If the computed equilibrium volumes of all optimized compounds are considered and applied to Reaction 6.5, a volume reduction of approximately 20% is expected. This is summarized in Table 6.8. Because the AIMD simulations were performed at constant volume the reacted interphase only has two options to compensate for the volume mismatch. First, the material counteracts the volume reduction by building up strain. This might be possible for the initial phase of the reaction. At an advanced stage, however, the volume mismatch certainly becomes too

large to be only compensated by the inclusion of strain. Therefore, the second option is the formation of free volume, i.e., pores, to reduce the strain.

TABLE 6.8: Volumes V per formula unit of all crystalline phases that take part in Reaction 6.5 and expected total volumes V_{tot} for the entire educts and products of the reaction.

	$12\,Li_7SiPS_8$	$+\ 150\,Li$	$\longrightarrow$	$96\,Li_2S$	$+\ 12\,Li_3P$	$+\ 12\,Si$	$+\ 6\,Li$
V [Å^3/f.u.]	323.50	20.04		46.33	58.22	20.44	20.04
V_{tot} [Å^3]	6888.00		$\longrightarrow$	5511.84			

It is unclear how the strain and pore formation influence the reaction. At the finite temperatures of the simulations the thermal expansion is likely to reduce the effect. Furthermore, the interphase turned out to be amorphous for the cases analyzed in this section. It is therefore likely that the amorphous structure is less dense compared to the crystalline phases. Lastly, the assumed reaction is only an approximation. For example, not even the onset of a Si phase has been observed. Instead, the Si either still belongs to SiS_4^{4-} units or its remnants, or is fully dissociated and surrounded by Li^+. Therefore, the volume considerations of Table 6.8 are also only an approximation. Due to these reasons the interface reaction is like to be influenced only to a low extent by the evolved strain and pore formation.

In conclusion, the tetra-Li_7SiPS_8 | Li interface is highly reactive, similarly to other sulfide SEs. Especially the PS_4^{3-} units are prone to the reaction with Li metal whereas the SiS_4^{4-} units exhibit a more pronounced stability. Therefore, Si-containing SEs might show improved stability against Li metal compared to pure LiPS materials. The extensive reaction is likely to result in an amorphous interphase consisting of an defective, amorphous Li_2S matrix that embeds the remaining reaction products such as SiS_4^{4-} and its remnants, remnants of PS_4^{3-} units and fully dissociated P and Si ions. As we will see in the following, however, the formation of an amorphous phase is not inevitable.

6.4.3 Formation of an Ordered Interphase

Due to the random velocity initialization of the atoms at the start of every AIMD simulation, the system may evolve independently even when started from exactly the same initial structure. The AIMD simulations of the tetra-Li_7SiPS_8 | Li interface were furthermore started from two slightly different initial interface models (Figure 6.11 (b) and (c)). Therefore, it is reasonable that the simulations may evolve differently. Nevertheless, the two AIMD simulations at 300 K led to a very similar evolution of the interface and the obtained results are in line with the simulation at 500 K presented above and the two simulations conducted at 700 K. All these simulations led to an amorphous interphase. The second simulation at 500 K, however, progressed distinctly differently and the formation of an ordered interphase is observed. The corresponding structures

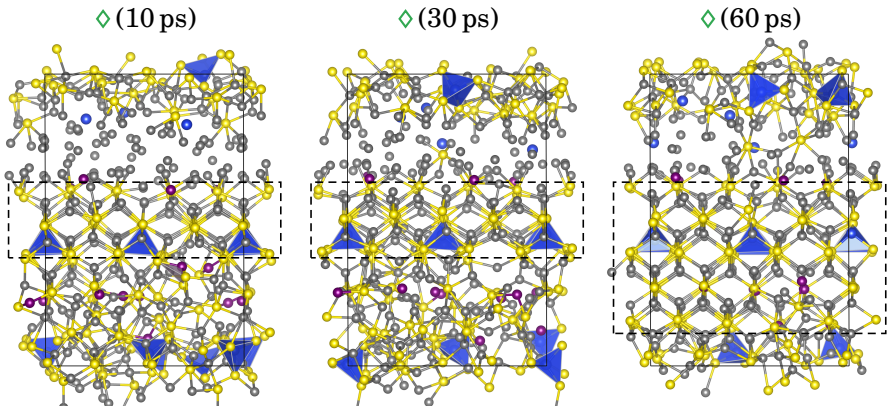

FIGURE 6.14: Relaxed snapshot structures of the tetra-Li_7SiPS_8 | Li interface at 500 K. The structures belong to the data set illustrated with a deep green line and marked with green diamonds in Figure 6.12. Ordered regions in the structures are indicated with dashed boxes.

can be viewed in Figure 6.14 and belong to the deep green line marked with diamonds in Figure 6.12.

After 10 ps, all PS_4^{3-} have dissociated while the majority of the SiS_4^{4-} units stayed intact and several Li of the Li metal slab have diffused into the tetra-Li_7SiPS_8 slab. This is very similar to the observations described above for all other simulations. However, unlike the other simulations, in this case an ordered phase has formed at the former PS_4^{3-}-rich side of the tetra-Li_7SiPS_8 slab. The ordered part of the interface layer is indicated with a dashed box in Figure 6.14 and mainly consists of S^{2-}, Li^+ and embedded SiS_4^{4-} units. The remaining interphase is again amorphous. Until a simulation time of 30 ps the interface model does not change much upon visual inspection. Towards the end of the simulation, at 60 ps, however, the ordered interphase has clearly grown at the expense of the amorphous interphase and almost reaches the bottom of the simulation cell. Remarkably, the interphase now also accommodates P ions and several of the embedded SiS_4^{4-} units have released one of their S and are left as SiS_3 units. As a next step we analyzed the electronic structure of the system with two questions in mind. First, how does the ordered interphase changes the electronic structure of the system compared to an amorphous interphase? Second, is it possible to identify what crystalline phases have formed in the ordered interphase based on the eDOS?

6.4.4 Influence of the Interphase Formation on the Electronic Structure

To be able to answer the question of how the electronic structure of the ordered and amorphous interphases differ and whether crystalline phases can be identified based on the eDOS, it is helpful to also consider the eDOS of the pristine bulk tetra-Li_7SiPS_8. It is shown in Figure 6.15 together with the eDOS of the reacted interface model where the ordered interphase has formed, of the reacted interface model where the interphase remained amorphous, and of the reference materials Li_2S and Li_3P.

According to the convention adopted in `VASP`, the VMB coincides with the Fermi level and is set at an energy of 0 eV. We left this convention unaltered for the two reacted interface models shown in Figure 6.15 (a) and (b). However, aligning materials with different compositions to their VMB is not physically meaningful: that is why all eDOS are aligned with respect to the energy of the Li(1s) core levels. Fortunately, the weighted average position of the Li(1s) levels of both interface models were found to be located at −47.03 eV, highlighted with a red dashed line spanning over all eDOS plots, and the bulk materials have been aligned accordingly. When comparing the eDOS several observations are apparent:

1. It is somewhat surprising that the eDOS of the interface models with the ordered and the amorphous interphase are virtually identical. Certainly, there are subtle differences in the shape, width and height of several peaks in the eDOS. These differences, however, lie within the accuracy of the DFT calculations. Therefore, a distinction between the ordered and amorphous interphase in their current states is not possible based only on the eDOS.

2. The eDOS of both interface models at their VMB ($E = 0$) is small but does not vanish completely. This indicates that the reacted interfaces still exhibit a slightly metallic character. For comparison, bulk tetra-Li_7SiPS_8 exhibits a band gap of 2.12 eV according to our DFT calculations. The metallic character is therefore attributed to the thin remaining Li metal layer and/or intermediate reaction products. We expect that the metallic contributions will vanish eventually in the course of a proceeding reaction because this observation is made for the interface at 700 K: For the interface model where the formation of a pore has been observed, the Li metal slab fully reacted with the SE (see Figure 6.13 (c) on the right). Correspondingly, the reacted interface model exhibits a true band gap (not shown).

3. Both reacted interface models are missing shared S−P contributions that are found in the eDOS of bulk tetra-Li_7SiPS_8. This is reasonable because all PS_4^{3-} tetrahedra have been fully dissolved during the interface reaction

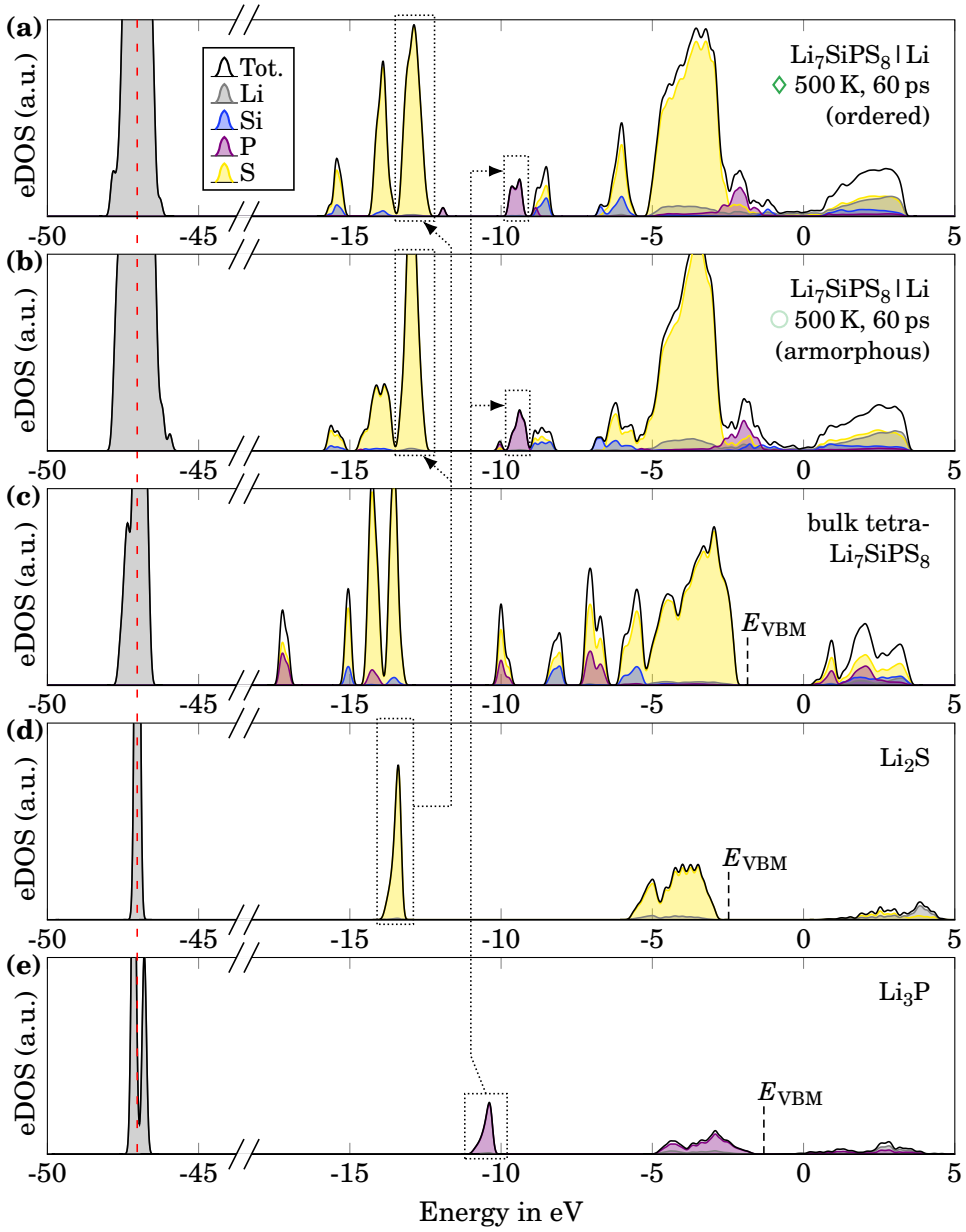

FIGURE 6.15: Total electronic density of states (eDOS) and its contributions from the individual atom types of (a) the tetra-Li_7SiPS_8 | Li interface where the ordered interphase has formed, (b) where the interphase remained amorphous, (c) bulk tetra-Li_7SiPS_8, (d) Li_2S, and (e) Li_3P. The VMB of bulk tetra-Li_7SiPS_8, Li_2S and Li_3p are not located at 0 eV because their eDOS have been shifted such that their Li(1s) core levels are aligned to those of the interface models (red, dashed line).

after 60 ps at 500 K. Several shared S−Si contributions, however, remain because SiS_4^{4-} and SiS_3 units are still present and embedded in both the ordered and the amorphous interphase.

4. From approximately -5 to -2 eV the eDOS is dominated by S contributions that are a result of the lone electron pairs of the S^{2-}. Exactly the same contributions have been observed for LiPS SEs.

5. Some features in the eDOS of both interfaces resemble those of Li_2S and Li_3P as exemplarily indicated in Figure 6.15. This suggests that at least on a local scale the atomic arrangements in both the ordered and the amorphous interphase are similar to those found in Li_2S and Li_3P. The fact that the peaks of Li_2S and Li_3P are not perfectly aligned to those in the interface models is most likely due to the disturbed local structure in both interphase. Furthermore, Li_2S and Li_3P (even if defect-free) would fit into the simulation cell of the interface models only if they were subjected to small strains that may lead to shifts of the energy levels. Additionally, also the positions of the Li(1s) core levels are certainly influenced by the chemical surrounding which also affects the relative positions of the remaining energy levels.

The insights gained from analyzing the eDOS are rather unsatisfactory and we have visually inspected the ordered interphase more closely to compare its structure to the crystalline phases.

6.4.5 Identification of the Ordered Phase via Visual Inspection

A side view of the ordered structure after 60 ps is shown in Figure 6.16 (a). In this illustration Li and Si are used to generate coordination polyhedra (yellow) around S. Purple coordination polyhedra depict Li around P. The side view clearly confirms that an ordered phase is present. For comparison, Figure 6.16 (b) shows the structure of Li_2S, in which all S^{2-} are surrounded by 8 Li^+ arranged as cube. Exactly these cubic Li_8S coordination polyhedra are found frequently in the interphase. This can be seen in Figure 6.16 (c)-(g) where slices of the interface model are shown.

In the upper slices (c) and (d) the ordered structure is still disturbed considerably and the majority of Li_xS polyhedra is Li-deficient. This can mainly be ascribed to the embedded SiS_4^{4-} units and partly dissociated SiS_3 units. As a result, coordination polyhedra such as $(SiLi_6)S$ are formed. Such configurations can also be understood as Li_2S where Li has been partly substituted with Si resulting in a large number of structural Li^+ vacancies. The latter might be beneficial for the ionic transport properties of the interphase layer.

Slice (c) furthermore contains various Li_xP coordination polyhedra that seem to disturb the structure of the slice. Nevertheless, the onset of an ordered arrangement of S^{2-} can be speculated. The interactions of the Li_xP polyhedra

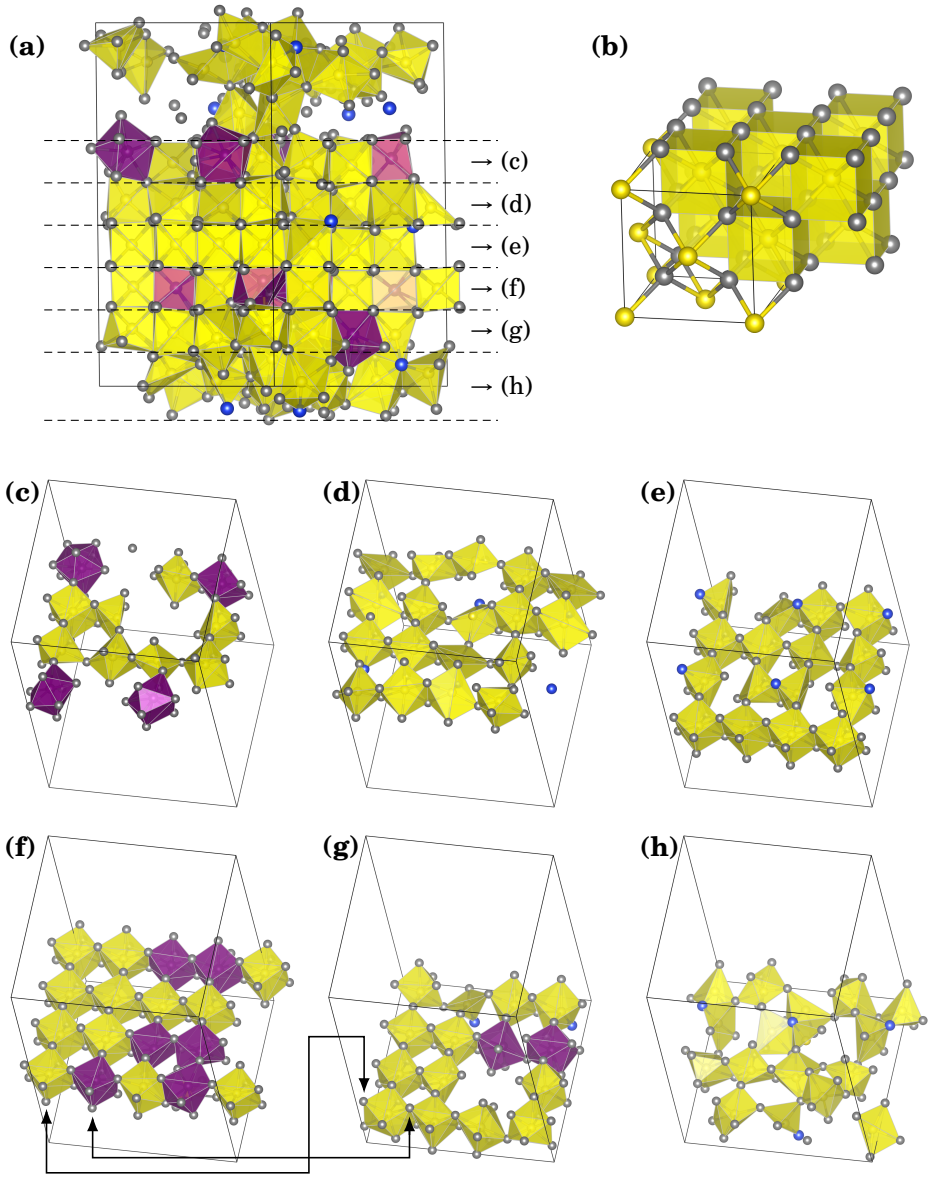

FIGURE 6.16: (a) Side view of the interface model after 60 ps at 500 K (same structure as shown in Figure 6.14 on the right). The dashed lines indicate the approximate slices of the interface model shown in part (c) to (h) of the figure. b) Structural model of Li_2S and its Li_8S coordination polyhedra shown in yellow. Li_xP coordination polyhedra are colored purple in the slices. The intact SiS_4^{4-} tetrahedra are not displayed to improve the clarity of the figure. Arrows connecting part (f) and (g) have been added as a guide to the eye to indicate two common ions of the two slices.

extend to slice (d) and together with SiS_4^{4-} and SiS_3 units they prevent the formation of an undisturbed Li_2S structure. Still, the S^{2-} are able to arrange in a regular pattern in slice (d). In contrast to that, no ordering of S^{2-} occurs in the bottom slice (h) which also comprises SiS_4^{4-} as well as SiS_3 units and is adjacent to a slice comprising Li_xP coordination polyhedra. Due to the observed growth of the ordered phase during the AIMD simulations, however, an ordering of slice (h) will presumably set in at a later point in time if the calculations are continued.

The structure within the slices (e), (f) and (g) strongly resembles that of Li_2S and various regions can be unambiguously assigned to Li_2S. Interestingly, slice (f) shows that also P ions partly arrange in the Li_2S structure. Some of them are also coordinated by 8 Li^+ that form cubic polyhedra, whereas others exhibit more distorted polyhedra. Additionally, several Li_9P coordination polyhedra are found. The larger number of Li^+ around P fits to the structure of Li_3P in which every P is coordinated by 11 Li^+ at three different distances. In our optimized models of bulk Li_3P, 3 Li^+ are found at a distance of 2.44 Å, 2 at 2.52 Å and 6 at 2.74 Å. These values are comparable to the majority of P–Li bonds observed in the interface model. Due to the strong distortions of some Li_8P and Li_9P polyhedra, however, also a few bonds with a considerably larger bond distance up to 3 Å are observed. Furthermore, slice (f) gives the impression that the Li_xP polyhedra have clustered. This might indicate the onset of the formation of Li_3P.

The presence of P as well as SiS_4^{4-} and SiS_3 units obviously does not hinder the formation of a defect-rich but crystalline Li_2S phase. However, such an ordered phase was not observed in the remaining simulations. This suggests that the formation of the ordered phase strongly depends on the applied temperatures and the covered simulation time. Presumably, the interphase only starts to grow once a crystallization seed has reached a critical size. For the simulations at 300 K the kinetics might have been simply too slow to observe the formation of such a seed and the subsequent growth within reasonable simulation times. At 700 K, on the other hand, the temperature might have been too high leading to an unstable seed that dissolves prior to its growth. Apparently, 500 K is a reasonable temperature to observe the formation of an ordered interphase within affordable simulation times. The kinetics and statistics, however, seem to play an important role, which explains why the growth of the Li_2S-like interphase is only observed in one of the two simulations.

A thin Li_2S layer, for example, has already been suggested as a protective coating for Li_3PS_4 against Li metal and improved the cycling performance of Li metal anodes in cells employing $Li_4Ti_5O_{12}$.[174,437] Therefore, the formation of Li_2S might indeed be beneficial for the stabilization of the interface. The drawback of Li_2S, however, is its rather low ionic conductivity of the order of 10^{-10} mS/cm.[436] In this regard the observed interphase might exhibit beneficial properties because it contains a large number of defects. These might lead to improved Li^+ diffusion compared to pure Li_2S and result in comparably low interface resistances. This, however, only holds true if the growth of the interphase

stops at rather thin thicknesses. If the formed Li_2S is too defective and also enables the diffusion of other species, its growth might continue. Under these circumstances a thick interphase will form and eventually lead to increased interface resistances making the material unsuitable as SE against Li metal anodes without any further protection schemes. Our models are limited in size and time and do not allow for an entire clarification of this issue. Experiments conducted by our experimental partners, however, indeed suggest that a thick interphase forms over time. Therefore, plain Li_7SiPS_8 seems to be unsuitable for the direct utilization against Li metal anodes. Nevertheless, the insights gained from our interface simulations improve the general understanding of interface reactions between Li metal and sulfide SEs, especially for other Si-containing compounds such as $Li_{10}SiP_2S_{12}$ or Li_4SiS_4. The generated knowledge might additionally support the tuning of interfaces and the development of protective coatings.

6.5 Summary

Li_7SiPS_8 crystallizes in two different phases that both exhibit structural disorder among the Si/P sites as well as a complicated Li substructure. We therefore first showed comprehensively how the two phases can be approached via electronic structure calculations despite exhibiting such complicated structures. The generated structural models were then analyzed with respect to their stability, Li^+ transport properties, elastic properties and interface stability against Li metal.

We could show that the orthorhombic phase of Li_7SiPS_8 (ortho-Li_7SiPS_8) is more stable than its tetragonal variant (tetra-Li_7SiPS_8). The average energy difference of 11.8 meV/atom between the two phases, however, is small and it is likely that entropic contributions can outweigh them at finite temperatures. The Si/P arrangement seems to have a negligible influence on the relative energy, suggesting no preferential ordering as confirmed by experiments.

An analysis of the Li^+ transport properties shows that the Si/P arrangement also has an insignificant impact on the diffusion. For ortho-Li_7SiPS_8 nearly isotropic diffusion is observed and only a slightly faster diffusion can be expected along the c direction. Unfortunately, its migration barrier with approximately 290-330 meV is comparably high. In contrast to that, the migration barrier of tetra-Li_7SiPS_8 with approximately 130-150 meV is found to be much lower than that of ortho-Li_7SiPS_8, making tetra-Li_7SiPS_8 the superior Li^+ conductor, particularly at lower temperatures. Tetra-Li_7SiPS_8, however, exhibits highly anisotropic transport properties with a high diffusion coefficient along the crystallographic c direction but comparably low diffusion coefficients along a and b. Therefore, the material might only be able to unfold its true potential by enabling faster diffusion along the a and b direction or by texturing.

The transport properties of tetra-Li_7SiPS_8 were further examined under mechanical loading. Our simulations indicate that the bulk transport properties deteriorate slightly upon compressive loading. These results corroborate the assumption that the improved ionic conductivity observed after compressing compacted powder sample of tetra-Li_7SiPS_8 does not originate from bulk effects. Instead, the compression is likely to lead to a further densification of the sample with improved particle-particle contacts such that more conduction pathways are established.

Because elastic moduli from speed-of-sound measurements appeared to be suspiciously low, we computed the elastic properties of tetra-Li_7SiPS_8 by making use of two different approaches. First, calculated energy-volume curves of the material were fitted to the Birch-Murnaghan equation of states to determine the bulk modulus. Second, the full elastic tensor was calculated and used to compute macroscopically averaged elastic moduli. The first approach delivers a bulk modulus of 22.8 GPa. With the latter approach a slightly larger bulk modulus of 25.3 GPa and a Young's modulus of 29.7 GPa are obtained. These values are comparable to other sulfide SEs and indicate that issues were faced during the speed-of-sound measurements.

Finally, the interface stability of tetra-Li_7SiPS_8 against Li metal was analyzed. A thermodynamic estimation predicted an instability against Li metal and explicit interface simulations were then conducted to verify this prediction. Indeed, an interface reaction is already observed during static optimizations of the initial interface models. Most notably, mainly the PS_4^{3-} units dissociate while all SiS_4^{4-} units stay intact during this initial reaction phase. The evolution of the interface/interphase was then monitored by conducting AIMD simulations at different temperatures. In all simulations the reaction proceeded and the Li metal layer reacted with the SE.

Already after 10 ps at 300 K all PS_4^{3-} units have dissociated while several SiS_4^{4-} are able to remain intact even after 55 ps at 700 K, indicating their superior stability. Furthermore, the formation of a pore is observed, which is attributed to an overall volume reduction in the course of the reaction, potentially promoted by the constant volume conditions of the simulations. In the majority of cases, the formed interphase is found to be amorphous and can be described as a defective, amorphous Li_2S matrix that embeds the remaining reaction products. Only for one calculation at 500 K the formation of an ordered interphase is observed. Remarkably, the eDOS of ordered and amorphous interphase are virtually identical and both show features of Li_2S and Li_3P. Via visual inspection of the ordered interphase, we undoubtedly identify a Li_2S-like structure. However, the structure is highly defective and locally distorted because other species such as SiS_4^{4-} units, their partially dissociated remnants or P ions are embedded in it. Moreover, clustering of Li_xP units indicates the onset of Li_3P formation and we assume that the high defect density of the Li_2S matrix leads to improved transport properties for Li^+ ions and therefore lower interface resistance compared to pure Li_2S. On the other hand, the high defect

density might also enable the diffusion of other species, possibly leading to a further growth of the interphase resulting in an increased interface resistance. This assumption is corroborated by experiments that observe a growing interphase with time if tetra-Li_7SiPS_8 is contacted to Li metal.[438] The results of our interface simulations might therefore be helpful to develop protection schemes for tetra-Li_7SiPS_8 or similar SEs.

In conclusion, the tetragonal phase of Li_7SiPS_8 is a promising SE in terms of Li^+ transport properties with elastic properties that are comparable to other sulfide SEs. Two main obstacles, however, have been identified that could prevent its employment. First, the distinct anisotropy of the Li^+ diffusion might require a texturing or further tuning of the material to deliver optimal performance. Second, when employed with Li metal anodes a protective scheme seems to be inevitable to avoid excessive interface reactions. The last point, however, is not exclusive to Li_7SiPS_8 and seems to apply to all sulfide SEs. Therefore, more research concerning interface issues is needed to enable an effective breakthrough of sulfide SEs.

7 Conclusion and Outlook

Electronic structure calculations in the framework of DFT have been applied to analyze various sulfide SEs. Let us refer to the initial research questions that were stated in Section 2.3 to summarize the most important achievements and findings (see the summary sections at the end of every chapter for more details). Afterward, the similarities and difference between the materials are contrasted in an overarching context. Finally, open questions are addressed and next possible steps are outlined.

7.1 Pure Lithium Thiophospates

In Chapter 4, we dealt with ternary LiPS phases that comprise crystalline and glassy phases as well as glass-ceramics. Various glass models at different compositions within the compositional triangle Li_3PS_4–$Li_4P_2S_7$–$Li_4P_2S_6$ have successfully been generated using simulated melt-quenching schemes and their structure was validated with available experimental data. All glasses are metastable and exhibit relative stabilities of to 18.8-40.0 meV/atom with respect to the crystalline boundary phases at 0 K. By including entropic effects, the glasses become 3-10 meV more stable but remain metastable. The relative stability follows certain trends: more stable glasses tend to contain $P_2S_7^{4-}$ units, whereas less stable glasses comprise $P_2S_6^{4-}$ units.

Structurally, all glasses exhibit three common peaks in RDFs at low distances that are attributed to P–S and S–S bonds as well as Li–S correlations. Several other features could be attributed to certain intramolecular correlations within the structural units. Intra- and intermolecular S–S contributions to the RDFs were disentangled, which will be helpful future structural analyses of LiPS materials. Interestingly, the RDFs of all glasses are very similar despite the fact that they comprise different ratios of the underlying structural units PS_4^{3-}, $P_2S_6^{4-}$ and $P_2S_6^{4-}$. By applying a “brute-force” melt-quenching scheme, the formation of a variety of “unusual” structural units, partly with low excess energies, is observed. Furthermore, structural units are able to cross-link via S–S bonds under Li-deficient conditions, which could be an important mechanism near the interface with the electrodes or at GBs. Unusual units as well as

cross-linking S−S bonds lower the band gap, potentially turning the materials into mixed electronic-ionic conductors under extreme conditions.

The best Li^+ transport properties are found for c-$Li_7P_3S_{11}$; other crystalline phases can exhibit Li^+ diffusion coefficients that are orders of magnitudes lower. All LiPS glasses showed very similar transport properties despite their different structural units. In particular, their Li^+ diffusion coefficients surpass c-Li_3PS_4, are similar to the hypothetical phase c-$Li_4P_2S_7$, but cannot reach the values found for c-$Li_7P_3S_{11}$. Highly concerted and correlated Li^+ jumps were observed in AIMD simulations, which cannot be captured properly with NEB methods. For poor ionic conductors such as c-$Li_4P_2S_6$, however, the treatment of defects in combination with NEB simulations have proven to be the methods of choice, and it was found that external defect equilibria have negligible influence on the transport properties of c-$Li_4P_2S_6$. Moreover, defect formation energies of neutral defects were successfully used to predict unstable SE | Li interfaces and stable SE | SE interfaces of LiPS glass-ceramics. Explicit interface simulation revealed the formation of a Li layer at the glass-ceramic interface, which might be indicative of the formation of a space charge layer.

7.2 Influence of Br^-/S^{2-} Site-Exchange on the Properties of Li_6PS_5Br

How Br^-/S^{2-} site-exchange affects the properties of Li_6PS_5Br was analyzed in Chapter 5. In agreement with experiments, decreasing lattice constants with a minimum at 50% site-exchange are found. In terms of stability, the ordered phase with 0% site-exchange is the most stable phase at 0 K, whereas 50% yields the least stable structures. The inclusion of vibrational entropy and configurational entropy due to the Br^-/S^{2-} site-exchange is not able to reproduce the experimentally observed site-exchange from quenching experiments, and we believe that configurational entropy of the Li^+ sublattice needs to be accounted for, too.

The Li^+ transport properties are found to critically depend on the Br^-/S^{2-} site-exchange. At 0% site-exchange, Li^+ diffusion is mainly confined to the Li^+ cages around the S^{2-} ions (4*d* sites) and we reported a new internal reorganization mechanism for the intracage diffusion. Without site-exchange, effective intercage diffusion is only possible at high temperatures and is initiated by formation of a Li^+ Frenkel pair. At lower temperatures, such Frenkel pairs are likely to be annihilated by back-jumps immediately after their formation.

The introduction of Br^-/S^{2-} site-exchange dissolves the strict cage arrangement and long-range diffusion is observed at much lower temperatures. The highest D^* are obtained at 50% site-exchange and the extrapolated ionic conductivity at room temperature is two orders of magnitude higher than the one for the 0% structure. The Haven ratios for structures with 25% and 50% site-exchange are in the range of 0.5-0.8. A site-exchange higher than 50% leads to

decreasing D^* and at 100% the Li^+ diffusion is again localized in cages around the S^{2-} ions that are now centered around the 4*a* sites.

Calculated activation volumes $\Delta^{\ddagger}V$ are positive, indicating that D^* decreases under compressive conditions. Notably, $\Delta^{\ddagger}V$ of the 0% structure is 2-3 times larger than the ones of the 25% and 50% structures, which seems to be related to the diffusion mechanism: At 0% site-exchange, Frenkel pairs form and vanish repeatedly, which adds to the activation volume related to the defect formation, whereas at least one Frenkel pair is constantly present in structures with site-exchange. This was rationalized by analyzing the diffusion mechanism. We find that $Br_S^{\bullet}$ defects are responsible for the facilitation of Li^+ Frenkel pairs with mobile $Li_i^{\bullet}$, jumping between the cages via interstitial or interstitialcy mechanisms. The compensating $V_{Li}^{\prime}$ is mostly immobile and strongly bound to $Br_S^{\bullet}$. $S_{Br}^{\prime}$ defects act as a sink for $Li_i^{\bullet}$, but may induce local disturbances in the Li^+ substructure that supports the overall transport. To quantify the effect of Br^-/S^{2-} site-exchange on the dynamic Li^+ substructure, tetrahedral occupancies have been determined. The changes indicate that 50% site-exchange yields the most homogeneous Li^+ distribution, which explains the observed dependence of the lattice constants.

Finally, Σ5 twist and tilt GBs are found to have an ambivalent character: At 0%, they locally disturb the strict structure of the Li^+ cages and enhance the local Li^+ diffusion. At 25% and 50%, however, the Li^+ transport is slightly reduced compared to the bulk material, most likely because Li^+ diffusion pathways are less favorable along and across the GB.

7.3 Properties of Li_7SiPS_8

The recently developed Li_7SiPS_8 was analyzed in Chapter 6. We find that ortho-Li_7SiPS_8 is more stable than tetra-Li_7SiPS_8 at 0 K. The small energy difference of 11.8 meV/atom, however, is likely to be outweighed by entropic contributions at finite temperatures. The Si/P arrangement has a negligible influence on the relative energy, suggesting no preferential ordering as confirmed by experiments. Likewise, it also has a negligible influence on the Li^+ diffusion. Ortho-Li_7SiPS_8 exhibits nearly isotropic diffusion with only a slightly faster diffusion along the *c* direction, but comparably high activation barriers of 290-330 meV. Tetra-Li_7SiPS_8 exhibits better transport properties with average migration barriers of 130-150 meV, but shows anisotropy with faster diffusion along *c*.

The bulk transport properties deteriorate under compression and we reason that the experimentally observed conductivity increase under compression of Li_7SiPS_8 samples needs to originate from improved particle-particle contacts. In this regard, the elastic properties are of interest and were calculated in two different ways. Bulk moduli in the range of 22.8-25.3 GPa, consistent with other sulfide SEs, are obtained.

Finally, the interface stability of tetra-Li_7SiPS_8 against Li metal was analyzed. A thermodynamic estimation predicted instability against Li metal, which was verified in explicit interface simulations. AIMD simulations show that the interface continues to react and PS_4^{3-} units are found to dissociate quickly while SiS_4^{4-} units remain stable for a longer time, indicating their superior stability. Moreover, pore formation is attributed to an overall volume decrease during the reaction, but might be artificially promoted by the constant volume conditions of the simulations.

In the majority of cases, the formed interphase resembles an amorphous Li_2S matrix that embeds the remaining reaction products. For one calculation at 500 K, however, an ordered interphase is observed and undoubtedly assigned to Li_2S. Its structure is highly defective because other species such as SiS_4^{4-} units, their partially dissociated remnants, and P ions are embedded in it. Moreover, clustering of Li_xP units indicates the onset of Li_3P formation and we assume that the high defect density of the Li_2S matrix leads to improved transport of Li^+ ions. Possibly, even other species are mobile, which might be the reason for a growing interphase layer that leads to an increased interface resistance.

7.4 Similarities, Differences and General Issues

Our analyses show that the three considered material systems can achieve Li^+ transport properties that qualify them as SEs for ASSBs. However, the transport properties are not necessarily sufficient and require a careful synthesis or other strategies to be optimized. One issue concerns glass phases that seem to be commonly observed in all sulfide SEs. In the case of LiPS glass-ceramics, phases other than c-$Li_7P_3S_{11}$ seem to negatively affect the bulk transport properties of the material. Therefore, synthesis should aim at maximizing the phase fraction of c-$Li_7P_3S_{11}$ and avoid any of the crystalline materials with lower conductivity, such as c-Li_3PS_4 or c-$Li_4P_2S_6$. Apparently, residual glass phases can never be avoided completely and the question arises whether the glassy part of the glass-ceramics can be further optimized. The calculations indicate that this is not the case without changing the composition: All LiPS glasses with the considered compositions exhibit comparable transport properties.

Structural disorder is another prominent feature of many sulfide SEs and we showed that a control of the Br^-/S^{2-} site-exchange via temperature treatments is necessary to optimize Li_6PS_5Br. Interestingly, we find that disorder among PS_4^{3-}/SiS_4^{4-} units in Li_7SiPS_8 has a negligible influence on the Li^+ transport properties. Similar to the LiPS system, however, we need to avoid unwanted phases such as ortho-Li_7SiPS_8 or residual glasses during syntehsis. Moreover, the anisotropy of tetra-Li_7SiPS_8 with fast diffusion along its *c* axis might demand texturing or other modifications to access the full potential of the material.

Another common feature of sulfide SEs seems to be the presence of metastable phases, and we speculate that this is related to flat potential energy landscapes.

The calculations show that neither LiPS glasses, nor site-exchange in Li_6PS_5Br, nor the tetragonal phase of Li_7SiPS_8 are thermodynamically stable at 0 K. Obviously, entropic contributions need to be taken into account to assess the stability at finite temperatures, and we included them for the analysis of LiPS glasses and Li_6PS_5Br. Still, our calculations and also the quenching experiments of Li_6PS_5Br indicate that not all sulfide SEs are actually thermodynamically stable at operation temperatures. Instead, it is likely that they are kinetically stabilized: At room temperature, LiPS glasses will not rapidly crystallize and even a high degree of Br^-/S^{2-} site-exchange is not able to reorder. The actual time scales of these processes, however, are not well understood and it is unclear whether the materials can endure the lifetime of a ASSB.

As seen for Li_6PS_5Br and Li_7SiPS_8, Li^+ diffusion is reduced upon compression of the materials. Therefore, an excessive compression should be avoided to facilitate the full performance of these sulfide SEs. However, other issues need to be considered as well: compression is needed to enable good contact between the materials during the operation of the battery, especially if volume changes in the electrodes are large. Hence, the optimal parameters for assembling batteries need to be evaluated keeping both these issues in mind. In this regard, electronic structure calculations can be used to determine elastic properties, as shown for Li_7SiPS_8, to facilitate an assessment of pressure-related issues.

This point brings us to interfaces, which presumably remain the biggest challenge for achieving durable ASSBs. The interface simulations confirm that sulfide SEs exhibit a low electrochemical stability and require protection schemes if they are used with Li metal anodes. But also GBs as well as internal interfaces (e.g., phase boundaries in LiPS glass-ceramics or composite SEs) need to be better understood to derive further, system-specific optimization strategies. At this point, atomistic simulations are able to provide insights that are difficult to obtain experimentally, and we were able to show this for several interfaces involving all three investigated materials.

7.5 Open Questions and Next Steps

Throughout this thesis, we have seen that sulfide SEs are complex materials with system-specific issues that could not all be addressed within the scope of this work. Concerning the LiPS system, it would be of great importance if experimental studies could characterize the structural units of LiPS glasses in more detail. This could either prove the actual presence of unusual units, as observed in our glasses, or reveal that they are only artifacts of our simulated melt-quenching schemes. Also, the presence of S–S bonds and its relation to local Li-deficiency could be investigated. In terms of Li^+ transport properties, we saw that not all Li^+ ions contribute to diffusion because they may be trapped at certain sites in LiPS glasses. For a further improvement of the Li^+ diffusion in

LiPS glass-ceramics, it would therefore be helpful to understand the character of such trapping sites and to develop schemes to avoid them.

Another point of interest concerns the general effect of (dis)order in the material: Why does disorder help the transport properties of certain materials (e.g., Br^{-}/S^{2-} site-exchange in Li_6PS_5Br), whereas it hardly shows any effect in others (e.g., PS_4^{3-}/SiS_4^{4-} disorder in Li_7SiPS_8)? How does this compare to other sulfide or oxide SEs (e.g., NASICON)? Are there specific factors, properties or topologies that favor certain types of (dis)order for improved transport properties? Such knowledge would be of high value for the development of SEs in general.

Furthermore, internal interfaces deserve a more thorough analysis as they have not been fully understood in sulfide SEs. This includes GBs, whose effects are unclear for a multitude of SEs. Similar investigations as we performed for twist- and tilt-GBs in Li_6PS_5Br might be insightful to develop optimization schemes for syntheses or post-treatments of SEs. Additionally, internal interfaces in glass-ceramic need to be better understood because many sulfide SEs exhibit residual glass phases.

The same applies to interfaces against the electrodes and all results indicate that sulfide SEs require protective layers. Therefore, protective coating materials need to be developed that are stable against the specific combination of SE and electrode. In this regard, it would be helpful to more thoroughly benchmark the applicability of using defect formation energies with Frenkel pairs “across material boundaries”. This method, possibly combined with other approaches, could then be used to screen for promising material combinations.

Curriculum Vitae

Research Experience

	Scientific staff member (*Wissenschaftlicher Mitarbeiter*) Materials modeling group, Prof. Karsten Albe Technische Universität Darmstadt, Germany Projects:
since 11/2022	'*In-silico design and synthesis of single-crystalline ultrahigh-Ni cathode materials with optimized coatings*' (BMBF)
10/2021 - 10/2022	'*Mitigating mechanical failure in cathode active materials with atomistic simulations*' (BASF SE)
09/2018 - 08/2021	'*Kompetenzcluster für Festkörperbatterien – Atomistische Modellierung sulfidischer Festelektrolyte: Von der elektronischen Struktur zur Ionenleitfäigkeit'* (BMBF)
01/2018 - 08/2018	'*Grenzlächenphänomene in ionenleitenden Systemen: Untersuchung mit Methoden der Oberflächenforschung*' (DFG)
04/2019 - 06/2019	Visiting scientist (with DAAD scholarship) at THEOS group, Prof. Nicola Marzari, EPFL Lausanne, Switzerland '*Self-consistent Hubbard U parameters*'
10/2017 - 12/2017	Internship BASF SE, Ludwigshafen, Germany '*Modeling of materials for heterogeneous catalysis and batteries*'
09/2014 - 02/2015	Internship Robert Bosch GmbH, Stuttgart, Germany '*Sputter synthesis and electrochemical characterization of LiPON thin films*'

Education

09/2017	Master of Science in Materials Science (Grade: 1.3) Technische Universität Darmstadt, Germany
11/2015	Bachelor of Science in Materials Science (Grade: 1.6) Technische Universität Darmstadt, Germany
03/2011	Secondary education (*Abitur*, Grade: 1.2) Gymnasium am Kurfürstlichen Schloss, Mainz, Germany

Peer-Reviewed Articles

M. Sadowski, L. Koch, K. Albe and S. Sicolo, *Planar Gliding and Vacancy Condensation: The Role of Dislocations in the Chemomechanical Degradation of Layered Transition-Metal Oxides*, Chemistry of Materials 35, 2, 584-594 (2023).

L. Riegger, , S.-K. Otto, M. Sadowski, S. Jovanovic, S. Harm, L. Balzat, S. Merz, O. Kötz, S. Burkhardt, F. H. Richter, J. Sann, B. V. Lotsch, J. Granwehr, K. Albe and J. Janek, *New insights into the Reduction Stability of Thiophosphate Electrolytes Containing Metal Ions: Li_7SiPS_8 in Contact with a Lithium Metal Anode*, Chemistry of Materials 34, 8, 3659-3669 (2022).

M. Sadowski, and K. Albe, *Influence of Br^-/S^{2-} site-exchange on Li Diffusion Mechanism in Li_6PS_5Br: A Computational Study*, Philosophical Transaction of the Royal Society A 379, 20190458 (2021).

A. Gautam, M. Sadowski [Gautam and Sadowski contributed equally], M. Ghidiu, N. Minafra, A. Senyshyn, K. Albe, and W. Zeier, *Engineering the Site-Disorder and Lithium Distribution in the Lithium Superionic Argyrodite Li_6PS_5Br*, Advanced Energy Materials 11, 5, 2003369 (2021).

M. Sadowski and K. Albe, *Computational Study of Crystalline and Glassy Lithium Thiophosphates: Structure, Thermodynamic Stability and Transport Properties*, Journal of Power Sources 478, 229041 (2020).

A. Gautam, M. Sadowski, N. Prinz, H. Eickhoff, N. Minafra, M. Ghidiu, S. Culver, K. Albe, T. Fässler, M. Zobel, and W. Zeier, *Rapid Crystallization and Kinetic Freezing of Site-Disorder in the Lithium Superionic Argyrodite Li_6PS_5Br*, Chemistry of Materials 31, 24, 10178-10185 (2019).

M. Sadowski, S. Sicolo and K. Albe, *Defect Thermodynamics and Interfacial Instability of Crystalline $Li_4P_2S_6$*, Solid State Ionics 319, 53-60 (2018).

C. Deitrich, M. Sadowski, S. Sicolo, D. Weber, S. Sedlmaier, K. Weldert, S. Indris, K. Albe, J, Janek and W. Zeier, *Local Structural Investigations, Defect Formation,*

and Ionic Conductivity of the Lithium Ionic Conductor $Li_4P_2S_6$, Chemistry of Materials 28, 23, 8764-8773 (2016).

Conference Contributions

03/2023 DPG Frühjahrestagung, Dresden, Germany, Presentation: *Planar Gliding and Vacancy Condensation: The Role of Dislocations in the Chemomechanical Degradation of Layered Transition-Metal Oxides*, M. Sadowski, K. Albe and S. Sicolo.

12/2021 MRS, Boston, USA, Virtual Presentation: *Consequences of Br/S site-exchange on the properties of Li_6PS_5Br argyrodites*, M. Sadowski and K. Albe.

05/2021 E-MRS, Straßburg, France, Virtual Poster: *Effect of S/Br site-disorder on Li transport in the superionic solid electrolyte Li_6PS_5Br – a computational study*, M. Sadowski and K. Albe.

03/2019 16th Symposium on Modeling and Experimental Validation of Electrochemical Energy Technologies, Braunschweig, Germany, Presentation: *First-principles modeling of crystalline and amorphous lithium thiophosphate solid electrolytes*, M. Sadowski and K. Albe.

11/2018 Third Bunsen Colloquium on Solid-State Batteries, Gießen, Germany, Presentation: *First-principles modeling of lithium thiophosphate solid electrolytes*, M. Sadowski and K. Albe.

09/2018 MSE, Darmstadt, Germany, Presentation: *Predicting interface (in)stabilities via analysis of defect thermodynamics from first-principles calculations*, M. Sadowski, S. Sicolo and K. Albe.

03/2018 1st International Symposium on Solid-State Batteries, Dübendorf, Switzerland, Poster: *Defect chemistry of solid electrolyte $Li_4P_2S_6$ by first-principles calculations*, M. Sadowski and K. Albe. Poster prize: 3rd place.

05/2017 E-MRS, Straßburg, France, Presentation: *Defect chemistry of solid electrolyte $Li_4P_2S_6$ by first-principles calculations*, M. Sadowski, S. Sicolo and K. Albe.

03/2017 DPG Frühjahrestagung, Dresden, Germany, Presentation: *Defect chemistry of solid electrolyte $Li_4P_2S_6$ by first-principles calculations*, M. Sadowski, S. Sicolo and K. Albe.

Bibliography

[1] J. Janek and W. G. Zeier, *A solid future for battery development*, Nature Energy 1, 16141 (2016).

[2] Y. Chen, Y. Kang, Y. Zhao, L. Wang, J. Liu, Y. Li, Z. Liang, X. He, X. Li, N. Tavajohi, and B. Li, *A review of lithium-ion battery safety concerns: The issues, strategies, and testing standards*, Journal of Energy Chemistry 59, 83–99 (2021).

[3] J. Lau, R. H. DeBlock, D. M. Butts, D. S. Ashby, C. S. Choi, and B. S. Dunn, *Sulfide Solid Electrolytes for Lithium Battery Applications*, Advanced Energy Materials 8, 1800933 (2018).

[4] S. Ohno, A. Banik, G. F. Dewald, M. A. Kraft, T. Krauskopf, N. Minafra, P. Till, M. Weiss, and W. G. Zeier, *Materials design of ionic conductors for solid state batteries*, Progress in Energy 2, 022001 (2020).

[5] K. Nie, Y. Hong, J. Qiu, Q. Li, X. Yu, H. Li, and L. Chen, *Interfaces Between Cathode and Electrolyte in Solid State Lithium Batteries: Challenges and Perspectives*, Frontiers in Chemistry 6 (2018).

[6] Y. Zhu, X. He, and Y. Mo, *Origin of Outstanding Stability in the Lithium Solid Electrolyte Materials: Insights from Thermodynamic Analyses Based on First-Principles Calculations*, ACS applied materials & interfaces 7, 23685–23693 (2015).

[7] X. Li, J. Liang, X. Yang, K. R. Adair, C. Wang, F. Zhao, and X. Sun, *Progress and perspectives on halide lithium conductors for all-solid-state lithium batteries*, Energy & Environmental Science 13, 1429–1461 (2020).

[8] H. Tsukasaki, S. Mori, H. Morimoto, A. Hayashi, and M. Tatsumisago, *Direct observation of a non-crystalline state of Li_2S-P_2S_5 solid electrolytes*, Scientific Reports 7, 4142 (2017).

[9] A. Gautam, M. Sadowski, N. Prinz, H. Eickhoff, N. Minafra, M. Ghidiu, S. P. Culver, K. Albe, T. F. Fässler, M. Zobel, and W. G. Zeier, *Rapid Crystallization and Kinetic Freezing of Site-Disorder in the Lithium Superionic Argyrodite Li_6PS_5Br*, Chemistry of Materials 31, 10178–10185 (2019).

[10] A. Gautam, M. Sadowski, M. Ghidiu, N. Minafra, A. Senyshyn, K. Albe, and W. G. Zeier, *Engineering the Site-Disorder and Lithium Distribution in the Lithium Superionic Argyrodite Li_6PS_5Br*, Advanced Energy Materials 11, 2003369 (2021).

[11] S. Harm, A.-K. Hatz, I. Moudrakovski, R. Eger, A. Kuhn, C. Hoch, and B. V. Lotsch, *Lesson Learned from NMR: Characterization and Ionic Conductivity of LGPS-like Li_7SiPS_8*, Chemistry of Materials 31, 1280–1288 (2019).

[12] A. Yoshino, *The Birth of the Lithium-Ion Battery*, Angewandte Chemie International Edition 51, 5798–5800 (2012).

[13] M. V. Reddy, A. Mauger, C. M. Julien, A. Paolella, and K. Zaghib, *Brief History of Early Lithium-Battery Development*, Materials 13, 1884 (2020).

[14] Y. Liang, C.-Z. Zhao, H. Yuan, Y. Chen, W. Zhang, J.-Q. Huang, D. Yu, Y. Liu, M.-M. Titirici, Y.-L. Chueh, H. Yu, and Q. Zhang, *A review of rechargeable batteries for portable electronic devices*, InfoMat 1, 6–32 (2019).

[15] C. L. Schmidt and P. M. Skarstad, *The future of lithium and lithium-ion batteries in implantable medical devices*, Journal of Power Sources 97-98, 742–746 (2001).

[16] A. Masias, J. Marcicki, and W. A. Paxton, *Opportunities and Challenges of Lithium Ion Batteries in Automotive Applications*, ACS Energy Letters 6, 621–630 (2021).

[17] A. Farmani and T. A. Nguyen, *Chapter seventeen - battery-on-a-chip*, Nanobatteries and Nanogenerators (H. Song, R. Venkatachalam, T. A. Nguyen, H. B. Wu, and P. Nguyen-Tri, eds.), Micro and Nano Technologies, Elsevier, 2021, pp. 447–461.

[18] T. Chen, Y. Jin, H. Lv, A. Yang, M. Liu, B. Chen, Y. Xie, and Q. Chen, *Applications of Lithium-Ion Batteries in Grid-Scale Energy Storage Systems*, Transactions of Tianjin University 26, 208–217 (2020).

[19] A. El Kharbachi, O. Zavorotynska, M. Latroche, F. Cuevas, V. Yartys, and M. Fichtner, *Exploits, advances and challenges benefiting beyond Li-ion battery technologies*, Journal of Alloys and Compounds 817, 153261 (2020).

[20] K. Kubota, M. Dahbi, T. Hosaka, S. Kumakura, and S. Komaba, *Towards K-Ion and Na-Ion Batteries as "Beyond Li-Ion"*, The Chemical Record 18, 459–479 (2018).

[21] Q. Huang and Q. Wang, *Next-Generation, High-Energy-Density Redox Flow Batteries*, ChemPlusChem 80, 312–322 (2015).

[22] G. Yang, C. Abraham, Y. Ma, M. Lee, E. Helfrick, D. Oh, and D. Lee, *Advances in Materials Design for All-Solid-state Batteries: From Bulk to Thin Films*, Applied Sciences 10, 4727 (2020).

[23] J. F. Rohan, M. Hasan, S. Patil, and D. P. C. a. T. Clancy, *Energy Storage: Battery Materials and Architectures at the Nanoscale*, ICT - Energy - Concepts Towards Zero - Power Information and Communication Technology (2014).

[24] J.-M. Tarascon and M. Armand, *Issues and challenges facing rechargeable lithium batteries*, Nature 414, 359–367 (2001).

[25] M. Hu, X. Pang, and Z. Zhou, *Recent progress in high-voltage lithium ion batteries*, Journal of Power Sources 237, 229–242 (2013).

[26] M. J. Lain, J. Brandon, and E. Kendrick, *Design Strategies for High Power vs. High Energy Lithium Ion Cells*, Batteries 5, 64 (2019).

[27] N. Nitta, F. Wu, J. T. Lee, and G. Yushin, *Li-ion battery materials: present and future*, Materials Today 18, 252–264 (2015).

[28] Y. Ding, Z. P. Cano, A. Yu, J. Lu, and Z. Chen, *Automotive Li-Ion Batteries: Current Status and Future Perspectives*, Electrochemical Energy Reviews 2, 1–28 (2019).

[29] J. R. M. Delos Reyes, R. V. Parsons, and R. Hoemsen, *Winter Happens: The Effect of Ambient Temperature on the Travel Range of Electric Vehicles*, IEEE Transactions on Vehicular Technology 65, 4016–4022 (2016).

[30] D. Pevec, J. Babic, A. Carvalho, Y. Ghiassi-Farrokhfal, W. Ketter, and V. Podobnik, *A survey-based assessment of how existing and potential electric vehicle owners perceive range anxiety*, Journal of Cleaner Production 276, 122779 (2020).

[31] A. Varzi, R. Raccichini, S. Passerini, and B. Scrosati, *Challenges and prospects of the role of solid electrolytes in the revitalization of lithium metal batteries*, Journal of Materials Chemistry A 4, 17251–17259 (2016).

[32] L. Wang, J. Li, G. Lu, W. Li, Q. Tao, C. Shi, H. Jin, G. Chen, and S. Wang, *Fundamentals of Electrolytes for Solid-State Batteries: Challenges and Perspectives*, Frontiers in Materials 7 (2020).

[33] S. Santhanagopalan, K. Smith, J. Neubauer, G.-H. Kim, A. Pesaran, and M. Keyser, *Design and Analysis of Large Lithium-Ion Battery Systems*, Artech House, December 2014.

[34] J. Jiang and C. Zhang, *Fundamentals and Applications of Lithium-ion Batteries in Electric Drive Vehicles*, John Wiley & Sons, May 2015.

[35] J. T. Warner, *Lithium-Ion Battery Chemistries: A Primer*, Elsevier, May 2019.

[36] P. Arora and Z. J. Zhang, *Battery Separators*, Chemical Reviews 104, 4419–4462 (2004).

[37] H. Lee, M. Yanilmaz, O. Toprakci, K. Fu, and X. Zhang, *A review of recent developments in membrane separators for rechargeable lithium-ion batteries*, Energy & Environmental Science 7, 3857–3886 (2014).

[38] C. F. J. Francis, I. L. Kyratzis, and A. S. Best, *Lithium-Ion Battery Separators for Ionic-Liquid Electrolytes: A Review*, Advanced Materials 32, 1904205 (2020).

[39] A. Li, A. C. Y. Yuen, W. Wang, I. M. De Cachinho Cordeiro, C. Wang, T. B. Y. Chen, J. Zhang, Q. N. Chan, and G. H. Yeoh, *A Review on Lithium-Ion Battery Separators towards Enhanced Safety Performances and Modelling Approaches*, Molecules 26 (2021).

[40] E. Quartarone and P. Mustarelli, *Review-Emerging Trends in the Design of Electrolytes for Lithium and Post-Lithium Batteries*, Journal of The Electrochemical Society 167, 050508 (2020).

[41] G. Yang, Y. Song, Q. Wang, L. Zhang, and L. Deng, *Review of ionic liquids containing, polymer/inorganic hybrid electrolytes for lithium metal batteries*, Materials & Design 190, 108563 (2020).

[42] K. Karuppasamy, J. Theerthagiri, D. Vikraman, C.-J. Yim, S. Hussain, R. Sharma, T. Maiyalagan, J. Qin, and H.-S. Kim, *Ionic Liquid-Based Electrolytes for Energy Storage Devices: A Brief Review on Their Limits and Applications*, Polymers 12 (2020).

[43] A. Zimmerman, *Self-discharge losses in lithium-ion cells*, IEEE Aerospace and Electronic Systems Magazine 19, 19–24 (2004).

[44] C. Liu, Z. G. Neale, and G. Cao, *Understanding electrochemical potentials of cathode materials in rechargeable batteries*, Materials Today 19, 109–123 (2016).

[45] F. Wu, J. Maier, and Y. Yu, *Guidelines and trends for next-generation rechargeable lithium and lithium-ion batteries*, Chemical Society Reviews 49, 1569–1614 (2020).

[46] J. Asenbauer, T. Eisenmann, M. Kuenzel, A. Kazzazi, Z. Chen, and D. Bresser, *The success story of graphite as a lithium-ion anode material - fundamentals, remaining challenges, and recent developments including silicon (oxide) composites*, Sustainable Energy & Fuels 4, 5387–5416 (2020).

[47] H. Yan, D. Zhang, Qilu, X. Duo, and X. Sheng, *A review of spinel lithium titanate ($Li_4Ti_5O_{12}$) as electrode material for advanced energy storage devices*, Ceramics International 47, 5870–5895 (2021).

[48] B. Zhao, R. Ran, M. Liu, and Z. Shao, *A comprehensive review of $Li_4Ti_5O_{12}$-based electrodes for lithium-ion batteries: The latest advancements and future perspectives*, Materials Science and Engineering: R: Reports 98, 1–71 (2015).

[49] W.-F. Ren, Y. Zhou, J.-T. Li, L. Huang, and S.-G. Sun, *Si anode for next-generation lithium-ion battery*, Current Opinion in Electrochemistry 18, 46–54 (2019).

[50] A. Casimir, H. Zhang, O. Ogoke, J. C. Amine, J. Lu, and G. Wu, *Silicon-based anodes for lithium-ion batteries: Effectiveness of materials synthesis and electrode preparation*, Nano Energy 27, 359–376 (2016).

[51] X. Zhang, Y. Yang, and Z. Zhou, *Towards practical lithium-metal anodes*, Chemical Society Reviews 49, 3040–3071 (2020).

[52] D.-H. Liu, Z. Bai, M. Li, A. Yu, D. Luo, W. Liu, L. Yang, J. Lu, K. Amine, and Z. Chen, *Developing high safety Li-metal anodes for future high-energy Li-metal batteries: strategies and perspectives*, Chemical Society Reviews 49, 5407–5445 (2020).

[53] R. Wang, W. Cui, F. Chu, and F. Wu, *Lithium metal anodes: Present and future*, Journal of Energy Chemistry 48, 145–159 (2020).

[54] X.-B. Cheng, R. Zhang, C.-Z. Zhao, and Q. Zhang, *Toward Safe Lithium Metal Anode in Rechargeable Batteries: A Review*, Chemical Reviews 117, 10403–10473 (2017).

[55] S. Chae, M. Ko, K. Kim, K. Ahn, and J. Cho, *Confronting Issues of the Practical Implementation of Si Anode in High-Energy Lithium-Ion Batteries*, Joule 1, 47–60 (2017).

[56] C. Fang, X. Wang, and Y. S. Meng, *Key Issues Hindering a Practical Lithium-Metal Anode*, Trends in Chemistry 1, 152–158 (2019).

[57] M. Ghiji, V. Novozhilov, K. Moinuddin, P. Joseph, I. Burch, B. Suendermann, and G. Gamble, *A Review of Lithium-Ion Battery Fire Suppression*, Energies 13, 5117 (2020).

[58] A. Jana, D. R. Ely, and R. E. Garcia, *Dendrite-separator interactions in lithium-based batteries*, Journal of Power Sources 275, 912–921 (2015).

[59] S. Wang, K. Rafiz, J. Liu, Y. Jin, and J. Y. S. Lin, *Effects of lithium dendrites on thermal runaway and gassing of $LiFePO_4$ batteries*, Sustainable Energy & Fuels 4, 2342–2351 (2020).

[60] A. Manthiram, *A reflection on lithium-ion battery cathode chemistry*, Nature Communications 11, 1550 (2020).

[61] S. B. Chikkannanavar, D. M. Bernardi, and L. Liu, *A review of blended cathode materials for use in Li-ion batteries*, Journal of Power Sources 248, 91–100 (2014).

[62] J. U. Choi, N. Voronina, Y.-K. Sun, and S.-T. Myung, *Recent Progress and Perspective of Advanced High-Energy Co-Less Ni-Rich Cathodes for Li-Ion Batteries: Yesterday, Today, and Tomorrow*, Advanced Energy Materials 10, 2002027 (2020).

[63] D. Zhao and S. Li, *Regulating the Performance of Lithium-Ion Battery Focus on the Electrode-Electrolyte Interface*, Frontiers in Chemistry 8, 821 (2020).

[64] B. Rowden and N. Garcia-Araez, *A review of gas evolution in lithium ion batteries*, Energy Reports 6, 10–18 (2020).

[65] L. B. Diaz, X. He, Z. Hu, F. Restuccia, M. Marinescu, J. V. Barreras, Y. Patel, G. Offer, and G. Rein, *Review–Meta-Review of Fire Safety of Lithium-Ion Batteries: Industry Challenges and Research Contributions*, Journal of The Electrochemical Society 167, 090559 (2020).

[66] X. Zhang, A. Wang, X. Liu, and J. Luo, *Dendrites in Lithium Metal Anodes: Suppression, Regulation, and Elimination*, Accounts of Chemical Research 52, 3223–3232 (2019).

[67] J. G. Kim, B. Son, S. Mukherjee, N. Schuppert, A. Bates, O. Kwon, M. J. Choi, H. Y. Chung, and S. Park, *A review of lithium and non-lithium based solid state batteries*, Journal of Power Sources 282, 299–322 (2015).

[68] K. J. Kim, M. Balaish, M. Wadaguchi, L. Kong, and J. L. M. Rupp, *Solid-State Li Metal Batteries: Challenges and Horizons of Oxide and Sulfide Solid Electrolytes and Their Interfaces*, Advanced Energy Materials 11, 2002689 (2021).

[69] K. Takada, *Solid electrolytes and solid-state batteries*, ELECTROCHEMICAL STORAGE MATERIALS: SUPPLY, PROCESSING, RECYCLING AND MODELLING: Proceedings of the 2nd International Freiberg Conference on Electrochemical Storage Materials, 020008 (2016).

[70] K. Takada and T. Ohno, *Experimental and Computational Approaches to Interfacial Resistance in Solid-State Batteries*, Frontiers in Energy Research 4, 10 (2016).

[71] Y. Zhao, L. Wang, Y. Zhou, Z. Liang, N. Tavajohi, B. Li, and T. Li, *Solid Polymer Electrolytes with High Conductivity and Transference Number of Li Ions for Li-Based Rechargeable Batteries*, Advanced Science 8, 2003675 (2021).

[72] K. D. Fong, J. Self, K. M. Diederichsen, B. M. Wood, B. D. McCloskey, and K. A. Persson, *Ion Transport and the True Transference Number in Nonaqueous Polyelectrolyte Solutions for Lithium Ion Batteries*, ACS Central Science 5, 1250–1260 (2019).

[73] F. Wohde, M. Balabajew, and B. Roling, *Li^+ Transference Numbers in Liquid Electrolytes Obtained by Very-Low-Frequency Impedance Spectroscopy at Variable Electrode Distances*, Journal of The Electrochemical Society 163, A714 (2016).

[74] W. E. Tenhaeff, E. Rangasamy, Y. Wang, A. P. Sokolov, J. Wolfenstine, J. Sakamoto, and N. J. Dudney, *Resolving the Grain Boundary and Lattice Impedance of Hot-Pressed $Li_7La_3Zr_2O_{12}$ Garnet Electrolytes*, ChemElectroChem 1, 375–378 (2014).

[75] S. Breuer, D. Prutsch, Q. Ma, V. Epp, F. Preishuber-Pflügl, F. Tietz, and M. Wilkening, *Separating bulk from grain boundary Li ion conductivity in the sol-gel prepared solid electrolyte $Li_{1.5}Al_{0.5}Ti_{1.5}(PO_4)_3$*, Journal of Materials Chemistry A 3, 21343–21350 (2015).

[76] T. Polczyk, W. Zajac, M. Ziabka, and K. Świerczek, *Mitigation of grain boundary resistance in $La_{2/3-x}Li_{3x}TiO_3$ perovskite as an electrolyte for solid-state Li-ion batteries*, Journal of Materials Science 56, 2435–2450 (2021).

[77] J. A. Dawson, P. Canepa, M. J. Clarke, T. Famprikis, D. Ghosh, and M. S. Islam, *Toward Understanding the Different Influences of Grain Boundaries on Ion Transport in Sulfide and Oxide Solid Electrolytes*, Chemistry of Materials 31, 5296–5304 (2019).

[78] M. B. Dixit, M. Regala, F. Shen, X. Xiao, and K. B. Hatzell, *Tortuosity Effects in Garnet-Type $Li_7La_3Zr_2O_{12}$ Solid Electrolytes*, ACS Applied Materials & Interfaces 11, 2022–2030 (2019).

[79] R. Wei, S. Chen, T. Gao, and W. Liu, *Challenges, fabrications and horizons of oxide solid electrolytes for solid-state lithium batteries*, Nano Select 2, 2256–2274 (2021).

[80] K. H. Kim, Y. Iriyama, K. Yamamoto, S. Kumazaki, T. Asaka, K. Tanabe, C. A. J. Fisher, T. Hirayama, R. Murugan, and Z. Ogumi, *Characterization of the interface between $LiCoO_2$ and $Li_7La_3Zr_2O_{12}$ in an all-solid-state rechargeable lithium battery*, Journal of Power Sources 196, 764–767 (2011).

[81] Y. Zhu, X. He, and Y. Mo, *First principles study on electrochemical and chemical stability of solid electrolyte-electrode interfaces in all-solid-state Li-ion batteries*, Journal of Materials Chemistry A 4, 3253–3266 (2016).

[82] K. Hofstetter, A. J. Samson, S. Narayanan, and V. Thangadurai, *Present understanding of the stability of Li-stuffed garnets with moisture, carbon dioxide, and metallic lithium*, Journal of Power Sources 390, 297–312 (2018).

[83] R. Murugan, V. Thangadurai, and W. Weppner, *Fast Lithium Ion Conduction in Garnet-Type $Li_7La_3Zr_2O_{12}$*, Angewandte Chemie International Edition 46, 7778–7781 (2007).

[84] T. Krauskopf, H. Hartmann, W. G. Zeier, and J. Janek, *Toward a Fundamental Understanding of the Lithium Metal Anode in Solid-State Batteries-An Electrochemo-Mechanical Study on the Garnet-Type Solid Electrolyte $Li_{6.25}Al_{0.25}La_3Zr_2O_{12}$*, ACS Applied Materials & Interfaces 11, 14463–14477 (2019).

[85] J. G. Connell, T. Fuchs, H. Hartmann, T. Krauskopf, Y. Zhu, J. Sann, R. Garcia-Mendez, J. Sakamoto, S. Tepavcevic, and J. Janek, *Kinetic versus Thermodynamic Stability of LLZO in Contact with Lithium Metal*, Chemistry of Materials 32, 10207–10215 (2020).

[86] S. Wenzel, T. Leichtweiss, D. Krüger, J. Sann, and J. Janek, *Interphase formation on lithium solid electrolytes-An in situ approach to study interfacial reactions by photoelectron spectroscopy*, Solid State Ionics 278, 98–105 (2015).

[87] R. DeWees and H. Wang, *Synthesis and Properties of NaSICON-type LATP and LAGP Solid Electrolytes*, ChemSusChem 12, 3713–3725 (2019).

[88] L. Yang, Y. Song, H. Liu, Z. Wang, K. Yang, Q. Zhao, Y. Cui, J. Wen, W. Luo, and F. Pan, *Stable Interface between Lithium and Electrolyte Facilitated by a Nanocomposite Protective Layer*, Small Methods 4, 1900751 (2020).

[89] S. Wenzel, D. A. Weber, T. Leichtweiss, M. R. Busche, J. Sann, and J. Janek, *Interphase formation and degradation of charge transfer kinetics between a lithium metal anode and highly crystalline $Li_7P_3S_{11}$ solid electrolyte*, Solid State Ionics 286, 24–33 (2016).

[90] S. Wenzel, S. Randau, T. Leichtweiss, D. A. Weber, J. Sann, W. G. Zeier, and J. Janek, *Direct Observation of the Interfacial Instability of the Fast Ionic Conductor $Li_{10}GeP_2S_{12}$ at the Lithium Metal Anode*, Chemistry of Materials 28, 2400–2407 (2016).

[91] S. P. Culver, R. Koerver, W. G. Zeier, and J. Janek, *On the Functionality of Coatings for Cathode Active Materials in Thiophosphate-Based All-Solid-State Batteries*, Advanced Energy Materials 9, 1900626 (2019).

[92] G. Bucci, B. Talamini, A. Renuka Balakrishna, Y.-M. Chiang, and W. C. Carter, *Mechanical instability of electrode-electrolyte interfaces in solid-state batteries*, Physical Review Materials 2, 105407 (2018).

[93] R. Koerver, W. Zhang, L. d. Biasi, S. Schweidler, A. O. Kondrakov, S. Kolling, T. Brezesinski, P. Hartmann, W. G. Zeier, and J. Janek, *Chemo-mechanical expansion of lithium electrode materials - on the route to mechanically optimized all-solid-state batteries*, Energy & Environmental Science 11, 2142–2158 (2018).

[94] H. Ye, Y. Zhang, Y.-X. Yin, F.-F. Cao, and Y.-G. Guo, *An Outlook on Low-Volume-Change Lithium Metal Anodes for Long-Life Batteries*, ACS Central Science 6, 661–671 (2020).

[95] D. Cao, X. Sun, Q. Li, A. Natan, P. Xiang, and H. Zhu, *Lithium Dendrite in All-Solid-State Batteries: Growth Mechanisms, Suppression Strategies, and Characterizations*, Matter 3, 57–94 (2020).

[96] K. Takada, N. Ohta, L. Zhang, X. Xu, B. T. Hang, T. Ohnishi, M. Osada, and T. Sasaki, *Interfacial phenomena in solid-state lithium battery with sulfide solid electrolyte*, Solid State Ionics 225, 594–597 (2012).

[97] Y. Nomura, K. Yamamoto, T. Hirayama, S. Ouchi, E. Igaki, and K. Saitoh, *Direct Observation of a Li-Ionic Space-Charge Layer Formed at an Electrode/Solid-Electrolyte Interface*, Angewandte Chemie 131, 5346–5350 (2019).

[98] P. Yao, H. Yu, Z. Ding, Y. Liu, J. Lu, M. Lavorgna, J. Wu, and X. Liu, *Review on Polymer-Based Composite Electrolytes for Lithium Batteries*, Frontiers in Chemistry 7 (2019).

[99] T. Zhang, W. He, W. Zhang, T. Wang, P. Li, Z. Sun, and X. Yu, *Designing composite solid-state electrolytes for high performance lithium ion or lithium metal batteries*, Chemical Science 11, 8686–8707 (2020).

[100] Y. Zheng, Y. Yao, J. Ou, M. Li, D. Luo, H. Dou, Z. Li, K. Amine, A. Yu, and Z. Chen, *A review of composite solid-state electrolytes for lithium batteries: fundamentals, key materials and advanced structures*, Chemical Society Reviews 49, 8790–8839 (2020).

[101] D. Karabelli, K. P. Birke, and M. Weeber, *A Performance and Cost Overview of Selected Solid-State Electrolytes: Race between Polymer Electrolytes and Inorganic Sulfide Electrolytes*, Batteries 7, 18 (2021).

[102] S. P. Ong, O. Andreussi, Y. Wu, N. Marzari, and G. Ceder, *Electrochemical Windows of Room-Temperature Ionic Liquids from Molecular Dynamics and Density Functional Theory Calculations*, Chemistry of Materials 23, 2979–2986 (2011).

[103] J. Yang and J. S. Tse, *First-principles molecular simulations of Li diffusion in solid electrolytes Li_3PS_4*, Computational Materials Science 107, 134–138 (2015).

[104] I.-H. Chu, H. Nguyen, S. Hy, Y.-C. Lin, Z. Wang, Z. Xu, Z. Deng, Y. S. Meng, and S. P. Ong, *Insights into the Performance Limits of the $Li_7P_3S_{11}$ Superionic Conductor: A Combined First-Principles and Experimental Study*, ACS Applied Materials & Interfaces 8, 7843–7853 (2016).

[105] A. Urban, D.-H. Seo, and G. Ceder, *Computational understanding of Li-ion batteries*, npj Computational Materials 2, 16002 (2016).

[106] J. Kang and B. Han, *First-Principles Characterization of the Unknown Crystal Structure and Ionic Conductivity of $Li_7P_2S_8I$ as a Solid Electrolyte for High-Voltage Li Ion Batteries*, The Journal of Physical Chemistry Letters 7, 2671–2675 (2016).

[107] D. Chang, K. Oh, S. J. Kim, and K. Kang, *Super-Ionic Conduction in Solid-State $Li_7P_3S_{11}$-Type Sulfide Electrolytes*, Chemistry of Materials 30, 8764–8770 (2018).

[108] A. Wang, S. Kadam, H. Li, S. Shi, and Y. Qi, *Review on modeling of the anode solid electrolyte interphase (SEI) for lithium-ion batteries*, npj Computational Materials 4, 1–26 (2018).

[109] T. Binninger, A. Marcolongo, M. Mottet, V. Weber, and T. Laino, *Comparison of computational methods for the electrochemical stability window of solid-state electrolyte materials*, Journal of Materials Chemistry A 8, 1347–1359 (2020).

[110] B. Gao, R. Jalem, and Y. Tateyama, *First-Principles Study of Microscopic Electrochemistry at the $LiCoO_2$ Cathode / $LiNbO_3$ Coating / β-Li_3PS_4 Solid Electrolyte Interfaces in an All-Solid-State Battery*, ACS Applied Materials & Interfaces 13, 11765–11773 (2021).

[111] F. Chen, S. Cheng, J.-B. Liu, S. Li, W. Ouyang, and B. Liu, *Insights into the Electrochemical Stability and Lithium Conductivity of Li_4MS_4 (M = Si, Ge, and Sn)*, ACS Applied Materials & Interfaces 13, 22438–22447 (2021).

[112] Q. Zhang, D. Cao, Y. Ma, A. Natan, P. Aurora, and H. Zhu, *Sulfide-Based Solid-State Electrolytes: Synthesis, Stability, and Potential for All-Solid-State Batteries*, Advanced Materials 31, 1901131 (2019).

[113] O. U. Kudu, T. Famprikis, B. Fleutot, M.-D. Braida, T. Le Mercier, M. S. Islam, and C. Masquelier, *A review of structural properties and synthesis methods of solid electrolyte materials in the Li_2S-P_2S_5 binary system*, Journal of Power Sources 407, 31–43 (2018).

[114] A. Sakuda, A. Hayashi, Y. Takigawa, K. Higashi, and M. Tatsumisago, *Evaluation of elastic modulus of Li_2S-P_2S_5 glassy solid electrolyte by ultrasonic sound velocity measurement and compression test*, Journal of the Ceramic Society of Japan 121, 946–949 (2013).

[115] C. Dietrich, D. A. Weber, S. J. Sedlmaier, S. Indris, S. P. Culver, D. Walter, J. Janek, and W. G. Zeier, *Lithium ion conductivity in Li_2S-P_2S_5 glasses – building units and local structure evolution during the crystallization of superionic conductors Li_3PS_4, $Li_7P_3S_{11}$ and $Li_4P_2S_7$*, Journal of Materials Chemistry A 5, 18111–18119 (2017).

[116] M. Tatsumisago, S. Hama, A. Hayashi, H. Morimoto, and T. Minami, *New lithium ion conducting glass-ceramics prepared from mechanochemical Li_2S-P_2S_5 glasses*, Solid State Ionics 154, 635–640 (2002).

[117] F. Mizuno, A. Hayashi, K. Tadanaga, and M. Tatsumisago, *High lithium ion conducting glass-ceramics in the system Li_2S-P_2S_5*, Solid State Ionics 177, 2721–2725 (2006).

[118] M. Tatsumisago, F. Mizuno, and A. Hayashi, *All-solid-state lithium secondary batteries using sulfide-based glass-ceramic electrolytes*, Journal of Power Sources 159, 193–199 (2006).

[119] A. Hayashi, K. Minami, and M. Tatsumisago, *Development of sulfide glass-ceramic electrolytes for all-solid-state lithium rechargeable batteries*, Journal of Solid State Electrochemistry 14, 1761–1767 (2010).

[120] C. Dietrich, M. Sadowski, S. Sicolo, D. A. Weber, S. J. Sedlmaier, K. S. Weldert, S. Indris, K. Albe, J. Janek, and W. G. Zeier, *Local Structural Investigations, Defect Formation, and Ionic Conductivity of the Lithium Ionic Conductor $Li_4P_2S_6$*, Chemistry of Materials 28, 8764–8773 (2016).

[121] K. Homma, M. Yonemura, T. Kobayashi, M. Nagao, M. Hirayama, and R. Kanno, *Crystal structure and phase transitions of the lithium ionic conductor Li_3PS_4*, Solid State Ionics 182, 53–58 (2011).

[122] K. Minami, A. Hayashi, and M. Tatsumisago, *Mechanochemical synthesis of Li_2S-P_2S_5 glass electrolytes with lithium salts*, Solid State Ionics 181, 1505–1509 (2010).

[123] C. Dietrich, D. A. Weber, S. Culver, A. Senyshyn, S. J. Sedlmaier, S. Indris, J. Janek, and W. G. Zeier, *Synthesis, Structural Characterization, and Lithium Ion Conductivity of the Lithium Thiophosphate $Li_2P_2S_6$*, Inorganic Chemistry 56, 6681–6687 (2017).

[124] K. Minami, F. Mizuno, A. Hayashi, and M. Tatsumisago, *Lithium ion conductivity of the Li_2S-P_2S_5 glass-based electrolytes prepared by the melt quenching method*, Solid State Ionics 178, 837–841 (2007).

[125] H. Tsukasaki, S. Mori, S. Shiotani, and H. Yamamura, *Ionic conductivity and crystallization process in the Li_2S-P_2S_5 glass electrolyte*, Solid State Ionics 317, 122–126 (2018).

[126] M. Calpa, N. C. Rosero-Navarro, A. Miura, and K. Tadanaga, *Preparation of sulfide solid electrolytes in the Li_2S-P_2S_5 system by a liquid phase process*, Inorganic Chemistry Frontiers 5, 501–508 (2018).

[127] Y. Wang, D. Lu, M. Bowden, P. Z. El Khoury, K. S. Han, Z. D. Deng, J. Xiao, J.-G. Zhang, and J. Liu, *Mechanism of Formation of $Li_7P_3S_{11}$ Solid Electrolytes through Liquid Phase Synthesis*, Chemistry of Materials 30, 990–997 (2018).

[128] Z. Wang, Y. Jiang, J. Wu, Y. Jiang, S. Huang, B. Zhao, Z. Chen, and J. Zhang, *Reaction mechanism of Li_2S-P_2S_5 system in acetonitrile based on wet chemical synthesis of $Li_7P_3S_{11}$ solid electrolyte*, Chemical Engineering Journal 393, 124706 (2020).

[129] R. Maniwa, M. Calpa, N. C. Rosero-Navarro, A. Miura, and K. Tadanaga, *Synthesis of sulfide solid electrolytes from Li_2S and P_2S_5 in anisole*, Journal of Materials Chemistry A 9, 400–405 (2021).

[130] Y. Onodera, K. Mori, T. Otomo, A. C. Hannon, S. Kohara, K. Itoh, M. Sugiyama, and T. Fukunaga, *Crystal Structure of $Li_7P_3S_{11}$ Studied by Neutron and Synchrotron X-ray Powder Diffraction*, Journal of the Physical Society of Japan 79, 87–89 (2010).

[131] C. Dietrich, R. Koerver, M. W. Gaultois, G. Kieslich, G. Cibin, J. Janek, and W. G. Zeier, *Spectroscopic characterization of lithium thiophosphates by XPS and XAS - a model to help monitor interfacial reactions in all-solid-state batteries*, Physical Chemistry Chemical Physics 20, 20088–20095 (2018).

[132] H. Stöffler, T. Zinkevich, M. Yavuz, A.-L. Hansen, M. Knapp, J. Bednarcik, S. Randau, F. H. Richter, J. Janek, H. Ehrenberg, and S. Indris, *Amorphous versus Crystalline Li_3PS_4: Local Structural Changes during Synthesis and Li Ion Mobility*, The Journal of Physical Chemistry C 123, 10280–10290 (2019).

[133] Y. Onodera, K. Mori, T. Otomo, M. Sugiyama, and T. Fukunaga, *Structural Evidence for High Ionic Conductivity of $Li_7P_3S_{11}$ Metastable Crystal*, Journal of the Physical Society of Japan 81, 044802 (2012).

[134] K. Ohara, A. Mitsui, M. Mori, Y. Onodera, S. Shiotani, Y. Koyama, Y. Orikasa, M. Murakami, K. Shimoda, K. Mori, T. Fukunaga, H. Arai, Y. Uchimoto, and Z. Ogumi, *Structural and electronic features of binary Li_2S:P_2S_5 glasses*, Scientific Reports 6, 21302 (2016).

[135] T. Baba and Y. Kawamura, *Structure and Ionic Conductivity of Li_2S-P_2S_5 Glass Electrolytes Simulated with First-Principles Molecular Dynamics*, Frontiers in Energy Research 4 (2016).

[136] J.-S. Kim, W. D. Jung, J.-W. Son, J.-H. Lee, B.-K. Kim, K.-Y. Chung, H.-G. Jung, and H. Kim, *Atomistic Assessments of Lithium-Ion Conduction Behavior in Glass-Ceramic Lithium Thiophosphates*, ACS Applied Materials & Interfaces 11, 13–18 (2019).

[137] Y. Seino, T. Ota, K. Takada, A. Hayashi, and M. Tatsumisago, *A sulphide lithium super ion conductor is superior to liquid ion conductors for use in rechargeable batteries*, Energy & Environmental Science 7, 627–631 (2014).

[138] A. Hayashi, K. Minami, S. Ujiie, and M. Tatsumisago, *Preparation and ionic conductivity of $Li_7P_3S_{11-z}$ glass-ceramic electrolytes*, Journal of Non-Crystalline Solids 356, 2670–2673 (2010).

[139] Z. Liu, W. Fu, E. A. Payzant, X. Yu, Z. Wu, N. J. Dudney, J. Kiggans, K. Hong, A. J. Rondinone, and C. Liang, *Anomalous High Ionic Conductivity of Nanoporous β-Li_3PS_4*, Journal of the American Chemical Society 135, 975–978 (2013).

[140] H. Stöffler, T. Zinkevich, M. Yavuz, A. Senyshyn, J. Kulisch, P. Hartmann, T. Adermann, S. Randau, F. H. Richter, J. Janek, S. Indris, and H. Ehrenberg, *Li^+-Ion Dynamics in β-Li_3PS_4 Observed by NMR: Local Hopping and Long-Range Transport*, The Journal of Physical Chemistry C 122, 15954–15965 (2018).

[141] S. Teragawa, K. Aso, K. Tadanaga, A. Hayashi, and M. Tatsumisago, *Liquid-phase synthesis of a Li_3PS_4 solid electrolyte using N-methylformamide for all-solid-state lithium batteries*, Journal of Materials Chemistry A 2, 5095–5099 (2014).

[142] H. Wang, Z. D. Hood, Y. Xia, and C. Liang, *Fabrication of ultrathin solid electrolyte membranes of β-Li_3PS_4 nanoflakes by evaporation-induced self-assembly for all-solid-state batteries*, Journal of Materials Chemistry A 4, 8091–8096 (2016).

[143] M. Tachez, J.-P. Malugani, R. Mercier, and G. Robert, *Ionic conductivity of and phase transition in lithium thiophosphate Li_3PS_4*, Solid State Ionics 14, 181–185 (1984).

[144] D. A. Ziolkowska, W. Arnold, T. Druffel, M. Sunkara, and H. Wang, *Rapid and Economic Synthesis of a Li_7PS_6 Solid Electrolyte from a Liquid Approach*, ACS Applied Materials & Interfaces 11, 6015–6021 (2019).

[145] A. Hayashi, S. Hama, T. Minami, and M. Tatsumisago, *Formation of superionic crystals from mechanically milled Li_2S-P_2S_5 glasses*, Electrochemistry Communications 5, 111–114 (2003).

[146] S. Teragawa, K. Aso, K. Tadanaga, A. Hayashi, and M. Tatsumisago, *Formation of Li_2S-P_2S_5 Solid Electrolyte from N-Methylformamide Solution*, Chemistry Letters 42, 1435–1437 (2013).

[147] J. Trevey, J. S. Jang, Y. S. Jung, C. R. Stoldt, and S.-H. Lee, *Glass-ceramic Li_2S-P_2S_5 electrolytes prepared by a single step ball billing process and their application for all-solid-state lithium-ion batteries*, Electrochemistry Communications 11, 1830–1833 (2009).

[148] Z. Zhang and J. H. Kennedy, *Synthesis and characterization of the B_2S_3:Li_2S, the P_2S_5:Li_2S and the B_2S_3:P_2S_5:Li_2S glass systems*, Solid State Ionics 38, 217–224 (1990).

[149] A. Hayashi, S. Hama, H. Morimoto, M. Tatsumisago, and T. Minami, *Preparation of Li_2S-P_2S_5 Amorphous Solid Electrolytes by Mechanical Milling*, Journal of the American Ceramic Society 84, 477–79 (2001).

[150] N. A. W. Holzwarth, N. D. Lepley, and Y. A. Du, *Computer modeling of lithium phosphate and thiophosphate electrolyte materials*, Journal of Power Sources 196, 6870–6876 (2011).

[151] N. D. Lepley and N. a. W. Holzwarth, *Computer Modeling of Crystalline Electrolytes: Lithium Thiophosphates and Phosphates*, Journal of The Electrochemical Society 159, A538–A547 (2012).

[152] A. Daidouh, M. L. Veiga, C. Pico, and M. Martinez-Ripoll, *A New Polymorph of Li4P2O7*, Acta Crystallographica Section C: Crystal Structure Communications 53, 167–169 (1997).

[153] F. Mizuno, A. Hayashi, K. Tadanaga, and M. Tatsumisago, *New, Highly Ion-Conductive Crystals Precipitated from Li_2S-P_2S_5 Glasses*, Advanced Materials 17, 918–921 (2005).

[154] A. Hayashi, K. Minami, F. Mizuno, and M. Tatsumisago, *Formation of Li^+ superionic crystals from the Li_2S-P_2S_5 melt-quenched glasses*, Journal of Materials Science 43, 1885–1889 (2008).

[155] H. Yamane, M. Shibata, Y. Shimane, T. Junke, Y. Seino, S. Adams, K. Minami, A. Hayashi, and M. Tatsumisago, *Crystal structure of a superionic conductor, $Li_7P_3S_{11}$*, Solid State Ionics 178, 1163–1167 (2007).

[156] Y. Onodera, K. Mori, T. Otomo, H. Arai, Y. Uchimoto, Z. Ogumi, and T. Fukunaga, *Structural origin of ionic conductivity for $Li_7P_3S_{11}$ metastable crystal by neutron and X-ray diffraction*, Journal of Physics: Conference Series 502, 012021 (2014).

[157] K. Mori, K. Enjuji, S. Murata, K. Shibata, Y. Kawakita, M. Yonemura, Y. Onodera, and T. Fukunaga, *Direct Observation of Fast Lithium-Ion Diffusion in a Superionic Conductor: $Li_7P_3S_{11}$ Metastable Crystal*, Physical Review Applied 4, 054008 (2015).

[158] K. Mori, T. Ichida, K. Iwase, T. Otomo, S. Kohara, H. Arai, Y. Uchimoto, Z. Ogumi, Y. Onodera, and T. Fukunaga, *Visualization of conduction pathways in lithium superionic conductors: Li_2S-P_2S_5 glasses and $Li_7P_3S_{11}$ glass-ceramic*, Chemical Physics Letters 584, 113–118 (2013).

[159] I.-H. Chu, H. Nguyen, S. Hy, Y.-C. Lin, Z. Wang, Z. Xu, Z. Deng, Y. S. Meng, and S. P. Ong, *Correction to Insights into the Performance Limits of the $Li_7P_3S_{11}$ Superionic Conductor: A Combined First-Principles and Experimental Study*, ACS Applied Materials & Interfaces 10, 10598–10598 (2018).

[160] M. R. Busche, D. A. Weber, Y. Schneider, C. Dietrich, S. Wenzel, T. Leichtweiss, D. Schröder, W. Zhang, H. Weigand, D. Walter, S. J. Sedlmaier, D. Houtarde, L. F. Nazar, and J. Janek, *In Situ Monitoring of Fast Li-Ion Conductor $Li_7P_3S_{11}$ Crystallization Inside a Hot-Press Setup*, Chemistry of Materials 28, 6152–6165 (2016).

[161] S. Ohno, T. Bernges, J. Buchheim, M. Duchardt, A.-K. Hatz, M. A. Kraft, H. Kwak, A. L. Santhosha, Z. Liu, N. Minafra, F. Tsuji, A. Sakuda, R. Schlem, S. Xiong, Z. Zhang, P. Adelhelm, H. Chen, A. Hayashi, Y. S. Jung, B. V. Lotsch, B. Roling, N. M. Vargas-Barbosa, and W. G. Zeier, *How Certain Are the Reported Ionic Conductivities of Thiophosphate-Based Solid Electrolytes? An Interlaboratory Study*, ACS Energy Letters 5, 910–915 (2020).

[162] W. D. Richards, T. Tsujimura, L. J. Miara, Y. Wang, J. C. Kim, S. P. Ong, I. Uechi, N. Suzuki, and G. Ceder, *Design and synthesis of the superionic conductor $Na_{10}SnP_2S_{12}$*, Nature Communications 7, 11009 (2016).

[163] S. Sicolo, C. Kalcher, S. J. Sedlmaier, J. Janek, and K. Albe, *Diffusion mechanism in the superionic conductor Li_4PS_4I studied by first-principles calculations*, Solid State Ionics 319, 83–91 (2018).

[164] X. He, Y. Zhu, A. Epstein, and Y. Mo, *Statistical variances of diffusional properties from ab initio molecular dynamics simulations*, npj Computational Materials 4, 18 (2018).

[165] A. Marcolongo and N. Marzari, *Ionic correlations and failure of Nernst-Einstein relation in solid-state electrolytes*, Physical Review Materials 1, 025402 (2017).

[166] W. D. Jung, B.-N. Yun, H.-G. Jung, S. Choi, J.-W. Son, J.-H. Lee, J.-H. Lee, and H. Kim, *Configuring PS_x tetrahedral clusters in Li-excess $Li_7P_3S_{11}$ solid electrolyte*, APL Materials 6, 047902 (2018).

[167] K. Homma, M. Yonemura, M. Nagao, M. Hirayama, and R. Kanno, *Crystal Structure of High-Temperature Phase of Lithium Ionic Conductor, Li_3PS_4*, Journal of the Physical Society of Japan 79, 90–93 (2010).

[168] S. Iikubo, K. Shimoyama, S. Kawano, M. Fujii, K. Yamamoto, M. Matsushita, T. Shinmei, Y. Higo, and H. Ohtani, *Novel stable structure of Li_3PS_4 predicted by evolutionary algorithm under high-pressure*, AIP Advances 8, 015008 (2018).

[169] R. Mercier, J.-P. Malugani, B. Fahys, G. Robert, and J. Douglade, *Structure du tetrathiophosphate de lithium*, Acta Crystallographica Section B: Structural Crystallography and Crystal Chemistry 38, 1887–1890 (1982).

[170] Y. Chen, L. Cai, Z. Liu, C. R. dela Cruz, C. Liang, and K. An, *Correlation of anisotropy and directional conduction in β-Li_3PS_4 fast Li^+ conductor*, Applied Physics Letters 107, 013904 (2015).

[171] K. Yamamoto, S. Yang, M. Takahashi, K. Ohara, T. Uchiyama, T. Watanabe, A. Sakuda, A. Hayashi, M. Tatsumisago, H. Muto, A. Matsuda, and Y. Uchimoto, *High Ionic Conductivity of Liquid-Phase-Synthesized Li_3PS_4 Solid Electrolyte, Comparable to That Obtained via Ball Milling*, ACS Applied Energy Materials 4, 2275–2281 (2021).

[172] K. Hayamizu, Y. Aihara, T. Watanabe, T. Yamada, S. Ito, and N. Machida, *NMR studies on lithium ion migration in sulfide-based conductors, amorphous and crystalline Li_3PS_4*, Solid State Ionics 285, 51–58 (2016).

[173] M. Murayama, N. Sonoyama, A. Yamada, and R. Kanno, *Material design of new lithium ionic conductor, thio-LISICON, in the Li_2S-P_2S_5 system*, Solid State Ionics 170, 173–180 (2004).

[174] N. D. Lepley, N. A. W. Holzwarth, and Y. A. Du, *Structures, Li^+ mobilities, and interfacial properties of solid electrolytes Li_3PS_4 and Li_3PO_4 from first principles*, Physical Review B 88, 104103 (2013).

[175] Y. Yang, Q. Wu, Y. Cui, Y. Chen, S. Shi, R.-Z. Wang, and H. Yan, *Elastic Properties, Defect Thermodynamics, Electrochemical Window, Phase Stability, and Li^+ Mobility of Li_3PS_4: Insights from First-Principles Calculations*, ACS Applied Materials & Interfaces 8, 25229–25242 (2016).

[176] J. Haruyama, K. Sodeyama, L. Han, K. Takada, and Y. Tateyama, *Space-Charge Layer Effect at Interface between Oxide Cathode and Sulfide Electrolyte in All-Solid-State Lithium-Ion Battery*, Chemistry of Materials 26, 4248–4255 (2014).

[177] J. Haruyama, K. Sodeyama, and Y. Tateyama, *Cation Mixing Properties toward Co Diffusion at the $LiCoO_2$ Cathode / Sulfide Electrolyte Interface in a Solid-State Battery*, ACS Applied Materials & Interfaces 9, 286–292 (2017).

[178] F. Walther, F. Strauss, X. Wu, B. Mogwitz, J. Hertle, J. Sann, M. Rohnke, T. Brezesinski, and J. Janek, *The Working Principle of a Li_2CO_3 / $LiNbO_3$ Coating on NCM for Thiophosphate-Based All-Solid-State Batteries*, Chemistry of Materials 33, 2110–2125 (2021).

[179] H. Eckert, Z. Zhang, and J. H. Kennedy, *Structural transformation of non-oxide chalcogenide glasses. The short-range order of lithium sulfide (Li_2S)-phosphorus pentasulfide (P_2S_5) glasses studied by quantitative ^{31}P and $^{6,7}Li$ high-resolution solid-state NMR*, Chemistry of Materials 2, 273–279 (1990).

[180] H.-J. Deiseroth, S.-T. Kong, H. Eckert, J. Vannahme, C. Reiner, T. Zaiss, and M. Schlosser, *Li_6PS_5X: A Class of Crystalline Li-Rich Solids With an Unusually High Li^+ Mobility*, Angewandte Chemie International Edition 47, 755–758 (2008).

[181] S. T. Kong, O. Gün, B. Koch, H. J. Deiseroth, H. Eckert, and C. Reiner, *Structural Characterisation of the Li Argyrodites Li_7PS_6 and Li_7PSe_6 and their Solid Solutions: Quantification of Site Preferences by MAS-NMR Spectroscopy*, Chemistry - A European Journal 16, 5138–5147 (2010).

[182] S.-T. Kong, H.-J. Deiseroth, C. Reiner, O. Gün, E. Neumann, C. Ritter, and D. Zahn, *Lithium Argyrodites with Phosphorus and Arsenic: Order and Disorder of Lithium Atoms, Crystal Chemistry, and Phase Transitions*, Chemistry - A European Journal 16, 2198–2206 (2010).

[183] H.-J. Deiseroth, J. Maier, K. Weichert, V. Nickel, S.-T. Kong, and C. Reiner, *Li_7PS_6 and Li_6PS_5X (X: Cl, Br, I): Possible Three-dimensional Diffusion Pathways for Lithium Ions and Temperature Dependence of the Ionic Conductivity by Impedance Measurements*, Zeitschrift für anorganische und allgemeine Chemie 637, 1287–1294 (2011).

[184] N. J. J. de Klerk, I. Rosloń, and M. Wagemaker, *Diffusion Mechanism of Li Argyrodite Solid Electrolytes for Li-Ion Batteries and Prediction of Optimized Halogen Doping: The Effect of Li Vacancies, Halogens, and Halogen Disorder*, Chemistry of Materials 28, 7955–7963 (2016).

[185] R. P. Rao, N. Sharma, V. K. Peterson, and S. Adams, *Formation and conductivity studies of lithium argyrodite solid electrolytes using in-situ neutron diffraction*, Solid State Ionics 230, 72–76 (2013).

[186] Z. D. Hood, C. Kates, M. Kirkham, S. Adhikari, C. Liang, and N. A. W. Holzwarth, *Structural and electrolyte properties of $Li_4P_2S_6$*, Solid State Ionics 284, 61–70 (2016).

[187] S. Neuberger, S. P. Culver, H. Eckert, W. G. Zeier, and J. S. a. d. Günne, *Refinement of the crystal structure of $Li_4P_2S_6$ using NMR crystallography*, Dalton Transactions 47, 11691–11695 (2018).

[188] A. R. Stamminger, B. Ziebarth, M. Mrovec, T. Hammerschmidt, and R. Drautz, *Fast diffusion mechanism in $Li_4P_2S_6$ via a concerted process of interstitial Li ions*, RSC Advances 10, 10715–10722 (2020).

[189] H. Nagata and J. Akimoto, *Ionic Conductivity of Low-Crystalline $Li_4P_2S_6$ and $Li_4P_2S_6$-LiX (X=Cl, Br, and I) Systems and Their Role in Improved Positive Electrode Performance in All-Solid-State LiS Battery*, ChemistrySelect 5, 9926–9931 (2020).

[190] H. Y.-P. Hong, *Crystal structure and ionic conductivity of $Li_{14}Zn(GeO_4)_4$ and other new Li^+ superionic conductors*, Materials Research Bulletin 13, 117–124 (1978).

[191] Z. A. Grady, C. J. Wilkinson, C. A. Randall, and J. C. Mauro, *Emerging Role of Non-crystalline Electrolytes in Solid-State Battery Research*, Frontiers in Energy Research 8 (2020).

[192] A. Kato, M. Yamamoto, A. Sakuda, A. Hayashi, and M. Tatsumisago, *Mechanical Properties of Li_2S-P_2S_5 Glasses with Lithium Halides and Application in All-Solid-State Batteries*, ACS Applied Energy Materials 1, 1002–1007 (2018).

[193] J. G. Smith and D. J. Siegel, *Low-temperature paddlewheel effect in glassy solid electrolytes*, Nature Communications 11, 1483 (2020).

[194] H. Guo, Q. Wang, A. Urban, and N. Artrith, *Artificial Intelligence-Aided Mapping of the Structure-Composition-Conductivity Relationships of Glass-Ceramic Lithium Thiophosphate Electrolytes*, Chemistry of Materials (2022).

[195] S. Sicolo and K. Albe, *First-principles calculations on structure and properties of amorphous $Li_5P_4O_8N_3$ (LiPON)*, Journal of Power Sources 331, 382–390 (2016).

[196] S. Sicolo, M. Fingerle, R. Hausbrand, and K. Albe, *Interfacial instability of amorphous LiPON against lithium: A combined Density Functional Theory and spectroscopic study*, Journal of Power Sources 354, 124–133 (2017).

[197] V. Lacivita, N. Artrith, and G. Ceder, *Structural and Compositional Factors That Control the Li-Ion Conductivity in LiPON Electrolytes*, Chemistry of Materials 30, 7077–7090 (2018).

[198] M. Ebrahiminia, J. B. Hooper, and D. Bedrov, *Structural, Mechanical, and Dynamical Properties of Amorphous Li_2CO_3 from Molecular Dynamics Simulations*, Crystals 8, 473 (2018).

[199] A. Jonderian and E. McCalla, *The role of metal substitutions in the development of Li batteries, part II: solid electrolytes*, Materials Advances (2021).

[200] L. Zhou, A. Assoud, A. Shyamsunder, A. Huq, Q. Zhang, P. Hartmann, J. Kulisch, and L. F. Nazar, *An Entropically Stabilized Fast-Ion Conductor: $Li_{3.25}[Si_{0.25}P_{0.75}]S_4$*, Chemistry of Materials 31, 7801–7811 (2019).

[201] B. T. Leube, K. K. Inglis, E. J. Carrington, P. M. Sharp, J. F. Shin, A. R. Neale, T. D. Manning, M. J. Pitcher, L. J. Hardwick, M. S. Dyer, F. Blanc, J. B. Claridge, and M. J. Rosseinsky, *Lithium Transport in $Li_{4.4}M_{0.4}M'_{0.6}S_4$ ($M = Al^{3+}$, Ga^{3+}, and $M' = Ge^{4+}$, Sn^{4+}): Combined Crystallographic, Conductivity, Solid State NMR, and Computational Studies*, Chemistry of Materials 30, 7183–7200 (2018).

[202] N. Kamaya, K. Homma, Y. Yamakawa, M. Hirayama, R. Kanno, M. Yonemura, T. Kamiyama, Y. Kato, S. Hama, K. Kawamoto, and A. Mitsui, *A lithium superionic conductor*, Nature Materials 10, 682–686 (2011).

[203] Y. Kato, S. Hori, T. Saito, K. Suzuki, M. Hirayama, A. Mitsui, M. Yonemura, H. Iba, and R. Kanno, *High-power all-solid-state batteries using sulfide superionic conductors*, Nature Energy 1, 16030 (2016).

[204] C. Yu, F. Zhao, J. Luo, L. Zhang, and X. Sun, *Recent development of lithium argyrodite solid-state electrolytes for solid-state batteries: Synthesis, structure, stability and dynamics*, Nano Energy 83, 105858 (2021).

[205] H. Wang, C. Yu, S. Ganapathy, E. R. H. van Eck, L. van Eijck, and M. Wagemaker, *A lithium argyrodite $Li_6PS_5Cl_{0.5}Br_{0.5}$ electrolyte with improved bulk and interfacial conductivity*, Journal of Power Sources 412, 29–36 (2019).

[206] L. Zhou, A. Assoud, Q. Zhang, X. Wu, and L. F. Nazar, *New Family of Argyrodite Thioantimonate Lithium Superionic Conductors*, Journal of the American Chemical Society 141, 19002–19013 (2019).

[207] B. J. Morgan, *Mechanistic Origin of Superionic Lithium Diffusion in Anion-Disordered Li_6PS_5X Argyrodites*, Chemistry of Materials, acs.chemmater.0c03738 (2021).

[208] N. Minafra, M. A. Kraft, T. Bernges, C. Li, R. Schlem, B. J. Morgan, and W. G. Zeier, *Local Charge Inhomogeneity and Lithium Distribution in the Superionic Argyrodites Li_6PS_5X (X = Cl, Br, I)*, Inorganic Chemistry 59, 11009–11019 (2020).

[209] H. M. Chen, C. Maohua, and S. Adams, *Stability and ionic mobility in argyrodite-related lithium-ion solid electrolytes*, Physical Chemistry Chemical Physics 17, 16494–16506 (2015).

[210] Z. Wang and G. Shao, *Theoretical design of solid electrolytes with superb ionic conductivity: alloying effect on Li^+ transportation in cubic Li_6PA_5X chalcogenides*, Journal of Materials Chemistry A 5, 21846–21857 (2017).

[211] Z. Zhu, I.-H. Chu, and S. P. Ong, *$Li_3Y(PS_4)_2$ and $Li_5PS_4Cl_2$: New Lithium Superionic Conductors Predicted from Silver Thiophosphates using Efficiently Tiered Ab Initio Molecular Dynamics Simulations*, Chemistry of Materials 29, 2474–2484 (2017).

[212] P. Adeli, J. D. Bazak, K. H. Park, I. Kochetkov, A. Huq, G. R. Goward, and L. F. Nazar, *Boosting Solid-State Diffusivity and Conductivity in Lithium Superionic Argyrodites by Halide Substitution*, Angewandte Chemie International Edition 58, 8681–8686 (2019).

[213] B. Ouyang, Y. Wang, Y. Sun, and G. Ceder, *Computational Investigation of Halogen-Substituted Na Argyrodites as Solid-State Superionic Conductors*, Chemistry of Materials 32, 1896–1903 (2020).

[214] P. Wang, H. Liu, S. Patel, X. Feng, P.-H. Chien, Y. Wang, and Y.-Y. Hu, *Fast Ion Conduction and Its Origin in $Li_{6-x}PS_{5-x}Br_{1+x}$*, Chemistry of Materials 32, 3833–3840 (2020).

[215] J. Zhang, L. Li, C. Zheng, Y. Xia, Y. Gan, H. Huang, C. Liang, X. He, X. Tao, and W. Zhang, *Silicon-Doped Argyrodite Solid Electrolyte Li_6PS_5I with Improved Ionic Conductivity and Interfacial Compatibility for High-Performance All-Solid-State Lithium Batteries*, ACS Applied Materials & Interfaces (2020).

[216] O. Pecher, S.-T. Kong, T. Goebel, V. Nickel, K. Weichert, C. Reiner, H.-J. Deiseroth, J. Maier, F. Haarmann, and D. Zahn, *Atomistic Characterisation of Li^+ Mobility and Conductivity in $Li_{7-x}PS_{6-x}I_x$ Argyrodites from Molecular Dynamics Simulations, Solid-State NMR, and Impedance Spectroscopy*, Chemistry - A European Journal 16, 8347–8354 (2010).

[217] R. P. Rao and S. Adams, *Studies of lithium argyrodite solid electrolytes for all-solid-state batteries*, physica status solidi (a) 208, 1804–1807 (2011).

[218] P. R. Rayavarapu, N. Sharma, V. K. Peterson, and S. Adams, *Variation in structure and Li^+-ion migration in argyrodite-type Li_6PS_5X (X = Cl, Br, I) solid electrolytes*, Journal of Solid State Electrochemistry 16, 1807–1813 (2012).

[219] C. Yu, S. Ganapathy, N. J. J. de Klerk, I. Roslon, E. R. H. van Eck, A. P. M. Kentgens, and M. Wagemaker, *Unravelling Li-Ion Transport from Picoseconds to Seconds: Bulk versus Interfaces in an Argyrodite Li_6PS_5Cl-Li_2S All-Solid-State Li-Ion Battery*, Journal of the American Chemical Society 138, 11192–11201 (2016).

[220] Z. Deng, Z. Zhu, I.-H. Chu, and S. P. Ong, *Data-Driven First-Principles Methods for the Study and Design of Alkali Superionic Conductors*, Chemistry of Materials 29, 281–288 (2017).

[221] A. R. Stamminger, B. Ziebarth, M. Mrovec, T. Hammerschmidt, and R. Drautz, *Ionic Conductivity and Its Dependence on Structural Disorder in Halogenated Argyrodites Li_6PS_5X (X = Br, Cl, I)*, Chemistry of Materials 31, 8673–8678 (2019).

[222] V. Epp, O. Gün, H.-J. Deiseroth, and M. Wilkening, *Highly Mobile Ions: Low-Temperature NMR Directly Probes Extremely Fast Li^+ Hopping in Argyrodite-Type Li_6PS_5Br*, The Journal of Physical Chemistry Letters 4, 2118–2123 (2013).

[223] S. Yubuchi, M. Uematsu, M. Deguchi, A. Hayashi, and M. Tatsumisago, *Lithium-Ion-Conducting Argyrodite-Type Li_6PS_5X (X = Cl, Br, I) Solid Electrolytes Prepared by a Liquid-Phase Technique Using Ethanol as a Solvent*, ACS Applied Energy Materials 1, 3622–3629 (2018).

[224] M. Brinek, C. Hiebl, and H. M. R. Wilkening, *Understanding the Origin of Enhanced Li-Ion Transport in Nanocrystalline Argyrodite-Type Li6PS5I*, Chemistry of Materials 32, 4754–4766 (2020).

[225] M. A. Kraft, S. Ohno, T. Zinkevich, R. Koerver, S. P. Culver, T. Fuchs, A. Senyshyn, S. Indris, B. J. Morgan, and W. G. Zeier, *Inducing High Ionic Conductivity in the Lithium Superionic Argyrodites $Li_{6+x}P_{1-x}Ge_xS_5I$ for All-Solid-State Batteries*, Journal of the American Chemical Society 140, 16330–16339 (2018).

[226] S. Ohno, B. Helm, T. Fuchs, G. Dewald, M. A. Kraft, S. P. Culver, A. Senyshyn, and W. G. Zeier, *Further Evidence for Energy Landscape Flattening in the Superionic Argyrodites $Li_{6+x}P_{1-x}M_xS_5I$ (M = Si, Ge, Sn)*, Chemistry of Materials 31, 4936–4944 (2019).

[227] C. Yu, S. Ganapathy, E. R. H. v. Eck, L. v. Eijck, S. Basak, Y. Liu, L. Zhang, H. W. Zandbergen, and M. Wagemaker, *Revealing the relation between the structure, Li-ion conductivity and solid-state battery performance of the argyrodite Li_6PS_5Br solid electrolyte*, Journal of Materials Chemistry A 5, 21178–21188 (2017).

[228] S. Ganapathy, C. Yu, E. R. H. van Eck, and M. Wagemaker, *Peeking across Grain Boundaries in a Solid-State Ionic Conductor*, ACS Energy Letters 4, 1092–1097 (2019).

[229] Y. Mishin, *Interatomic potentials for metals*, pp. 459–478, Springer Netherlands, Dordrecht, 2005.

[230] D. Brenner, *The Art and Science of an Analytic Potential*, physica status solidi (b) 217, 23–40 (2000).

[231] J. A. Harrison, J. D. Schall, S. Maskey, P. T. Mikulski, M. T. Knippenberg, and B. H. Morrow, *Review of force fields and intermolecular potentials used in atomistic computational materials research*, Applied Physics Reviews 5, 031104 (2018).

[232] T. Mueller, A. Hernandez, and C. Wang, *Machine learning for interatomic potential models*, The Journal of Chemical Physics 152, 050902 (2020).

[233] C. M. Handley and J. Behler, *Next generation interatomic potentials for condensed systems*, The European Physical Journal B 87, 152 (2014).

[234] M. Born and R. Oppenheimer, *Zur Quantentheorie der Molekeln*, Annalen der Physik 389, 457–484 (1927).

[235] M. P. Teter, M. C. Payne, and D. C. Allan, *Solution of Schrödinger's equation for large systems*, Physical Review B 40, 12255–12263 (1989).

[236] R. Zhang and C. Deng, *Exact solutions of the Schrödinger equation for some quantum-mechanical many-body systems*, Physical Review A 47, 71–77 (1993).

[237] *The Nobel Prize in Chemistry 1998*, `https://www.nobelprize.org/prizes/chemistry/1998/summary/` last visited on 2021-09-28, NobelPrize.org.

[238] P. Hohenberg and W. Kohn, *Inhomogeneous Electron Gas*, Physical Review 136, B864–B871 (1964).

[239] W. Kohn and L. J. Sham, *Self-Consistent Equations Including Exchange and Correlation Effects*, Physical Review 140, A1133–A1138 (1965).

[240] R. P. Feynman, *Forces in Molecules*, Physical Review 56, 340–343 (1939).

[241] W. H. Press (ed.), *Numerical recipes: the art of scientific computing*, 3rd ed ed., Cambridge University Press, Cambridge, UK ; New York, 2007.

[242] G. Kresse and J. Hafner, *Ab initio molecular-dynamics simulation of the liquid-metal-amorphous-semiconductor transition in germanium*, Physical Review B 49, 14251–14269 (1994).

[243] G. Kresse, *Ab initio molecular dynamics for liquid metals*, Journal of Non-Crystalline Solids 192-193, 222–229 (1995).

[244] G. Kresse and J. Furthmüller, *Efficiency of ab-initio total energy calculations for metals and semiconductors using a plane-wave basis set*, Computational Materials Science 6, 15–50 (1996).

[245] G. Kresse and J. Furthmüller, *Efficient iterative schemes for ab initio total-energy calculations using a plane-wave basis set*, Physical Review B 54, 11169–11186 (1996).

[246] D. Sheppard, R. Terrell, and G. Henkelman, *Optimization methods for finding minimum energy paths*, The Journal of Chemical Physics 128, 134106 (2008).

[247] R. M. Martin, *Electronic Structure: Basic Theory and Practical Methods*, 2 ed., Cambridge University Press, Cambridge, United Kingdom ; New York, NY, August 2020.

[248] K. Momma and F. Izumi, *VESTA 3 for three-dimensional visualization of crystal, volumetric and morphology data*, Journal of Applied Crystallography 44, 1272–1276 (2011).

[249] A. Stukowski, *Visualization and analysis of atomistic simulation data with OVITO–the Open Visualization Tool*, Modelling and Simulation in Materials Science and Engineering 18, 015012 (2010).

[250] P. Kratzer and J. Neugebauer, *The Basics of Electronic Structure Theory for Periodic Systems*, Frontiers in Chemistry 7, 106 (2019).

[251] A. Kahn, *Fermi level, work function and vacuum level*, Materials Horizons 3, 7–10 (2016).

[252] Z. Hu, Z. Lin, J. Su, J. Zhang, J. Chang, and Y. Hao, *A Review on Energy Band-Gap Engineering for Perovskite Photovoltaics*, Solar RRL 3, 1900304 (2019).

[253] J. P. Perdew, *Density functional theory and the band gap problem*, International Journal of Quantum Chemistry 28, 497–523 (1985).

[254] P. Borlido, J. Schmidt, A. W. Huran, F. Tran, M. A. L. Marques, and S. Botti, *Exchange-correlation functionals for band gaps of solids: benchmark, reparametrization and machine learning*, npj Computational Materials 6, 1–17 (2020).

[255] J. P. Perdew, K. Burke, and M. Ernzerhof, *Generalized Gradient Approximation Made Simple*, Physical Review Letters 77, 3865–3868 (1996).

[256] J. P. Perdew, K. Burke, and M. Ernzerhof, *Generalized Gradient Approximation Made Simple [Phys. Rev. Lett. 77, 3865 (1996)]*, Physical Review Letters 78, 1396–1396 (1997).

[257] Y. Zhang and W. Yang, *Comment on "Generalized Gradient Approximation Made Simple"*, Physical Review Letters 80, 890–890 (1998).

[258] J. P. Perdew, K. Burke, and M. Ernzerhof, *Perdew, Burke, and Ernzerhof Reply:*, Physical Review Letters 80, 891–891 (1998).

[259] N. Mardirossian and M. Head-Gordon, *Thirty years of density functional theory in computational chemistry: an overview and extensive assessment of 200 density functionals*, Molecular Physics 115, 2315–2372 (2017).

[260] B. Douglas and S.-M. Ho, *Structure and Chemistry of Crystalline Solids*, Springer-Verlag, New York, 2006.

[261] Z. H. Stachurski, *Fundamentals of Amorphous Solids: Structure and Properties*, 1 ed., Wiley-VCH, Beijing, 2015.

[262] W. Borchardt-Ott, *Kristallographie: Eine Einführung für Naturwissenschaftler*, 7 ed., Springer-Lehrbuch, Springer-Verlag, Berlin Heidelberg, 2009.

[263] S. Grazulis, A. Daskevic, A. Merkys, D. Chateigner, L. Lutterotti, M. Quirś, N. R. Serebryanaya, P. Moeck, R. T. Downs, and A. Le Bail, *Crystallography Open Database (COD): an open-access collection of crystal structures and platform for world-wide collaboration*, Nucleic Acids Research 40, D420–D427 (2012).

[264] A. Jain, S. P. Ong, G. Hautier, W. Chen, W. D. Richards, S. Dacek, S. Cholia, D. Gunter, D. Skinner, G. Ceder, and K. A. Persson, *Commentary: The Materials Project: A materials genome approach to accelerating materials innovation*, APL Materials 1, 011002 (2013).

[265] A. R. Oganov, C. J. Pickard, Q. Zhu, and R. J. Needs, *Structure prediction drives materials discovery*, Nature Reviews Materials 4, 331–348 (2019).

[266] P. Liu, B. Guo, T. An, H. Fang, G. Zhu, C. Jiang, and X. Jiang, *High throughput materials research and development for lithium ion batteries*, Journal of Materiomics 3, 202–208 (2017).

[267] F. Bloch, *Über die Quantenmechanik der Elektronen in Kristallgittern*, Zeitschrift für Physik 52, 555–600 (1929).

[268] P. Morgante and R. Peverati, *The devil in the details: A tutorial review on some undervalued aspects of density functional theory calculations*, International Journal of Quantum Chemistry 120, e26332 (2020).

[269] N. D. M. Hine, K. Frensch, W. M. C. Foulkes, and M. W. Finnis, *Supercell size scaling of density functional theory formation energies of charged defects*, Physical Review B 79, 024112 (2009).

[270] H.-P. Komsa, T. T. Rantala, and A. Pasquarello, *Finite-size supercell correction schemes for charged defect calculations*, Physical Review B 86, 045112 (2012).

[271] D. J. Singh and L. Nordstrom, *Planewaves, Pseudopotentials, and the LAPW Method*, 2 ed., Springer US, 2006.

[272] M. C. Payne, M. P. Teter, D. C. Allan, T. A. Arias, and J. D. Joannopoulos, *Iterative minimization techniques for ab initio total-energy calculations: molecular dynamics and conjugate gradients*, Reviews of Modern Physics 64, 1045–1097 (1992).

[273] P. E. Blöchl, *Projector augmented-wave method*, Physical Review B 50, 17953–17979 (1994).

[274] G. Kresse and D. Joubert, *From ultrasoft pseudopotentials to the projector augmented-wave method*, Physical Review B 59, 1758–1775 (1999).

[275] G. Lucovsky and T. M. Hayes, *Short-range order in amorphous semiconductors*, Amorphous Semiconductors (M. H. Brodsky, ed.), Topics in Applied Physics, Springer, Berlin, Heidelberg, 1985, pp. 215–250.

[276] D. A. Keen, *A comparison of various commonly used correlation functions for describing total scattering*, Journal of Applied Crystallography 34, 172–177 (2001).

[277] D. Marx and J. Hutter, *Ab Initio Molecular Dynamics: Basic Theory and Advanced Methods*, Cambridge University Press, Cambridge, 2009.

[278] L. Verlet, *Computer "Experiments" on Classical Fluids. I. Thermodynamical Properties of Lennard-Jones Molecules*, Physical Review 159, 98–103 (1967).

[279] N. S. Martys and R. D. Mountain, *Velocity Verlet algorithm for dissipative-particle-dynamics-based models of suspensions*, Physical Review E 59, 3733–3736 (1999).

[280] P. H. Hünenberger, *Thermostat Algorithms for Molecular Dynamics Simulations*, Advanced Computer Simulation (A. Abe, J.-F. Joanny, A.-C. Albertsson, R. Duncan, H.-H. Kausch, S. Kobayashi, K. Dusek, K.-S. Lee, W. de Jeu, L. Leibler, O. Nuyken, T. E. Long, E. Terentjev, B. Voit, I. Manners, G. Wegner, M. Möller, C. Dr. Holm, and K. Prof. Dr. Kremer, eds.), vol. 173, Springer Berlin Heidelberg, Berlin, Heidelberg, January 2005, pp. 105–149.

[281] R. A. Lippert, C. Predescu, D. J. Ierardi, K. M. Mackenzie, M. P. Eastwood, R. O. Dror, and D. E. Shaw, *Accurate and efficient integration for molecular dynamics simulations at constant temperature and pressure*, The Journal of Chemical Physics 139, 164106 (2013).

[282] J. Hickman and Y. Mishin, *Temperature fluctuations in canonical systems: Insights from molecular dynamics simulations*, Physical Review B 94 (2016).

[283] D. J. Evans and B. L. Holian, *The Nose-Hoover thermostat*, The Journal of Chemical Physics 83, 4069–4074 (1985).

[284] Z. P. Lu and C. T. Liu, *Glass Formation Criterion for Various Glass-Forming Systems*, Physical Review Letters 91, 115505 (2003).

[285] Z. Li, Z. Huang, F. Sun, X. Li, and J. Ma, *Forming of metallic glasses: mechanisms and processes*, Materials Today Advances 7, 100077 (2020).

[286] P. G. Debenedetti and F. H. Stillinger, *Supercooled liquids and the glass transition*, Nature 410, 259–267 (2001).

[287] J. W. P. Schmelzer and A. S. Abyzov, *How Do Crystals Nucleate and Grow: Ostwald's Rule of Stages and Beyond*, Thermal Physics and Thermal Analysis: From Macro to Micro, Highlighting Thermodynamics, Kinetics and Nanomaterials (J. Sestak, P. Hubik, and J. J. Mares, eds.), Hot Topics in Thermal Analysis and Calorimetry, Springer International Publishing, Cham, 2017, pp. 195–211.

[288] T. R. Anantharaman and C. Suryanarayana, *Review: A decade of quenching from the melt*, Journal of Materials Science 6, 1111–1135 (1971).

[289] S. Boulineau, M. Courty, J.-M. Tarascon, and V. Viallet, *Mechanochemical synthesis of Li-argyrodite Li_6PS_5X (X=Cl, Br, I) as sulfur-based solid electrolytes for all solid state batteries application*, Solid State Ionics 221, 1–5 (2012).

[290] M. Ishimaru, S. Munetoh, and T. Motooka, *Generation of amorphous silicon structures by rapid quenching: A molecular-dynamics study*, Physical Review B 56, 15133–15138 (1997).

[291] S. Caravati, M. Bernasconi, T. D. Kühne, M. Krack, and M. Parrinello, *Coexistence of tetrahedral- and octahedral-like sites in amorphous phase change materials*, Applied Physics Letters 91, 171906 (2007).

[292] H. E. Boyer, P. Archambault, F. Moreaux, and N. I. Kobasko, *Techniques of Quenching*, Theory and Technology of Quenching: A Handbook (B. Liscic, H. M. Tensi, and W. Luty, eds.), Springer, Berlin, Heidelberg, 1992, pp. 341–389.

[293] L.-Q. Chen, *Thermodynamic Equilibrium and Stability of Materials*, Springer Singapore, 2021.

[294] P. Grammatikopoulos, M. Sowwan, and J. Kioseoglou, *Computational Modeling of Nanoparticle Coalescence*, Advanced Theory and Simulations 2, 1900013 (2019).

[295] A. Bhandari, C. Peng, J. Dziedzic, L. Anton, J. R. Owen, D. Kramer, and C.-K. Skylaris, *Electrochemistry from first-principles in the grand canonical ensemble*, The Journal of Chemical Physics 155, 024114 (2021).

[296] B. Zhang, L. Yang, L.-W. Wang, and F. Pan, *Cooperative transport enabling fast Li-ion diffusion in Thio-LISICON $Li_{10}SiP_2S_{12}$ solid electrolyte*, Nano Energy 62, 844–852 (2019).

[297] S. P. Ong, L. Wang, B. Kang, and G. Ceder, *Li-Fe-P-O_2 Phase Diagram from First Principles Calculations*, Chemistry of Materials 20, 1798–1807 (2008).

[298] Y. Mo, S. P. Ong, and G. Ceder, *First Principles Study of the $Li_{10}GeP_2S_{12}$ Lithium Super Ionic Conductor Material*, Chemistry of Materials 24, 15–17 (2012).

[299] W. D. Richards, L. J. Miara, Y. Wang, J. C. Kim, and G. Ceder, *Interface Stability in Solid-State Batteries*, Chemistry of Materials 28, 266–273 (2016).

[300] C. B. Barber, D. P. Dobkin, and H. Huhdanpaa, *The quickhull algorithm for convex hulls*, ACM Transactions on Mathematical Software 22, 469–483 (1996).

[301] S. Goldstein, J. L. Lebowitz, R. Tumulka, and N. Zanghì, *Gibbs and Boltzmann Entropy in Classical and Quantum Mechanics*, Statistical Mechanics and Scientific Explanation, WORLD SCIENTIFIC, August 2019, pp. 519–581.

[302] P. Brüesch, *Phonons: Theory and Experiments I: Lattice Dynamics and Models of Interatomic Forces*, Springer Series in Solid-State Sciences, Springer, Berlin, Heidelberg, 1982.

[303] W. Qian and C. Zhang, *Review of the phonon calculations for energetic crystals and their applications*, Energetic Materials Frontiers 2, 154–164 (2021).

[304] A. Togo and I. Tanaka, *First principles phonon calculations in materials science*, Scripta Materialia 108, 1–5 (2015).

[305] T. R. Anthony, *Metastable synthesis of diamond*, Vacuum 41, 1356–1359 (1990).

[306] M. H. Cohen and D. Turnbull, *Metastability of Amorphous Structures*, Nature 203, 964–964 (1964).

[307] E. G. Lewars, *The Concept of the Potential Energy Surface*, Computational Chemistry: Introduction to the Theory and Applications of Molecular and Quantum Mechanics (E. G. Lewars, ed.), Springer International Publishing, Cham, 2016, pp. 9–49.

[308] J. B. Goodenough and Y. Kim, *Challenges for rechargeable batteries*, Journal of Power Sources 196, 6688–6694 (2011).

[309] M. Fingerle, R. Buchheit, S. Sicolo, K. Albe, and R. Hausbrand, *Reaction and Space Charge Layer Formation at the $LiCoO_2$-LiPON Interface: Insights on Defect Formation and Ion Energy Level Alignment by a Combined Surface Science-Simulation Approach*, Chemistry of Materials 29, 7675–7685 (2017).

[310] X. G. Zhang, *Passivation and Surface Film Formation*, Corrosion and Electrochemistry of Zinc (X. G. Zhang, ed.), Springer US, Boston, MA, 1996, pp. 65–91.

[311] A. M. Nolan, Y. Zhu, X. He, Q. Bai, and Y. Mo, *Computation-Accelerated Design of Materials and Interfaces for All-Solid-State Lithium-Ion Batteries*, Joule (2018).

[312] K. Leung, *DFT modelling of explicit solid-solid interfaces in batteries: methods and challenges*, Physical Chemistry Chemical Physics 22, 10412–10425 (2020).

[313] M. Sumita, Y. Tanaka, M. Ikeda, and T. Ohno, *Theoretically Designed Li_3PO_4 (100)/$LiFePO_4$ (010) Coherent Electrolyte/Cathode Interface for All Solid-State Li Ion Secondary Batteries*, The Journal of Physical Chemistry C 119, 14–22 (2015).

[314] M. Sumita, Y. Tanaka, M. Ikeda, and T. Ohno, *Theoretical insight into charging process in a Li_3PO_4 (100)/$LiFePO_4$ (010) coherent interface system*, Solid State Ionics 285, 59–65 (2016).

[315] M. Sumita, Y. Tanaka, and T. Ohno, *Possible Polymerization of PS_4 at a Li_3PS_4/$FePO_4$ Interface with Reduction of the $FePO_4$ Phase*, The Journal of Physical Chemistry C 121, 9698–9704 (2017).

[316] M. Sadowski, S. Sicolo, and K. Albe, *Defect thermodynamics and interfacial instability of crystalline $Li_4P_2S_6$*, Solid State Ionics 319, 53–60 (2018).

[317] Z. Ahmad, V. Venturi, H. Hafiz, and V. Viswanathan, *Interfaces in Solid Electrolyte Interphase: Implications for Lithium-Ion Batteries*, The Journal of Physical Chemistry C 125, 11301–11309 (2021).

[318] N. D. Lepley and N. A. W. Holzwarth, *Modeling interfaces between solids: Application to Li battery materials*, Physical Review B 92, 214201 (2015).

[319] S. Wang, R. Fang, Y. Li, Y. Liu, C. Xin, F. H. Richter, and C.-W. Nan, *Interfacial challenges for all-solid-state batteries based on sulfide solid electrolytes*, Journal of Materiomics 7, 209–218 (2021).

[320] Y. Tateyama, B. Gao, R. Jalem, and J. Haruyama, *Theoretical picture of positive electrode-solid electrolyte interface in all-solid-state battery from electrochemistry and semiconductor physics viewpoints*, Current Opinion in Electrochemistry 17, 149–157 (2019).

[321] M. Benoit, C. Langlois, N. Combe, H. Tang, and M.-J. Casanove, *Structural and electronic properties of the Au(001)/Fe(001) interface from density functional theory calculations*, Physical Review B 86, 075460 (2012).

[322] S. Ping Ong, Y. Mo, W. Davidson Richards, L. Miara, H. Sug Lee, and G. Ceder, *Phase stability, electrochemical stability and ionic conductivity of the $Li_{10\pm1}MP_2X_{12}$ (M = Ge, Si, Sn, Al or P, and X = O, S or Se) family of superionic conductors*, Energy & Environmental Science 6, 148–156 (2013).

[323] Y. Tian, T. Shi, W. D. Richards, J. Li, J. C. Kim, S.-H. Bo, and G. Ceder, *Compatibility issues between electrodes and electrolytes in solid-state batteries*, Energy & Environmental Science 10, 1150–1166 (2017).

[324] H. Reiss, *The Fermi level and the redox potential*, Journal of Physical Chemistry 89, 3783–3791 (1985).

[325] N. J. J. de Klerk and M. Wagemaker, *Space-Charge Layers in All-Solid-State Batteries; Important or Negligible?*, ACS Applied Energy Materials 1, 5609–5618 (2018).

[326] Z. Cheng, M. Liu, S. Ganapathy, C. Li, Z. Li, X. Zhang, P. He, H. Zhou, and M. Wagemaker, *Revealing the Impact of Space-Charge Layers on the Li-Ion Transport in All-Solid-State Batteries*, Joule 4, 1311–1323 (2020).

[327] L. Katzenmeier, S. Helmer, S. Braxmeier, E. Knobbe, and A. S. Bandarenka, *Properties of the Space Charge Layers Formed in Li-Ion Conducting Glass Ceramics*, ACS Applied Materials & Interfaces 13, 5853–5860 (2021).

[328] Z. Lu and F. Ciucci, *Metal Borohydrides as Electrolytes for Solid-State Li, Na, Mg, and Ca Batteries: A First-Principles Study*, Chemistry of Materials 29, 9308–9319 (2017).

[329] A. Kelly and K. M. Knowles, *Crystallography and Crystal Defects, second edition*, John Wiley & Sons, Ltd, 2012.

[330] S. Spannenberger, V. Miss, E. Klotz, J. Kettner, M. Cronau, A. Ramanayagam, F. di Capua, M. Elsayed, R. Krause-Rehberg, M. Vogel, and B. Roling, *Annealing-induced vacancy formation enables extraordinarily high Li^+ ion conductivity in the amorphous electrolyte 0.33 LiI+0.67 Li_3PS_4*, Solid State Ionics 341, 115040 (2019).

[331] C. Wagner, *Point Defects and Their Interaction*, Annual Review of Materials Science 7, 1–24 (1977).

[332] S. K. Rattan, P. Singh, S. Prakash, and J. Singh, *Strain field due to point defects in metals*, Physical Review B 47, 599–607 (1993).

[333] R. C. Newman, *Defects in silicon*, Reports on Progress in Physics 45, 1163–1210 (1982).

[334] M. J. Gillan, *The elastic dipole tensor for point defects in ionic crystals*, Journal of Physics C: Solid State Physics 17, 1473–1488 (1984).

[335] M. Leslie and N. J. Gillan, *The energy and elastic dipole tensor of defects in ionic crystals calculated by the supercell method*, Journal of Physics C: Solid State Physics 18, 973–982 (1985).

[336] J. S. Wróbel, M. R. Zemla, D. Nguyen-Manh, P. Olsson, L. Messina, C. Domain, T. Wejrzanowski, and S. L. Dudarev, *Elastic dipole tensors and relaxation volumes of point defects in concentrated random magnetic Fe-Cr alloys*, Computational Materials Science 194, 110435 (2021).

[337] S.-k. Lin, C.-k. Yeh, B. Puchala, Y.-L. Lee, and D. Morgan, *Ab initio energetics of charge compensating point defects: A case study on MgO*, Computational Materials Science 73, 41–55 (2013).

[338] J. S. Park, S. Kim, Z. Xie, and A. Walsh, *Point defect engineering in thin-film solar cells*, Nature Reviews Materials 3, 194–210 (2018).

[339] G. H. Vineyard and G. J. Dienes, *The Theory of Defect Concentration in Crystals*, Physical Review 93, 265–268 (1954).

[340] J. Maier, *Solid State Electrochemistry I: Thermodynamics and Kinetics of Charge Carriers in Solids*, Modern Aspects of Electrochemistry, Modern Aspects of Electrochemistry, Springer, Boston, MA, 2005, pp. 1–173.

[341] A. Hagopian, M.-L. Doublet, J.-S. Filhol, and T. Binninger, *Advancement of the Homogeneous Background Method for the Computational Simulation of Electrochemical Interfaces*, arXiv:2201.04537 [cond-mat, physics:physics] (2022).

[342] J. Buckeridge, *Equilibrium point defect and charge carrier concentrations in a material determined through calculation of the self-consistent Fermi energy*, Computer Physics Communications 244, 329–342 (2019).

[343] L. Zhou, K.-H. Park, X. Sun, F. Lalère, T. Adermann, P. Hartmann, and L. F. Nazar, *Solvent-Engineered Design of Argyrodite Li_6PS_5X (X = Cl, Br, I) Solid Electrolytes with High Ionic Conductivity*, ACS Energy Letters 4, 265–270 (2019).

[344] K. Lejaeghere, V. Van Speybroeck, G. Van Oost, and S. Cottenier, *Error Estimates for Solid-State Density-Functional Theory Predictions: An Overview by Means of the Ground-State Elemental Crystals*, Critical Reviews in Solid State and Materials Sciences 39, 1–24 (2014).

[345] C. Kittel, *Introduction to solid state physics*, 8th ed ed., Wiley, Hoboken, NJ, 2005.

[346] R. Juza and W. Uphoff, *Zur Kenntnis des Lithiumsulfids*, Zeitschrift fÃijr anorganische und allgemeine Chemie 287, 113–119 (1956).

[347] S. Stegmaier, J. Voss, K. Reuter, and A. C. Luntz, *Li+ Defects in a Solid-State Li Ion Battery: Theoretical Insights with a Li_3OCl Electrolyte*, Chemistry of Materials 29, 4330–4340 (2017).

[348] J. C. Conesa, *Computing with DFT Band Offsets at Semiconductor Interfaces: A Comparison of Two Methods*, Nanomaterials 11, 1581 (2021).

[349] L. Priester, *Grain Boundaries: From Theory to Engineering*, Springer Series in Materials Science, Springer Netherlands, 2013.

[350] X. Liu, R. Garcia-Mendez, A. R. Lupini, Y. Cheng, Z. D. Hood, F. Han, A. Sharafi, J. C. Idrobo, N. J. Dudney, C. Wang, C. Ma, J. Sakamoto, and M. Chi, *Local electronic structure variation resulting in Li "filament" formation within solid electrolytes*, Nature Materials, 1–6 (2021).

[351] S. Sasano, R. Ishikawa, K. Kawahara, T. Kimura, Y. H. Ikuhara, N. Shibata, and Y. Ikuhara, *Grain boundary Li-ion conductivity in $(Li_{0.33}La_{0.56})TiO_3$ polycrystal*, Applied Physics Letters 116, 043901 (2020).

[352] G. Knöner, K. Reimann, R. Röwer, U. Södervall, and H.-E. Schaefer, *Enhanced oxygen diffusivity in interfaces of nanocrystalline $ZrO_2{\cdot}Y_2O_3$*, Proceedings of the National Academy of Sciences 100, 3870–3873 (2003).

[353] K. Shen, Y. Wang, J. Zhang, Y. Zong, G. Li, C. Zhao, and H. Chen, *Revealing the effect of grain boundary segregation on Li ion transport in polycrystalline anti-perovskite Li_3ClO: a phase field study*, Physical Chemistry Chemical Physics 22, 3030–3036 (2020).

[354] J. A. Dawson, P. Canepa, T. Famprikis, C. Masquelier, and M. S. Islam, *Atomic-Scale Influence of Grain Boundaries on Li-Ion Conduction in Solid Electrolytes for All-Solid-State Batteries*, Journal of the American Chemical Society 140, 362–368 (2018).

[355] H. Grimmer, *Coincidence-site lattices*, Acta Crystallographica Section A: Crystal Physics, Diffraction, Theoretical and General Crystallography 32, 783–785 (1976).

[356] A. H. King and A. Singh, *Generalizing the coincidence site lattice model to non-cubic materials*, Journal of Physics and Chemistry of Solids 55, 1023–1033 (1994).

[357] S. Gokhale, K. H. Nagamanasa, R. Ganapathy, and A. K. Sood, *Grain growth and grain boundary dynamics in colloidal polycrystals*, Soft Matter 9, 6634–6644 (2013).

[358] W. Meyer and H. Neldel, *Relation between the energy constant and the quantity constant in the conductivity-temperature formula of oxide semiconductors*, Z. tech. Phys 18, 588–593 (1937).

[359] S. Muy, J. C. Bachman, H.-H. Chang, L. Giordano, F. Maglia, S. Lupart, P. Lamp, W. G. Zeier, and Y. Shao-Horn, *Lithium Conductivity and Meyer-Neldel Rule in Li_3PO_4-Li_3VO_4-Li_4GeO_4 Lithium Superionic Conductors*, Chemistry of Materials 30, 5573–5582 (2018).

[360] Y. Gao, N. Li, Y. Wu, W. Yang, and S.-H. Bo, *Rethinking the Design of Ionic Conductors Using Meyer-Neldel-Conductivity Plot*, Advanced Energy Materials 11, 2100325 (2021).

[361] P. Vadhva, J. Hu, M. J. Johnson, R. Stocker, M. Braglia, D. J. L. Brett, and A. J. E. Rettie, *Electrochemical Impedance Spectroscopy for All-Solid-State Batteries: Theory, Methods and Future Outlook*, ChemElectroChem 8, 1930–1947 (2021).

[362] J. Koettgen, T. Zacherle, S. Grieshammer, and M. Martin, *Ab initio calculation of the attempt frequency of oxygen diffusion in pure and samarium doped ceria*, Physical Chemistry Chemical Physics 19, 9957–9973 (2017).

[363] A. Van der Ven, G. Ceder, M. Asta, and P. D. Tepesch, *First-principles theory of ionic diffusion with nondilute carriers*, Physical Review B 64, 184307 (2001).

[364] K. Compaan and Y. Haven, *Correlation factors for diffusion in solids*, Transactions of the Faraday Society 52, 786 (1956).

[365] J. Bocquet, *Correlation factor for diffusion in cubic crystals with soluteâĂŞvacancy interactions of arbitrary range*, Philosophical Magazine 94, 3603–3631 (2014).

[366] J.-H. Yang, J.-S. Park, J. Kang, and S.-H. Wei, *First-principles multiple-barrier diffusion theory: The case study of interstitial diffusion in CdTe*, Physical Review B 91, 075202 (2015).

[367] H. JÓNSSON, G. MILLS, and K. W. JACOBSEN, *Nudged elastic band method for finding minimum energy paths of transitions*, pp. 385–404, 1998.

[368] G. Henkelman and H. Jónsson, *Improved tangent estimate in the nudged elastic band method for finding minimum energy paths and saddle points*, The Journal of Chemical Physics 113, 9978–9985 (2000).

[369] G. Henkelman, B. P. Uberuaga, and H. Jónsson, *A climbing image nudged elastic band method for finding saddle points and minimum energy paths*, The Journal of Chemical Physics 113, 9901–9904 (2000).

[370] R. Jalem, Y. Yamamoto, H. Shiiba, M. Nakayama, H. Munakata, T. Kasuga, and K. Kanamura, *Concerted Migration Mechanism in the Li Ion Dynamics of Garnet-Type Li7La3Zr2O12*, Chemistry of Materials 25, 425–430 (2013).

[371] O. C. Ibe, *Elements of random walk and diffusion processes*, John Wiley & Sons, Ltd, 2013.

[372] M. A. Islam, *Einstein-Smoluchowski Diffusion Equation: A Discussion*, Physica Scripta 70, 120–125 (2004).

[373] W. Zhang, H.-C. Yu, L. Wu, H. Liu, A. Abdellahi, B. Qiu, J. Bai, B. Orvananos, F. C. Strobridge, X. Zhou, Z. Liu, G. Ceder, Y. Zhu, K. Thornton, C. P. Grey, and F. Wang, *Localized concentration reversal of lithium during intercalation into nanoparticles*, Science Advances 4, eaao2608 (2018).

[374] B. J. Alder, D. M. Gass, and T. E. Wainwright, *Studies in Molecular Dynamics. VIII. The Transport Coefficients for a Hard-Sphere Fluid*, The Journal of Chemical Physics 53, 3813–3826 (1970).

[375] L. J. Miara, N. Suzuki, W. D. Richards, Y. Wang, J. C. Kim, and G. Ceder, *Li-ion conductivity in Li_9S_3N*, Journal of Materials Chemistry A 3, 20338–20344 (2015).

[376] G. E. Murch, *The haven ratio in fast ionic conductors*, Solid State Ionics 7, 177–198 (1982).

[377] J. Qi, S. Banerjee, Y. Zuo, C. Chen, Z. Zhu, M. L. Holekevi Chandrappa, X. Li, and S. P. Ong, *Bridging the gap between simulated and experimental ionic conductivities in lithium superionic conductors*, Materials Today Physics 21, 100463 (2021).

[378] J.-M. Doux, Y. Yang, D. H. S. Tan, H. Nguyen, E. A. Wu, X. Wang, A. Banerjee, and Y. S. Meng, *Pressure effects on sulfide electrolytes for all solid-state batteries*, Journal of Materials Chemistry A 8, 5049–5055 (2020).

[379] T. Famprikis, O. U. Kudu, J. A. Dawson, P. Canepa, F. Fauth, E. Suard, M. Zbiri, D. Dambournet, O. J. Borkiewicz, H. Bouyanfif, S. P. Emge, S. Cretu, J.-N. Chotard, C. P. Grey, W. G. Zeier, M. S. Islam, and C. Masquelier, *Under Pressure: Mechanochemical Effects on Structure and Ion Conduction in the Sodium-Ion Solid Electrolyte Na_3PS_4*, Journal of the American Chemical Society 142, 18422–18436 (2020).

[380] R. W. Keyes, *Volumes of Activation for Diffusion in Solids*, The Journal of Chemical Physics 29, 467–475 (1958).

[381] M. Kumari and N. Dass, *Pressure-dependent self-diffusion and activation volume in solids: Sodium*, Physical Review B 49, 844–848 (1994).

[382] P. L. Gould, *Introduction to Linear Elasticity*, 3rd ed., Springer, New York, 2013.

[383] F. Birch, *Finite Elastic Strain of Cubic Crystals*, Physical Review 71, 809–824 (1947).

[384] F. D. Murnaghan, *The Compressibility of Media under Extreme Pressures*, Proceedings of the National Academy of Sciences 30, 244–247 (1944).

[385] A. Pavese, *About the relations between finite strain in non-cubic crystals and the related phenomenological P-V Equation of State*, Physics and Chemistry of Minerals 32, 269–276 (2005).

[386] M. A. Sattar, M. Javed, M. Benkraouda, and N. Amrane, *The structural stability, lattice dynamics, electronic, thermophysical, and mechanical properties of the inverse perovskites A_3OX: A comparative first-principles study*, International Journal of Energy Research 45, 4793–4810 (2021).

[387] A. Sakuda, A. Hayashi, and M. Tatsumisago, *Sulfide Solid Electrolyte with Favorable Mechanical Property for All-Solid-State Lithium Battery*, Scientific Reports 3, 2261 (2013).

[388] Y. Liu, J. Liu, Q. Sun, D. Wang, K. R. Adair, J. Liang, C. Zhang, L. Zhang, S. Lu, H. Huang, X. Song, and X. Sun, *Insight into the Microstructure and Ionic Conductivity of Cold Sintered NASICON Solid Electrolyte for Solid-State Batteries*, ACS Applied Materials & Interfaces 11, 27890–27896 (2019).

[389] J. M. J. d. Toonder, J. A. W. v. Dommelen, and F. P. T. Baaijens, *The relation between single crystal elasticity and the effective elastic behaviour of polycrystalline materials: theory, measurement and computation*, Modelling and Simulation in Materials Science and Engineering 7, 909–928 (1999).

[390] R. Hill, *The Elastic Behaviour of a Crystalline Aggregate*, Proceedings of the Physical Society. Section A 65, 349–354 (1952).

[391] M. Sadowski and K. Albe, *Computational study of crystalline and glassy lithium thiophosphates: Structure, thermodynamic stability and transport properties*, Journal of Power Sources 478, 229041 (2020).

[392] K. Okhotnikov, T. Charpentier, and S. Cadars, *Supercell program: a combinatorial structure-generation approach for the local-level modeling of atomic substitutions and partial occupancies in crystals*, Journal of Cheminformatics 8, 17 (2016).

[393] S. Shiotani, K. Ohara, H. Tsukasaki, S. Mori, and R. Kanno, *Pair distribution function analysis of sulfide glassy electrolytes for all-solid-state batteries: Understanding the improvement of ionic conductivity under annealing condition*, Scientific Reports 7, 6972 (2017).

[394] G. S. E. Antipas and K. T. Karalis, *Direct determination of amorphous number density from the reduced pair distribution function*, MethodsX 6, 601–605 (2019).

[395] Z. Zhu, I.-H. Chu, Z. Deng, and S. P. Ong, *Role of Na+ Interstitials and Dopants in Enhancing the Na+ Conductivity of the Cubic Na3PS4 Superionic Conductor*, Chemistry of Materials 27, 8318–8325 (2015).

[396] A. A. Emery and C. Wolverton, *High-throughput DFT calculations of formation energy, stability and oxygen vacancy formation energy of ABO3 perovskites*, Scientific Data 4, 170153 (2017).

[397] W. Sun, S. T. Dacek, S. P. Ong, G. Hautier, A. Jain, W. D. Richards, A. C. Gamst, K. A. Persson, and G. Ceder, *The thermodynamic scale of inorganic crystalline metastability*, Science Advances 2, e1600225 (2016).

[398] S. Muy, J. C. Bachman, L. Giordano, H.-H. Chang, D. L. Abernathy, D. Bansal, O. Delaire, S. Hori, R. Kanno, F. Maglia, S. Lupart, P. Lamp, and Y. Shao-Horn, *Tuning mobility and stability of lithium ion conductors based on lattice dynamics*, Energy & Environmental Science 11, 850–859 (2018).

[399] Y. Zhang, Y. Zhao, and C. Chen, *Ab initio study of the stabilities of and mechanism of superionic transport in lithium-rich antiperovskites*, Physical Review B 87, 134303 (2013).

[400] G. K. P. Dathar, J. Balachandran, P. R. C. Kent, A. J. Rondinone, and P. Ganesh, *Li-ion site disorder driven superionic conductivity in solid electrolytes: a first-principles investigation of β-Li_3PS_4*, Journal of Materials Chemistry A 5, 1153–1159 (2017).

[401] J. Zhang, L. Wang, J. Zhu, and Y. Zhao, *Structural disorder, sublattice melting, and thermoelastic properties of anti-perovskite Li_3OBr under high pressure and temperature*, Applied Physics Letters 117, 081904 (2020).

[402] M. J. Mitchell and J. A. McCammon, *Free energy difference calculations by thermodynamic integration: Difficulties in obtaining a precise value*, Journal of Computational Chemistry 12, 271–275 (1991).

[403] C. Lee, D. Vanderbilt, K. Laasonen, R. Car, and M. Parrinello, *Ab initio studies on the structural and dynamical properties of ice*, Physical Review B 47, 4863–4872 (1993).

[404] A. Hayashi, S. Hama, F. Mizuno, K. Tadanaga, T. Minami, and M. Tatsumisago, *Characterization of Li2SâĂŞP2S5 glass-ceramics as a solid electrolyte for lithium secondary batteries*, Solid State Ionics 175, 683–686 (2004).

[405] M. Tatsumisago and A. Hayashi, *Sulfide Glass-Ceramic Electrolytes for All-Solid-State Lithium and Sodium Batteries*, International Journal of Applied Glass Science 5, 226–235 (2014).

[406] Y. Seino, M. Nakagawa, M. Senga, H. Higuchi, K. Takada, and T. Sasaki, *Analysis of the structure and degree of crystallisation of 70Li2SâĂŞ30P2S5 glass ceramic*, Journal of Materials Chemistry A 3, 2756–2761 (2015).

[407] K. Xiong, R. C. Longo, S. KC, W. Wang, and K. Cho, *Behavior of Li defects in solid electrolyte lithium thiophosphate $Li_7P_3S_{11}$: A first principles study*, Computational Materials Science 90, 44–49 (2014).

[408] Y. Luo, M. Shui, and J. Shu, *Understanding the lithium transport mechanism in monoclinic $li_3v_2(po_4)_3$ cathode material by atomistic simulation*, Results in Physics 14, 102490 (2019).

[409] Y. Noda, K. Nakano, M. Otake, R. Kobayashi, M. Kotobuki, L. Lu, and M. Nakayama, *Research Update: Ca doping effect on the Li-ion conductivity in NASICON-type solid electrolyte $LiZr_2(PO_4)_3$: A first-principles molecular dynamics study*, APL Materials 6, 060702 (2018).

[410] D. Di Stefano, A. Miglio, K. Robeyns, Y. Filinchuk, M. Lechartier, A. Senyshyn, H. Ishida, S. Spannenberger, D. Prutsch, S. Lunghammer, D. Rettenwander, M. Wilkening, B. Roling, Y. Kato, and G. Hautier, *Superionic Diffusion through Frustrated Energy Landscape*, Chem 5, 2450–2460 (2019).

[411] B. Kozinsky, *Transport in Frustrated and Disordered Solid Electrolytes*, Handbook of Materials Modeling (W. Andreoni and S. Yip, eds.), Springer International Publishing, Cham, 2018, pp. 1–20.

[412] M. Burbano, D. Carlier, F. Boucher, B. J. Morgan, and M. Salanne, *Sparse Cyclic Excitations Explain the Low Ionic Conductivity of Stoichiometric $Li_7La_3Zr_2O_{12}$*, Physical Review Letters 116, 135901 (2016).

[413] B. J. Morgan, *Understanding fast-ion conduction in solid electrolytes*, Philosophical Transactions of the Royal Society A: Mathematical, Physical and Engineering Sciences 379, 20190451 (2021).

[414] A. Bhandari and J. Bhattacharya, *Origin of Fast Ion Conduction in $Li_{10}GeP_2S_{12}$, a Superionic Conductor*, The Journal of Physical Chemistry C 120, 29002–29010 (2016).

[415] R. F. W. Bader, *Atoms in Molecules: A Quantum Theory*, International Series of Monographs on Chemistry, Oxford University Press, Oxford, New York, May 1994.

[416] A. G. Squires, D. O. Scanlon, and B. J. Morgan, *Native Defects and Their Doping Response in the Lithium Solid Electrolyte $Li_7La_3Zr_2O_{12}$*, Chemistry of Materials 32, 1876–1886 (2020).

[417] Y. Zhu, J. G. Connell, S. Tepavcevic, P. Zapol, R. Garcia-Mendez, N. J. Taylor, J. Sakamoto, B. J. Ingram, L. A. Curtiss, J. W. Freeland, D. D. Fong, and N. M. Markovic, *Dopant-Dependent Stability of Garnet Solid Electrolyte Interfaces with Lithium Metal*, Advanced Energy Materials 9, 1803440 (2019).

[418] J. Wolfenstine, J. L. Allen, J. Read, and J. Sakamoto, *Chemical stability of cubic $Li_7La_3Zr_2O_{12}$ with molten lithium at elevated temperature*, Journal of Materials Science 48, 5846–5851 (2013).

[419] A. Moradabadi and P. Kaghazchi, *Thermodynamics and kinetics of defects in Li_2S*, Applied Physics Letters 108, 213906 (2016).

[420] L. Zhang and J. Guo, *Understanding the Reaction Mechanism of Lithium-Sulfur Batteries by In Situ/Operando X-ray Absorption Spectroscopy*, Arabian Journal for Science and Engineering 44, 6217–6229 (2019).

[421] A. Goyal, P. Gorai, H. Peng, S. Lany, and V. Stevanović, *A computational framework for automation of point defect calculations*, Computational Materials Science 130, 1–9 (2017).

[422] M. Sadowski and K. Albe, *Influence of Br^- / S^{2-} site-exchange on Li diffusion mechanism in Li_6P_S5Br: a computational study*, Philosophical Transactions of the Royal Society A: Mathematical, Physical and Engineering Sciences 379, 20190458 (2021).

[423] J. P. Perdew, A. Ruzsinszky, G. I. Csonka, O. A. Vydrov, G. E. Scuseria, L. A. Constantin, X. Zhou, and K. Burke, *Restoring the Density-Gradient Expansion for Exchange in Solids and Surfaces*, Physical Review Letters 100, 136406 (2008).

[424] Y. Lee, J. Jeong, H.-D. Lim, S.-O. Kim, H.-G. Jung, K. Y. Chung, and S. Yu, *Superionic Si-Substituted Lithium Argyrodite Sulfide Electrolyte $Li_{6+x}Sb_{1-x}Si_xS_5I$ for All-Solid-State Batteries*, ACS Sustainable Chemistry & Engineering 9, 120–128 (2021).

[425] P. Adeli, J. D. Bazak, A. Huq, G. R. Goward, and L. F. Nazar, *Influence of Aliovalent Cation Substitution and Mechanical Compression on Li-Ion Conductivity and Diffusivity in Argyrodite Solid Electrolytes*, Chemistry of Materials 33, 146–157 (2021).

[426] C. O'Rourke and B. J. Morgan, *Interfacial strain effects on lithium diffusion pathways in the spinel solid electrolyte Li-doped $MgAl_2O_4$*, Physical Review Materials 2, 045403 (2018).

[427] N. Minafra, S. P. Culver, C. Li, A. Senyshyn, and W. G. Zeier, *Influence of the Lithium Substructure on the Diffusion Pathways and Transport Properties of the Thio-LISICON $Li_4Ge_{1-x}Sn_xS_4$*, Chemistry of Materials 31, 3794–3802 (2019).

[428] Z. Deng, Z. Wang, I.-H. Chu, J. Luo, and S. P. Ong, *Elastic Properties of Alkali Superionic Conductor Electrolytes from First Principles Calculations*, Journal of The Electrochemical Society 163, A67–A74 (2016).

[429] N. Kuwata, X. Lu, T. Miyazaki, Y. Iwai, T. Tanabe, and J. Kawamura, *Lithium diffusion coefficient in amorphous lithium phosphate thin films measured by secondary ion mass spectroscopy with isotope exchange methods*, Solid State Ionics 294, 59–66 (2016).

[430] Y. A. Du and N. a. W. Holzwarth, *Li Ion Diffusion Mechanisms in the Crystalline Electrolyte γ-Li_3PO_4*, Journal of The Electrochemical Society 154, A999 (2007).

[431] Y. A. Du and N. A. W. Holzwarth, *Mechanisms of li^+ diffusion in crystalline γ- and β-li_3po_4 electrolytes from first principles*, Physical Review B 76, 174302 (2007).

[432] S. Zhao, C. Chen, H. Li, and W. Zhang, *Theoretical insights into the diffusion mechanism of alkali ions in Ruddlesden-Popper antiperovskites*, New Journal of Chemistry 45, 4219–4226 (2021).

[433] S. Yu and D. J. Siegel, *Grain Boundary Contributions to Li-Ion Transport in the Solid Electrolyte $Li_7La_3Zr_2O_{12}$ (LLZO)*, Chemistry of Materials 29, 9639–9647 (2017).

[434] P. Bron, S. Johansson, K. Zick, J. Schmedt auf der Günne, S. Dehnen, and B. Roling, *$Li_{10}SnP_2S_{12}$: An Affordable Lithium Superionic Conductor*, Journal of the American Chemical Society 135, 15694–15697 (2013).

[435] H. Jiang, Y. Han, H. Wang, Y. Zhu, Q. Guo, H. Jiang, C. Zheng, and K. Xie, *Facile synthesis of a mixed-conductive Li_2S composites for all-solid-state lithium-sulfur batteries*, Ionics 26, 4257–4265 (2020).

[436] Z. Lin, Z. Liu, N. J. Dudney, and C. Liang, *Lithium Superionic Sulfide Cathode for All-Solid Lithium-Sulfur Batteries*, ACS Nano 7, 2829–2833 (2013).

[437] H. Chen, A. Pei, D. Lin, J. Xie, A. Yang, J. Xu, K. Lin, J. Wang, H. Wang, F. Shi, D. Boyle, and Y. Cui, *Uniform High Ionic Conducting Lithium Sulfide Protection Layer for Stable Lithium Metal Anode*, Advanced Energy Materials 9, 1900858 (2019).

[438] L. M. Riegger, S.-K. Otto, M. Sadowski, S. Jovanovic, O. Kötz, S. Harm, L. G. Balzat, S. Merz, S. Burkhardt, F. H. Richter, J. Sann, R.-A. Eichel, B. V. Lotsch, J. Granwehr, K. Albe, and J. Janek, *Instability of the Li_7SiPS_8 Solid Electrolyte at the Lithium Metal Anode and Interphase Formation*, Chemistry of Materials 34, 3659–3669 (2022).

[439] A.-K. Hatz, R. Calaminus, J. Feijoo, F. Treber, J. Blahusch, T. Lenz, M. Reichel, K. Karaghiosoff, N. M. Vargas-Barbosa, and B. V. Lotsch, *Chemical Stability and Ionic Conductivity of LGPS-Type Solid Electrolyte Tetra-Li_7SiPS_8 after Solvent Treatment*, ACS Applied Energy Materials 4, 9932–9943 (2021).

[440] *FestBatt Project*, `https://festbatt.net/`.

[441] L. Haarmann and K. Albe, *From ionic to superionic conductivity: The influence of cation order on sodium diffusion in $Na_3Zr_2Si_2PO_{12}$*, Solid State Ionics 363, 115604 (2021).

[442] Z.-H. Fu, X. Chen, C.-Z. Zhao, H. Yuan, R. Zhang, X. Shen, X.-X. Ma, Y. Lu, Q.-B. Liu, L.-Z. Fan, and Q. Zhang, *Stress Regulation on Atomic Bonding and Ionic Diffusivity: Mechanochemical Effects in Sulfide Solid Electrolytes*, Energy & Fuels 35, 10210–10218 (2021).

[443] Z. Q. Wang, M. S. Wu, G. Liu, X. L. Lei, B. Xu, and C. Y. Ouyang, *Elastic Properties of New Solid State Electrolyte Material $Li_{10}GeP_2S_{12}$: A Study from First-Principles Calculations*, Int. J. Electrochem. Sci. 9, 7 (2014).

[444] N. Ramakrishnan, *Speed of sound in porous materials*, Bulletin of Materials Science 17, 499–504 (1994).

[445] Radjai, Maouche, Guechi, Cheddadi, and Kechidi, *Investigation of structural and elastic properties of monoclinic Ba_2P_7X (X = Cl, Br, I) Zintl Salts compounds*, Condensed Matter Physics 22, 33702 (2019).

[446] A. Kato, M. Nose, M. Yamamoto, A. Sakuda, A. Hayashi, and M. Tatsumisago, *Mechanical properties of sulfide glasses in all-solid-state batteries*, Journal of the Ceramic Society of Japan 126, 719–727 (2018).

[447] R. Xu, F. Han, X. Ji, X. Fan, J. Tu, and C. Wang, *Interface engineering of sulfide electrolytes for all-solid-state lithium batteries*, Nano Energy 53, 958–966 (2018).

[448] L. E. Camacho-Forero and P. B. Balbuena, *Exploring interfacial stability of solid-state electrolytes at the lithium-metal anode surface*, Journal of Power Sources 396, 782–790 (2018).

[449] B. Chen, J. Ju, J. Ma, J. Zhang, R. Xiao, G. Cui, and L. Chen, *An insight into intrinsic interfacial properties between Li metals and $Li_{10}GeP_2S_{12}$ solid electrolytes*, Physical Chemistry Chemical Physics 19, 31436–31442 (2017).